Topics in Heterocyclic Chemistry 34
Series Editors: B.U.W. Maes · J. Cossy · S. Polanc

Roberto Paolesse *Editor*

Applications of Porphyrinoids

Springer

34
Topics in Heterocyclic Chemistry

Aims and Scope

The series Topics in Heterocyclic Chemistry presents critical reviews on present and future trends in the research of heterocyclic compounds. Overall the scope is to cover topics dealing with all areas within heterocyclic chemistry, both experimental and theoretical, of interest to the general heterocyclic chemistry community.

The series consists of topic related volumes edited by renowned editors with contributions of experts in the field.

More information about this series at
http://www.springer.com/series/7081

Roberto Paolesse
Editor

Applications of Porphyrinoids

With contributions by

S. Bettini · N.V.S.D.K. Bhupathiraju · A. D'Urso · M.E. Fragalà · G. Giancane · C. Goletti · R.K. Pandey · N.J. Patel · R. Purrello · L. Valli · M.G.H. Vicente · S. Zhang

Springer

Editor
Roberto Paolesse
Dept. of Chemical Science and Technologies
University of Rome Tor Vergata
Rome
Italy

ISSN 1861-9282 ISSN 1861-9290 (electronic)
ISBN 978-3-662-43996-8 ISBN 978-3-662-43997-5 (eBook)
DOI 10.1007/978-3-662-43997-5
Springer Heidelberg New York Dordrecht London

Library of Congress Control Number: 2014957174

Printed on acid-free paper

Springer is part of Springer Science+Business Media (www.springer.com)

Preface

Porphyrins are ubiquitous in nature, where they are essential for life. With simple synthetic modifications, nature is able to use porphyrinoids to perform functions that are completely different and difficult to realize, such as solar energy conversion or oxygen activation and transport. For this reason, these macrocycles have attracted the attention of researchers belonging to different disciplines, such as biomedicine, catalysts, photonics, molecular electronics, and sensors' development, with the aim to mimic these functions for practical applications.

Porphyrins are versatile playthings for organic chemists, owing to the possibility to transfer their peculiar properties from a single molecule to mesoscopic scale, achieving functional materials or novel therapeutic drugs.

While the complete coverage of porphyrinoid exploitations is not possible, considering the large area interested by these macrocycles, this second volume related to porphyrinoid chemistry of Topics in Heterocyclic Chemistry is focused on some examples of porphyrinoid application fields, presenting five contributions authored by leading researchers in the field.

The first chapter of this second volume is provided by Ravindra K. Pandey, with Shunqing Zhang and Nayan J. Patel. In the chapter the authors describe the recent developments of compounds as theranostic agents, able to perform both imaging (e.g., PET/fluorescence, MRI/fluorescence) and photodynamic therapy (PDT) functions.

The second chapter presents another promising application of porphyrinoids in the clinical field, reporting the development of boronated porphyrins and derivatives, as a class of highly promising third-generation boron delivery agents for boron neutron capture therapy (BNCT), a binary and highly localized form of treatment for brain tumors. This chapter is authored by N.V.S. Dinesh K. Bhupathiraju and M. Graça H. Vicente.

The third chapter moves to a different application field of porphyrinoids, and Claudio Goletti describes the results obtained by using the reflectance anisotropy spectroscopy (RAS) to characterize the optical anisotropy of thin and ultrathin porphyrin films. This technique, originally conceived for inorganic surfaces, can

be particularly useful to give unique information of porphyrin films, to be applied for optical sensing and photovoltaic applications.

Following this route, the next chapter reports several examples of LB and LS films of porphyrin derivatives both used for the realization of photovoltaic devices and for studying the charge transfer processes. The thin film deposition of dyes is in fact of paramount importance for the realization of photovoltaic devices, where porphyrinoids can mimic the role played in the biological systems. The chapter is authored by Simona Bettini, Ludovico Valli, and Gabriele Giancane.

In the last chapter Alessandro D'Urso, Maria Elena Fragalà, and Roberto Purrello report a complete overview of porphyrinoid–duplex DNA complexes. These supramolecular complexes are widely studied for their potential applications in different fields, ranging from biosensors to medicinal chemistry.

I hope that the two volumes dedicated to the porphyrinoids chemistry can allow the readers to appreciate the richness and the enormous potentialities of our beautiful macrocycles, which was my aim in editing these books. For this result, I should give my thanks to the chapter authors for their excellent contributions.

Rome, Italy Roberto Paolesse

Contents

Top Heterocycl Chem (2014) 34: 1–30
DOI: 10.1007/7081_2013_117

Published online: 7 March 2014

Chlorophyll-*a* Analogs for Cancer Imaging and Therapy (Theranostics)

Shunqing Zhang, Nayan J. Patel, and Ravindra K. Pandey

Abstract The utility of porphyrin-based compounds as photosensitizers in photodynamic therapy (PDT) has been evolving since the mid-1970s. There are a large number of publications including research papers, reviews, and books on basic sciences and clinical applications of PDT. The current research on PDT has been focused on developing agents with enhanced tumor specificity. Efforts are also under way in various laboratories to develop multifunctional agents. In other words, is it possible to use a single agent for cancer imaging and PDT? This chapter briefly describes the recent developments in developing such agents, which could be used for dual-function imaging (e.g., PET/fluorescence, MRI/fluorescence) with an option of PDT. The utility of biocompatible and biodegradable nanoparticles over the synthetic approach for achieving the desired goal is also discussed.

Keywords Image-guided cancer therapy · Photodynamic therapy · Polymer conjugates · Porphyrin derivatives · Theranostics

Contents

S. Zhang
PDT Center, Cell Stress Biology, Buffalo, NY 14263, USA

N.J. Patel and R.K. Pandey (✉)
PDT Center, Cell Stress Biology, Buffalo, NY 14263, USA

Department of Pharmacology and Therapeutics, Roswell Park Cancer Institute, Buffalo, NY 14263, USA
e-mail: Ravindra.Pandey@RoswellPark.org

Abbreviations

AHM	3-(Acryloyloxy)-2-hydroxypropyl methacrylate
APMA	*N*-(3-Aminopropyl)methacrylamide
CA	Contrast agent
CE	Contrast enhancement
CLIO	Cross-linked iron oxide
CT	Computed tomography
DOTA	1,4,7,10-Tetraazacyclododecane-1,4,7,10-tetraacetic acid
DTPA	Diethylene triamine pentaacetic acid
FDA	Food and drug administration
FDG	Fluorodeoxyglucose
FITC	Fluorescein isothiocyanate
FMT	Fluorescence-mediated tomography
FRET	Fluorescence resonance energy transfer
GQL	Good quality of life
HPPH	3-(1′-hexyloxy)ethyl-3-devinyl pyropheophorbide-alpha
ICG	Indocyanine green
MB	Methylene blue
MRI	Magnetic resonance imaging
NIR	Near infrared
NP	Nanoparticle
PAA	Polyacrylamide
PDT	Photodynamic therapy
PEG	Polyethylene glycol
PET	Positron emission tomography
PS	Photosensitizer
ROI	Region of interest
SPECT	Single-photon emission computed tomography
US	Ultrasound

1 Introduction

1.1 Importance of Imaging

Heart disease remains the major cause of death among Americans; however, public awareness coupled with improved diet and medicines has led to a drastic reduction in annual number of deaths per 100,000 people [1]. Unfortunately even with

decades of advancements in the development of anticancer compounds, studies still show that age-related death rates for people with cancer have not improved [2]. Next-generation drugs are able to overcome resistances to first-line chemotherapeutics and in many cases improve safety profiles. However, if there is ultimately no improvement in survival rates, then the only effect these new drugs are having on the public is maintaining high health-care costs. Current advancements in medical imaging techniques are aimed at offering the opportunity to make a significant change in cancer treatment, which could produce cancer cures or long-term survival with good quality of life (GQL). While conventional imaging instrumentation is very effective, advancements in machinery and improved understanding of computer models and the physics behind a lot of these technologies have ushered in an era of exponential growth in cancer imaging. It is now the belief of many that while chemotherapeutics hold an undeniable importance in the treatment of cancer, it is through improved imaging systems where the real improvements can be made to lead to the overall reduction in cancer deaths.

Among these conventional imaging modalities, magnetic resonance imaging (MRI) bears the greatest clinical utility due to its versatility [3]. Not only does MRI provide superb spatial resolution and unparalleled soft tissue contrast in living subjects, but it can also detect certain tissue functions and molecular species via the use of specialized MRI techniques, some of which do not rely on the use of target-specific contrast-enhancing agents [4]. Therefore, MRI permits concurrent collection of anatomical and physiological information of the disease state. In addition, MRI has two advantages that make it stand out among other imaging modalities [5]. Unlike positron emission tomography (PET), single-photon emission computed tomography (SPECT), or computed tomography (CT), MRI does not use dangerous ionizing radiation which leads to the second advantage which is that there is no upper limit to the scanning frequency of a patient in a specific time span. However, MRI has very poor sensitivity when compared with other imaging modalities, and this has many manifestations [6]. First, MRI acquisition can take a long time and a large dose of imaging agents to produce adequate signal. As a result, a particular subset of patients is predisposed to potential health complications when using contrast-enhancing agents (insert renal toxicity data). Another result of the poor sensitivity, and therefore high requirement of MRI contrast agents, is that it creates a difficult-to-solve challenge for researchers to design target-specific probes when cellular and molecular targets exist in low concentrations in living subjects [7]. The high amounts of image contrast agents are one of the major reasons why MRI is such an expensive imaging modality. When considering cost, one must also consider not only the high cost of purchasing MRI machines but also the high cost of their maintenance. MRI magnets can only effectively function when they are cooled below their critical temperature. In order to achieve this, liquid helium is used as a coolant; however, with the current global supply of helium shrinking, the cost to operate MRI machines has increased. Overall, MR imaging is extremely potent, although it is not the most sensitive and cost-effective modality. Not only has MRI revolutionized clinical cancer diagnostics, it also adds a powerful tool to

researchers' repertoire in cancer research, enabling them to scrutinize molecular processes in single cells, perfused organs, and intact living animals [8–13].

CT employs tomographic imaging to reconstruct the differential X-ray attenuation by tissues within the body into three-dimensional images reflecting anatomy. It is among the most widely used imaging tools in hospitals [14]. At present, CT is a structural imaging modality, which identifies anatomical patterns, and its use in oncology is that it provides information regarding tumor location, size, and spread based on endogenous contrast. CT contrast agents are predominantly based on iodine-containing molecules, although efforts are under way to develop target-specific gold nanoparticles and enable the application of CT in molecular imaging.

PET and SPECT depend upon the identification or synthesis of target-specific pharmaceuticals, which are tagged with a radionuclide and are used as imaging agents [15]. Through tracing their distribution in the body, PET and SPECT are functional imaging modalities that enable whole-body evaluation of the level of molecular targets/processes within a living subject. Like CT, PET and SPECT employ ionizing radiation, which raise concern about their safety profiles. As a result, there is a limit to how many scans a subject can have in a given time frame.

Ultrasound (US) is another structural imaging modality [16] and utilizes the characteristic properties and behavior of high-frequency sound waves as they travel through biological tissue to reconstruct anatomical images. Although it is primarily used to attain structural information, targeted microbubbles are currently being explored for their feasibility as contrast agents that allow US to image processes such as angiogenesis or inflammation. In comparison to CT, US is more cost-effective, more portable, and much safer. However, US is not suitable for body parts containing bones or air. And although resolution of US can improve significantly with higher frequencies, it comes at the cost of depth of tissue penetration of the sound waves.

In terms of clinical usage, one of the fastest growing imaging modalities is fluorescence optical imaging [17]. Fluorescence optical imaging utilizes the phenomenon of fluorescence and uses a noninvasive propagation of visible or near-infrared (NIR) range light through tissue to develop an image. For decades, fluorescence optical imaging techniques have been used in the academic setting where it has been used to trace movement of cells or organelles, production and reaction rates of proteins, and even recombination events within complex organisms. However, light propagation through biological tissue is limited because light is too easily absorbed, reflected, and/or scattered by biological tissue and their components. This has led to limited use clinically, but advancements in image capturing technology and improvements in image reconstruction algorithms have the potential to change that. Perhaps the biggest advantage of optical imaging is that it avoids the DNA-damaging side effects found with imaging modalities which employ ionizing radiation such as CT or PET which is one reason for the increased desire to transition the optical imaging modality into the clinic. Other advantages of optical imaging include fast acquisition, high sensitivity, and lower cost in comparison to other modalities. However, the resolution of optical imaging is very poor as light has limited depth of penetration.

Fluorescence-mediated tomography (FMT) is a subset of optical imaging that plays a prominent role in the preclinical settings for the investigation of molecular processes in intact animals [18]. A major drawback of older optical reflectance imaging is the lack of quantification in the fluorescent light from the source. Fluorescence-mediated tomography is an alternative modality which allows for quantization of signals. This is accomplished because fluorescence tomography enlists multiple light sources, which are paired with multiple detector pairings to generate numerous experimental data to assist the effort to pinpoint and quantify the fluorescence reporter within the tissue. Another benefit of fluorescence tomographic imaging is the ability to reconstruct three-dimensional images, something that traditional reflectance imaging cannot do. Tomographic images have been overlaid with high-resolution datasets generated from MRI, thereby leading to two very complimentary imaging modalities resulting in superior imaging information. In proof of principle study, mouse brain implanted with human glioma tumor cells was examined using MRI-FMT co-registration and led to an improvement in tumor localization [19, 20].

The idea behind creating dual-function or multifunctional compounds lies in the fact that no imaging technique is perfect and all have some drawbacks. Simply, if one technique has a disadvantage and another modality can compensate for this, then the two modalities could be complementary to each other. In case of MRI, the aforementioned cost, sensitivity, and acquisition times are major hindrances, but it excels in resolution and depth of penetration and provides physiological information. Optical imaging on the other hand uses inexpensive probes and has excellent sensitivity, requires small doses, can be used for image-guided therapy, but yields very poor spatial resolution and has limited clinical usage due to depth of penetration. Therefore, it becomes necessary to develop long-wavelength optical imaging agents and combine its use with other imaging techniques.

1.2 Image-Guided Therapy

Real-time imaging of the entire tumor is the goal of image-guided therapy [21]. Conventionally, imaging is done preoperatively, then surgical resection of the tumor is performed, and possibly postsurgical imaging is performed to ensure that the entire tumor has been removed. However, imaging modalities such as fluorescence optical imaging, due to its very short acquisition time and cancer specific probes, offer the ability to imaging during the surgical resection process, thereby ensuring that the entire tumor is removed. Van Dam et al. [22] illustrated the importance of image-guided therapy in their work with intraoperative fluorescence imaging of ovarian cancer in which they used folate-FITC to determine what areas of the patients' ovaries contain cancer which needed to surgically be removed and which areas were normal tissue. In addition to surgery, other methods for tumor ablation can work well with image-guided therapy. One such method is photodynamic therapy (PDT) which currently serves as either a primary or adjunctive

Fig. 1 General structures of porphyrin-based compounds: porphyrins, chlorins, and bacteriochlorins

treatment for solid cancers of the head and neck, brain, lung, pancreas, intraperitoneal cavity, breast, prostate, or skin [23].

2 Tetrapyrrole-Based Compounds for Cancer Imaging and Therapy

Tetrapyrrole-based compounds (e.g., porphyrins, chlorins, and bacteriochlorins, Fig. 1) have shown great potential in the area of photodynamic therapy (PDT) [24–31], which consists of three components: a photosensitizing drug (photosensitizer), light of specific wavelength, and oxygen. Photosensitizer or the prodrug, injected intravenously (i. v.), intraperitoneally (i. p.), or applied topically, circulates systemically and is retained in tumor preferentially compared to normal tissues. When the accumulation of photosensitizer in tumor is optimal, the tumor is illuminated by monochromatic laser light of a specific wavelength.

The photosensitizer, when irradiated with the light, promotes one of its electrons from a ground triplet state to an excited singlet state. This electron can either relax back to the ground state to emit a photon (fluorescence) or undergo intersystem crossing and convert from the excited singlet ($^1\mathbf{PS}^*$) to the excited triplet state ($^3\mathbf{PS}^*$). The excited triplet state can then transfer energy to the surrounding molecules directly in a type I reaction, producing radicals, or it can transfer energy to molecular oxygen in a type II reaction, producing singlet oxygen ($^1\mathbf{O_2}^*$). Although both reaction types are known to happen, experimental evidence suggests that the type II reaction is dominant during PDT [32] (Fig. 2). Singlet oxygen is cytotoxic, damaging cellular molecules and structures directly and decreasing membrane stability, triggering cell death through either necrosis or apoptosis. Furthermore, it destroys the microvasculature, cutting off the tumor oxygen supply, leading to hypoxia in tumor tissues posttreatment. In addition, PDT has been shown to initiate inflammatory and immune responses attacking tumor cells, which serves as an auxiliary mechanism [33].

The class of photosensitizers known as porphyrins holds the greatest promise in image-guided therapy because they can easily be modified to improve target

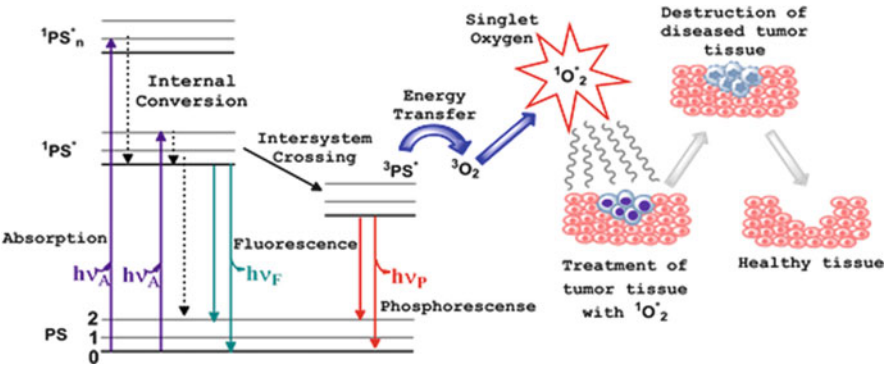

Fig. 2 Ablation of tumor cells after the three essential components (PS, light of the appropriate wavelength, and oxygen) of photodynamic therapy are combined. This usually results in the destruction of diseased tissue without affecting normal tissue. Jablonski diagram for the electronic states of the photosensitizer (PS) is shown on the *left* [32]

specificity and also their tetrapyrrolic structure offers great stability. Porphyrins and their derivative macrocycles, which contain four pyrrole rings joining one another via methane bridges, are by far the most commonly used photosensitizers in PDT. The most notable porphyrin-based photosensitizer is Photofrin™, the FDA-approved photosensitizer currently in use for cancer treatment. By altering the saturation of the bonds by reduction of one or both of the two peripheral cross-conjugated double bonds in the opposite pyrrolic rings that does not affect the macrocycle's aromaticity, porphyrin derivatives are formed. Reducing one of the double bonds of a pyrrole ring yields chlorins; reducing one double bond on two of the pyrrole rings yields bacteriochlorins. The difference in the extent of conjugation has significant effects on their properties as photosensitizers. First of all, porphyrins, e.g., Photofrin™, exhibit weak absorption maxima around 630 nm, while chlorins and bacteriochlorins have strong absorption maxima around 650 and 710 nm, respectively. Since the longer the wavelength of visible light the deeper into human tissue it can penetrate, chlorins and bacteriochlorins are more effective in treating deep-seated tumors than Photofrin™. Furthermore, previous studies have shown that some of the analogs of chlorins and bacteriochlorins have much reduced skin phototoxicity in comparison to Photofrin [34–36]. Therefore, chlorins and bacteriochlorins are better candidates for photosensitizer development than porphyrins. Among the long wavelength-absorbing porphyrin-based photosensitizers (660–800 nm), developed in our laboratory, HPPH stands out because of its tumor avidity, outstanding PDT efficacy, and much reduced skin phototoxicity than Photofrin (an FDA-approved agent and other porphyrin-based compounds) and is currently in phase I/II human clinical trials [37–46].

In this review, we will outline several imaging modalities that are currently being used clinically as well as other underutilized modalities which offer great promise in the future (summarized in Table 1). In addition to imaging, other promising therapeutic approaches to cancer treatment centered on tetrapyrrolic

Table 1 Advantages and limitations of various imaging modalities (table adapted from [7])

Modality	Temporal resolution	Spatial resolution	Depth of penetration	Sensitivity	Cost	Safety profile
Computed tomography	Minutes	High	Limitless	Low	$$	Ionizing radiation
Magnetic resonance imaging	Minutes to hours	High	Limitless	Low	$$$	Non-ionizing radiation
Positron emission tomography	Seconds to minutes	Reasonable	Limitless	High	$$$	Ionizing radiation
Single-photon emission tomography	Minutes	Reasonable	Limitless	High	$$	Ionizing radiation
Ultrasound	Seconds to minutes	Reasonable	Poor	High (w/ microbubbles)	$	Good
Optical fluorescence imaging	Seconds to minutes	Poor	Poor	High	$	Good
Optical bioluminescence imaging	Seconds to minutes	Poor	Poor	High	$	Good

systems are also discussed. Tetrapyrroles are a very diverse class of chemical compounds that offer the ability to be easily manipulated and can serve as an effective scaffold to make multifunctional compounds which allow for both therapy and imaging within a single compound.

2.1 Fluorescence Image-Guided PDT

As with other noninvasive techniques, fluorescence imaging has the potential for performing in vivo diagnosis in situ, with real-time display of the resulting information. Optical tomographic techniques are being devised to visualize the fluorescent probes within tumor volumes. Optical imaging instruments may be simpler and less expensive to operate than those required for other imaging technologies permitting their eventual application by less specialized medical centers. Therapeutically, in applications such as endoscopic examination, fluorescence imaging can allow precise assessment of the localization and a size of the tumor and provide information on its invasiveness. During debulking surgery, where malignant loci can be difficult to identify, the presence of fluorescent signal might assist the surgeon in identifying the diseased site.

The optimal wavelength range for in vivo fluorescence excitation and emission is determined by tissue optical properties. Hemoglobin has strong absorption at wavelength less than 600 nm and there can be significant background fluorescence from endogenous biomolecules up to about 680 nm. At longer wavelengths into the NIR, tissue absorption and scattering decrease with wavelength [47, 48]. There is a large increase in light penetration as wavelength increases from 600 to 800 nm. In addition, the difference between the optical imaging fluorophore's absorption and emission bands (i.e., its Stokes shift) should be at least 20 nm, to readily discriminate between the excitation and emission light. Many NIR fluorescent dyes are based on carbocyanine molecules such as indocyanine green (ICG), an FDA-approved agent with a 730 nm excitation and 830 nm emission maxima. A challenge has been to deliver the dyes selectively and in high enough concentration to detect small tumors. Use of ICG alone to image hypervascular or "leaky" angiogenic vessels around tumors has been disappointing, due to the dye's limited intrinsic tumor selectivity. Multiple approaches have been employed to improve optical probe localization, including administering it in a quenched form that is activated within tumors, or coupling the fluorescent agents to antibodies, or small molecules such as receptor ligands. Some of the peptides and folic acid analogs of certain ICG derivatives have shown some tumor specificity. A few years ago, Achilefu's group [49] reported that certain multicarboxylate-containing carbocyanine probes used as optical scaffolds not only serve as fluorescent antennae but also participate in structural assembly of the multivalent molecular construct. However, none of these compounds were designed for both tumor detection and therapy.

In addition to their therapeutic functions, porphyrin-based structures are also viable fluorophore for optical fluorescence imaging [50, 51]. Because of their tumor avidity, porphyrins can differentiate normal tissues and tumors, which enable them to enlist the help of imaging to locate tumor and guide treatment efforts with surgery and PDT. Porphyrins, therefore, fall into the category of theranostic agents, which combine diagnostic and therapeutic functionalities and are capable of simultaneous diagnosis of cancer and treatment. Furthermore, porphyrin structures have several functional groups on their periphery that are accessible for further chemical modifications that introduce additional imaging functionalities. This enables the use of porphyrin-based compounds for multimodal imaging, the synergistic use of multiple imaging modalities to complement detailed gross anatomy with disease-state physiology [52]. However, most of the porphyrin-based compounds (with a few exceptions) are not ideal candidates for optical imaging due to limited Stokes shift(s) between longest wavelength absorption and emission. Finally, most of them have relatively short absorption wavelengths, <800 nm, which are not optimal for tissue penetration.

In our attempts to investigate the utility of tumor-avid porphyrin-based agents as vehicles to deliver non-tumor-specific cyanine dyes (CD), we linked it to a clinically relevant photosensitizer, the hexyl ether derivative of pyropheophorbide-a (HPPH) [53, 54]. The resulting candidate (HPPH-CD) was found to be an efficient tumor-imaging (fluorescence imaging) and PDT agent. Interestingly, compared to HPPH, the HPPH-CD conjugate produced a significantly higher uptake in tumor than skin, with limited skin phototoxicity. However, there was a significant difference between the imaging and therapy dose. The reason being a part of the singlet oxygen (a key cytotoxic agent in PDT) produced by exciting the PS with light (665 nm) was quenched by the cyanine dye moiety. Therefore, several PS-CD conjugates were designed with strategies such as increasing the length of linkers joining the PS and CD moieties and introducing the CD at variable position of the PS [55, 56]. Such strategies showed an indirect correlation between FRET and singlet oxygen producing efficiency. In other words, conjugate with more FRET showed less singlet oxygen production and reduced PDT efficacy. In another approach, increasing the number of HPPH moiety in HPPH-CD conjugate from 1 to 2 (Fig. 3) further enhanced its PDT efficacy with similar tumor-imaging ability. The development of tumor imaging or efficient PDT agent by itself represents an important step, but a dual-function agent provides the potential for tumor detection and targeted PDT (Scheme 1).

Among the purpurinimide-CD conjugates in which the CD containing a carboxylic acid functionality was covalently linked with N-substituted purpurinimides bearing variable number of N-alkyl amines (Fig. 4), the conjugate containing a linker with two carbon chains (CH_2–CH_2) was most effective and also showed excellent tumor uptake and fluorescence-imaging ability at 24 h postinjection in BALB/c mice bearing Colon26 tumors [57].

To investigate the impact of certain metallated PS-CD conjugates in fluorescence imaging and PDT, we synthesized a series of purpurinimide-CD conjugates in which the CD was introduced at position-20 of the tetrapyrrolic system [58]. In

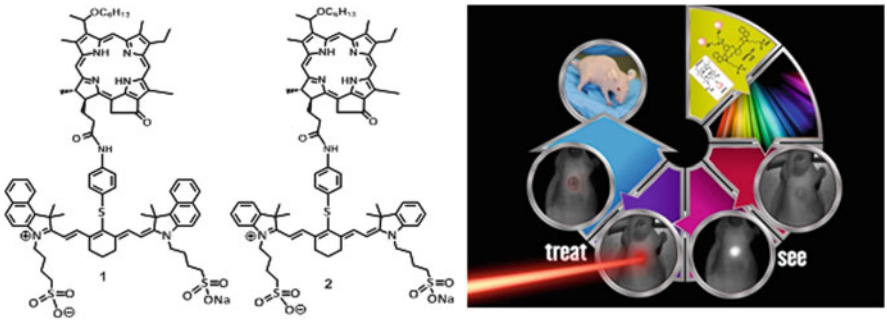

Fig. 3 Structures of dual-function agents in which the HPPH is conjugated to a cyanine dye containing bis-benzoindole and bis-indole moieties with amide linkages

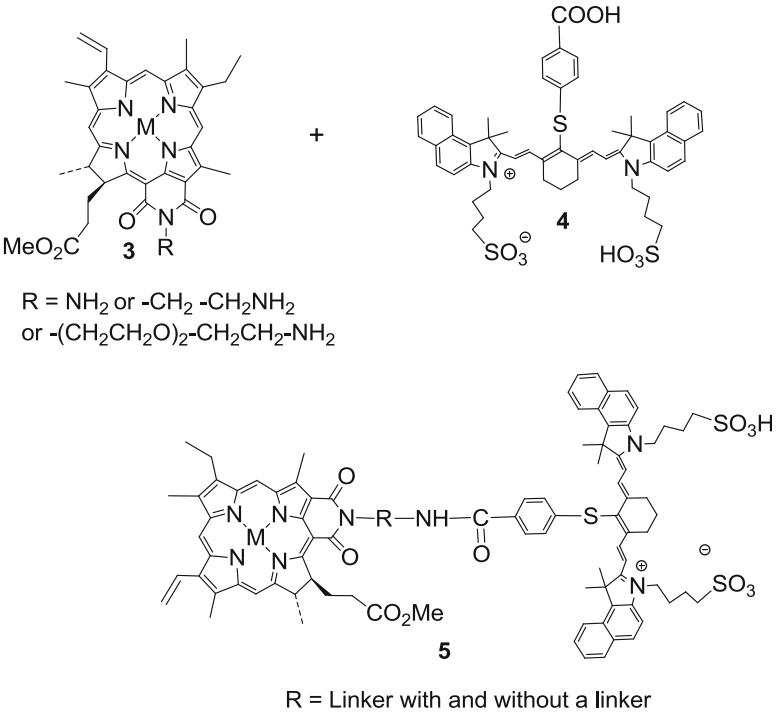

Scheme 1 Purpurinimide-CD conjugates. Among these analogs, the conjugate X (R = CH_2–CH_2) showed improved PDT efficacy than the HPPH-CD conjugate in BALB/c mice bearing Colon26 tumors

brief, the reaction of *meso*-substituted purinimide with *N*-bromosuccinimide regioselectively introduced a bromo-functionality at position-20, which on further reacting with a variety of boronic acids under Suzuki reaction conditions yielded the corresponding *meso*-substituted analogs (Scheme 2).

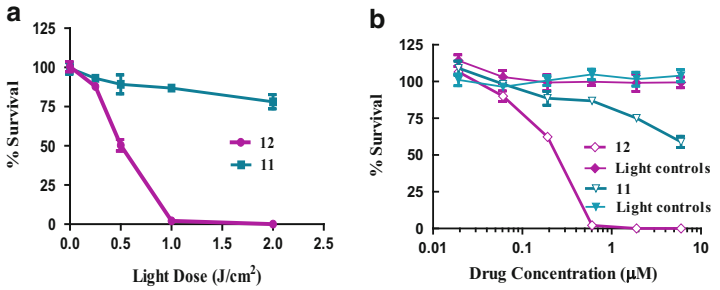

Fig. 4 In vitro photosensitizing efficacy (MTT assay) of Ni(II) purpurinimide-cyanine dye conjugate **11** and the corresponding non-metallated analog **12**; (**a**) PDT efficacy at a fixed concentration of the photosensitizers, but the cells were exposed to variable light doses, (**b**) PDT efficacy at a fixed light dose, but at variable concentrations. On exposing the cells with light without incubating with photosensitizers **11** and **12**, no dark toxicity (cell kill) was observed. The cells were incubated for 24 h before the light exposure

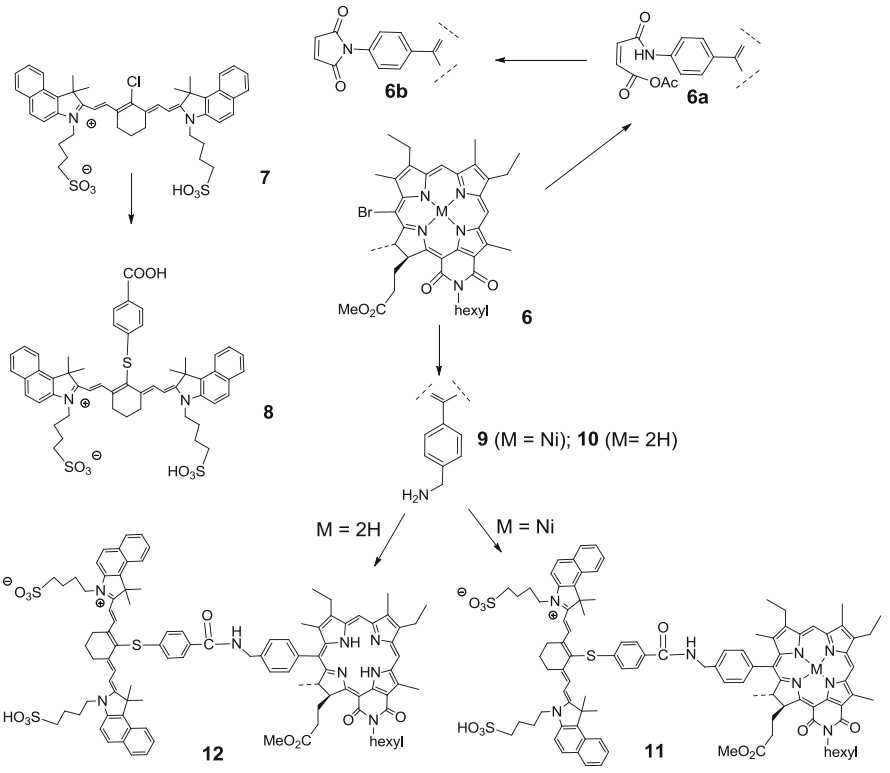

Scheme 2 Synthesis of metallated [Ni(II)] and free-base mesopurpurinimide-cyanine dye conjugates

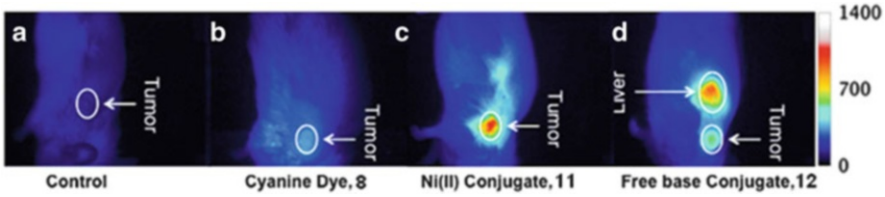

Fig. 5 Whole-body fluorescence imaging of (**a**) control mouse, (**b**) cyanine dye **8**, (**c**) conjugate **11**, and (**d**) conjugate **12** at a dose of 0.3 μmol/kg, 24 h post-intravenous injection

The free base showed significant in vitro PDT efficacy, but limited tumor avidity in mice bearing tumors, whereas the corresponding Ni(II) derivative did not produce any PDT-mediated cell kill but showed excellent tumor-imaging ability at a dose of 0.3 μmol/kg at 24, 48, and 72 h postinjection (Figs. 4 and 5). The limited PDT efficacy of Ni(II) analog could be due to its inability to produce singlet oxygen. Based on electrochemical and spectroelectrochemical data in DMSO, the first one-electron oxidation and the first one-electron reduction of both the free base and the corresponding Ni(II) conjugates were centered, while the second one-electron reduction of the two conjugates is assigned to the purpurinimide part of the molecule. Reduction of the CD unit is facile and occurs prior to reduction of the purpurinimide group, suggesting that the CD unit could be a driving force to quench the produced singlet oxygen as an oxidant. An obvious interaction between the CD and the purpurinimide group is observed for the free-base conjugate, as compared to a negligible interaction between two the functional groups in the case of the Ni(II) conjugate. As a result, the larger HOMO–LUMO gap of the free-base conjugate and the corresponding smaller quenching constant is considered to be a reason to avoid singlet oxygen quenching to some degree.

2.2 MR/Fluorescence Imaging and PDT

Currently, the most widespread MRI contrast agents (CAs) are gadolinium (Gd)-based nonspecific agents such as Magnevist® (Gd-DTPA) for contrast enhancement (CE). While providing powerful contrast efficacy and excellent safety in patients without severe dysfunction, these CAs lack real specificity for depicting certain tissue, organ, and disease. These characteristics have limited the diagnostic capacity of contrast-enhanced MRI in both clinical and experimental settings.

Therefore, the use of tumor-avid porphyrin-based compounds as vehicles to deliver the Gd(III) ion to tumor has been investigated in various laboratories. Since the ring structure of porphyrins and chlorins are too small to adequately accommodate Gd, Gd-labeled porphyrins and metalloporphyrins were difficult to synthesize and found to be unstable. However, in expanded porphyrin systems, the Gd can be inserted with a high stability of the resulting product, and certain Gd analogs, e.g., Gd(III) Texaphyrin [59], are under clinical trials with promising

results. The approach which has been quite successful in incorporating Gd to porphyrin-based compounds has been to link the tetrapyrrolic system to diethylene triamine pentaacetic acid (DTPA) or 1,4,7,10-tetraazacyclododecane-1,4,7,10-tetraacetic acid (DOTA) in which Gd can easily be chelated. Gadoporphyrin-2 [60], in which the paramagnetic metal was chelated to DTPA side chains, showed a favorable safety profile with high stability. Additionally, it showed remarkable target specificity to necrotic tumor tissue. For the last few years, the Roswell Park group has been developing dual-function imaging agents (MR/fluorescence) with an option of NIR PDT. In their initial study, HPPH was conjugated with variable number of Gd-DTPA [61]. The synthetic methodologies for HPPH-2Gd(III)DTPA and HPPH-3Gd(III)DTPA are illustrated in Schemes 3 and 4, respectively. It was observed that by increasing the number of Gd(III)DTPA, moiety enhances the tumor contrast to some extent (Table 2). Among the conjugates investigated containing 2 to 6 Gd(III)DTPA moieties [62, 63], both 2- and 3-Gd(III)DTPA-HPPH conjugates showed excellent tumor-imaging (MR and fluorescence) and PDT efficacy in tumored mice and rats (Figs. 6, 7, 8, and 9). However, the conjugate with 3-Gd(III)DTPA was easier to formulate in PBS and was selected for a detailed investigation. Interestingly, the conjugate even at 8-fold higher than the imaging dose did not show any normal organ toxicity. Compared to Magnevist (current clinical standard), the MR imaging dose of HPPH-3Gd(III)DTPA was 10-fold lower and provides a unique opportunity to develop a single agent for both cancer imaging and therapy.

Shim and coworkers [64] extended this approach and synthesized a series of Gd(III)DTPA-based purpurinimide analogs, in which one or two moieties of purpurin-18-*N*-(2-aminoethyl) were conjugated with DTPA, which on further reaction with gadolinium chloride yielded the desired product (Scheme 5). However, the imaging and PDT efficacy of the Gd-complexes are under investigation.

2.3 PET/Fluorescence Imaging and PDT

In recent years, multimodality systems for in vivo imaging of small animals have become important tools for modern biomedical research, as they offer advantages of combining complimentary characteristics of different modalities. Representative examples of multimodality system are the combination of MRI and CT (computed tomography), CT and fluorescence, and CT and positron emission tomography (PET). A system with PET or SPECT and fluorescence offers advantages because the co-registration of PET and fluorescence images is quite convenient. In recent years, several agents combining both fluorescence and PET-imaging abilities have been developed in various laboratories and have definite advantages over the use of two independent agents with different pharmacokinetic profiles. However, in developing nuclear imaging agents, the selection of radionuclide plays very important role, and it should coincide with the pharmacokinetic properties of the molecule in which the radionuclide is attached.

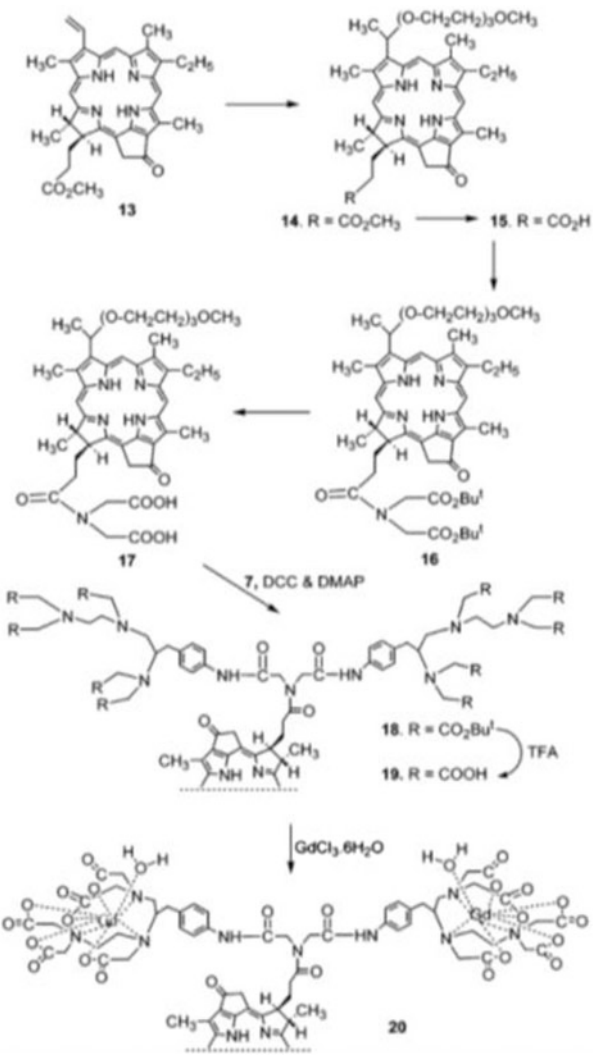

Scheme 3 Synthesis of HPPH-2 Gd(III)DTPA conjugates

The strategy of employing tumor-specific molecules as a vehicle to carry radioactive tracers to target tissue turned out to be very successful and has led to the development of many novel tumor-imaging radiopharmaceuticals [65]. In this regard, ^{111}In-complexes of certain porphyrins have shown significant potential for SPECT imaging. Roswell Park group was the first to show the utility of tumor-avid chlorophyll-*a*-based NIR photosensitizer for dual imaging (PET/fluorescence) with an option of photodynamic therapy [66–70]. Most of the porphyrin-based compounds show optimal tumor uptake at 24–48 h post-administration. Therefore, the radionuclide initially selected was ^{124}I- with a half-life of 4 days, which provides several advantages: (1) the ^{124}I-labeled agent can be synthesized in high yield and

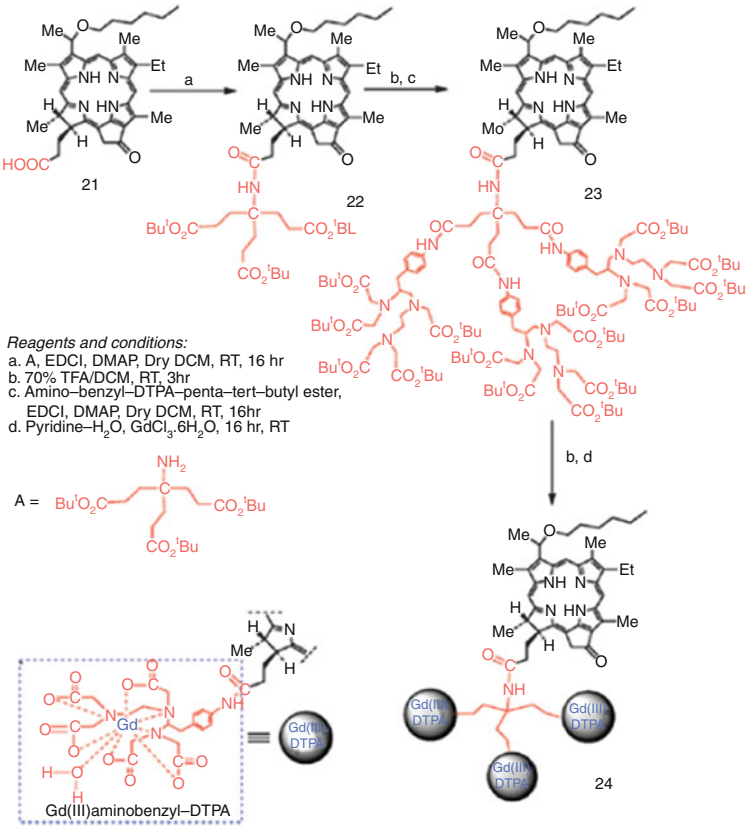

Scheme 4 Synthesis of HPPH-3Gd(III)DTPA conjugates

Table 2 Comparative T_1 and T_2 relaxivity of HPPH-Gd (DTPA) complexes

	T_1 relaxivity	T_2 relaxivity
HPPH-di-DTPA-Gd(III)	10.7	58.6
HPPH-tri-DTPA-Gd(III)	14.14	85.32

specificity, (2) unlike ^{18}F-FDG, it can be transported to various distances, (3) it is not necessary to have cyclotron at each center, which may reduce the PET-imaging cost significantly, (4) ^{18}F-FDG is not recommended for PET imaging of diabetic, pancreatic cancer patients, and (5) because of high glucose metabolism in normal brain, more efficient brain cancer-imaging agents than ^{18}F-FDG are needed.

For developing improved cancer-imaging agents with an option of PDT, we used two different approaches. In our first approach, chlorophyll-*a* was converted into methyl pyropheophorbide-a, which in a sequence of reactions was converted to both radioactive and nonradioactive iodo-analogs (Scheme 6). To investigate the impact of carbohydrates in tumor selectivity, we prepared the corresponding galactose, glucose, lactose (glucose + galactose), and cellobiose (glucose + glucose) analogs of pyropheophorbide-a. These compounds were synthesized to investigate

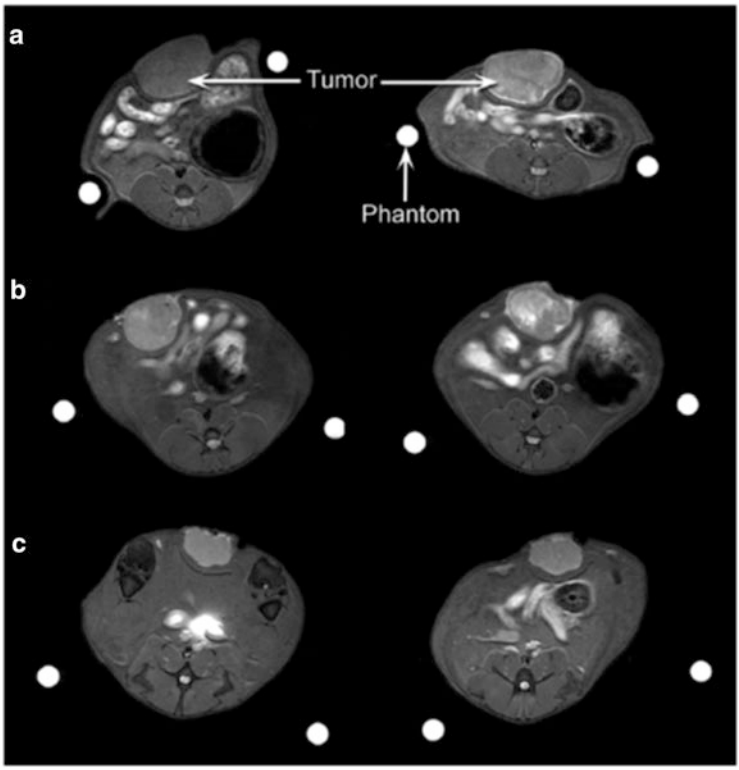

Fig. 6 Visible increase in signal intensity was seen in rat Ward colon tumors (*arrow*) from preinjection (*left*) to 24 h postinjection (*right*) of HPPH-3Gd(III)DTPA at 10 μmol/kg (**a**) and at 5 μmol/kg (**b**).Tumor contrast enhancement of HPPH-3Gd compares favorably to (**c**) Gd-DTPA (current MRI standard)

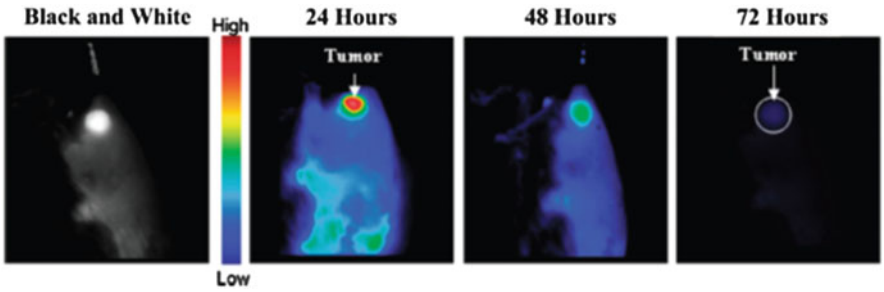

Fig. 7 In vivo fluorescence images of HPPH-3Gd in BALB/c mice at 24, 48, and 72 h with an imaging and therapeutic dose of 10 mmol/kg. Spectral unmixed images are presented with a false color representing fluorescence intensity of the imaging agent. Best tumor images were obtained at 24 h postinjection. A pre-analysis black and white image at 24 h is given for comparison with the false-color images provided

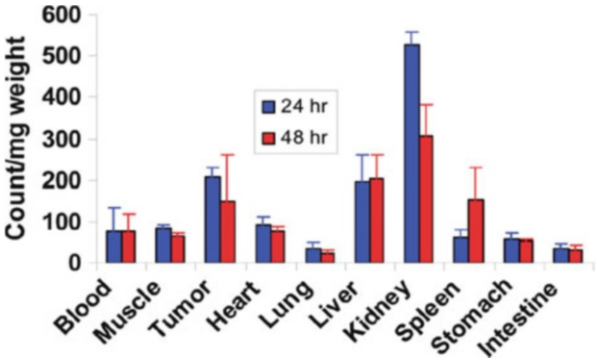

Fig. 8 In vivo biodistribution of ^{14}C-labeled HPPH-3Gd(III) DTPA in Ward colon tumors (3 rats/group). At 24, 48 after injection, 3 rats/time point were sacrificed. Preferable uptake of the conjugate in the tumor was seen at 24 and 48 h after compared to most normal tissues

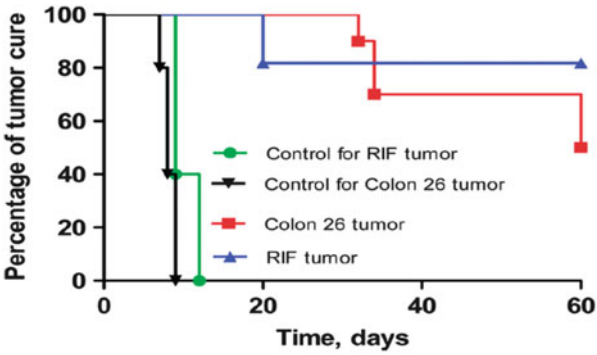

Fig. 9 In vivo PDT efficacy of HPPH-3Gd(III) DTPA in (**a**) C3H mice bearing RIF tumors and (**b**) BALB/c mice bearing Colon26 tumors at an imaging dose (10 mmol/kg). Mice were irradiated with a laser light (665 nm, 70 J/cm^2, 70 mW/cm^2) and the tumor size was measured daily

their target specificity with similar lipophilicity. For example, glucose and galactose analogs showed similar overall lipophilicity, but a significant difference in PDT efficacy and tumor specificity. The galactose and glucose conjugates were also evaluated for in vivo imaging and PDT. Among the analogs tested for PET imaging, the noncarbohydrate and the galactose analogs showed higher tumor imaging. However, the galactose analog retained in tumor for a longer time, but it also showed a significantly high uptake in liver. On the basis of detailed in vivo studies for cancer imaging (PET/fluorescence and PET) and photodynamic therapy, the noncarbohydrate photosensitizer in combination of ^{124}I-radioactive and nonradioactive (^{127}I-) analogs proved to be an excellent candidate for cancer diagnosis (Fig. 10) and fluorescence image-guided therapy. Efforts are under way to advance this product to phase I human clinical trials.

3 Multimodality Agents: Advantages of Nanoparticles

Although nanoplatforms and nanovectors (i.e., a nanoplatform that delivers a therapeutic or imaging agent) for biomedical applications are still evolving, they show enormous promise for cancer diagnosis and therapy.

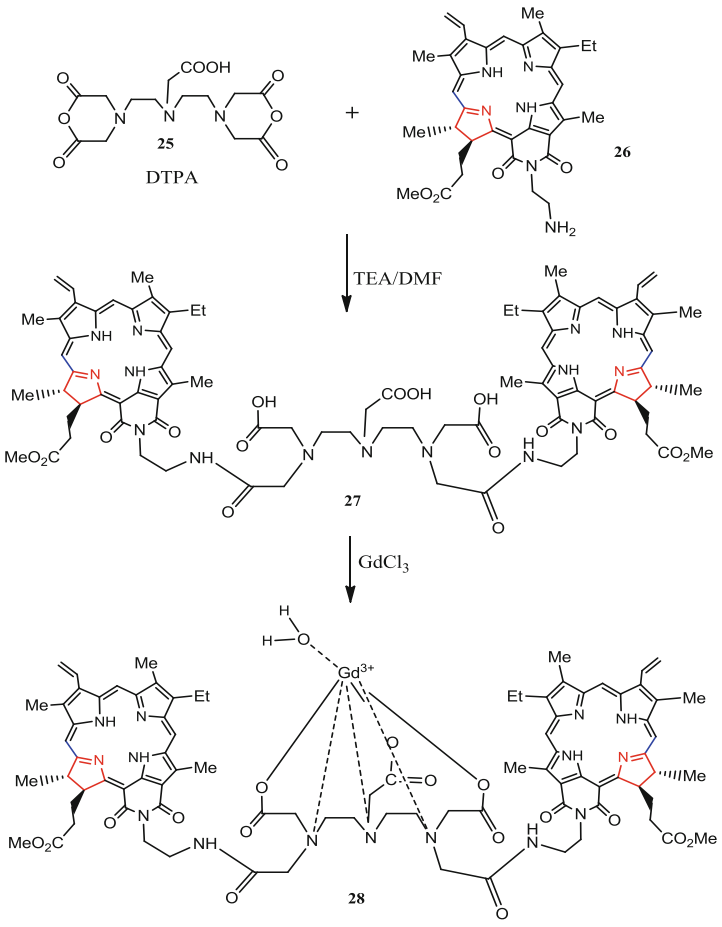

Scheme 5 Synthesis of purpurinimide-N-Gd(III)DTPA conjugate imide methyl ester

Therapeutic examples include NP containing PDT agents, boron containing dendrimers for neutron capture, and NP-directed thermal therapy. Diagnostically NP formulations have been used for imaging and therapy (Theranostics). In nanotechnology approach various disciplines, e. g., chemistry, physics and biology play important roles [71] (Fig. 11).

This particular article is focused on polyacrylamide-based NPs and can be utilized as carriers of photosensitizers (PS) for photodynamic therapy (PDT) by means of encapsulation of PSs into the NPs, post-loading of PSs, or via covalent conjugation of PSs to the functional groups at the surface of the NPs. Most PSs are hydrophobic and aggregate easily under physiological conditions; therefore, under the suboptimal preparation that most acceptable pharmaceutical formulations offer, the PDT efficacy of the PS can be hindered. On the other hand, some NPs have been

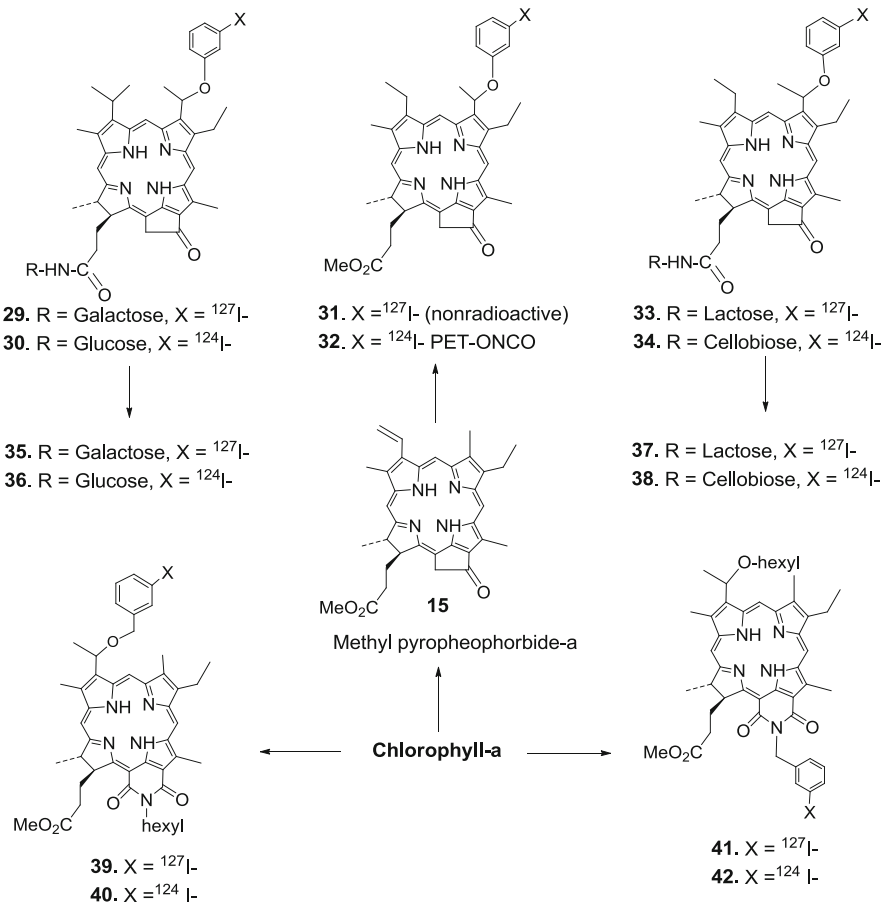

Scheme 6 Synthesis of iodinated agents for PET imaging with an option of cancer therapy by PDT

shown to increase the hydrophilic nature of compounds when they are coupled to them in any of the aforementioned loading methods. Therefore, the use of NPs can circumvent the issue of PS hydrophobicity. Additionally, NPs have been shown to accumulate within tumors and tumor vasculature via the enhanced permeability retention (EPR) effect [72]. Furthermore, increases in tumor-specific localization have been shown by the addition of tumor-targeting ligands (i.e., peptides, monoclonal antibodies) which can be covalently attached to surface functional groups of the NPs. For these reasons, NPs present the benefit of improving the therapeutic effectiveness of PDT PSs.

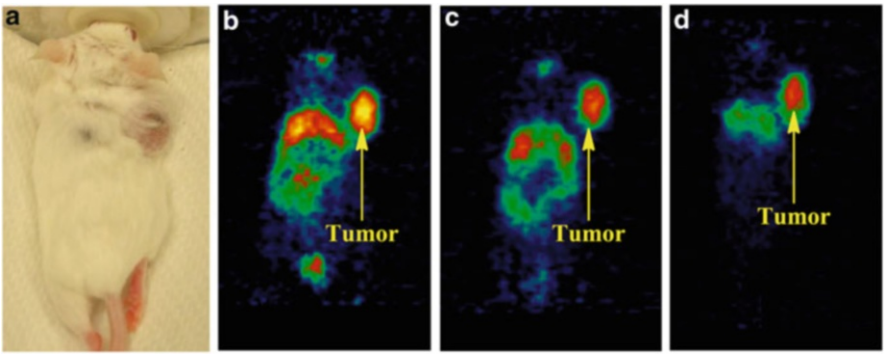

Fig. 10 Whole-body PET images of a BALB/c mouse bearing Colon26 tumor with ^{124}I-compound taken at 24 (B), 48 (C), and 72 h (D) postinjection. The maximum uptake of the PS was observed at 24 h postinjection. However, the best contrast was obtained at 72 h after injecting the ^{124}I-agent

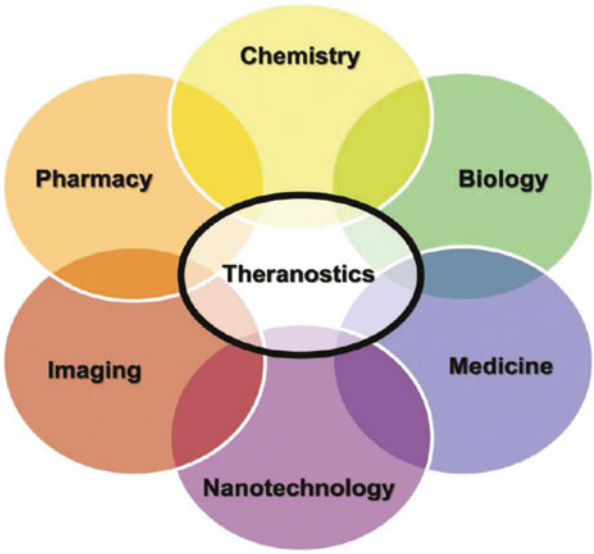

Fig. 11 Various fields encompassing development of "theranostics" for cancer

3.1 Polyacrylamide-Based Nanoparticles

Initially, Kopelman et al. [73] developed and characterized PAA NPs encapsulated with methylene blue (MB). MB is a promising PS with high quantum yield of $^1O_2$ generation, long excitation wavelength, and low toxicity. However, the clinical use of MB was hampered primarily because it is enzymatically reduced to by-products with negligible PDT efficacy post-administration. To realize MB's potential, PAA NPs seemed to be an ideal carrier because they can spare MB from such reduction and conserve its PDT effectiveness. Included in Kopelman's preliminary study

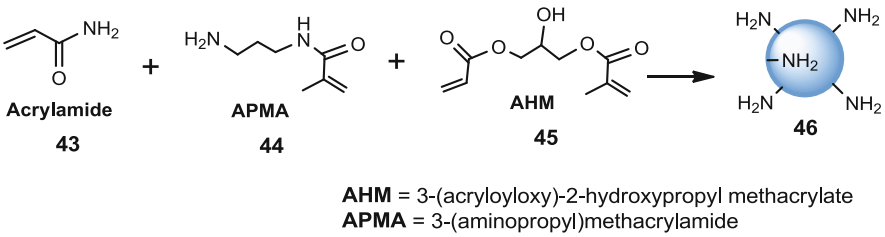

Fig. 12 A general method for the synthesis of amino-functionalized PAA NPs

were MB-loaded nanoparticles composed of PAA, sol-gel, and ORMOSIL. Upon comparison, it was observed that of the possible NP vehicles, PAA NPs showed the most efficient delivery of $^1O_2$, but its loading efficiency of MB was the lowest. In the follow-up study, Kopelman et al. confirmed that the MB-encapsulated PAA nanoparticle allowed minimal enzymatic reduction of MB and it demonstrated good PDT efficacy in vitro [74]. To address the issue of loading efficiency, Kopelman covalently conjugated MB with the precursor of PAA nanoparticle, *N*-(3-Aminopropyl)methacrylamide (APMA), and designed two nanoplatforms in a more recent study [75]. In addition, these PAA nanoparticles were PEGylated to afford longer blood circulation and were conjugated to targeting F3-Cys peptides. The nanoplatform thus resulted showed much improved targeting efficiency as well as PDT efficacy, an indicator of better loading efficiency, in vitro.

A general synthetic approach for amino-functionalized PAA NPs, its structure, SEM images, and a systemic presentation of target-specific multimodality platform is shown in Figs. 12, 13, and 14.

The most common designs of tumor-specific nanosized imaging agents were cross-linked iron oxide (CLIO) nanoparticles, in which iron oxide core is coated with the cross-linked dextran, and the incorporation of iron oxide into polymer matrices such as PAA. Although either of these designs can be further functionalized with targeting moieties, to specifically enhance the T_2 contrast in MRI, the ease to add surface functional groups for further modification made the latter design slightly advantageous. Moffat et al. first developed an iron-oxide-encapsulated PAA particles functionalized with PEG and reported significant enhancement of R_2 and R_2^* relaxivity in the tumor region [76]. In comparison to iron oxide coated by dextran, these PAA nanoparticles contain more crystals of iron oxide per particle. They were also able to better shield the iron oxide from interacting with tumor vascular component to avoid interruption to their imaging functionalities.

In addition to the applications of PAA in designing improved PDT and imaging agents, the dual operation of diagnostic imaging is also possible, using PAA as the platform to carry both the PS and imaging agents (e.g., MRI/fluorescence or PET/fluorescence). In a preliminary report, Reddy et al. described such an attempt in designing a PAA nanoparticle that carries (1) Photofrin (a PS for PDT) (which exhibited suboptimal selectivity in terms of tumor-to-normal tissue ratios), (2) iron

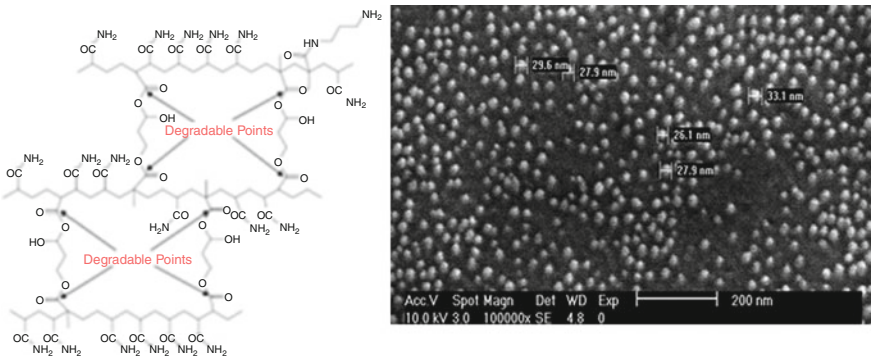

Fig. 13 Structure of amino-functionalized PAA NPs and its scanning electron microscopy (SEM) image (sixe: 28–30 nm in diameter)

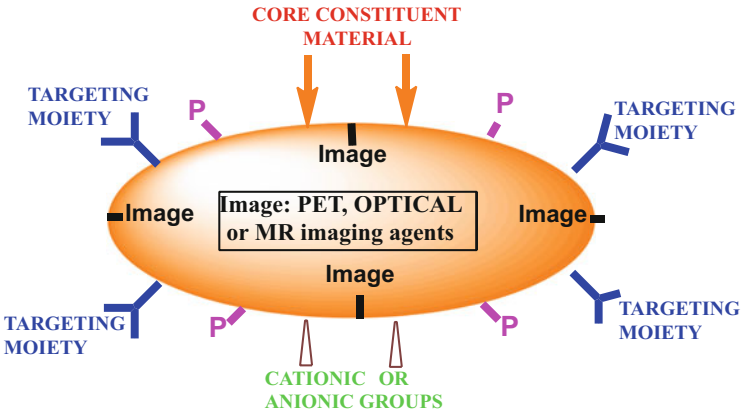

Fig. 14 A simple representation of multifunctional, targeted PAA nanoparticle for cancer imaging and photodynamic therapy (PDT). P = Photosensitizer

oxide (MRI), (3) F3-peptide (which specifically binds to nucleolin, a receptor highly expressed on many cancers), and (4) PEG (for improved lifetime during circulation) [77]. In vitro analysis of singlet oxygen production, targeting efficiency of nucleolin cell surface receptor, and conferral of phototoxicity revealed that the developed nanoparticles were indeed bound, internalized, transported, and concentrated within the tumor cell nuclei which lead to loss of cell viability upon photoactivation. In vivo studies using 9 L glioma rat model showed outstanding R_2 relaxivity in tumor, and using the developed nanoparticle as PS, there was a significantly increased survival time compared to the use of nontargeted Photofrin nanoparticle or Photofrin alone.

To investigate the tumor avidity of PAA-based NPs, the amino-functionalized PAA NPs (nonfluorescent) were conjugated with a CD containing a carboxylic acid (−COOH) group by following the standard peptide chemistry (Patel and Pandey,

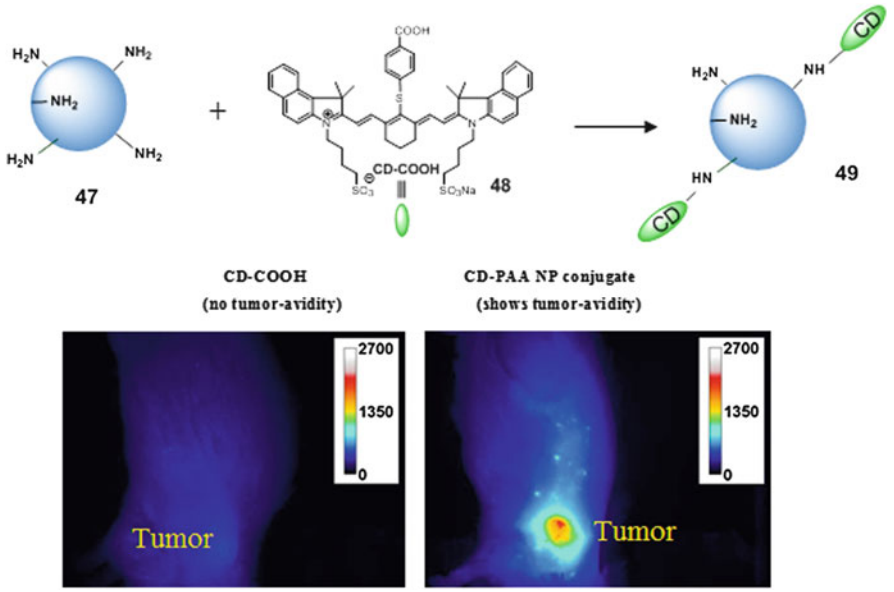

Fig. 15 Comparative tumor uptake and fluorescence-imaging potential of a cyanine dye (CD-COOH) and the corresponding CD-PAA NP conjugate. The cyanine dye was conjugated at the periphery of the nanoparticles (NPs) (BALB/c mice bearing Colon26 tumors at 24 h postinjection, dose of the CD: 0.3 μmol/kg)

unpublished results). The free and post-loaded CD-COOH was removed by spin-filter (100 KD) with a continuous wash with ethanol. The release of the CD-COOH was confirmed by measuring the absorption spectra of the filtrates (ethanol wash). The concentration of the CD in nanoparticles was calculated by subtracting the amount recovered in ethanol washes from the total amount used for conjugating to NPs.

The tumor avidity of the free CD-COOH and the corresponding CD-PAANPs conjugate was compared in BALB/c mice bearing Colon26 tumors at similar parameters (dose: 0.3 μmol/kg). The mice were imaged at variable time points using the IVIS spectrum (PerkinElmer) by exciting the dye at its longest wavelength absorption. The results summarized in Fig. 15 indicate that the cyanine dye (CD-COOH) alone had limited tumor avidity (1–72 h, only 24 h data is shown), whereas the corresponding NPs showed significant tumor-imaging potential.

More recently, Wang et al. and Gupta et al. [78, 79] conducted a series of studies designing a multifunctional PAA NP which incorporated 3-(1′-hexyloxy)ethyl-3-devinyl pyropheophorbide-alpha (HPPH), a PS with far greater tumor-targeting efficiency, excellent PDT efficacy, and a longer excitation wavelength; additionally, an NIR CD fluorescence imaging agent was also incorporated (Fig. 16). In the first study, Wang et al. demonstrated that among the NPs synthesized using covalent conjugation, encapsulation, and post-loading (loading of agents into the porous nanoparticle post its synthesis) approach. The post-loaded PAA NP

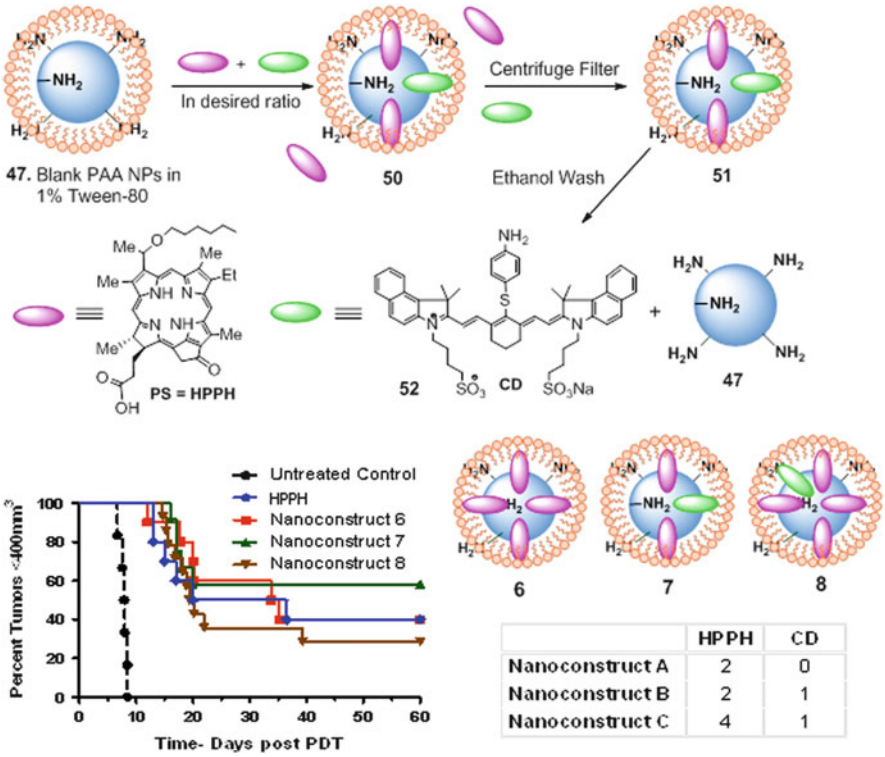

	HPPH	CD
Nanoconstruct A	2	0
Nanoconstruct B	2	1
Nanoconstruct C	4	1

Fig. 16 Post-loading of HPPH and CD-COOH in PAA NPs at variable ratios and their comparative in vivo PDT efficacy in BALB/c mice (10 mice/group). The imaging and therapy dose: 0.47 μmol/kg. For PDT, the tumors were irradiated with light (665 nm, 135 J/cm^2, 75 mW/cm^2) at 24 h postinjection

approach best conserved the PDT efficacy of HPPH [80]. In the follow-up studies, different HPPH to CD ratios were examined to minimize the undesirable quenching of HPPH electronic excitation energy due to FRET (fluorescence resonance energy transfer). The finalized nanoparticle incorporated HPPH and CD with an amine functional group in 2:1 ratio and demonstrated excellent tumor-imaging (NIR fluorescence) and PDT efficacy in vivo [79]. A direct correlation between FRET and PDT efficacy was observed. The nanoconstruct that showed higher FRET produced lower long-term tumor cure.

Incorporation of different CD derivatives (either with an amine or a chlorine functional group) was attempted for further optimization. Furthermore, F3 peptide and PEG were covalently conjugated to the surface of the PAA nanoparticle [80].

4 Conclusion and Future Directions

Porphyrins including reduced porphyrins (chlorins and bacteriochlorins) and phthalocyanines are a class of chemically and biologically important compounds that have found a significant application in cancer imaging and therapy. The tumor avidity can be improved by structure-activity relationship studies, and such molecules can also be used for delivering the desired imaging agents (MRI, PET, and fluorescence) to tumors. The imaging and therapeutic agents at a desired ratio in post-loaded or conjugated or combined conjugated and post-loaded forms to biocompatible nanoparticles could generate effective multifunctional nanoplatforms for both cancer imaging and therapy. The new PDT agents certainly eliminate the problems associated with prolong skin phototoxicity.

Future design strategies for new multimodality agents and nanoplatforms for the imaging and treatment of cancer should be directed towards tumor specificity/selectivity. Use of PDT in combination with other cancer treatment modalities (e.g., surgery, chemotherapy, virotherapy, photothermal) will certainly help to treat primary and metastatic tumors. Efforts should also focus on developing porphyrin-based agents, which could help to detect the tumors at initial stages, i.e., before metastasis.

Acknowledgments The financial assistance provided by the NIH (CA 127369, CA 119358, CA 114053, CA 109914, PO1 55791) and Alliance Foundation is highly appreciated.

References

1. National Center for Health Statistics (2011) Health, United States, 2010: with special feature on death and dying. National Center for Health Statistics, Hyattsville
2. American Cancer Society (2013) Cancer facts & figures 2013. American Cancer Society, Atlanta
3. Runge VM (2002) Clinical MRI. Saunders, Philadelphia, pp 454–457
4. Han JS, Mandell DM, Poublanc J, Mardimae A, Slessarev M, Jaigobin C, Fisher JA, Mikulis DJ (2008) BOLD-MRI cerebrovascular reactivity findings in cocaine-induced cerebral vasculitis. Nat Clin Pract Neurol 4:628–632
5. Weissleder R, Pittet MJ (2008) Imaging in the era of molecular oncology. Nature 452:580–589
6. Bushong SC (2003) Magnetic resonance imaging: physical and biological principles. C.V. Mosby, Maryland Heights
7. James ML, Gambhir SS (2012) A molecular imaging primer: modalities, imaging agents, and applications. Physiol Rev 92:897–965
8. Afaq A, Koh DM, Padhani A, van As N, Sohaib SA (2011) Clinical utility of diffusion-weighted magnetic resonance imaging in prostate cancer. BJU Int 108:1716–1722
9. McLaughlin BSA,Vallow LA, Hines SL, Tan W (2009) Lymph node micro-architecture can be imaged using optical coherence tomography. Cancer Res 69(2 Suppl 1)
10. Walker-Samuel S, Orton O, McPhail LD, Boult KR, Box G, Eccles SA, Robinson SP (2010) Bayesian estimation of changes in transverse relaxation rates. Magn Reson Med 64:914–921

11. Walker-Samuel S, Orton M, McPhail LD, Robinson SP (2009) Robust estimation of the apparent diffusion coefficient (ADC) in heterogeneous solid tumours. Magn Reson Med 62:420–429
12. Varma G, Clough RE, Acher P et al (2011) Positive visualization of implanted devices with susceptibility gradient mapping using the Original resolution (SUMO). Magn Reson Med 65:1483–1490
13. Husband JE (2002) CT/MRI of nodal metastases in pelvic cancer. Cancer Imaging 2:123–129
14. Ametamey SM, Honer M, Schubiger PA (2008) Molecular imaging with PET. Chem Rev 108:1501–1516
15. Behn CZ, Lindner JR (2006) Cellular and molecular imaging with targeted contrast ultrasound. Ultrasound Q 22:62–72
16. Azar FS, Intes X (2008) Translational multimodality optical imaging. Artech House, Boston
17. Stuker F, Ripoll J et al (2011) Fluorescence molecular tomography: principles and potential for pharmaceutical research. Pharmaceutics 3:229–274
18. Veiseh O, Sun C et al (2005) Optical and MRI multifunctional nanoprobe for targeting gliomas. Nanoletters 5:1003–1008
19. Veiseh O, Sun C, Fang C et al (2009) Specific targeting of brain tumor with an optical/magnetic resonance imaging nanoprobe across the blood–brain barrier. Cancer Res 69:6200–6207
20. Bell LK, Ainsworth NL, Lee S, Griffiths JR (2011) MRI & MRS assessment of the role of the tumour microenvironment in response to therapy. NMR Biomed 24:612–635
21. Van Dam GM, Themelis G, Crane LMA et al (2011) Intraoperative tumor-specific fluorescence imaging in ovarian cancer by folate receptor-α targeting: first in-human results. Nat Med 17:1315–1319
22. Dougherty TJ (2002) An update on photodynamic therapy applications. J Clin Laser Med Surg 20:3–7
23. Dougherty TJ, Levy JG (2003) In: Horspool W, Lenci F (eds) Clinical applications of photodynamic therapy in organic photochemistry and photobiology. CRC, Boca Raton
24. Ethirajan M, Chen Y, Joshi P, Pandey RK (2011) The role of porphyrin chemistry in tumor imaging and photodynamic therapy. Chem Soc Rev 40:340–362
25. Ethirajan M, Patel NJ, Pandey RK (2010) Porphyrin-based multifunctional agents for tumor-imaging and photodynamic therapy (PDT). Handbook of porphyrin science. World Scientific, New Jersey
26. Pandey RK, Goswami LN, Chen Y, Gryshuk A, Missert JR, Oseroff A, Dougherty TJ (2006) Nature: a rich source for developing multifunctional agents. Tumor-imaging and photodynamic therapy. Lasers Surg Med 38:445–467
27. Pandey RK, James NS, Chen Y, Missert J, Sajjad M (2010) Bifunctional agents for imaging and therapy in photodynamic therapy. Methods and protocols, Springer protocols. Springer and Humana Press, New York
28. Castano AP, Mroz P, Hamblin MR (2006) Photodynamic therapy and antitumor immunity. Nature 6:535–545
29. Dolmans DE, Fukumura D, Jain RK (2003) Photodynamic therapy of cancer nature tevies. Cancer 3:380–387
30. Bonnett R, Martinez G (2001) Photobleaching of sensitisers used in photodynamic therapy. Tetrahedron 57:9513–9547
31. Weishaupt KR, Gomer CJ, Dougherty TJ (1976) Identification of singlet oxygen as the cytotoxic agent in photoinactivation of a murine tumor. Cancer Res 36:2326–2329
32. Henderson BW, Gollnick SO (2002) In: Vo-Dinh T (ed) Mechanistic principles of photodynamic therapy in Biomedical Photonics Handbook. CRC Press, Boca Raton
33. MacDonald IJ, Dougherty TJ (2001) Basic principles of photodynamic therapy. J Porphyr Phthalocyanines 5:105–129
34. Pandey RK, Bellnier DA, Smith KM, Dougherty TJ (1991) Chlorin and porphyrin derivatives as potential photosensitizers in photodynamic therapy. Photochem Photobiol 53:65–72

35. Li G, Graham A, Chen Y, Dobhal MP, Morgan J, Zheng G, Kozyrev A, Oseroff A, Pandey RK (2003) Synthesis comparative photosensitizing efficacy, human serum albumin (site II) binding ability, and intracellular localization characteristics of novel benzobacteriochlorins derived from vic-dihydroxybacteriochlorins. J Med Chem 46:5349–5359
36. Gryshuk AL, Chen Y, Potter W, Ohulchanskyy T, Oseroff A, Pandey RK (2006) In vivo stability and photodynamic efficacy of fluorinated bacteriopurpurinimides derived from bacteriochlorophyll-a. J Med Chem 49:1874–1881
37. Pandey RK, Sumlin AB, Potter WR, Bellnier DA, Henderson BW, Constantine S, Aoudia M, Rodgers MR, Smith KM, Dougherty TJ (1996) Structure and photodynamic efficacy among alkyl ether analogs of chlorophyll-a derivatives. Photochem Photobiol 63:194–205
38. Henderson BW, Bellnier DA, Greco WR, Sharma A, Pandey RK, Vaughan K, Weishaupt R, Rodgers MAJ, Smith KM, Dougherty TJ (1996) Alkyl ether analogs of chlorophyll-a derivatives: part 1. Synthesis, photophysical properties and photodynamic efficacy. Cancer Res 64:194–204
39. Lowen GM, Pandey RK, Bellnier DA, Henderson BW, Dougherty TJ (2006) Endobronchial photodynamic therapy for lung cancer. Lasers Surg Med 38:364–370
40. Chen Y, Miclea R, Srikrishnan T, Balasubramanian S, Dougherty TJ, Pandey RK (2005) Investigation of human serum albumin (HSA) binding specificity of certain photosensitizers related to pyropheophorbide-a and bacteriopurpurinimide by circular dichroism spectroscopy and its correlation with in vivo photosensitizing efficacy. Bioorg Med Chem Lett 15:3189–3192
41. Bellnier DA, Greco WR, Loewen GL, Nava H, Oseroff A, Pandey RK, Dougherty TJ (2003) Population pharmacokinetics of the photodynamic therapy agent 2-[1-hexyloxyethyl]-2-devinyl pyropheophorbide-a in cancer patients. Cancer Res 63:1806–1813
42. Bellnier DA, Greco WR, Loewen GM, Oseriff AO, Dougherty TJ (2005) Mild skin photosensitivity in cancer patients following injection of Photochlor (2-[1-hexyloxyethyl]-2-devinyl pyropheophorbide-a; HPPH) for photodynamic therapy. Cancer Chemother Pharmacol 57:40–45
43. Lobel J, MacDonald I, Ciesielski MJ, Barone T, Potter WR, Pollina J, Plunkett RJ, Fenstermaker RA, Dougherty TJ (2001) 2-[1-hexyloxyethyl]-2-devinyl pyropheophorbide-a (HPPH) in a nude rat glioma model: implications for photodynamic therapy. Lasers Surg Med 29:397–405
44. Dougherty TJ, Pandey RK, Nava H, Smith A, Douglass HO, Edge SB, Bellnier DA, Cooper M (2000) Optical methods for tumor treatment and detection: mechanisms and techniques in photodynamic therapy IX. Proc SPIE 3909:25–27
45. Magnem ML, Rodriguez CO, Autry SA, Edwards BF, Theon AP, Madewell BR (1997) Photodynamic therapy of facial squamous cell carcinoma in cats using a new photosensitizer. Lasers Surg Med 20:202–209
46. Potter WR, Henderson BW, Bellnier DA, Pandey RK, Vaughan LA, Weishaupt KR, Dougherty TJ (1999) Parabolic quantitative structure-activity relationships and photodynamic therapy: application of a three-compartment model with clearance to the in vivo quantitative structure-activity relationships of a congeneric series of pyropheophorbide derivatives used as photosensitizers for photodynamic therapy. Photochem Photobiol 70:781–788
47. Wilson BC, Farrell TJ, Patterson MS (1999) An optical fiber-based diffuse reflectance spectrometer for non-invasive investigation of photodynamic sensitizers in vivo. Proc SPIE 156:219–231
48. Lomnes SJ, Healey AH, Fomitchov PA (2008) Intraoperative near-infrared fluorescent imaging exogenous fluorescence contrast agents in Translational Multimodality Optical Imaging. Artech House, Boston
49. Achilefu S, Dorshow RB, Bugaj JE, Rajagopalan R (2000) Novel receptor-targeted fluorescent contrast agents for in vivo tumor imaging. Investigating Radiol 35:479–485
50. Eljamel MS (2008) Photodiagnosis Photodyn Ther 5:29–35
51. Azar FS, Intes X (2005) Translational multimodality optical imaging. Artech House, Boston

52. Lee T, Zhang X, Dhar S, Faas H, Lippard SL, Jasanoff A (2010) In vivo imaging with a cell-permeable porphyrin-based MRI contrast agent. Chem Biol 17:665–673
53. Chen Y, Ohkubo K, Zhang M, Wenbo E, Liu W, Pandey SK, Ciesielski M, Baumann H, Erin T, Fukuzumi S, Kadish KM, Fenstermaker R, Pandey RK (2007) Photophysical, electrochemical characteristics and cross-linking of STAT-3 protein by an efficient bifunctional agent for fluorescence image-guided photodynamic therapy. Photochem Photobiol Sci 6:1257–1267
54. Chen Y, Gryshuk A, Achilefu A, Ohulchanskyy T, Morgan J, Chance B, Prasad PN, Henderson BW, Oseroff A, Pandey RK (2005) A novel approach to a bifunctional photosensitizer for tumor imaging and phototherapy. Bioconjug Chem 16:1264–1274
55. James NS, Chen Y, Joshi P, Ohulchanskyy TY, Ethirajan M, Henary M, Strekowsk L, Pandey RK (2013) Evaluation of polymethine dyes as potential probes for near infrared fluorescence imaging of tumors: part 1. Theranostics 3:692–702
56. James NS, Ohulchanskyy TY, Vjen Y, Joshi P, Zheng X, Goswami LN, Pandey RK (2013) Evaluation of polymethine dyes as potential probes for near infrared fluorescence imaging of tumors: part 2. Theranostics 3:703–718
57. Williams MPA, Ethirajan M, Ohkubo K, Chen P, Pera P, Morgan J, White WM, Shibata M, Fukuzumi S, Kadish KM, Pandey RK (2011) ynthesis, photophysical, electrochemical, tumor-imaging, and phototherapeutic properties of purpurinimide-N-substituted cyanine dyes joined with variable lengths of linkers. Bioconjug Chem 22:2283–2295
58. Ethirajan M, Chen P, Ohulchanskyy TY, Goswami LN, Gupta A, Srivatsan A, Dobhal MP, Missert JR, Prasad PN, Kadish KM, Pandey RK (2013) Regioselective synthesis and photophysical and electrochemical studies of 20-substituted cyanine dye-purpurinimide conjugates: incorporation of Ni(II) into the conjugate enhances its tumor-uptake and fluorescence-imaging ability. Chem Eur J 19:6670–6684
59. Young SW, Sidhu MK, Qing F, Muller HH, Neuder M, Zanassi G, Mody TD, Hemmi G, Dow W, Mutch JD (1994) Preclinical evaluation of gadolinium (III) texaphyrin complex. A new paramagnetic contrast agent for magnetic resonance imaging. Investig Radiol 29:330–338
60. Ni Y, Adzamli K, Miao Y, Cresens E et al (2001) MRI contrast enhancement of necrosis by MP-2269 and gadoporphyrin-2 in a rat model of liver infarction. Invest Radiol 36:97–103
61. Li G, Slansky A, Dobhal MP, Goswami LN, Pandey RK et al (2005) Chlorophyll-a analogues conjugated with aminobenzyl DTPA as potential bifunctional agents for magnetic resonance imaging and photodynamic therapy. Bioconjug Chem 16:32–42
62. Goswami LN, White WH, Pandey RK et al (2010) Synthesis of tumor-avid photosensitizer-Gd (III)DTPA conjugates: impact of the number of gadolinium units in T1/T2 relaxivity, intracellular localization, and photosensitizing efficacy. Bioconjug Chem 21:816–827
63. Spernyak JA, White WH, Pandey RK et al (2010) Hexylether derivative of pyropheophorbide-a (HPPH) on conjugating with 3Gadolinium (III) aminobenzyldiethylenetriaminepentaacetic acid shows potential for in vivo tumor imaging (MR, Fluorescence) and photodynamic therapy. Bioconjug Chem 21:828–835
64. Galindev O, Dalantal M, Ahn WS, Shim YK (2009) Gadolinium complexes of chlorin derivatives applicable for MRI contrast agents and PDT. J Porphyrins Phthalocyanines 13:823–831
65. Stanciu AE (2012) Rev Radionuclides in targeted therapy of cancer. Roum Chim 57:5–13
66. Pandey SK, Gryshuk AL, Sajjad M, Zheng X, Chen Y, Abouzeid MM, Morgan J, Charamisinau I, Nabi HA, Oseroff A, Pandey RK (2005) Multimodality agents for tumor imaging (PET, fluorescence) and photodynamic therapy. A possible "see and treat" approach. J Med Chem 48:6286–6295
67. Pandey SK, Sajjad M, Chen Y, Pandey A, Missert JR, Batt C, Yao R, Nabi HA, Oseroff AR, Pandey RK (2009) Compared to purpurinimides, the pyropheophorbide containing an iodobenzyl group showed enhanced PDT efficacy and tumor imaging (124I-PET) ability. Bioconjug Chem 20:274–282
68. Chen Y, Sajjad M, Wang Y, Batt C, Nabi HA, Pandey RK (2011) TSPO 18 kDa (PBR) targeted photosensitizers for cancer imaging (PET) and PDT. ACS Med Chem Lett 2:136–141

69. Srivatsan A, Wang Y, Joshi P, Sajjad M, Chen Y, Liu C, Thankppn K, Missert JR, Tracy E, Morgan J, Rigual N, Baumann H, Pandey RK (2011) In vitro cellular uptake and dimerization of signal transducer and activator of transcription-3 (STAT3) identify the photosensitizing and imaging-potential of isomeric photosensitizers derived from chlorophyll-a and bacteriochlorophyll-a. J Med Chem 54:6859–6873
70. Konecky SD, Yodh AG (2008) Diffuse optical imaging and PET imaging in translational multimodality optical imaging. Artech House, Boston
71. Kelkar SS, Reineke TM (2011) Theranostics: combining imaging and therapy. Bioconjug Chem 22:1879–1903
72. Maeda HJ (2012) Macromolecular therapeutics in cancer treatment: the EPR effect and beyond. Control Release 164:138–144
73. Kopelman R, Philbert M et al (2005) Multifunctional nanoparticle platforms for in vivo MRI enhancement and photodynamic therapy of a rat brain cancer. J Magn Magn Mater 293:404–410
74. Tang W, Xu H, Park EJ, Philbert MA, Kopelman R et al (2008) Encapsulation of methylene blue in polyacrylamide nanoparticle platforms protects its photodynamic effectiveness. Biochem Biophys Res Commun 369:579–583
75. Qin M, Hah HJ, Kim G, Nie G, Lee YE, Kopelman R et al (2011) Methylene blue covalently loaded polyacrylamide nanoparticles for enhanced tumor-targeted photodynamic therapy. Photochem Photobiol Sci 10:832–841
76. Moffat BA, Reddy GR, McConville P, Hall DE et al (2003) A novel polyacrylamide magnetic nanoparticle contrast agent for molecular imaging using MRI. Mol Imaging 2:324–332
77. Reddy GR, Bhojani MS, McConville P, Moody J, Moffat BA, Hall DE et al (2006) Vascular targeted nanoparticles for imaging and treatment of brain tumors. Clin Cancer Res 12:6677–6686
78. Wang S, Kim G, Lee YE, Hah HJ, Ethirajan M, Pandey RK, Kopelman R (2012) Multifunctional biodegradable polyacrylamide nanocarriers for cancer theranostics—a "See and Treat" strategy. ACS Nano 6:6843–6851
79. Gupta A, Wang S, Pera P, Rao KV, Patel N, Ohulchanskyy TY et al (2012) Multifunctional nanoplatforms for fluorescence imaging and photodynamic therapy developed by post-loading photosensitizer and fluorophore to polyacrylamide nanoparticles. Nanomedicine 8:941–950
80. Gupta A, Pandey RK (2012) Ph.D. Thesis, RPCI Graduate Division, SUNY Buffalo

Top Heterocycl Chem (2014) 34: 31–52
DOI: 10.1007/7081_2013_111

Published online: 8 June 2013

Synthesis of Carborane-Containing Porphyrin Derivatives for the Boron Neutron Capture Therapy of Tumors

N.V.S. Dinesh K. Bhupathiraju and M. Graça H. Vicente

Abstract The treatment of malignant brain tumors using conventional therapies and surgery often leads to tumor recurrence and/or unwanted side effects. Boron neutron capture therapy (BNCT) is a binary and localized form of treatment for brain tumors and other difficult-to-treat cancers that uses nontoxic boron-containing agents. Boronated porphyrins and derivatives constitute a class of highly promising third-generation boron delivery agents for BNCT. These stable, tumor-specific, and fluorescent macrocycles can be synthesized with high boron content, can deliver therapeutic amounts of boron to target sites, and allow tumor detection and treatment planning by optical imaging. In addition, boronated porphyrins have shown low toxicity and enhanced tumor selectivity and retention times compared with clinically approved BNCT agents, BSH and BPA. In this article the synthesis of carboranyl-containing porphyrins and derivatives for application in BNCT is reviewed, with special emphasis on macrocycles reported in the last decade. Current strategies for enhancing the biological efficacy of BNCT agents involve their association with tumor-targeting molecules, such as polyamines and peptides, for improved tumor selectivity and accumulation.

Keywords BNCT · Carborane · Chlorin · Phthalocyanine · Porphyrin

Contents

N.V.S.D.K. Bhupathiraju and M.G.H. Vicente (✉)
Department of Chemistry, Louisiana State University, Baton Rouge, LA 70803, USA
e-mail: vicente@lsu.edu

1 Introduction

Boron neutron capture therapy (BNCT) is a binary therapy that involves the irradiation of ^{10}B-containing tumors with low energy thermal neutrons [1–4]. The nuclear capture reaction produces excited ^{11}B nuclei which spontaneously fission to give high linear-energy transfer (high-LET) alpha and ^{7}Li particles, γ radiation and release of about 2.4 MeV of kinetic energy, as shown in Fig. 1. The high-LET particles produced during the fission reaction have limited path lengths in tissue (5–9 μm), therefore making BNCT a localized form of treatment, able to destroy ^{10}B-containing malignant cells in the presence of ^{10}B-free healthy cells. In addition, the much lower nuclear cross-sections of biologically abundant nuclei ^{12}C (0.0034 barn), ^{1}H (0.33 barn), and ^{14}N (1.8 barn) in comparison with ^{10}B (3,838 barns) limit interference with the ^{10}B(n,α)^{7}Li capture reaction. Although the natural abundance of the boron-10 isotope is 20%, it can be incorporated at the 95–96% level into BNCT agents from ^{10}B-enriched starting materials.

BNCT clinical trials in brain tumor patients started about 50 years ago at the Brookhaven National Laboratory and the Massachusetts Institute of Technology (MIT), using neutron beams with limited tissue penetration of up to 4 cm. Modern nuclear reactors, such as the MIT research reactor, use epithermal neutron beams that can reach up to 10 cm, allowing the treatment of deep seated tumors [4]. Currently, there are two clinically approved BNCT agents, the sodium salt of the sulfhydryl boron hydride $Na_2B_{12}H_{11}SH$ (BSH, **1**) and L-4-dihydroxy-borylphenylalanine (BPA, **2**), used either alone or in combination for the treatment of malignant brain tumors, melanomas, and squamous cell carcinomas (Fig. 2) [5–9]. For example, BNCT using ^{18}F-labeled BPA assisted by positron emission tomography (PET) was recently used to treat recurring head and neck cancer, with significant improvement of the mean patient's survival time [9]. Although BSH and BPA have demonstrated low toxicity and efficacy in BNCT clinical trials, improved boron delivery agents with higher tumor selectivity and ability to deliver therapeutic amounts of boron (>20 μg/g tumor) to target tumors with low systemic toxicity have been the focus of intense research [4]. These so-called third-generation boron delivery agents include boronated amino acids, proteins, antibodies, nucleosides, sugars, lipids, liposomes, nanoparticles, and porphyrin derivatives [10, 11]. Among these, boronated porphyrins are particularly promising due to their demonstrated (1) low dark toxicities, (2) high uptake and retention in tumors, (3) high tumor-to-blood and tumor-to-normal tissue boron concentration ratios, (4) delivery of therapeutic amounts of boron to tumors, (5) ability to produce cytotoxic oxygen species upon light activation, which is the basis for their use in photodynamic therapy (PDT) [12, 13] and the possibility of using PDT in combination with BNCT, (6) ability for DNA and RNA binding, and (7) fluorescent properties, which facilitate the quantification of tissue-localized boron and treatment planning [14–16]. The neutral isomeric carboranes

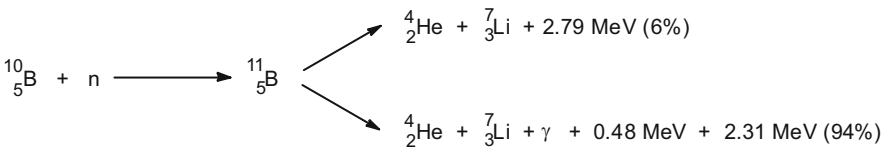

Fig. 1 The $^{10}B(n,\alpha)^{7}Li$ neutron capture and fission reactions

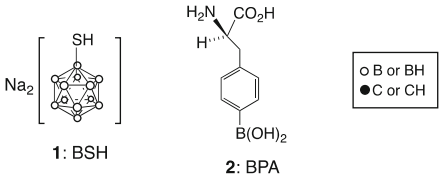

Fig. 2 Boron delivery agents in BNCT clinical trials

ortho-, *meta*-, and *para*-$C_2B_{10}H_{12}$, the anionic *closo*-carborane $CB_{11}H_{12}^-$ and the open-cage *nido*-$C_2B_9H_{12}^-$ (obtained from base-induced deboronation of *ortho*-carborane), and the bis(dicarbollide) [3,3′-Co(1,2-$C_2B_9H_{11})_2]^-$, have been the clusters of choice for attachment to porphyrin macrocycles because of their high boron content, amphiphilic properties, and their high photochemical, kinetic, and hydrolytic stabilities. In this chapter we review the synthesis of carboranyl-containing porphyrins and derivatives that have been reported for application in BNCT, with particular emphasis on the macrocycles reported in the last decade.

2 Synthetic Strategies and Early Reported Macrocycles

The synthesis of porphyrins **3** and **4**, among other *meso*-tetracarboranylporphyrins, were first carried out in 1978 by Haushalter and Rudolph [17, 18]. Porphyrin **3** was prepared in 11% yield by Rothemund condensation of pyrrole with 1-methyl-2-methylformyl-*ortho*-carborane, and porphyrin **4** was obtained from the reaction of pre-formed *meso*-tetra(4-aminophenyl)porphyrin with the corresponding *ortho*-methylcarborane acid chloride. The *closo*-carboranylporphyrins **3** and **4** were subsequently converted into their corresponding *nido*-carborane derivatives by base-induced removal of a boron atom from each *ortho*-carborane cage, using a mixture of pyridine and piperidine. About a decade later several groups reported the synthesis of carboranylporphyrins for application as boron delivery agents for BNCT [19–24]. These macrocycles were obtained from commercially available protoporphyrin-IX or hematoporphyrin-IX precursors, via functionalization of the vinyl, hydroxyethyl or the propionic side chains, producing VCDP (**5**) [21], **6** [22, 23],

BOPP (**7**) [19, 20] and **8** [24]. VCDP was prepared in about 40% yield from mercuration of Zn(II)-deuteroporphyrin-IX dimethyl ester, followed by reaction with vinyl-*ortho*-carborane in the presence of $LiPdCl_3$, demetallation and final deboronation and ester hydrolysis using KOH in methanol. BOPP was obtained in 85% yield by reacting bis(1,2-dihydroxyethyl)-deuteroporphyrin-IX dimethyl ester with the corresponding acid chloride of *ortho*-carborane in the presence of DMAP, followed by ester hydrolysis using dilute HCl.

Carborane-functionalized phthalocyanines were first reported by Soloway and coworkers [25], which carried out the functionalization of a tetrasulfonylchloride-phthalocyanine with *para*-aminophenylcarborane, giving a mixture of regioisomeric phthalocyanines.

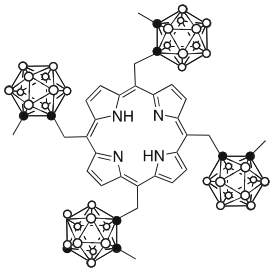

3

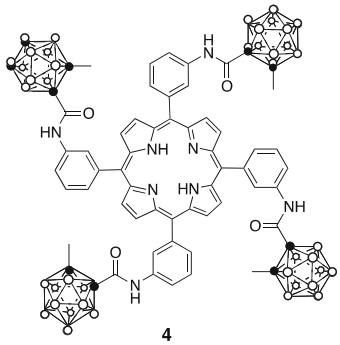

4

In the early 2000s several other carboranyl-containing porphyrins and phthalocyanines were reported [26–35]. These macrocycles were prepared using the following strategies: (1) functionalization of a pre-formed macrocycle, (2) cyclotetramerization of bononated pyrroles, or by (3) condensation of boronated aldehydes with pyrroles and dipyrromethanes. In the synthesis from pyrrole and aldehyde precursors, the Rothemund [36], Adler [37], and Lindsey [38] condensation conditions have all been reported. The highest yields are obtained with Lindsey's method which employs mild conditions, usually using $BF_3{\cdot}OEt_2$ or TFA as the acid catalyst at room temperature to form the porphyrinogen, followed by oxidation to porphyrin using 2,3-dichloro-5,6-dicyanobenzoquinone (DDQ) or *para*-chloranil (2,3,5,6-tetrachlorobenzoquinone). The total synthesis from boronated pyrroles and/or aldehydes is usually employed for the preparation of symmetric macrocycles, such as *meso*-tetraarylporphyrins of high boron content. On the other hand, unsymmetric systems are most often prepared by direct functionalization of a pre-formed macrocycle, obtained either by total synthesis or from a natural source (heme, chlorophyll-*a*). This approach is usually employed for the synthesis of carboranylporphyrin derivatives bearing a tumor-targeting moiety and can lead to high yields of the target macrocycles, as will be discussed in the following sections.

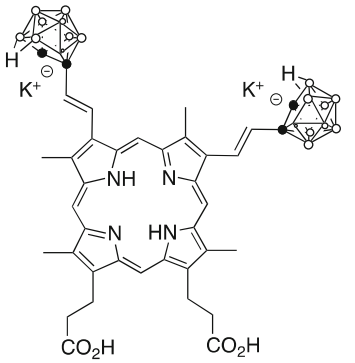

5

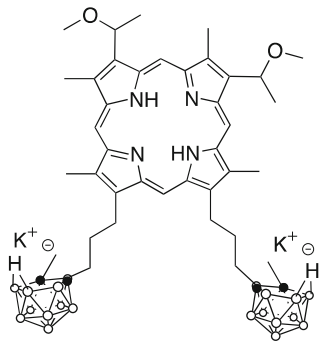

6

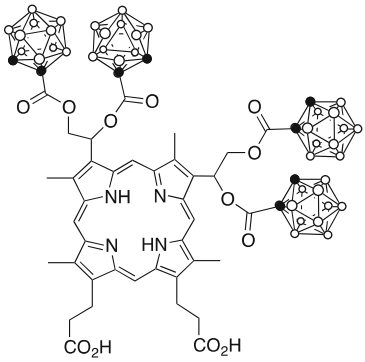

7

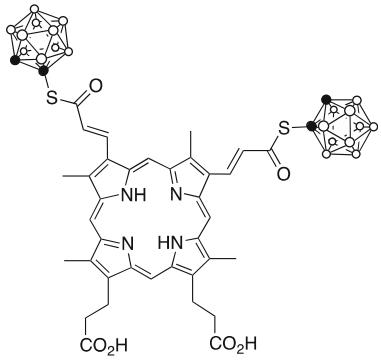

8

3 Recent Synthesis of Carboranyl-Containing Porphyrin Derivatives

3.1 Symmetric Carboranyl-Porphyrins and Chlorins

Symmetric carboranylporphyrin derivatives have been prepared either by total synthesis from boronated monomeric precursors, or from functionalization of a pre-formed symmetric porphyrin. Both metal-free and metallated derivatives, usually containing Zn(II), Cu(II), or Ni(II) ions, have been reported. Zn(II)-porphyrins often show enhanced photosensitizing properties, whereas Cu(II)-porphyrins show reduced photosensitization and allow tumor detection using PET (^{64}Cu) or SPECT (^{67}Cu).

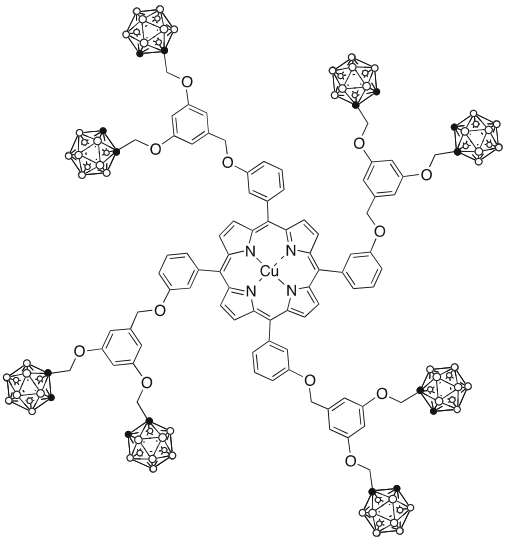

9

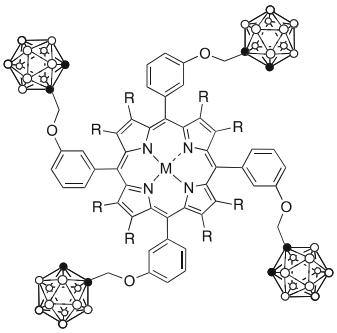

10: R = CH_2CO_2Me; M = Cu or Ni
11: R = H; M = Cu
12: R = Br; M = Cu

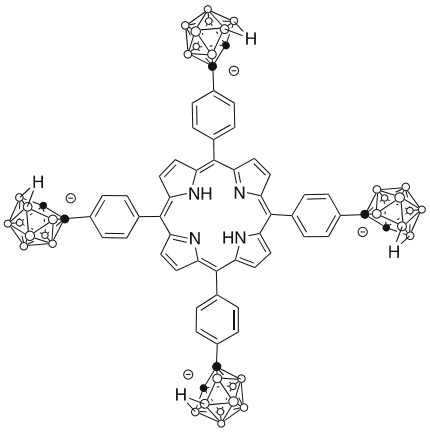

13

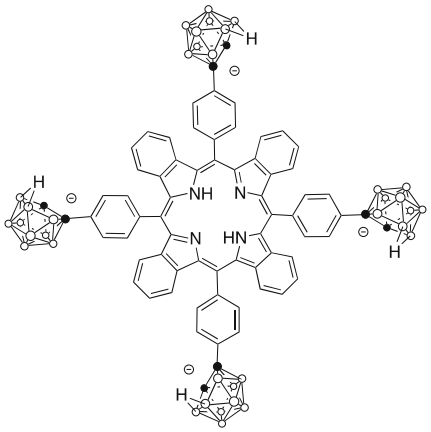

14

Cu(II)-porphyrin **9** was synthesized using Lindsey's method by condensation of 3-(3,5-di-*ortho*-carboranyl-methoxybenzyloxy)benzaldehyde with pyrrole in the presence of $BF_3{\cdot}OEt_2$ followed by copper insertion using Cu(II) acetate, in 20% overall yield [39]. Using a similar strategy, porphyrins **10**–**12** were prepared, from reaction of pyrrole or a β-substituted pyrrole with a boronated benzaldehyde, followed by metal insertion, and in the case of **12**, by bromination of CuTCPH (**11**)

in pyridine at room temperature [40, 41]. A more soluble derivative of CuTCPH (**11**) containing four hydroxy substituents at the *meta*-positions of the *meso*-phenyl groups was prepared in about 30% yield using similar condensation and metallation conditions [39]. The resulting tetrahydroxy-CuTCPH was obtained by dealkylation of the corresponding tetramethoxyporphyrin using BBr_3.

Using Lindsey's condensation conditions, H_2TCP **13** in both ^{10}B-enriched and non-enriched forms were synthesized by condensation of pyrrole with *para*(*ortho*-carboranyl)benzaldehyde using $BF_3{\cdot}OEt_2$ as catalyst, followed by oxidation with DDQ and deboronation with pyridine/piperidine 3:1, in about 50% yield [26, 29, 42–44]. An alternative but low-yielding reported synthesis of this porphyrin involves the functionalization of a pre-formed tetra(4-iodophenyl)porphyrin with *ortho*-carborane via Cu(I)-catalyzed coupling [45]. The tetrabenzo-carboranylporphyrin **14** was prepared by condensation of tetrahydroisoindole with *para*(*ortho*-carboranyl) benzaldehyde under Lindsey's conditions, followed by metallation with $CuCl_2$, oxidation to tetrabenzoporphyrin using excess DDQ, demetallation with conc. H_2SO_4, and final deboronation of the *ortho*-carboranes using tetrabutylammonium fluoride in THF, in about 30% overall yield [46, 47].

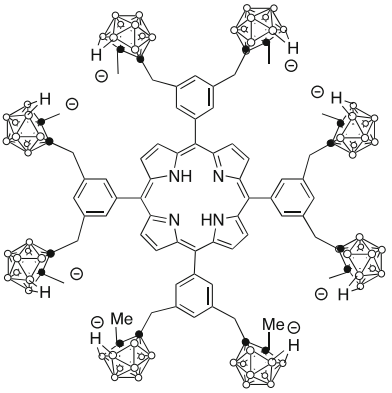

15

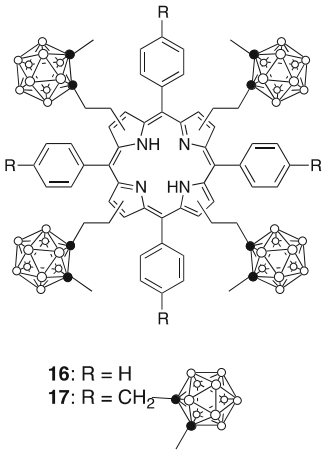

16: R = H
17: R = CH_2

The octa-*ortho*-carboranylporphyrin **15** of high boron content was synthesized in about 10% yield from condensation of pyrrole with bis[3,5-(methyl-*ortho*-carboranyl)methyl]benzaldehyde using TFA as the acid catalyst, followed by oxidation with *para*-chloranil and deboronation of the *ortho*-carborane cages [26, 48, 49].

meso-Tetraaryl-carboranylporphyrins **16** and **17** bearing carborane cages on the β-pyrrolic positions of the macrocycle have been synthesized from carboranyl-pyrroles and aldehydes under Lindsey's conditions, in 49% and 20% yields, respectively [50, 51]. Condensation of the boronated pyrrole with benzaldehyde,

or a boron-containing benzaldehyde in the presence of $BF_3{\cdot}OEt_2$, gave the target porphyrins as regioisomeric mixtures after oxidation with *para*-chloranil. Pure β-substituted carboranylporphyrins **18** and **19** were also synthesized in good yields (18–78%) by direct functionalization or pre-formed tetra- and octa-bromoporphyrins, using a Pd(0)-catalyzed coupling reaction in anhydrous toluene, excess carboranylmethylphenyl boronic acid, and anhydrous K_2CO_3 [52].

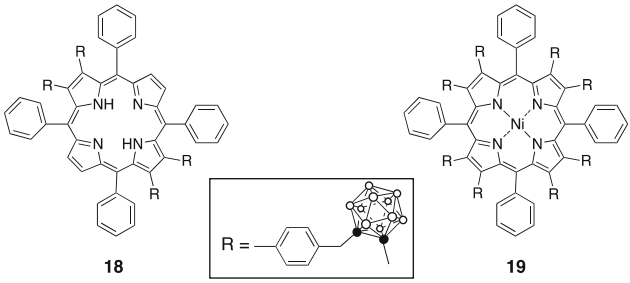

18 **19**

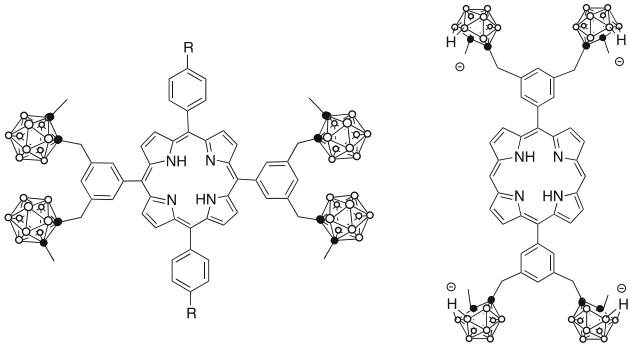

20: R = $PO(OH)_2$
21: R = NMe_3I

22

Using a MacDonald [2+2] condensation [53] between bis[3,5-(methyl-*ortho*-carboranyl)methyl]benzaldehyde and various dipyrromethanes, a series of carboranylporphyrins, including **20**–**22**, were prepared in 4–40% yields [54–56]. The lower yields obtained were due to acid-catalyzed scrambling during the condensation reaction. The water-soluble carboranylporphyrins were obtained by cleavage and hydrolysis of phosphonic esters using bromotrimethylsilane (to give **20**), by quaternization of the peripheral amine groups with methyl iodide (to give **21**), or by deboronation of the *ortho*-carboranes with pyridine/piperidine 3:1 (to give **22**).

Symmetric porphyrins **23** and **24** were synthesized in very high yields (>90%) from the reaction of the corresponding pre-formed *meso*-hydroxyphenylporphyrins

with zwitterionic [3,3′-Co(8-$C_4H_8O_2$-1,2-$C_2B_9H_{10}$)(1′,2′-$C_2B_9H_{11}$)] [57, 58]. Nucleophilic groups on the porphyrin macrocycle, such as hydroxy and pyridyl, efficiently open the dioxane ring of [3,3′-Co(8-$C_4H_8O_2$-1,2-$C_2B_9H_{10}$)(1′,2′-$C_2B_9H_{11}$)], producing porphyrins bearing Co(III) bis(dicarbollide) linked via a short PEG linkage [57–62]. In the absence of these groups, metal-free porphyrins produce the corresponding mono- and di-alkylated derivatives [61]. Since the Co(III) bis(dicarbolide) is negatively charged, porphyrins **23** and **24** are octa- and tetra-anionic, respectively. On the other hand, when pyridylporphyrins are used as the starting materials for the ring opening reaction of [3,3′-Co(8-$C_4H_8O_2$-1,2-$C_2B_9H_{10}$)(1′,2′-$C_2B_9H_{11}$)], zwitterionic carboranylporphyrins are formed [57, 61, 62].

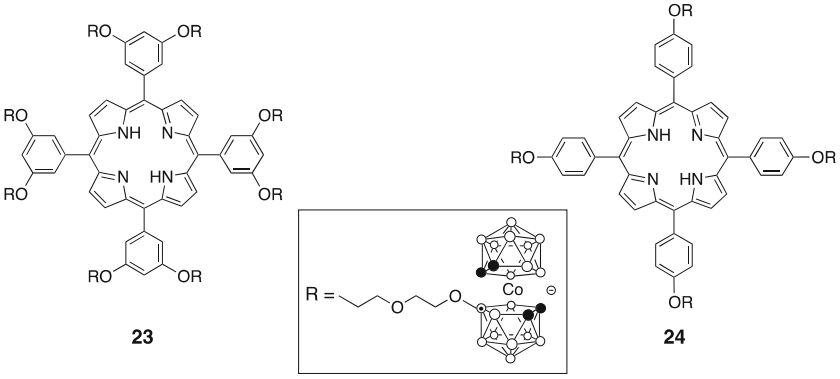

23 **24**

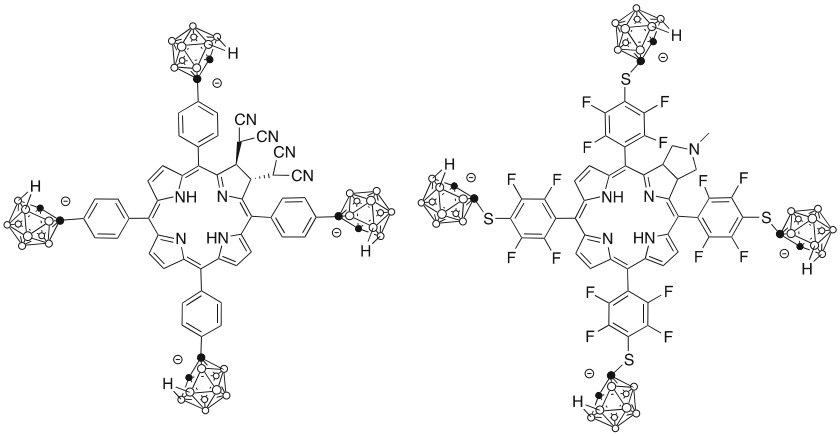

25 **26**

Symmetric boronated chlorins are obtained from functionalization of symmetric porphyrin precursors. For example, boronated *trans*-chlorin **25** was synthesized from the corresponding *meso*-tetra(4-*ortho*-carboranylphenyl)porphyrin (the *closo*-carboranylporphyrin precursor of porphyrin **13**) [63, 64], via Cu(II) complexation and nitration at a β-pyrrolic position using copper(II) nitrate in acetic acid/acetic anhydride, followed by demetallation using 2% H_2SO_4 and reaction with malononitrile in the presence of K_2CO_3. Base-induced deboronation of *ortho*-carborane cages of the chlorin using pyridine/piperidine 3:1 gave compound **25** in 41% overall yield.

Boronated chlorin **26** was synthesized from *meso*-tetra(pentafluorophenyl)porphyrin in 48% overall yield [65]. The fluorinated porphyrin was first converted into the corresponding chlorin using *N*-methylglycin in toluene, and then the *para*-fluoro groups were substituted in the presence of excess mercapto-*ortho*-carborane under mild conditions (K_2CO_3 and KF at room temperature), to give boronated chlorin **26**.

3.2 Unsymmetric Carboranyl-Porphyrins and Chlorins

The preferred methodology for the preparation of unsymmetric macrocycles is by direct functionalization of naturally occurring and readily available porphyrins (such as protoporphyrin-IX) and chlorins (such as methyl pheophorbide-a). Alternatively, unsymmetric synthetic porphyrins, usually formed by mixed aldehyde condensations, can undergo functionalization with appropriate carboranyl-containing reagents. For example, carboranylporphyrins **5–8** were prepared via functionalization of protoporphyrin-IX or its derivatives (hematoporphyrin-IX or deuteroporphyrin-IX), with appropriately substituted carborane cages. On the other hand, chlorophyll-*a* derivatives pheophorbide-a, pyropheophorbide-a, and chlorin-e_6 have been functionalized with carborane cages, mainly via their carboxylic acid substituents, to produce, for example, chlorins **27–32**. Chlorin **27** was prepared by nucleophilic opening of the exocyclic ring of methyl pheophorbide-a with ethylenediamine, followed by acylation of the free amine group with succinic anhydride and conjugation of the resulting carboxylic group with 3-amino-*ortho*-carborane in the presence of DCC in dichloromethane/pyridine [66–69]. Hydrolysis of the ester group at the 17^3 position using 70% aqueous TFA gave a free carboxylic group which was conjugated under similar conditions to give chlorin **27** [66]. Alternatively, the ethylene amine derivative of pheophorbide-a can undergo alkylation reactions with *ortho*-carboranylmethyl triflate or the cesium salt of *closo*-carboranylmethyl triflate in THF to give the corresponding chlorins in yields ranging from 12% to 88% [67–69].

Chlorin **28** was also prepared from the same pheophorbide-a ethylene amine precursor by ring opening reaction of zwitterionic [3,3′-Co(8-$C_4H_8O_2$-1,2-$C_2B_9H_{10}$)(1′,2′-$C_2B_9H_{11}$)] giving chlorin **28** in 61% yield [70, 71].

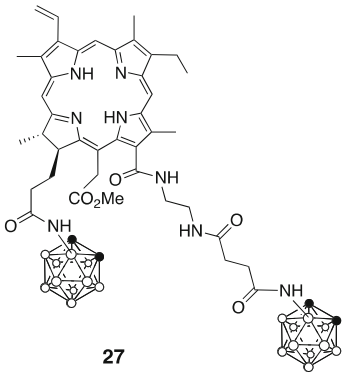

27

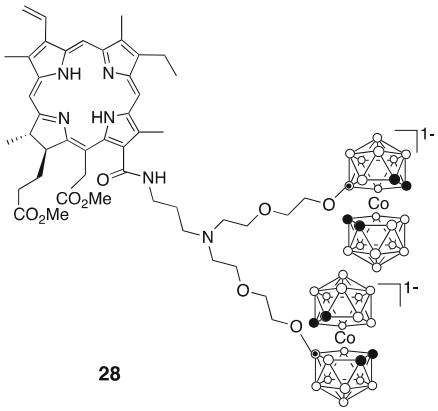

28

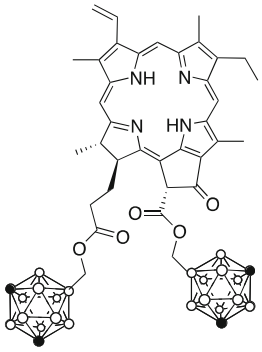

29

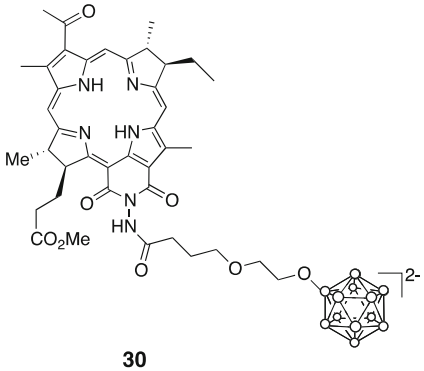

30

Other carborane-conjugates of methyl pheophorbide-a were obtained by transesterification of one or both of the methoxycarbonyl groups with carboranyl alcohols, using I_2 in refluxing toluene or 2-chloro-1-methylpyridinium iodide and DMAP for the mono-carboranyl conjugates, or $[Bu_2Sn(OH)(OTf)]_2$ in refluxing toluene for the di-carboranyl conjugates such as **29**, in yields up to 80% [72]. Ester, thioester, and amide derivatives of pyropheophorbide-a have also been prepared from the corresponding alcohol, thiol, or amine carboranes respectively, using either di-*tert*-butylpyrocarbonate and DMAP for the coupling reaction [73] or oxalyl chloride and $[Me_4N]_2[B_{12}H_{11}SH]$ [74].

The synthesis of bacteriochlorin derivative **30** involved the nucleophilic ring opening reaction of the oxonium derivative of the *closo*-dodecaborate dianion [75, 76]. Using an alternative strategy, **31** and **32** were prepared from the

corresponding amine-containing macrocycles, by reaction with *para*-iodobenzoyl chloride followed by a Sonogashira coupling reaction with Co(III)-bis(dicarbollide) containing a terminal acetylene group, using 5:1 triphenylphosphine and $Pd_2(dba)_3$ in benzene/DIPEA at 60°C [77].

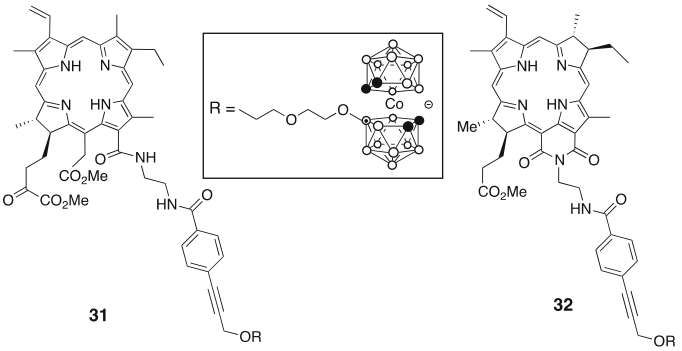

In order to increase the tumor uptake and overall biological efficacy of boronated porphyrins, the conjugations of unsymmetric systems to a cell-targeting moiety, such a peptide, polyethyleneglycol (PEG) or polyamine, have been investigated. The conjugation of PEG groups to biologically active molecules is a strategy often used for enhancing their aqueous solubility, serum life, and tissue permeability. On the other hand, polyamines are found in high concentrations in rapidly proliferating tumor cells due to up-regulation of the polyamine transport system, and their conjugation to biologically active molecules generally increases tumor selectivity and uptake. Another strategy used for increasing intracellular drug delivery is via conjugation to certain peptide sequences, in particular arginine- and/or lysine-rich cell-penetrating peptides (CPP) or nuclear localizing sequences (NLS), which are known to increase tumor cell uptake and nuclei-targeting.

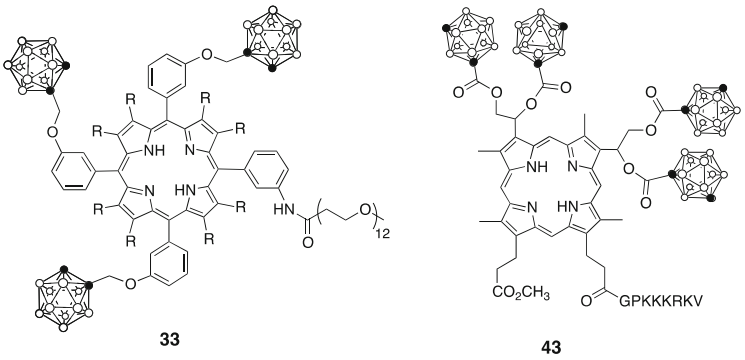

Porphyrin **33** containing three *ortho*-carboranes and a poly(ethylene glycol) group was synthesized in low yields by conjugation of the corresponding tri (carboranyl)porphyrin bearing a free amino group with a poly(ethylene glycol) monomethyl ether (MeOPEG550) chloroformate [78]. A higher yield was recently achieved for the synthesis of pegylated porphyrin **34** of larger boron content, via conjugation of a low molecular weight tri-PEG group to a *meso*-tetraarylporphyrin bearing six Co(III)-bis(dicarbollides) [60]. The precursor porphyrin was prepared by a mixed condensation of 3,5-dimethoxybenzaldehyde and methyl 4-formylbenzoate with pyrrole using Lindsey's method, followed by deprotection of the methoxy and ester groups with BBr_3 in 10% overall yield. The resulting free carboxylic acid group was conjugated to glycine *tert*-butyl ester followed by functionalization of the six hydroxyl groups with zwiterionic [3,3′-Co(8-$C_4H_8O_2$-1,2-$C_2B_9H_{10}$)(1′,2′-$C_2B_9H_{11}$)] and deprotection using TFA in 65% yield (three steps). Porphyrin **34** was obtained by conjugation of the PEG *tert*-butyl ester using HATU/HOBt/DIEA and deprotection with TFA in 19% overall yield.

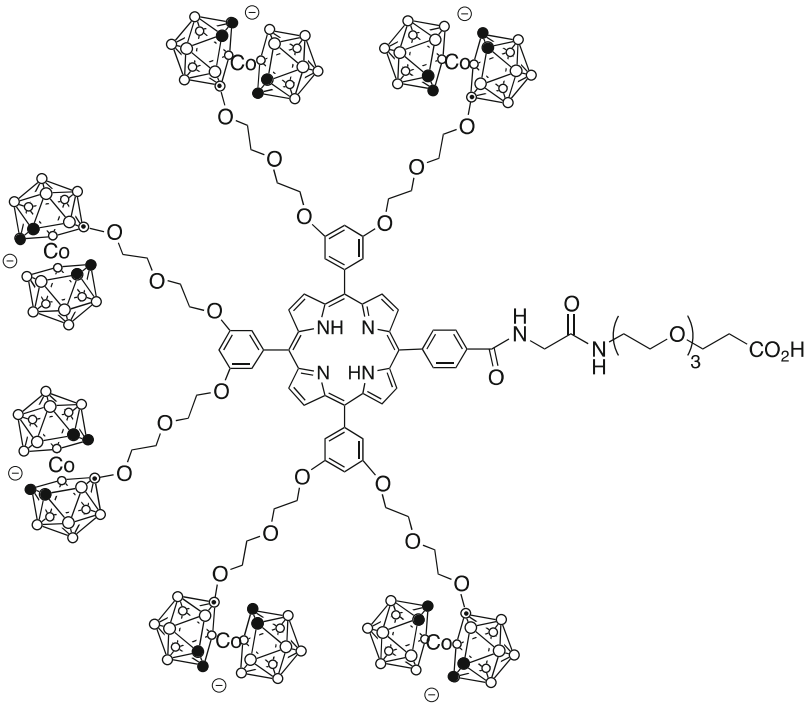

34

Recently, boronated porphyrin **35** bearing a tri-PEG was prepared in higher yields using an alternative conjugation procedure, involving nucleophilic substitution of

the *para*-fluoride of a pentafluorophenylporphyrin precursor [79]. Using this methodology, boronated porphyrins **36**–**42** bearing linear polyamines were also synthesized in high yields [79]. The tricarboranylporphyrin precursor to porphyrins **35**–**42** was obtained in 30% yield from reaction of *meso*-tetra(pentafluorophenyl) porphyrin with 1-mercaptomethyl-*para*-carborane. Conjugation of this porphyrin with the corresponding Boc-protected polyamines or *tert*-butyl-protected PEG using NMP at 100°C, followed by deprotection with TFA gave porphyrins **35**–**42** in >90% yields.

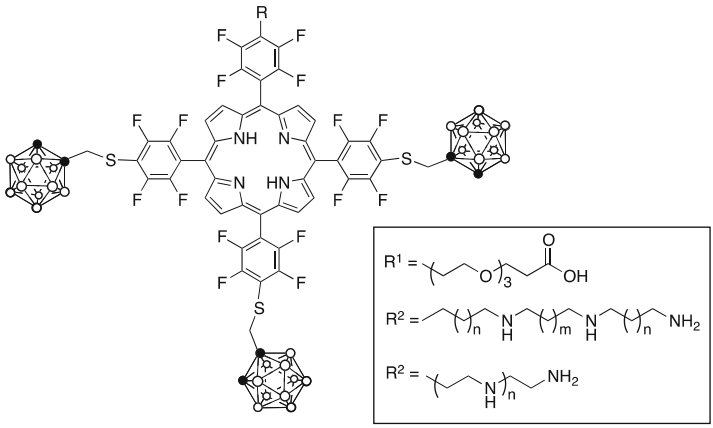

35: R = R^1
36: R = R^2, n = 0, m = 1
37: R = R^2, n = 1, m = 1
38: R = R^2, n = 1, m = 2
39: R = R^2, n = 1, m = 0
40: R = R^3, n = 2
41: R = R^3, n = 3
42: R = R^3, n = 4

The BOPP derivative **43** (as regioisomeric mixture) conjugated to a NLS was synthesized from *m*-BOPP (*meta*-carborane analogue of BOPP) by conjugation of a mixture of mono-methyl ester *m*-BOPP to the NLS peptide on rink amide resin, using HATU as the coupling agent [80].

Porphyrin **44** containing the cell-penetrating peptide HIV-1 Tat (48-60) with the sequence GRKKRRQRRRPPQ was prepared by conjugation of a porphyrin bearing three Co(III)-bis(dicarbollides) and a free carboxylic acid with the pegylated peptide on PAL-PEG-PS resin using HOBt/TBTU/DIPEA [59]. After cleavage from the solid support and deprotection using a mixture consisting of TFA/TIS/H_2O/phenol 88:2:5:5, porphyrin **44** was obtained in 8% yield.

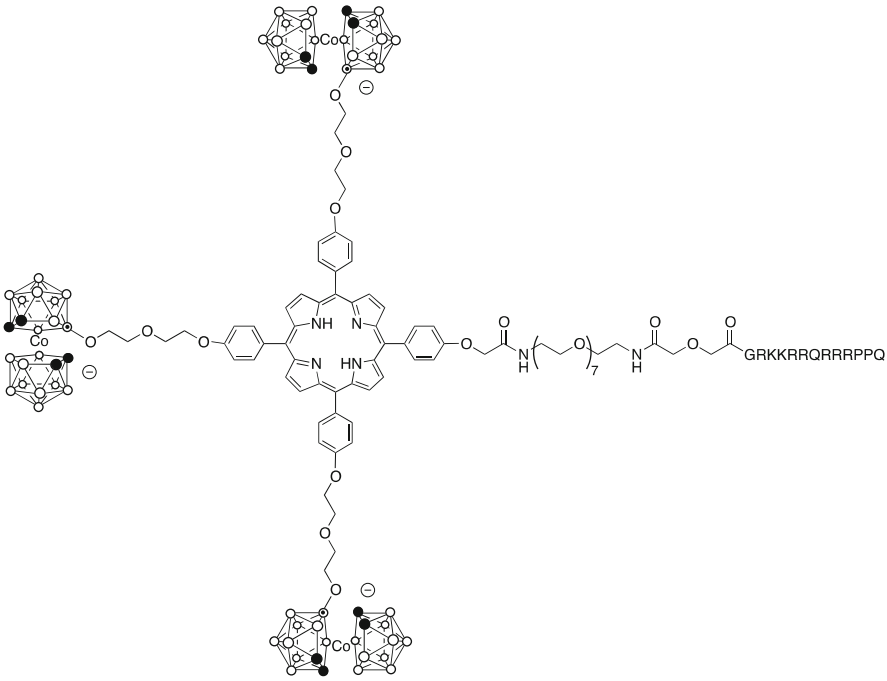

44

3.3 Carboranyl-Containing Corroles and Phthalocyanines

Corroles are tetrapyrrolic macrocycles with a direct pyrrole–pyrrole link. The total synthesis of tricarboranylcorroles **45** with the *nido*-carborane groups at *para*- or *meta*-phenyl positions was reported from the corresponding carboranyl-benzaldehydes and pyrrole, in about 10% yield [81]. The Lindsey method was used for the condensation reaction using excess of pyrrole (10 equiv.) to minimize the formation of the porphyrin. The insertion of Cu(III) ion using copper acetate in methanol was followed by fluoride-induced deboronation to give corroles **45** in quantitative yields.

The syntheses of several boron-containing phthalocyanines, including **46**–**52**, have been reported, both by tetramerization of a boron-substituted phthalonitrile and by direct functionalization of a pre-formed macrocycle. The total synthesis method is usually preferred, due to the poor solubility of these systems in most solvents, which renders the functionalization of the macrocycle difficult. However, in the case of *ortho*-carborane-containing phthalocyanines, functionalization of a pre-formed macrocycle is the preferred method because the basic conditions used during phthalocyanine synthesis often lead to degradation of the *ortho*-carborane cages. Zn(II)-phthalocyanines **46** were obtained as mixtures of regioisomers by

cyclotetramerization of the corresponding 3- or 4-*ortho*-carboranylphthalonitriles at 200°C, in the presence of zinc(II) acetate [82, 83].

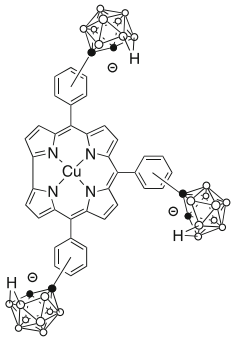

45

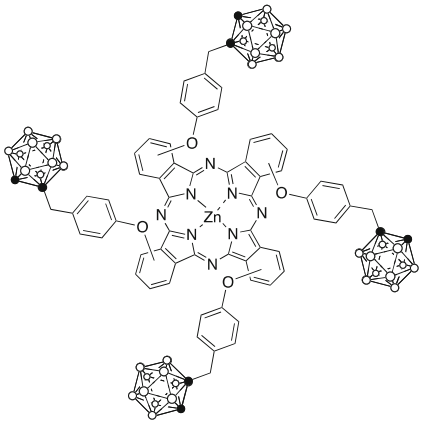

46

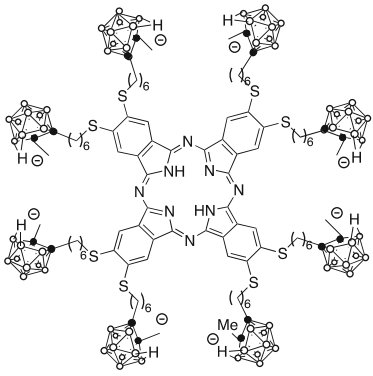

47

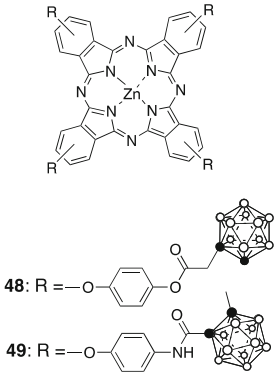

The symmetric and octa-anionic phthalocyanine **47** was synthesized in 30% yield via tetracyclization of the corresponding carborane-containing phthalonitrile in the presence of DBU and *n*-BuOH at 140°C [84]. The carboranylphthalonitrile was prepared by base-catalyzed aromatic nucleophilic substitution of 4,5-dichlorophthalonitrile with thiol-carborane.

Phthalocyanines **48** and **49**, as mixtures of regioisomers, bearing four *ortho*-carboranes were synthesized using the two strategies described above, by fuctionalization of a pre-formed macrocycle and by tetramerization of the corresponding carborane-containing phthalonitriles [85]. The former method gave the target compounds in 13–20% yields while self-condensation of the phthalonitrile

precursors gave only 1–10% yields. Regioisomerically pure phthalocyanines **50**–**52** were prepared by condensation of the corresponding boronated phthalonitrile with 30-fold excess of 1,2-dicyanobenzene, to produce the A_3B-type carboranylphthalocyanines as the only product in addition to the symmetric A_4-type phthalocyanine, which was removed by filtration [86, 87]. The carborane-containing phthalonitriles were prepared by nucleophilic ring opening of zwitterionic [3,3′-Co(8-$C_4H_8O_2$-1,2-$C_2B_9H_{10}$)(1′,2′-$C_2B_9H_{11}$)] by phenoxy- or pyridyl-functionalized phthalonitriles under basic conditions.

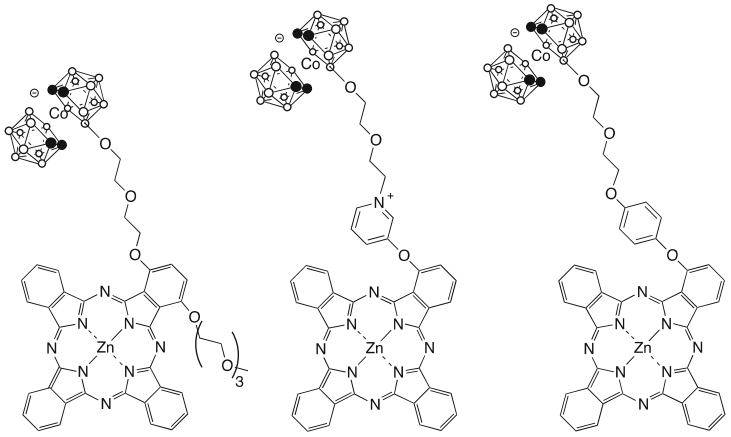

50 **51** **52**

4 Conclusions and Outlook

Over 100 boron-containing tetrapyrrolic macrocycles have been synthesized for application in BNCT following two main methodologies: by total synthesis from boronated monomeric precursors or from functionalization of a pre-formed macrocycle. However, only a few of these boronated macrocycles have been evaluated in preclinical biological investigations. The early reported carboranylporphyrins BOPP and CuTCPH were shown to deliver therapeutic amounts of boron to tumor-bearing mice, with high tumor-to-blood and tumor-to-brain boron concentration ratios [19, 34, 35, 39–41, 88–94]. Several other boronated macrocycles containing hydrolytically stable carbon–carbon linkages between the macrocycle and carborane groups (e.g., H_2TCP and H_2DCP) and/or higher amount of boron by weight than BOPP and CuTCPH (e.g., H_2OCP) were also shown to have low mice toxicity, and to deliver therapeutic amounts of boron to tumor-bearing mice [47, 54, 60, 65]. All other boronated porphyrin derivatives have only been evaluated in preliminary cellular studies, and their in vivo biological properties are still unknown.

Alternative routes for the in vivo administration of boronated porphyrin derivatives have been investigated with the aim to increase permeability across the BBB and tumor uptake. A very promising methodology is convection-enhanced delivery (CED), which is able to deliver extremely high amounts of boron (>100 μg/g) to intracerebral animal tumors, with very high tumor-to-normal brain and tumor-to-blood boron ratios, and no systemic toxicity [95–97].

Among the porphyrin derivatives, boronated chlorins, corroles, bacteriochlorins, and phthalocyanines can be used as dual BNCT and PDT sensitizers because of their absorptions of near-IR light that penetrates deeper into human tissues. The combination of the BNCT and PDT therapies could lead to higher efficacy of tumor treatment via the targeting of different mechanisms of tumor cell destruction. However, current clinical development of BNCT and investigation of the biological properties of new boron delivery agents are slow for a variety of reasons, including readily availability of adequate neutron sources and cost. Nevertheless, the outlook for BNCT is bright since this binary therapy offers new hope for otherwise untreatable cancers.

Acknowledgments The support from the US National Institutes of Health (grant number R01 CA 098902) is acknowledged.

References

1. Hawthorne MF (1993) The role of chemistry in the development of boron neutron capture therapy of cancer. Angew Chem Int Ed 32:950–984
2. Soloway AH, Tjarks W, Barnum BA et al (1998) The chemistry of neutron capture therapy. Chem Rev 98:1515–1562
3. Barth RF, Coderre JA, Vicente MGH (2005) Boron neutron capture therapy of cancer: current status and future prospects. Clin Cancer Res 11:3987–4002
4. Barth RF, Vicente MGH, Harling OK et al (2012) Current status of boron neutron capture therapy of high grade gliomas and recurrent head and neck cancer. Radiat Oncol 7:146
5. Hopewell JW, Gorlia T, Pellettieri L et al (2011) Boron neutron capture therapy for newly diagnosed glioblastoma multiforme: an assessment of clinical potential. Appl Radiat Isot 69:1737–1740
6. Kawabata S, Miyatake S, Hiramatsu R et al (2011) Phase II clinical study of boron neutron capture therapy combined with X-ray radiotherapy/temozolomide in patients with newly diagnosed glioblastoma multiforme – study design and current status report. Appl Radiat Isot 69:1796–1799
7. Kankaanranta L, Seppala T, Koivunoro H et al (2011) L-Boronophenylalanine-mediated boron neutron capture therapy for malignant glioma progressing after external beam radiation therapy: a phase I study. Int J Radiat Oncol Biol Phys 80:369–376
8. Yamamoto T, Nakai K, Nariai T et al (2011) The status of Tsukuba BNCT trial: BPA-based boron neutron capture therapy combined with X-ray irradiation. Appl Radiat Isot 69: 1817–1818
9. Kankaanranta L, Seppala T, Koivunoro H et al (2012) Boron neutron capture therapy in the treatment of locally recurred head-and-neck cancer: final analysis of a phase I/II trial. Int J Radiat Oncol Biol Phys 82:e67–e75

10. Sibrian-Vazquez M, Vicente MGH (2011) Boron tumor-delivery for BNCT: recent developments and perspectives. In: Hosmane NS (ed) Boron science: new technologies and applications. CRC, Boca Raton, pp 203–232
11. Sivaev IB, Bregadze VV (2009) Polyhedral boranes for medical applications: current status and perspectives. Eur J Inorg Chem 11:1433–1450
12. Dougherty TJ, Gomer CJ, Henderson BW (1998) Photodynamic therapy. J Natl Cancer Inst 90: 889–905
13. Pandey RK, Zhang G (2002) Porphyrins as photosensitizers in photodynamic therapy. In: Kadish KM, Smith KM, Guilard R (eds) The porphyrin handbook, vol 6. Academic, Boston, pp 157–230
14. Vicente MGH, Sibrian-Vazquez M (2010) Syntheses of boronated porphyrins and their application in BNCT. In: Kadish KM, Smith KM, Guilard R (eds) The porphyrin handbook, vol 4. Academic, Boston, pp 191–248
15. Ol'shevskaya VA, Zaytsev AV, Savchenko AN et al (2007) Boronated porphyrins and chlorins as potential anticancer drugs. Bull Korean Chem Soc 28:1910–1916
16. Renner MW, Miura M, Easson MW, Vicente MGH (2006) Recent progress in the syntheses and biological evaluation of boronated porphyrins for boron neutron-capture therapy. Anti-cancer Agents Med Chem 6:145–157
17. Haushalter RC, Rudolph RW (1978) *meso*-Tetracarboranylporphyrins. J Am Chem Soc 100: 4628–4629
18. Haushalter RC, Butler WM, Rudolph RW (1981) The preparation and characterization of several *meso*-tetracarboranylporphyrins. J Am Chem Soc 103:2620–2627
19. Kahl SB, Joel DD, Nawrocky MM (1990) Uptake of a *nido*-carboranylporphyrin by human glioma xenografts in athymic nude mice and by syngeneic ovarian carcinomas in immuno-competent mice. Proc Natl Acad Sci USA 87:7265–7269
20. Kahl SB, Koo M-S (1990) Synthesis of tetrakis-carborane-carboxylate esters of 2,4-bis-([a], [b]-dihydroxyethyl)-deuteroporphyrin IX. Chem Commun 1769–1771
21. Miura M, Gabel D, Oenbrink G, Fairchild RG (1990) Preparation of carboranyl porphyrins for boron neutron capture therapy. Tetrahedron Lett 31:2247–2250
22. Phadke AS, Morgan AR (1993) Synthesis of carboranyl porphyrins: potential drugs for boron neutron capture therapy. Tetrahedron Lett 34:1725–1728
23. Woodburn K, Phadke AS, Morgan AR (1993) An *in vitro* study of boronated porphyrins for potential use in boron neutron capture therapy. Bioorg Med Chem Lett 3:2017–2022
24. Gabel D, Harfst S, Moller D, Ketz H (1994) In: Kabalka GW (ed) Current topics in the chemistry of boron. The Royal Society of Chemistry, Cambridge, pp 161–164
25. Alam F, Soloway AH, Bapat BV et al (1989) In: Fairchild RG, Bond VP, Woodhead AD (eds) Clinical aspects of neutron capture therapy. Plenum, New York, pp 107–111
26. Vicente MGH, Shetty SJ, Wickramasinghe A, Smith KM (2000) Syntheses of carbon–carbon linked carboranylated porphyrins for boron neutron capture therapy of cancer. Tetrahedron Lett 41:7623–7627
27. Vicente MGH, Nurco DJ, Shetty SJ et al (2001) First structural characterization of a covalently bonded porphyrin-carborane system. Chem Commun 483–484
28. Vicente MGH, Edwards BF, Shetty SJ (2002) Syntheses and preliminary biological studies of four *meso*-tetra[(nido-carboranylmethyl)phenyl]porphyrins. Bioorg Med Chem 10:481–492
29. Vicente MGH, Nurco DJ, Shetty SJ (2002) Synthesis, dark toxicity and induction of *in vitro* DNA photodamage by a tetra(4-*nido*-carboranylphenyl)porphyrin. J Photochem Photobiol B 68:123–132
30. Kahl SB, Li J (1996) Synthesis and characterization of a boronated metallophthalocyanine for boron neutron capture therapy. Inorg Chem 35:3878–3880
31. Coderre JA, Morris GM, Kalef-Ezra J (1999) The effects of boron neutron capture irradiation on oral mucosa: evaluation using a rat tongue model. Radiat Res 152:113–118

32. Matsumura A, Shibata Y, Yamamoto T et al (1999) A new boronated porphyrin (STA-BX909) for neutron capture therapy: an in vitro survival assay and in vivo tissue uptake study. Cancer Lett 141:203–209
33. Fabris C, Jori G, Giuntini F, Roncucci G (2001) Photosensitizing properties of a boronated phthalocyanine: studies at the molecular and cellular level. J Photochem Photobiol B 64:1–7
34. Miura M, Joel DD, Smilowitz HM et al (2001) Biodistribution of copper carboranyltetraphenylporphyrins in rodents bearing an isogeneic or human neoplasm. J Neurooncol 52:111–117
35. Miura M, Morris GM, Micca PL et al (2001) Boron neutron capture therapy of a murine mammary carcinoma using a lipophilic carboranyltetraphenylporphyrin. Radiat Res 155: 603–610
36. Rothemund P (1935) Formation of porphyrins from pyrrole and aldehydes. J Am Chem Soc 57:2010–2011
37. Adler AD, Longo FR, Finarelli JD et al (1967) A simplified synthesis for *meso*-tetraphenylporphine. J Org Chem 32:476
38. Lindsey JS, Schreiman IC, Hsu HC et al (1987) Rothemund and Adler–Longo reactions revisited: synthesis of tetraphenylporphyrins under equilibrium conditions. J Org Chem 52: 827–836
39. Wu H, Micca PL, Makar MS, Miura M (2006) Total syntheses of three copper (II) tetracarboranylphenylporphyrins containing 40 or 80 boron atoms and their biological properties in EMT-6 tumor-bearing mice. Bioorg Med Chem 14:5083–5092
40. Kreimann EL, Miura M, Itoiz ME et al (2003) Biodistribution of a carborane-containing porphyrin as a targeting agent for boron neutron capture therapy of oral cancer in the hamster cheek pouch. Arch Oral Biol 48:223–232
41. Miura M, Morris GM, Micca PL et al (2004) Synthesis of copper octabromotetracarboranylphenylporphyrin for boron neutron capture therapy and its toxicity and biodistribution in tumour-bearing mice. Br J Radiol 77:573–580
42. Fabris C, Vicente MGH, Hao E et al (2007) Tumour-localizing and -photosensitising properties of *meso*-tetra(4-*nido*-carboranylphenyl)porphyrin (H_2TCP). J Photochem Photobiol B 89:131–138
43. Soncin M, Friso E, Jori G, Hao E, Vicente MGH et al (2008) Tumor-localizing and radiosensitizing properties of *meso*-tetra(4-*nido*-carboranylphenyl)porphyrin (H_2TCP). J Porphyr Phthalocyanines 12:866–873
44. Jori G, Soncin M, Friso E, Vicente MGH et al (2009) A novel boronated-porphyrin as a radiosensitizing agent for boron neutron capture therapy of tumors: *in vitro* and *in vivo* studies. Appl Radiat Isot 67:S321–S324
45. Frixa C, Mahon MF, Thompson AS et al (2002) Direct Cu(I)-catalysed coupling of a carborane to a *meso*-tetraphenylporphyrin. Tetrahedron Lett 43:1557–1559
46. Ongayi O, Gottumukkala V, Fronczek FR, Vicente MGH (2005) Synthesis and characterization of a carboranyl-tetrabenzoporphyrin. Bioorg Med Chem Lett 15:1665–1668
47. Gottumukkala V, Ongayi O, Baker DG, Lomax LG, Vicente MGH (2006) Synthesis, cellular uptake and animal toxicity of a tetra(carboranylphenyl)-tetrabenzoporphyrin. Bioorg Med Chem 14:1871–1879
48. Gottumukkala V, Luguya R, Fronczek FR, Vicente MGH (2005) Synthesis and cellular studies of an octa-anionic 5,10,15,20-tetra[3,5-(*nido*-carboranylmethyl)phenyl]porphyrin (H_2OCP) for application in BNCT. Bioorg Med Chem 13:1633–1640
49. Hiramatsu R, Kawabata S, Miyatake S-I et al (2011) Application of a boronated porphyrin (H_2OCP) as a dual sensitizer for both PDT and BNCT. Lasers Surg Med 43:52–58
50. Clark JC, Fronczek FR, Vicente MGH (2005) Novel carboranylporphyrins for application in boron neutron capture therapy (BNCT) of tumors. Tetrahedron Lett 46:2365–2368
51. Clark JC, Fabre B, Fronczek FR, Vicente MGH (2005) Syntheses and properties of carboranylpyrroles. J Porphyr Phthalocyanines 9:803–810
52. Hao E, Fronczek FR, Vicente MGH (2006) Carborane functionalized pyrroles and porphyrins via the Suzuki cross-coupling reaction. Chem Commun 4900–4902

53. Arsenault GP, Bullock E, MacDonald SF (1960) Pyrromethanes and porphyrins therefrom. J Am Chem Soc 82:4384–4389
54. Vicente MGH, Wickramasinghe A, Nurco DJ et al (2003) Synthesis, toxicity and biodistribution of two 5,15-di[3,5-(*nido*-carboranylmethyl)phenyl]porphyrins in EMT-6 tumor bearing mice. Bioorg Med Chem 11:3101–3108
55. Vicente MGH, Gottumukkala V, Wickramasinghe A et al (2004) Singlet oxygen generation and dark toxicity of a *nido*- and a *closo*-carboranylporphyrin. Proc SPIE 5315:33–40
56. Easson MW, Fronczek FR, Jensen TJ, Vicente MGH (2008) Synthesis and *in vitro* properties of trimethylamine- and phosphonate-substituted carboranylporphyrins for application in BNCT. Bioorg Med Chem 16:3191–3208
57. Hao E, Vicente MGH (2005) Expeditious synthesis of porphyrin-cobaltacarborane conjugates. Chem Commun 1306–1308
58. Hao E, Sibrian-Vazquez M, Serem W et al (2007) Synthesis, aggregation and cellular investigations of porphyrin-cobaltacarborane conjugates. Chem Eur J 13:9035–9042
59. Sibrian-Vazquez M, Hao E, Jensen TJ, Vicente MGH (2006) Enhanced cellular uptake with a cobaltacarborane-porphyrin-HIV-1 Tat 48-60 conjugate. Bioconjug Chem 17:928–934
60. Bhupathiraju NVSDK, Gottumukkala V, Hao E et al (2011) Synthesis and toxicity of cobaltabisdicarbollide-containing porphyrins of high boron content. J Porphyr Phthalocyanines 15:973–983
61. Hao E, Zhang M, Wenbo E et al (2008) Synthesis and spectroelectrochemistry of *N*-cobaltacarborane porphyrin conjugates. Bioconjug Chem 19:2171–2181
62. Hao E, Jensen TJ, Courtney BH, Vicente MGH (2005) Synthesis and cellular studies of porphyrin-cobaltacarborane conjugates. Bioconjug Chem 16:1495–1502
63. Luguya R, Fronczek FR, Smith KM, Vicente MGH (2004) Synthesis of novel carboranylchlorins with dual application in boron neutron capture therapy (BNCT) and photodynamic therapy (PDT). Appl Radiat Isot 61:1117–1123
64. Luguya R, Jensen TJ, Smith KM, Vicente MGH (2006) Synthesis and cellular studies of a carboranylchlorin for the PDT and BNCT of tumors. Bioorg Med Chem 14:5890–5897
65. Hao E, Friso E, Miotto G, Jori G et al (2008) Synthesis and biological investigations of tetrakis (*p*-carboranylthio-tetrafluorophenyl)chlorin (TPFC). Org Biomol Chem 6:3732–3740
66. Kuchin RAV, Mal'shakova MV, Belykh DV et al (2009) Synthesis of boronated derivatives of chlorin e6 with amide bond. Dokl Chem 425:80–83
67. Ol'shevskaya VA, Nikitina RG, Savchenko AN et al (2009) Novel boronated chlorin e6-based photosensitizers: synthesis, binding to albumin and antitumour efficacy. Bioorg Med Chem 17: 1297–1306
68. Belykh DV, Karmanova PL, Spirikhin LV, Kutchin AV (2002) Synthesis of chlorin e_6 amide derivatives. Mendeleev Commun 12:77–78
69. Ol'shevskaya VA, Savchenko AN, Zaitsev AV et al (2009) Novel metal complexes of boronated chlorin e_6 for photodynamic therapy. J Organomet Chem 694:1632–1637
70. Bregadze VI, Sivaev IB, Lobanova IA et al (2009) Conjugates of boron clusters with derivatives of natural chlorin and bacteriochlorin. Appl Radiat Isot 67:S101–S104
71. Mironov AF, Grin MA (2008) Synthesis of chlorin and bacteriochlorin conjugates for photodynamic and boron neutron capture therapy. J Porphyr Phthalocyanines 12:1163–1172
72. Ol'shevskaya VA, Zaitsev AV, Savchenko AN et al (2008) Synthesis of boronated derivatives of pheophorbide a. Dokl Chem 423:294–298
73. Luzgina VN, Ol'shevskaya VA, Sekridova AV et al (2007) Synthesis of boron-containing derivatives of pyropheophorbide (a) under-bar and investigation of their photophysical and biological properties. Russ J Org Chem 43:1243–1251
74. Ratajski M, Osterloh J, Gabel D (2006) Boron-containing chlorins and tetraazaporphyrins: synthesis and cell uptake of boronated pyropheophorbide a derivatives. Anticancer Agents Med Chem 6:159–166
75. Grin MA, Semioshkin AA, Titeev RA et al (2007) Synthesis of a cycloimide bacteriochlorin p conjugate with the *closo*-dodecaborate anion. Mendeleev Commun 17:14–25

76. Grin MA, Titeev RA, Brittal DI et al (2011) New conjugates of cobalt bis(dicarbollide) with chlorophyll *a* derivatives. Mendeleev Commun 21:84–86
77. Grin MA, Brittal DI, Chestnova AV et al (2010) Synthesis of cobalt bis(dicarbollide) conjugates with natural chlorins by the Sonogashira reaction. Russ Chem Bull Int Ed 59:219–224
78. Frixa C, Mahon MF, Thompson AS, Threadgill MD (2003) Synthesis of *meso*-substituted porphyrins carrying carboranes and oligo(ethylene glycol) units for potential applications in boron neutron capture therapy. Org Biomol Chem 1:306–317
79. Bhupathiraju NVSDK, Vicente MGH (2013) Synthesis and cellular studies of polyamine conjugates of a mercaptomethyl–carboranylporphyrin. Bioorg Med Chem 21:485–495
80. Dozzo P, Koo MS, Berger S et al (2005) Synthesis, characterization, and plasma lipoprotein association of a nucleus-targeted boronated porphyrin. J Med Chem 48:357–559
81. Luguya RJ, Fronczek FR, Smith KM, Vicente MGH (2005) Carboranylcorroles. Tetrahedron Lett 46:5365–5368
82. Giuntini F, Raoul Y, Dei D et al (2005) Synthesis of tetrasubstituted Zn(II)-phthalocyanines carrying four carboranyl-units as potential BNCT and PDT agents. Tetrahedron Lett 46: 2979–2982
83. Friso E, Roncucci G, Dei D et al (2006) A novel ^{10}B-enriched carboranyl-containing phthalocyanine as a radio- and photo-sensitising agent for boron neutron capture therapy and photodynamic therapy of tumours: *in vitro* and *in vivo* studies. Photochem Photobiol Sci 5:39–50
84. Pietrangeli D, Rosa A, Pepe A, Ricciardi G (2011) Symmetrically substituted *nido*-carboranylphthalocyanines: facile synthesis, characterization, and solution properties. Evidence for intra- and intermolecular H+/K+ exchange. Inorg Chem 50:4680–4682
85. Tsaryova O, Semioshkin A, Wöhrle D, Bregadze VI (2005) Synthesis of new carboran-based phthalocyanines and study of their activities in the photooxidation of citronellol. J Porphyr Phthalocyanines 9:268–274
86. Li H, Fronczek FR, Vicente MGH (2008) Synthesis and properties of cobaltacarborane-functionalized Zn(II)-phthalocyanines. Tetrahedron Lett 49:4828–4830
87. Li H, Fronczek FR, Vicente MGH (2009) Cobaltacarborane-phthalocyanine conjugates: syntheses and photophysical properties. J Organomet Chem 694:1607–1611
88. Fairchild RG, Kahl SB, Laster BH et al (1990) A in vitro determination of uptake, retention, distribution, biological efficacy, and toxicity of boronated compounds for neutron-capture therapy – a comparison of porphyrins with sulfhydryl boron hydrides. Cancer Res 50:4860–4865
89. Hill JS, Kahl SB, Kaye AH et al (1992) Selective tumor uptake of a boronated porphyrin in an animal-model of cerebral glioma. Proc Natl Acad Sci USA 89:1785–1789
90. Ceberg CP, Brun A, Kahl SB et al (1995) A comparative-study on the pharmacokinetics and biodistribution of boronated porphyrin (BOPP) and sulfhydryl boron hydride (BSH) in the rg2 rat glioma model. J Neurosurg 83:86–92
91. Tibbitts J, Fike JR, Lamborn KR et al (1999) Toxicology of a boronated porphyrin in dogs. Photochem Photobiol 69:587–594
92. Miura M, Micca P, Heinrichs J et al (1992) Biodistribution and toxicity of 2,4-divinyl-*nido*-*ortho*-carboranyldeuteroporphyrin IX in mice. Biochem Pharmacol 43:467–476
93. Miura M, Micca PL, Fisher CD et al (1996) Synthesis of a nickel tetracarboranylphenylporphyrin for boron neutron-capture therapy: biodistribution and toxicity in tumor-bearing mice. Int J Cancer 68:114–119
94. Miura M, Micca P, Fisher C et al (1998) Evaluation of carborane-containing porphyrins as tumour targeting agents for boron neutron capture therapy. Br J Radiol 71:773–781
95. Ozawa T, Santos RA, Lamborn KR et al (2004) In vivo evaluation of the boronated porphyrin TABP-1 in U-87 MG intracerebral human glioblastoma xenografts. Mol Pharm 1:368–374
96. Ozawa T, Afzal J, Lamborn KR et al (2005) Toxicity, biodistribution, and convection-enhanced delivery of the boronated porphyrin BOPP in the 9L intracerebral rat glioma model. Int J Radiat Oncol Biol Phys 63:247–252
97. Kawabata S, Yang W, Barth RF et al (2011) Convection enhanced delivery of carboranyl-porphyrins for neutron capture therapy of brain tumors. J Neurooncol 103:175–185

Top Heterocycl Chem (2014) 34: 53–116
DOI: 10.1007/7081_2014_135

Published online: 7 November 2014

Optical Anisotropy of Thin and Ultrathin Porphyrin Layers

Claudio Goletti

Abstract The use of porphyrins as the sensing elements in technical applications (e.g. electronic nose and electronic tongue) has anticipated the real comprehension of the mechanisms determining at the microscopic level the interaction between the analyte molecules and the layer itself. A huge bulk of phenomenological data has been accumulated, showing the high efficiency of these organic materials versus specific gaseous particles. It has been also reported that the sensitivity to gas is higher for highly disordered layers, probably due to the enhanced surface area of the resulting assembly. A better comprehension of the microscopic behavior would definitely allow a deeper exploitation of the properties of the layer in view of the most efficient electronic devices . Consequently, recently there has been an effort to gain a higher level of accuracy in characterizing the electronic properties and the morphology of the thin (sometimes ultrathin) layers deposited.

In this chapter, I will present and discuss the most significant results obtained by studying the optical anisotropy of thin and ultrathin porphyrin films. In particular, I will mostly limit to data obtained by using a powerful optical technique (originally developed in traditional surface science), namely, reflectance anisotropy spectroscopy (RAS). I will show how the measured spectral features in RAS spectra have their origin in the structure of the layer and can be connected to the interaction existing between molecules in the layer. I will briefly describe the technique, giving some details about the experimental setup and explaining how experimental data can be interpreted. A review of results will follow, from the very early applications on Langmuir–Blodgett and Langmuir–Schaefer films to the more recent study of ultrathin layers evaporated in ultrahigh vacuum.

Keywords Analyte discrimination · Langmuir–Blodgett layers · Langmuir–Schaefer layers · Optical anisotropy of Langmuir–Blodgett layers · Optical properties of thin layers · Optical sensors · Porphyrin layers · Reflectance anisotropy spectroscopy (RAS)

C. Goletti (✉)
Department of Physics, University of Rome Tor Vergata, 00133 Rome, Italy

Contents

1 Introduction

The use of porphyrins as materials for significant, widespread, and even innovative applications has produced a significant amount of results in the last few years. In particular, the realization of thin and ultrathin molecular layers has been pursued and achieved because of the interest for systems where the high surface-to-bulk ratio and the low quantity of mass are basic conditions towards the assembly of new molecular devices for organic-based electronics [1]. We have noticed a strong effort to characterize the structural and electronic properties of these layers as well as to control and to improve the methods of growth, obtaining important and sometimes unexpected results.

It is quite surprising that within this effort, only a small number of experiments have been reported about the investigation of the optical properties of porphyrin layers. Porphyrins actually exhibit prominent optical properties, with very intense transitions mainly related to the dominant absorption band, the so-called Soret band, whose details (photon energy position, line shape, width) are strongly related to the aggregation of molecules (in solution or in the solid state), that produce a blue or red shift (with respect to the position of the band of the not aggregate molecules) depending upon the coupling existing between adjacent porphyrins [2]. In addition, the use of optical spectroscopies – after their sensitivity to thickness has been demonstrated – is in principle compatible also with studying layers deposited or immersed in liquid environment, thus exploiting the powerful opportunities offered by chemistry in solutions.

In spite of that, a limited number of papers have been published on this particular topic, mainly using methods borrowed from the investigation of inorganic surfaces that naturally exhibit a very high sensitivity to low-thickness systems. In this chapter, I will report the most significant results about porphyrin layers obtained by a particular optical spectroscopy, namely, reflectance anisotropy spectroscopy (RAS). I will briefly describe the technique, give some details about the experimental setup, and discuss how experimental data can be interpreted. A review of the most significant results will follow, from the very early applications on Langmuir–

Blodgett and Langmuir–Schaefer films to the more recent study of ultrathin layers evaporated in ultrahigh vacuum.

2 Optics for Organics

The very first example of an optical spectroscopy applied to the investigation of the growth of an organic layer dates back to the 1990s [3]. At that time, the study of thin layers of organic molecules deposited on solid substrates began to be a pressing necessity for research. In fact, despite the well-established application of optical spectroscopy to detect surface states of metal and semiconductor surfaces [4], the extension of optics to organics was motivated by the occurrence of a scientific and technological issue related to the development of organic molecular beam epitaxy (OMBE) [5], also known as organic molecular beam deposition (OMBD). As it was clearly reported since the very early papers published on this subject, OMBE invention was a consequence of the preceding success of the inorganic counterpart (molecular beam epitaxy (MBE)) and of the increasing interest for a method able to control also for organics the growth with subnanometer accuracy from the very early steps of deposition, in view of the final device architecture. Several technical details were just taken from the inorganic case, sometimes without considering correctly the peculiarities of organics: to mention a significant example, the use of high-energy electrons to monitor in real time the deposition process often produced defects in the soft organic samples investigated (in reflected high-energy electron diffraction (RHEED), commonly used in MBE, the electron energy usually is raised up to 2–3 keV). The OMBE inventor himself wrote that "leaving the (RHEED electron) beam on during deposition (of the organic thin film), resulted in the development of broad rings characteristic of amorphous film growth. These features are possibly due to disruption of the grown layer due to charging and/or heating of the relatively insulating film, or even due to damage of the molecules by high energy electrons" [6]. The softness of the organic matter and the relative weakness of the related bonding made then necessary the use of a more *gentle* probe, but able to investigate the electronic and structural properties of the growing layer and to give information about the augmenting thickness.

Optics, mainly in the near ultraviolet (UV)-visible-near-infrared (IR) range (300–1,000 nm), offered the possible alternative to electronic diffraction techniques. At the end of the 1990s, three optical spectroscopies were more commonly used to investigate surface states (i.e., with the necessary sensitivity to very tiny quantities of organic material): surface differential spectroscopy (SDR), ellipsometry, and reflectance anisotropy spectroscopy (RAS).

In this review, ellipsometry will just be mentioned. It is a very powerful and sensitive technique, giving complete information on the optical properties of materials (isotropic and anisotropic), multilayers, and in general samples whose characteristics vary with thickness [7]. Ellipsometry has been also used for in situ and real-time growth control in MBE systems [8] and is therefore appropriate for

OMBE. However, ellipsometric quantities "as measured" are not easily interpreted and require modeling the sample and its dielectric tensor to extract meaningful information [9, 10]. This could possibly explain the lack of a really diffuse application of ellipsometry to monitor the growth and the properties of thin layers of porphyrins, although some interesting examples have been reported [11]. The interested reader could refer to LoSurdo and Hingerl [12] for a detailed and updated presentation of the technique.

For SDR and RAS, on the contrary, no modeling is strictly necessary to extract the basic significance from data, that is, (i) some changes have been caused by the process that the sample has undergone (SDR) or (ii) the sample exhibits an intrinsic optical anisotropy, intimately connected to its structure or to its electronic properties (RAS). Also in these cases, for a detailed interpretation of data, a further and deeper theoretical approach and simulation of the investigated system is needed, as well as a comparison with results from other techniques.

In SDR, the variation of the sample reflectance due to the surface modification, e.g., because of contamination (sometimes intentionally produced) or of the deposition of a film, is monitored by

$$\Delta R/R_{\mathrm{SDR}} = (R_{\mathrm{a}} - R_{\mathrm{b}})/R, \tag{1}$$

where R_{a} (R_{b}) is the reflectance of the sample *before* (*after*) its surface is modified, and R is the average reflectance $(R_{\mathrm{a}} + R_{\mathrm{b}})/2$. In the well-known application of SDR to clean semiconductor surfaces, "a" means the clean surface and "b" the oxidized surface, where the growth of the oxide layer has removed the surface state transitions by saturating the dangling bonds of the clean surface [4, 13].

Under the assumption that the reflectance change is directly a consequence of the variation in the sample conditions, by Eq. (1), we can disentangle the related effect from $\Delta R/R_{\mathrm{SDR}}$ data and attribute it to the modification that occurred at the outer layer. Effects due to a change in the substrate however cannot in principle be discarded and should be carefully considered case by case [14].

A more detailed interpretation in terms of the grown film is strongly dependent also upon the optical properties of the substrate. If this is not absorbing in the photon energy range used, the detection of new structures in the spectrum can be directly related to the film. If instead the substrate is absorbing, a more careful and complex interpretation of the signal is due, as the dielectric functions of the layer and of the substrate (if we assume – as it normally happens – that the outer medium, surrounding the sample, is transparent) are profoundly entangled in $\Delta R/R_{\mathrm{SDR}}$. In that case, a detailed deconvolution of spectra is necessary: this usually means an interpretation of the data within a classical three-layer model plus a Kramers–Kronig transform [13, 15] that will be discussed in Sect. 3.2.

A significant example is reported in Fig. 1, showing SDR spectra that have been measured *during* the deposition in ultrahigh vacuum by organic molecular beam epitaxy of a PTCDA (3,4,9,10-perylenetetracarboxylic dianhydride) film on muscovite mica(0001) at room temperature [16]. The film thickness ranges from 0.1 to 2.7 ML (with a coverage error estimated as 10%). The mica substrate is transparent

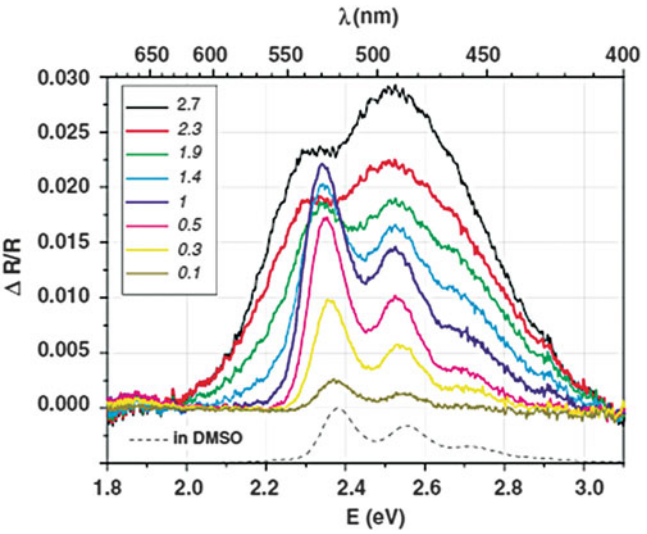

Fig. 1 Differential reflectance (SDR) spectra of PTCDA on mica during the growth from 0.1 to 2.7 ML. 2.7 ML corresponds to the total final thickness. Note the clear change in the characteristic spectral shape and the two intersection points at about 2.30 and 2.38 eV. For comparison, the absorption spectrum of PTCDA dissolved in dimethylsulfoxide is shown in the *bottom* (*dashed line*, shifted, arbitrary units). All the spectra are referred to the clean mica substrate (From Proehl et al. [16]. Reprinted with permission. Copyright 2004 by the American Physical Society.)

in the range 1.8–3.2 eV, and consequently, the reported $\Delta R/R_{SDR}$ signal can be straightforwardly connected to the aggregation of the PTCDA molecules in the film. At a nominal thickness of 1 molecular layer, the line shape of the $\Delta R/R_{SDR}$ curve suddenly changes: a significant alteration occurs in the relative height of the three peaks (at 2.35, 2.55, and 2.75 eV), the second becoming considerably more evident and broader. The spectral change is interpreted in terms of a monomer–dimer transition, occurring just above the completion of the first monolayer, that completely wets the substrate. In the first layer, only a weak electronic coupling is present among PTCDA molecules, but when the first layer is completed, the molecules stack on each other, forming dimers (Fig. 2).

Differently from mica, highly oriented pyrolitic graphite (HOPG) substrate is not optically transparent in the range 2–4 eV. It is often chosen for the deposition of organics: it is planar, easy to prepare (by simple scotch cleaving or exfoliation), inert enough to avoid complicating reactions with the ambient and with the deposited molecules, and compatible with organic and biological molecules because of its carbon termination.

In Fig. 3, the multilayer growth onto graphite of hexa-peri-hexabenzocoronene (HBC, $C_{42}H_{18}$), a disk-like polycyclic aromatic hydrocarbon, has been monitored by SDR [17]. At first glance, the thickness-dependent evolution of the spectra should suggest that new peaks at certain photon energies are apparently developing. However, given the non-negligible optical absorption of graphite, before discussing

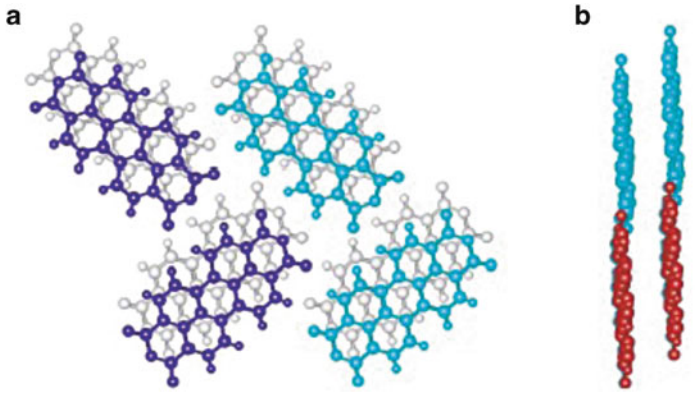

Fig. 2 Sketch of PTCDA molecules forming the so-called herringbone structure: (**a**) *top view* onto the (102) plane of the PTCDA crystal and (**b**) *side view*. The two types of dimers, **a** (in-plane) and **b** (stacked), are indicated (From Proehl et al. [16]. Reprinted with permission. Copyright 2004 by the American Physical Society.)

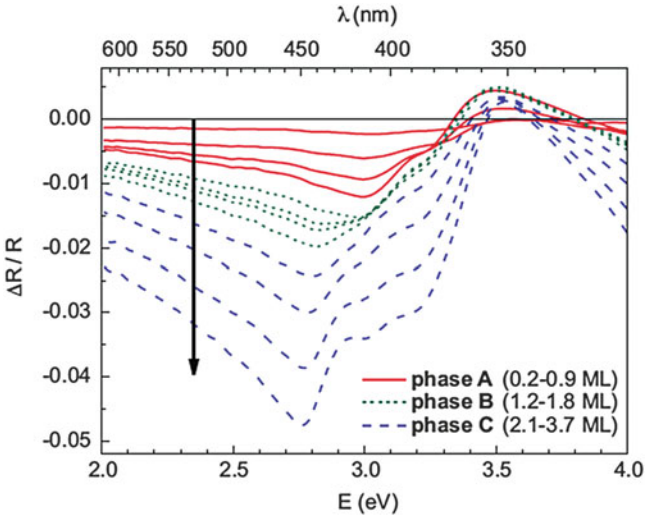

Fig. 3 Drift-corrected in situ SDR series of HBC on HOPG. The *arrow* points in the direction of increasing film thickness. The series is divided into three phases of the deposited film (for details, see the cited reference). *Solid lines*: 0.2–0.9 ML (phase A); *dotted lines*: 1.2–1.8 ML (phase B), *dashed lines*: 2.1–3.7 ML (phase C). All the spectra are referred to the clean HOPG substrate (From Forker et al. [17]. Reprinted with permission. Copyright 2006 by the American Physical Society.)

the *true* optical properties of the growing layers, the imaginary part of the layer dielectric function must be extracted, as reported in Fig. 4, exhibiting a different line shape.

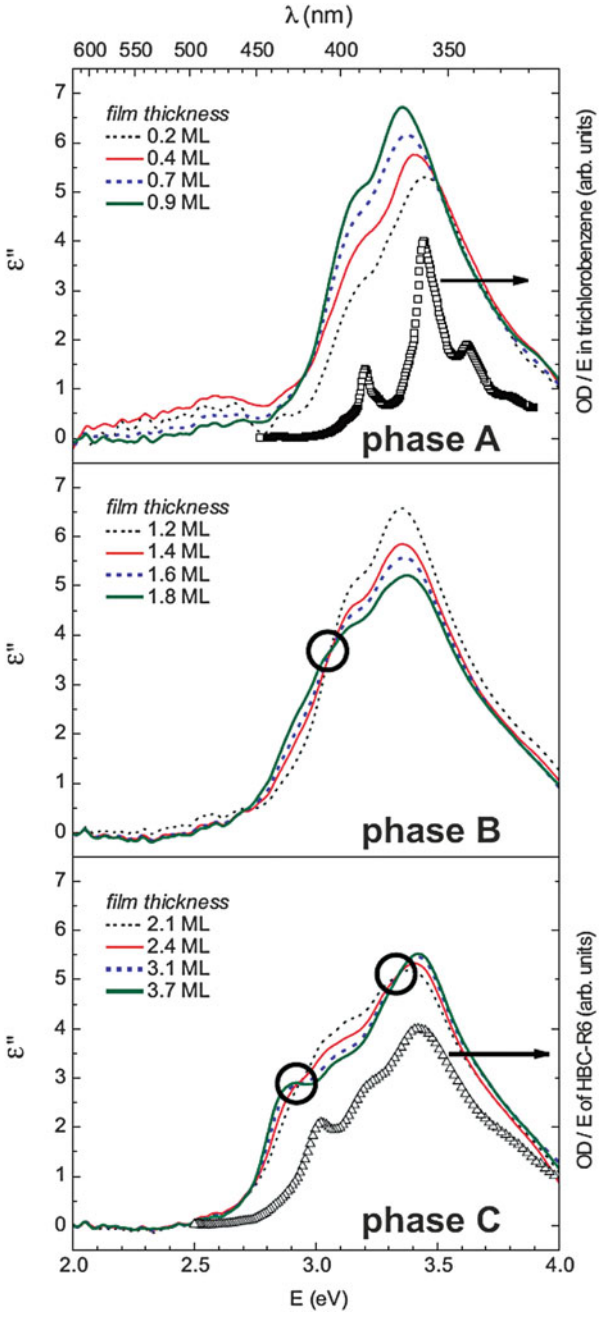

Fig. 4 Thickness-dependent ε'' spectra of HBC layers on HOPG, calculated from the SDR spectra shown in Fig. 3. The *circles* mark the visible isosbestic points (for details, see cited Forker et al. [17]). For comparison, the optical density of HBC in trichlorobenzene (*open squares* in phase A) and that of HBC-R6 aggregates (*open triangles* in phase C) are drawn on separate scales (From Forker et al. [17]. Reprinted with permission. Copyright 2006 by the American Physical Society.)

A significant restriction to the application of SDR exists when real-time monitoring of a process is essential: the SDR signal raises from a change in the sample that is necessarily induced via a process able to cause a modification of its properties, often (not always or necessarily) permanent or irreversible. This means that SDR cannot detect the state of the sample *as it is* in the moment of the experiment, but just its variation. In other words, the SDR signal is always intimately connected to both what the sample has been "before" and what it is "after" a certain modification.

Differently from SDR, reflectance anisotropy spectroscopy (RAS) [18, 19] allows to investigate the optical properties of a thin layer (as well as of a surface) by exploiting the different symmetry of the layer itself with respect to the underlying bulk. Linearly polarized light is shined at near-normal incidence onto the sample surface, detecting the reflected light while polarization is switched between two orthogonal directions α and β, usually suggested by the sample symmetry or structure. The difference of light intensity for different polarizations (i.e., the reflectance anisotropy), normalized to the average reflectance, is expressed as

$$\Delta R/R_{\mathrm{RAS}} = 2\left(R_{\alpha} - R_{\beta}\right)/\left(R_{\alpha} + R_{\beta}\right). \tag{2}$$

$\Delta R/R_{\mathrm{RAS}}$ can be directly related to the layer optical properties if the underlying bulk symmetry allows to cancel out its contribution, as it happens in centrosymmetric materials. Obviously, the meaningful application of RAS directly depends upon the anisotropy of the system to be investigated or to the existence of an unbalanced contribution of domains with well-defined and different symmetry. An isotropic layer, as well as a layer exhibiting domains equally balancing their contribution, produces a null RAS signal (Fig. 5).

The RAS signal, similarly to SDR, can be interpreted within a three-layer model, expressing $\Delta R/R_{\mathrm{RAS}}$ in terms of the dielectric properties of the bulk, of the layer itself, and of the surrounding media (usually vacuum or air, but not necessarily). Similarly to the case of SDR, if the substrate is transparent, the measured anisotropy can be directly interpreted in terms of an asymmetry descending from the layer. In Fig. 6, we report a significant example from surface physics. The (111) cleavage surface of diamond, 2×1 reconstructed, presents a very sharp anisotropy peak at about 1.5 eV [20], well inside the bulk energy gap (~5.5 eV at 300 K), thus clearly assessing its origin due to the π-bonded chain of the reconstructed surface, although the state-of-the-art theory for this surface is not able to explain yet its energy position given by experiments [21, and references therein].

If the substrate is absorbing, also for RAS, the presence of peaks cannot be directly interpreted as the sign of anisotropic optical transitions at certain photon energies, at least until the imaginary part of the anisotropic dielectric function has been computed, similarly to the case of SDR. A significant example will be presented in Sect. 3.2.

A third case must be taken into account: a substrate with intrinsic anisotropic optical properties. This situation can be met in inorganic semiconductors, for example, for vicinal surfaces, due to the directional strain caused by the surface termination, producing well-defined spectral features at bulk critical points [22, 23],

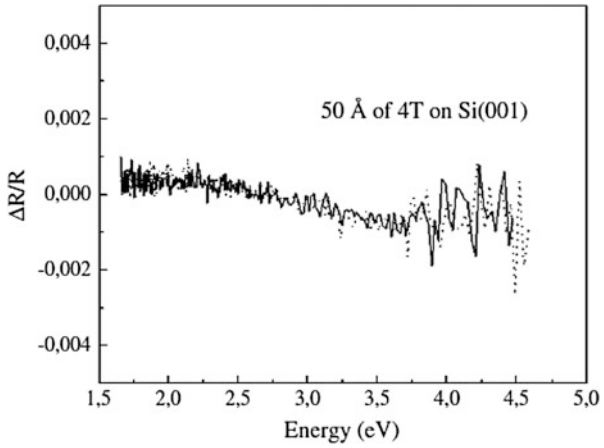

Fig. 5 RAS spectra measured on an oxidized Si(001) surface: (**a**) before (*full curve*) and (**b**) after (*dotted curve*) deposition of a 50-Å-thick layer of quaterthiophene (4T) in UHV. In this case, optical anisotropy has been measured along the [11^{-}0] and [110] directions of the Si surface (From Goletti et al. [19])

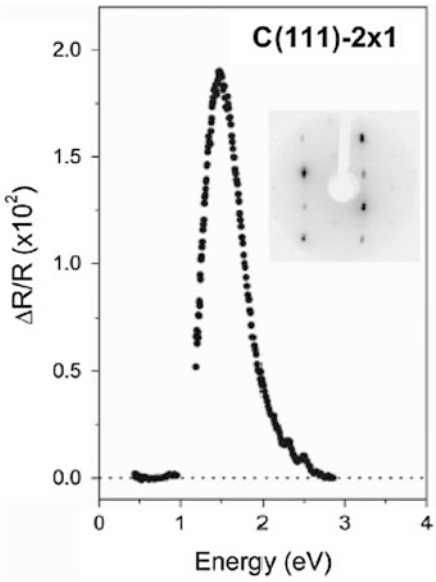

Fig. 6 $\Delta R/R_{\mathrm{RAS}}$ as a function of photon energy for a single-domain C(111)-2 × 1 surface, in the energy range 0.4–2.8 eV. Three apparatuses were used: in the IR (0.4–1.0 eV), in the intermediate range (1.1–2.2 eV), and in the visible range (2.2–2.8 eV). In the range 1.1–2.8 eV, the difference between the spectrum of the clean (2 × 1) and that of the fully oxidized surface (20,000 Langmuir of molecular oxygen) is reported. The inset shows a LEED picture taken at 70 eV. Doubling of the spots is due to the regular array of surface steps (From Bussetti et al. [20])

or in the growth of organic layers, when particular substrates are used to order the deposited layer via the strong interaction of the molecules with the surface bonds, or to align molecules along defined directions by steps present at the surface. Particularly meaningful is the example of the (010) surface of potassium acid phthalate, KAP [24]. In this case, strong artifacts appear in the spectrum that should be interpreted carefully to disentangle the substrate term from the true layer contribution [25]. Nevertheless, also in this complex case, RAS allows to follow the growth, sometimes with the help of additional experimental investigations or information, to get rid of such an intricate effect.

A significant example is reported in Fig. 7. Here, the three $\Delta R/R_{\mathrm{RAS}}$ spectra display an increasing intensity at about 380 nm due to the growing thickness of an

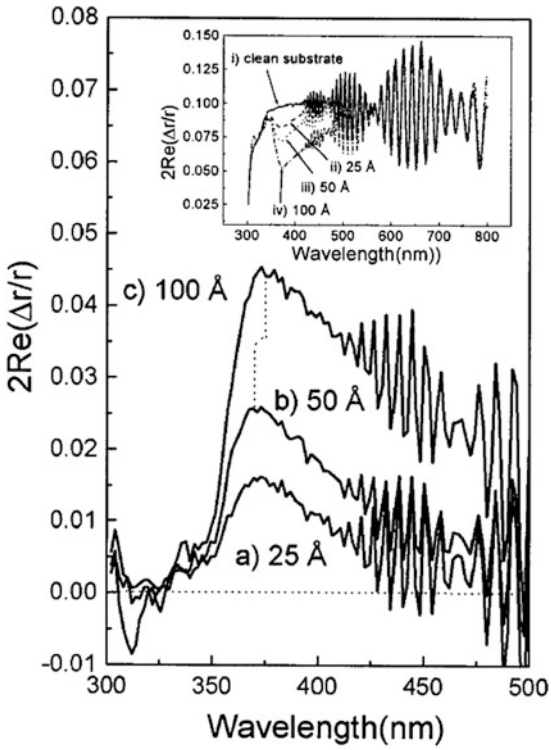

Fig. 7 Difference, with respect to the clean (010) KAP substrate, of experimental $\Delta R/R_{\mathrm{RAS}}$ spectra (here expressed as $2\mathrm{Re}(\Delta r/r)$, see next paragraph in main text) collected at different growth stages of 6 T. The difference has been necessary to highlight the contribution of the deposited organic layer. (*a*) After deposition of 25 Å of 6 T (about 1 ML); (*b*) after deposition of 50 Å of 6 T (about 2 ML); and (*c*) after deposition of 100 Å of 6 T (about 4 ML). The *dotted line* indicates the shift of the main peak from spectra **b** to **c**. *Inset*: extended RAS spectra collected at different growth stages of 6 T on (010) KAP: (i) clean KAP substrate; (ii) after deposition of 25 Å of 6 T (about 1 ML); (iii) after deposition of 50 Å of 6 T (about 2 ML); and (iv) after deposition of 100 Å of 6 T (about 4 ML) (From Goletti et al. [25]. Reproduced with permission. Copyright 2003, AIP Publishing LLC.)

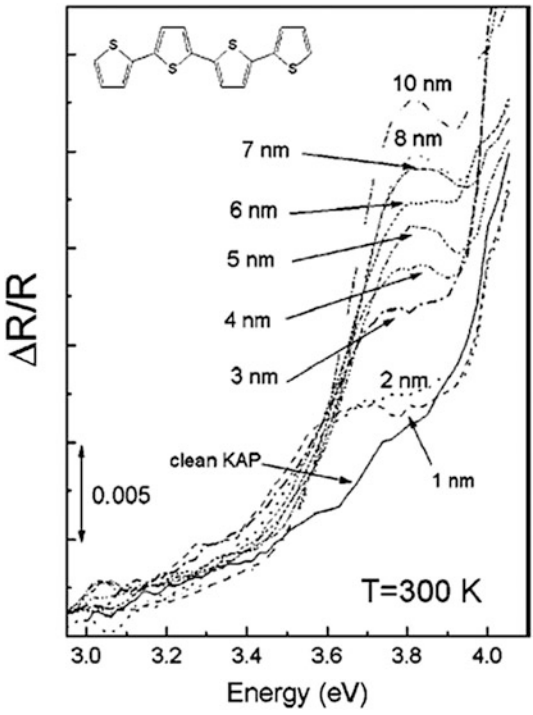

Fig. 8 RAS spectra of a 4T film grown on KAP(010) at 300 K, with thickness ranging from zero (clean KAP) up to 10 nm. Each spectrum has been collected after a single deposition step, corresponding to 1 nm nominal film thickness. At the *top*, the 4T molecular structure is sketched (From Sassella et al. [26])

ordered layer of α-sexithiophene (6 T) deposited onto KAP (which presents its main optical absorption at that wavelength). At larger wavelength, the anisotropy spectrum presents evident artifacts due to the anisotropic optical properties of KAP. Marked oscillations (due to the KAP birefringence) are superimposed onto the 6 T signal, modulated by a Fabry–Perot term due to the multiple reflections inside the sample. KAP rotates the plane of polarization of outcoming light with respect to the original polarization plane. When the beam passes through the second polarizer of the RAS apparatus (see next paragraph), a non-null signal is produced, whose intensity continuously varies with wavelength. For a more detailed discussion, the reader should read [25].

The importance of achieving a real-time monitoring of the growth is evident when the studied system can undergo a modification with time or with temperature, *after* or even *during* deposition: this is the case when the deposition is performed at low temperature (T) to get a better order of the layer and then the sample is thermalized at room T, for example, after its extraction from the deposition chamber for ex situ characterization. The spectra shown in Figs. 8 and 9 demonstrate this issue with self-explaining evidence [26].

Quaterthiophene (4T) thin films were grown by OMBE under 5×10^{-10} Torr base pressure on substrates of (010)-oriented potassium acid phthalate (KAP) at 300 K (room temperature (RT)) or at 123 K (low temperature (LT)). A quartz microbalance installed close to the substrate was used to measure the nominal film

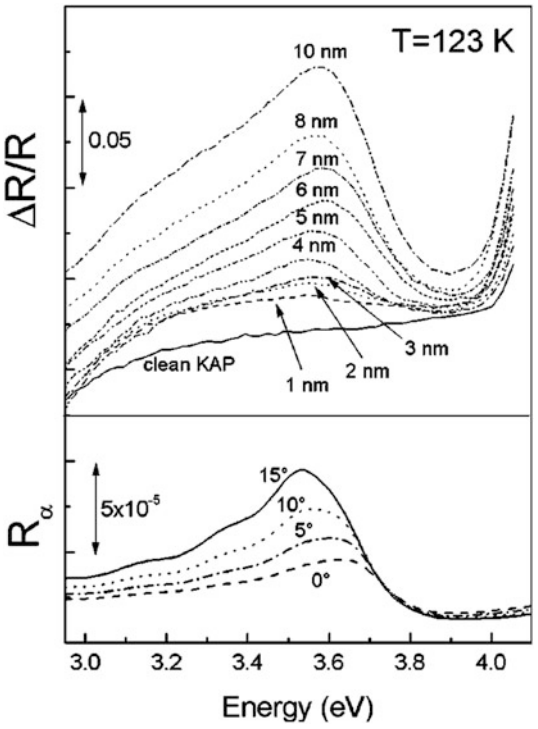

Fig. 9 *Top*: RAS spectra of a 4T film grown on KAP (010) at 123 K, with thickness ranging from zero (clean KAP) up to 10 nm. Each spectrum has been collected after a single deposition step, corresponding to 1 nm nominal film thickness. *Bottom*: Polarized reflectivity curves R_α calculated from the dielectric tensor (see Laicini et al. [27]) for different rotation angles of the crystal around the (010) direction. For more details, see the original article (From Sassella et al. [26])

thickness. The KAP substrate induces a preferential orientation of the 4T polycrystalline film and the complete in-plane anisotropy of its macroscopic optical response. The comparison of RAS spectra from layers deposited at different T gives evidence of a change from an island growth mode at RT (Fig. 8) to a layer-by-layer pseudomorphic growth for the LT experiments (Fig. 9), interpreted in terms of the formation of a coherent interface between substrate and film, attained by a tilt of the molecules [26]. In addition, a partial desorption of 4T molecules at the film surface is clearly observed (stronger at higher T, but not negligible even at 123 K) [26]. These results have permitted a quantitative evaluation of the interactions of the 4T molecules either with the bare KAP or with the film surface of a fully developed 4T layer.

When $\Delta R/R_{\mathrm{RAS}}$ data are measured at organic layers, differently from the inorganic case, a clear interpretation of RAS results is complicated by the presence of supplementary problems besides the simple disentanglement of the layer optical functions. Organic molecules are often extended objects, with internal degrees of freedom that can assume a significant role in defining the structure and the electronic state of the system. They can adopt various positions on the substrate (planar, tilted, aggregated in dimers, etc.), so that different phases are sometimes – even contemporarily – present at the surface. In addition, the perishability of organic molecules at high T normally does not allow to use annealing procedures for

desorbing molecules in excess and to level the layer thickness. Also the availability of realistic and reliable data from theory is not common. Finally, we should consider that the three-layer model validity is sometimes questionable, as the thickness of the layer and the strong absorption of some molecules (e.g., porphyrins) makes dubious the applicability of that approach. In conclusion, with respect to the case of inorganic materials, for organics, often RAS is not used to get a deeper knowledge of the layer electronic structure by a detailed interpretation of spectra, but rather to connect a particular, significant spectroscopic feature, even a whole spectrum, to some defined phase occurring at the layer in well-defined conditions, thus becoming a signature of the existing state, that will be monitored to characterize the evolution of the system with time, temperature, thickness, etc.

SDR and RAS spectroscopies are more similar than it can appear at first glance: they have common origins and extremely similar apparatuses, and more meaningfully, they have often passed through similar applications and development. RAS had a twofold derivation: on one side, it can be considered an evolution from ellipsometry, where the working condition for light at normal incidence reduces the otherwise formidably complex problem to be analyzed, to a heuristic and simpler finding, that is, the existence of anisotropy [28]. On the other, it can be interpreted as a particular case of SDR with polarized light, intentionally developed for the investigation of III–V compound surfaces in UHV [29]. The former case prototype was developed by D. Aspnes at Bell Labs (USA), the latter in St. Petersburg's Ioffe Institute (USSR) by the group of V. (Slava) Safarov, in the same period and independently, with some minor (although significant) technical

Table 1 Applicability of SDR and RAS in different experimental conditions ("x" means the spectroscopy can be profitably used)

	Substrate		Layer	
	Isotropic	Anisotropic	Isotropic	Anisotropic
SDR	x	x	x	x
RAS	x	x[a]		x

[a]To be used carefully (see examples in main text)

differences in the experimental apparatuses [30].

In consequence of their resemblance, RAS and SDR data are similarly interpreted within the same three-layer model and suffer common restrictions to its applicability. However, sufficient differences exist to justify in some circumstances a different application of these two techniques, as reported in Table 1. RAS – being not dependent upon the comparison with a reference sample – is more appropriate for investigating real-time processes. Then, its modulation at very high frequency (usually more than 50 kHz that is the frequency of the light polarization change between two orthogonal states) gives an unmatched time stability and signal-to-noise ratio (down to 10^{-6} in recent apparatuses, commonly better than 1×10^{-4}). However, the necessary existence of a non-null resulting layer anisotropy is sometimes a limit that cannot be overcome, for the intrinsic isotropy of the

electronic properties or for the presence of different domains balancing their contribution to zero on the average within the light spot size.

As a matter of fact, both spectroscopies have been applied to organics [16–19, 25, 26, 31, 32]. In the case of porphyrin layers, the use of RAS is largely justified by the existence of an intense optical signal of the molecule as well as of the layer (but the discussion will enter into details in a further section) and by the difficulty (sometimes the impossibility) to modify significantly and profitably the system by some external way (a necessary condition for SDR), as in Langmuir–Blodgett layers.

3 Reflectance Anisotropy Spectroscopy (RAS): A Closer View

3.1 Experimental Apparatus

A RAS equipment can be essentially described as an ellipsometer working at near-normal incidence. This experimental condition greatly simplifies the interpretation of acquired data. Although a (sometimes) complex deconvolution from rough data is still necessary to understand correctly the obtained results by some modeling of the system, the existence of a non-null optical anisotropy often represents a meaningful result *per se*, expressing a significant aspect of the layer.

In Fig. 10, the scheme of a typical RAS system is drawn. Light from a source (Xenon or tungsten lamp, emitting photons in the near UV-visible-near-IR range, 300–1,000 nm[1]) is shined and focused into a polarizer (e.g., Glan Taylor), then on the sample (properly oriented), eventually passing through a special low-birefringence window, if the sample is in UHV or in liquid, and finally on a photoelastic modulator (PEM) [33]. The PEM – properly driven by an oscillating circuit at the resonance frequency ω_0 of the piezoelastic crystal – modulates the linear polarization of light between two orthogonal, independent states α and β [18, 19, 31]. The light intensity reflected by the sample for two polarizations (R_α and R_β) is then collected and focused onto a second Glan Taylor polarizer (analyzer) and finally into a monochromator. At the exit slit, there is a detector (photomultiplier, photodiode, etc., chained to a preamplifier (if necessary) and then to a lock-in to filter the signal, tuned at the correct frequency [18, 19, 31].

The linear polarization states α and β usually are aligned with particular symmetry directions of the sample surface, in its turn suggested by the crystal or substrate structure. When an organic film is deposited onto a solid substrate, the orientation of α and β must be chosen, but sometimes such directions are not known "a priori," as for the deposition onto a polycrystalline metal or onto fused quartz. In

[1] To extend the investigated photon energy range, a different choice of the light source is sometimes necessary: in UV, for example, a deuterium lamp, or a photoemission beamline to couple with the RAS apparatus.

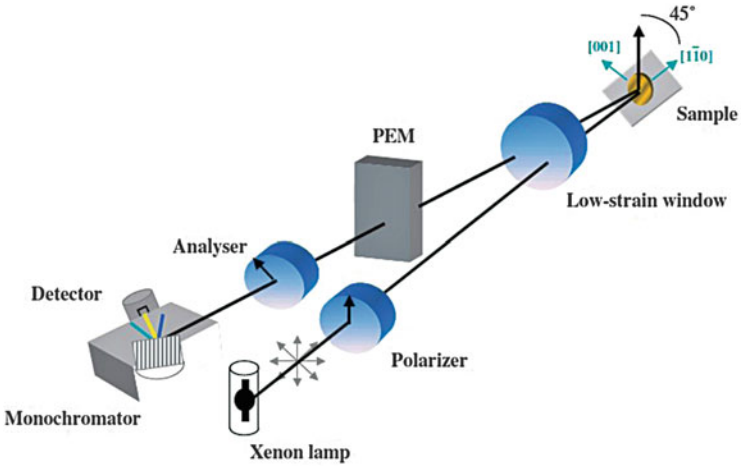

Fig. 10 Scheme of a RAS apparatus. Light emitted from a xenon lamp passes through the polarizer and low-strain window (not always present, but if the sample is in UHV or in liquid) and then is reflected at the sample surface. Reflected light passes again through the low-strain window, PEM, and analyzer and then enters the monochromator and finally the detector. Please note the orientation of the polarizer and analyzer axes, as well as of the sample. The reported apparatus is not the only possible version for the so-called Aspnes version of a RAS spectrometer. In alternative, a different apparatus with just one polarizer (which is without analyzer) can be also used. For details, see text and cited references (From Weightman et al. [18])

this case, an azimuthal investigation of the optical anisotropy dependence must be performed: the sample is rotated continuously around the normal to the surface by the angle θ, detecting the corresponding variation of the RAS spectra. It is possible to demonstrate that the expected dependence of $\Delta R/R_{\mathrm{RAS}}$ upon θ is simple and is expressed as

$$\Delta R/R_{\mathrm{RAS}}(\theta) = \Delta R/R_{\mathrm{max}} \cos(2\theta), \tag{3}$$

where $\Delta R/R_{\mathrm{max}}$ represents the maximum signal value, measured when the symmetry axes on the sample surface are coincident with the α and β directions of the RAS modulation. Even when the substrate crystal structure is lacking (being polycrystalline or amorphous), it is meaningful and possible to identify a preferential ordering of the layer: for Langmuir–Blodgett layers, in the direction along which the barriers in the trough are moved to compress the molecules on the liquid surface [34, 35], and in graphite, along the steps produced by exfoliation before deposition [36].

It is obvious that for a sample exhibiting anisotropy when light is modulated between α and β, the signal intensity time dependence after the detector should be as the one reported in Fig. 11, with a frequency modulation equal to $2\omega_0$ that is twice the resonance frequency ω_0 of the PEM. This modulation can be easily understood, as the detector – being sensitive to the intensity of light – monitors the square of the light electric field, in its turn modulated at ω_0 by PEM. This fact

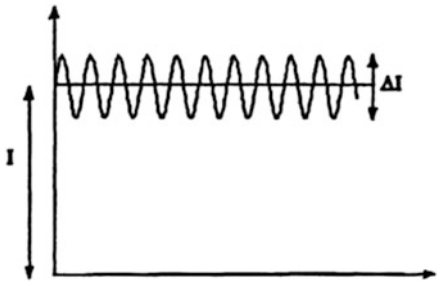

Fig. 11 Time dependence of the light intensity reflected by a sample with anisotropic reflectance R_α and R_β depending upon the light polarization states α and β (on the horizontal axis the time t is reported). In this case, $R_\alpha > R_\beta$ ($\Delta I = R_\alpha - R_\beta$). The polarization of light is switched by the PEM at the frequency ω_0 between polarization α and β. The resulting frequency for ΔI is $2\omega_0$ (see text)

explains also that $\Delta R/R$ signal must be analyzed by a lock-in amplifier tuned at the second harmonic of the modulated signal to extract the physically meaningful $\Delta I/I$ component (Fig. 11). A more detailed and rigorous mathematical derivation of the same result is possible [18, 30]. In this case, the light polarization vector is represented by a 2-component vector, modified by the progressive application of 2×2 matrices (Jones matrices) representing the different optical elements along the optical path [7]. The final electric field (entering the detector) is obtained by successive application of all the 2×2 matrices associated to the optical elements, in the order with which they appear along the light path. The square of the final electric field represents the final intensity, with the resulting time dependence.

A significant product of the calculation shows that if the RAS signal is expressed as $\Delta r/r$, where r is the complex Fresnel coefficient for reflection ($r^2 = \mathrm{R}$), in the expression for $\Delta r/r$, two terms appear, modulated at different frequencies: it is a complex quantity, whose real part $\mathrm{Re}(\Delta r/r)$, modulated at $2\omega_0$, coincides with $\Delta R/R_{\mathrm{RAS}}$ (apart from a factor of 2: $\Delta R/R_{\mathrm{RAS}} = 2\ \mathrm{Re}(\Delta r/r)$) and specifies the light intensity modulation, while the imaginary part $\mathrm{Im}(\Delta r/r)$ is modulated at ω_0, related to the phase term. Both terms can be measured by opportunely tuning the lock-in at the correct modulation frequency.

Another important outcome of the complete calculation is that the possible error sources due to the optical misalignment of the elements (polarizers, sample, PEM, etc.) enter as a first-order correction in the ω_0 contribution, but only as a second order term in the intensity modulation at $2\omega_0$. Then, the real part of the complex RAS signal, that is, $\Delta R/R_{\mathrm{RAS}}$, is less sensitive to the eventual lack of accuracy in setting the apparatus than the imaginary part (as can be easily checked in experiments) [18, 30].

This conclusion has an important practical significance. We have already reported that RAS was independently developed in the same years in the Bell Labs (by D. Aspnes) and at the Ioffe Institute (by S. Safarov). We also outlined how this has meant that two different experimental apparatuses have been projected and built: the main dissimilarity is represented by the use of just one polarizer in the

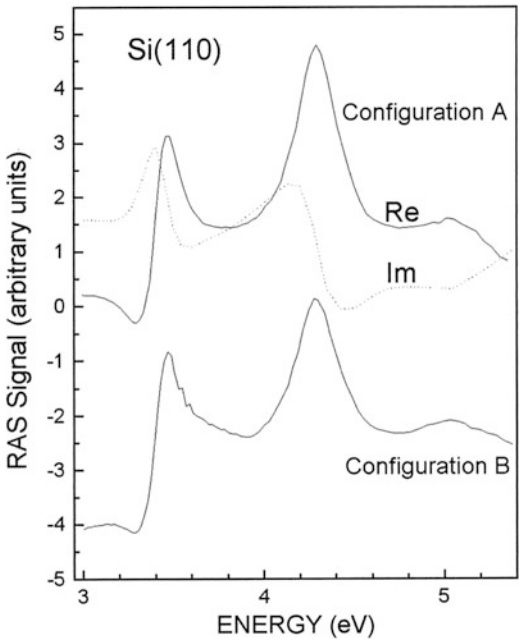

Fig. 12 RAS spectra of a test sample [oxidized Si (110) surface] recorded with the experimental setup including the analyzer (configuration A) and with the same setup without the analyzer (configuration B). In the first case, both the real and the imaginary parts of $\Delta r/r$ have been measured. The real part of $\Delta r/r$ of configuration A is essentially the same as the spectrum recorded with configuration B, apart from a shift along the vertical axis, due to an experimental offset. (From Salvati and Chiaradia [30])

Russian version (no analyzer), instead of two as in the Aspnes prototype. It is possible to obtain by calculations (and by accurate optics considerations) that in both cases, the resulting intensity modulation is the same, although the signal at ω_0 (the first harmonic of the signal that is the imaginary term) cannot be measured but in the Aspnes version. The practical identity of the results of two apparatuses, when $\Delta I/I$ is concerned (see Fig. 11), is fully confirmed by the experiment (Fig. 12).

At higher detail, we can infer that in the Russian version of a RAS apparatus, the sample anisotropy is monitored correctly, but using twice the level of light of the Aspnes system (one polarizer (1P) in the former, two polarizers (2P) in the latter), that means a better signal-to-noise ratio. The Aspnes version is instead necessary when also the imaginary part of $\Delta r/r$ is needed, to evaluate the physical consistency of spectra and the presence of significant contributions from optical misalignments: by a careful Kramers–Kronig deconvolution, the layer optical functions are obtained from the real part $\mathrm{Re}(\Delta r/r)$ and then used to compute independently the imaginary part of the signal $\mathrm{Im}(\Delta r/r)$ (whose expression is known within the three-layer model [37]), to be compared finally with the experimental result [18]. The level of similarity of the two spectra (computed and experimental), differently obtained, is a check of the presence of artifacts or fakes in the signal. The 2P version is also crucial if the detector optical window (e.g., the glass window of a photomultiplier or the CaF_2 window of some infrared detectors) presents birefringence, whose effect could simulate an intensity modulation (sometimes not negligible) of the anisotropic signal [38].

A valuable characteristic of the SDR apparatus is the possibility to use a multichannel detector (a diode array or a charge coupling device (CCD)), allowing a real-time monitoring of the signal evolution in a large photon energy range within the time window of the acquisition system (down to a few milliseconds) [39]. A similar implementation for RAS – originally developed for a single-channel detector – presents some difficulties. The correct PEM modulation – producing the necessary polarization plane rotation by 90° from α to β – depends upon the light wavelength and the voltage amplitude applied to the vibrating crystal [18, 30]. The true voltages at each value of λ are defined by a careful calibration [18] and can be sent sequentially along the spectrum to the PEM by a programmable voltage power supply driven by a computer. If the whole spectrum is acquired at one shot, as it happens with a multichannel detector, this situation cannot be achieved: nevertheless, it is still possible to correct the signal amplitude according to the PEM calibration, producing a known curve by software correction. The problem coming from the signal detection process is more subtle. Differently from SDR, in RAS, we need a phase-sensitive detector (a lock-in): this limits the number of single-channel detectors working in parallel to acquire a RAS spectrum. Until now, the best performance achieved has been by 16 independent acquisition lines or channels [39], however far from the 1,024 diodes of the Fritz SDR setup [16]. Each channel is sampled 16 times over a single period of the PEM, oscillating at about 50 kHz. Harmonic analysis of the signal in each channel is executed numerically by fast Fourier transform (FFT). In this way, the authors have reached a temporal resolution of a few milliseconds [39].

The usual photon energy range of a RAS apparatus covers the near UV-visible-near IR. The reason for that is related to the main scientific issues tackled since the early development of the research in the field: the III–V semiconductors' growth in MBE and MOCVD (metal organic vapor deposition) systems [40] and the surface state investigation for semiconductors [4, 29]. In addition, the above reported limits cover nicely the interval where photomultipliers have commonly their spectral response.

However, these limits in the photon energy range can be exceeded on both sides. In the UV, a RAS apparatus can be interfaced to a different light source: deuterium lamp [41], or a suitable beam line in synchrotron facilities, to exploit the photon extension possible in vacuum [42, 43]. In the near IR, on the contrary, some modifications have been necessary to broaden the range to 4 μm [38]. A differently engineered PEM (HINDS, commercially available) and an InSb detector have allowed to measure the transitions between surface states of the clean Si(111) 2×1 surface at 0.45 eV [38]. The infrared RAS (IRRAS) could offer very interesting opportunities for organics that often display important electronic properties in that range.

3.2 Interpretation of the Data

The main information coming from RAS, that is, the existence of anisotropy in the sample optical properties, is appreciable even at a ground-level examination of the data, as we already commented. Nevertheless, to understand in detail the meaning of experimental results, a deeper analysis is necessary. This requires to model the investigated system and its optical response in terms of the constituents and to compare the data with trustworthy theoretical results. The latter fact depends upon the development of new theories and simulations: recently, for semiconductors and metal surfaces, the theory has reached an incredibly high level, and the comparison of computed curves with experiments can be pushed to interpret sometimes even the tiniest details of spectra [44, 45]. This is not true at the moment for organics, where the stronger computational effort needed to calculate the optical properties of molecular aggregates in a layer does not allow a similar accuracy and reliability of results. The situation is however rapidly evolving: higher calculus power and better theoretical frames are improving results continuously [46].

The cited three-layer model is the more substantiated framework to mold the RAS response [37]. The surface (or layer) – under the assumption that its thickness d is by far lower than the used wavelength ($d \ll \lambda$) – is put onto a semi-infinite substrate, having known optical properties, and is surrounded by an external, transparent medium (usually air or vacuum, but the case can be extended also to liquid, e.g., water). The optical properties of the three media are expressed by the respective dielectric functions $\varepsilon_s = \varepsilon'_s - i\varepsilon''_s$ ($s = 1$ external medium, $s = 2$ surface or layer, $s = 3$ substrate), ε'_s being the real part and ε''_s the imaginary part. The response of the substrate (commonly assumed to be isotropic) could depend upon the polarization of light (as for the organic crystal KAP reported above, see Sassella et al. [24] and Goletti et al. [25]). To take this into account, the dielectric function of the layer will explicitly depend upon the polarization state. However, a similar polarization dependence cannot be extended to the substrate without complicating the formulas in an unmanageable way.

As a first approximation, we will then treat isotropic substrates. The final result for the computed $\Delta R/R$ is extremely simple:

$$\Delta R/R_{\mathrm{RAS}} = 8\pi d/\lambda \left[\mathrm{A}\, \Delta\varepsilon''_2 - \mathrm{B}\, \Delta\varepsilon'_2 \right] \tag{4}$$

$$\Delta R/R_{\mathrm{SDR}} = 8\pi d/\lambda \left[\mathrm{A} \left(\varepsilon''_{\mathrm{a}} - \varepsilon''_{\mathrm{b}} \right) - \mathrm{B} \left(\varepsilon'_{\mathrm{a}} - \varepsilon'_{\mathrm{b}} \right) \right] \tag{5}$$

where (i) in formula 4, $\Delta\varepsilon_2''$ and $\Delta\varepsilon_2'$ are, respectively, the real and the imaginary parts of the anisotropy of the dielectric function of the surface layer, and (ii) in formula 5, $\varepsilon_{\mathrm{a}}'$ ($\varepsilon_{\mathrm{b}}'$) and $\varepsilon_{\mathrm{a}}''$ ($\varepsilon_{\mathrm{b}}''$) are, respectively, the real and the imaginary parts of the dielectric function of the sample in the state "a" ("b"). A and B summarize the substrate properties in terms of the substrate dielectric functions.

The expression of A and B is as follows:

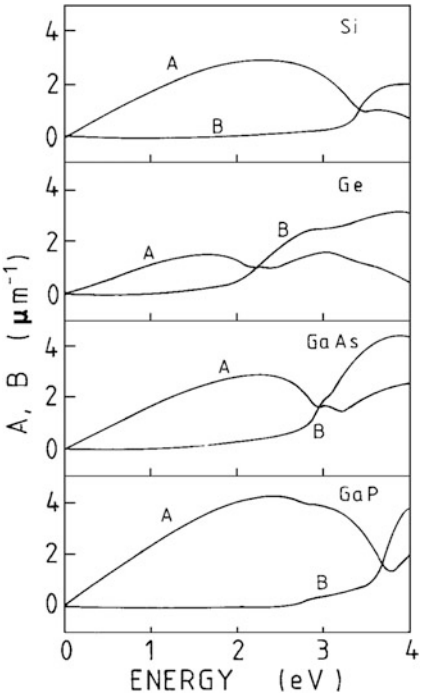

Fig. 13 Energy dependence of the quantities A and B entering Eqs. (5) and (6) reported in text, for some semiconductors: silicon, germanium, gallium arsenide, and gallium phosphide. The bulk optical functions have been taken from Palik [47]. Note that here A and B are reported in μm^{-1}, according to the definition for these coefficients used in Selci et al. [13], slightly different from formulas (7) for the multiplicative factor "*d*." This fact changes only the vertical scale: the overall line shape expressing the dependence upon photon energy is the same (From Selci et al. [13]. Reproduced with permission. Copyright 1987, American Vacuum Society.)

$$A = \frac{\varepsilon_s' - 1}{\left(1 - \varepsilon_s'\right)^2 + \left(\varepsilon_s''^2\right)} \quad \text{and} \quad B = \frac{\varepsilon_s''}{\left(1 - \varepsilon_s'\right)^2 + \varepsilon_s''^2}, \tag{6}$$

where ε_s' and ε_s'' are, respectively, the real and the imaginary parts of the dielectric function of the substrate. The values of A and B can be computed by using data reported in the literature [47]. Some examples are reported in Fig. 13.

From formula 4, two remarkable cases are considered and discussed:

a) In the photon energy range where the substrate is transparent ($B = 0$) or weakly absorbing ($A \gg B$), the RAS signal is given mainly (or only) by the anisotropy of the layer absorption. The anisotropy of the dielectric function imaginary part $\Delta\varepsilon_2''$ should be then computed by formula 4 (with $B = 0$) to value correctly the peak position and the line shape details, but the interpretation of the results is straightforward. An example is reported in Fig. 14, for the cleavage diamond surface C(111)2 × 1. The B coefficient (not reported here, computed from Palik [47]) is zero below 6.5 eV [21]. The reader can evaluate how the line shape of $\Delta R/R_{RAS}$ is preserved when $\Delta\varepsilon_2''$ is extracted.
b) If the substrate absorption is not negligible, the real and the imaginary parts of the layer anisotropic dielectric function are entangled, and a careful deconvolution via Kramers–Kronig analysis is necessary. An alternative

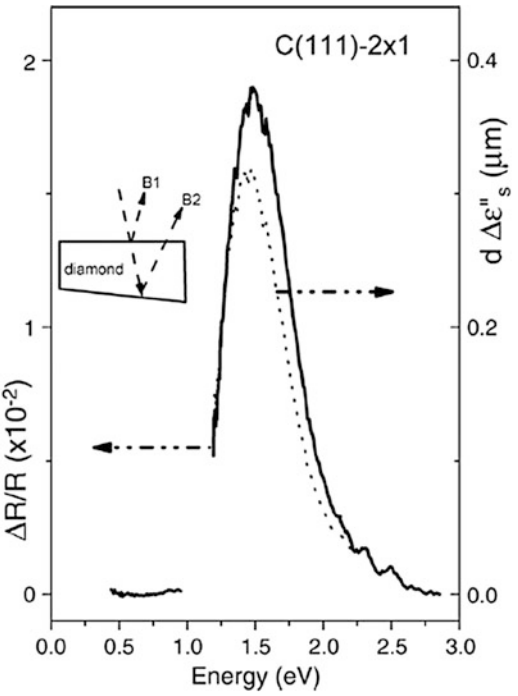

Fig. 14 (**a**) (*Left* axis, *full line*) experimental $\Delta R/R_{RAS}$ as a function of photon energy for a single-domain C(111)-2 × 1 surface, in the energy range from 0.4 to 2.8 eV, obtained subtracting the curve of the oxidized surface from the curve of the clean surface; (**b**) (*right* axis, *dotted line*) imaginary part of the dielectric function anisotropy for the clean C(111)-2 × 1 surface, computed from experimental RAS spectrum by Eq. (4) (see text) and multiplied by d, the ill-defined thickness of the surface layer (From Bussetti et al. [21])

elaboration of data is possible when both the real and the imaginary parts of $\Delta r/r$ are recorded: in this case, a simple mathematical treatment of 2 simultaneous linear equations is necessary to extract the anisotropy of both the real and the imaginary terms of the layer dielectric function [48]. The effect of bulk absorption could be significant. In Figs. 15 and 16, we report an example from the surface InAs(001), where the bulk absorption is not negligible in the whole photon energy range investigated in the cited experiment. Consequently, the deconvoluted dielectric function anisotropy appears well different in line shape from the experimental RAS spectra [49].

As we already commented, we have not considered the possibility to extract meaningful data from RAS spectra for the layer dielectric function anisotropy when the bulk (or more generally the substrate) is anisotropic. This is evident if one attempts to develop a three-layer-model approach describing this situation: formulas became quickly unmanageable and, at the end, of questionable utility. The same issue is instead easy to handle by using SDR with polarized light. Actually, in this case, two separate SDR experiments will allow to extract and to interpret the sample response in terms of the existing optical anisotropy: dealing separately with two different experiments and resulting sets of data, one for each well-defined polarization state of light, the application of the three-layer model to the substrate is

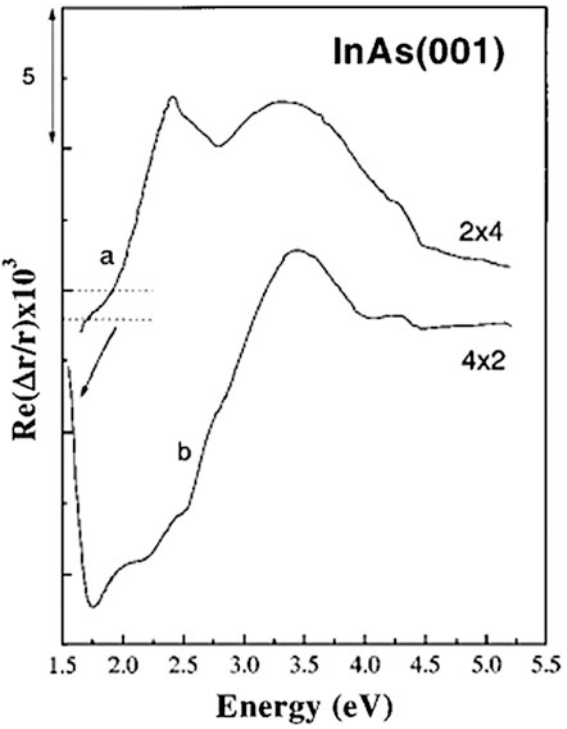

Fig. 15 Re($\Delta r/r$) versus photon energy for clean InAs(001) surfaces obtained after annealing at different temperatures: (*a*) $T = 340°C$ (LEED pattern: 2×4); (*b*) $T = 450°C$ (LEED pattern: 4×2). Each curve is referred to its own zero line (From Goletti et al. [49])

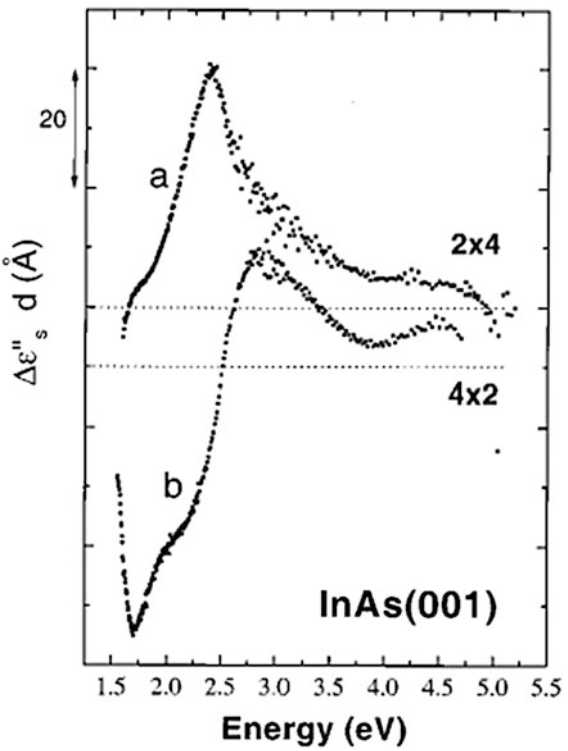

Fig. 16 $\Delta\varepsilon_2'' d$ versus photon energy for clean InAs(001) surfaces. $\Delta\varepsilon_2''$ (here indicated as $\Delta\varepsilon_s''$) is the anisotropy of the imaginary part of the surface dielectric function between directions [11^{-}0] and [110] of the clean surface and has been computed from experimental curves reported in Fig. 15. *d* is the thickness of the surface layer. Each curve has its own zero line (From Goletti et al. [49])

obviously possible independently for each polarization, if data are available for the anisotropic optical functions of the bulk.

4 RAS and Porphyrins

4.1 Langmuir–Blodgett and Langmuir–Schaefer Layers

The very first application of RAS to investigate thin layers of porphyrin-like molecules dates back to the year 2000 [32]. Two years before, it was demonstrated how RAS is capable to monitor the evolution with coverage of an organic film deposited by sublimation in UHV [50], thus exporting the application of this optical spectroscopy from traditional inorganic samples to organics.

The adsorption of 9-anthracene carboxylic acid onto the oxygen-terminated copper surface p(2 × 1)O/Cu(110) was investigated by STM (Scanning Tunneling Microscope) and LEED (Low Energy Electron Diffraction) to characterize the film structure and then by RAS to detect the film evolution while dosing organic molecules onto the surface. LEED pattern and STM images demonstrated the existence of order after adsorption, a necessary condition for a meaningful application of RAS (Fig. 17). RAS spectra (here reported as the real part of $\Delta r/r$) show an evident structure whose amplitude depends upon the dosing time and exhibits a well-defined azimuthal orientation in the surface plane that is along the [001] direction of the Cu surface (Fig. 18). This RAS peak (at about 4.3 eV) is consistent with the optical absorption structure characteristic of the molecule in solution, and the sign of the anisotropy fits with the orientation of linear molecules in the adsorbed layer as imaged by STM (Fig. 18). This experiment demonstrated for the first time that RAS could be applied successfully to determine the orientation of molecules on a solid substrate and to monitor the deposition with a sensitivity down to submonolayer quantities (although a really precise measurement of the deposited thickness was not reported in that paper).

This pioneering investigation was followed two years later by RAS experiments performed by the Rome group, to probe layers of sapphyrin molecules deposited onto a gold substrate [32]. Differently from Frederick et al. [50], the film was deposited under atmospheric pressure, by the Langmuir–Blodgett (LB) method [34, 35]. The exposure to air (which cannot be avoided when the LB method is used) does not modify significantly the optical properties of the organic layer: no surface states are expected, as well as a weak sensitivity to air contamination. The control of the deposited thickness (which is usually possible in UHV by different techniques) was achieved here by a careful preparation of the sample. Chromium and gold films (total thickness: about 200 nm) were successively evaporated onto a clean glass substrate (chromium was used to improve the adhesion of the Au film). Two monolayers at a time were expected to be deposited by dipping the substrate into the solution of the LB trough. At the beginning, the whole sample was then

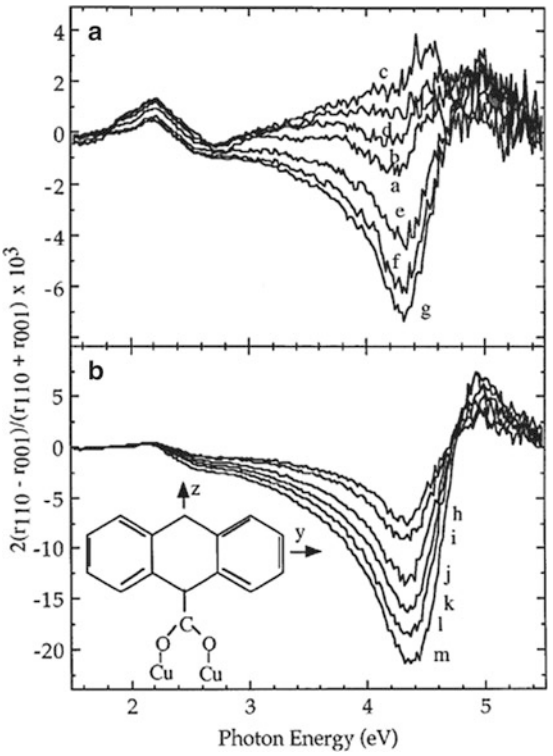

Fig. 17 (**a**) Real part of the RAS signal Re($\Delta r/r$) while dosing the organic molecule 9-AA on the oxygen-terminated copper surface p (2×1)O/Cu(110) to produce the carboxylate species shown in the *inset*. Dosing times: (*a*) 0 min, (*b*) 4 min, (*c*) 8 min, (*d*) 12 min, (*e*) 16 min, (*f*) 27 min, and (*g*) 51 min. (**b**) Spectra acquired after annealing to (*h*) 295 K, *i*) 348 K, (*j*) 365 K, (*k*) 373 K, (*l*) 405 K, and (*m*) 430 K (From Frederick et al. [50]. Reprinted with permission. Copyright 1998 by the American Physical Society.)

nominally covered by 2 ML (LB deposition type Y; see Roberts and Ulman [34, 35]) but a small area was left uncovered. The top boundary of the deposition area was then gradually shifted down by 3 mm, and the sample dipped again: two nominal monolayers were then deposited. This procedure was repeated 12 times: consequently, the film thickness was gradually changed from 2 to 26 nominal monolayers, each deposition step being 3 mm large. (A pictorial view of this "staircase" sample is reported as an inset in Fig. 24.) In this way, a gradual variation of the nominal thickness was reached, in some way mimicking the possibility in UHV to evaporate gradually an increasing quantity of material.

The efficiency in transferring the layer from the liquid to the substrate during the immersion in the trough was carefully calibrated by scanning tunneling microscopy and Kelvin probe [51]. The results showed that the nominal thickness and the "true" thickness do not coincide exactly: a critical nominal thickness of 10 ML (i.e., 5 immersions) is necessary to cover completely the metal substrate. From a profile analysis by STM across the rows of sapphyrin molecules, the angle between the molecular plane and the substrate has been measured. This angle amounts to about 70° [51]. The sample has been always kept at room temperature, in air. The linearly polarized electric field of the light focused onto the layer has been modulated between two directions **a** and **b** forming angles equal to +45° and −45° with respect

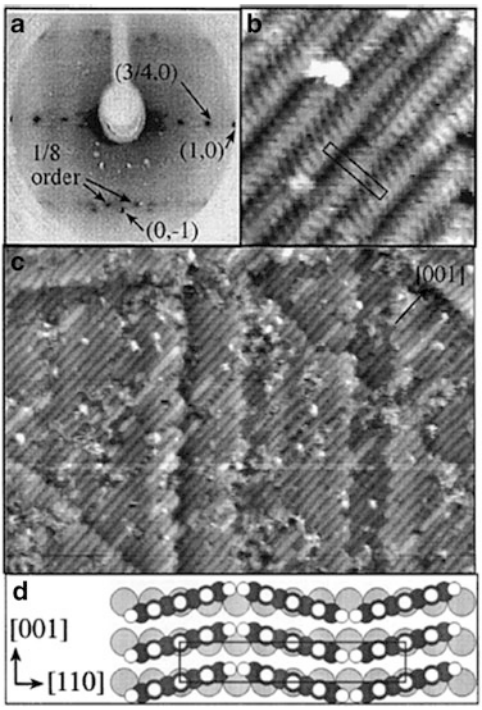

Fig. 18 (**a**) LEED pattern of the ordered layer adsorbed at 350 K onto the oxygen-terminated Cu surface; (**b**) STM image 60 Å × 60 Å (Vbias = −0.35 V, current 0.47 nA); (**c**) STM image 350 Å × 510 Å. (**d**) Model of an ideal p(8 × 1)g structure (unit cell shown) with the anthracene rings rotated by 15± from [110] to avoid steric repulsion (From Weightman et al. [18]. Reprinted with permission. Copyright 1998 by the American Physical Society.)

to the dipping direction. In Fig. 19, the RAS signal measured for nominal coverages from 0 to 10 monolayers is reported.

Spectrum a (lower panel of Fig. 19) refers to the uncovered, oxidized gold substrate evaporated onto glass. This spectrum, with the exception of minor, negligible features, is essentially structureless, as one would expect for a polycrystalline layer. However, the microscopic roughness of the Au layer (clearly visible in STM images [51]) is likely responsible for the two weak features at 495 and at 550 nm, visible at a closer inspection.

When sapphyrin molecules are deposited onto gold, at coverage lower than 8–10 nominal monolayers, RAS detects a minor, broad signal variation in most of the investigated range. It is known from STM that at 8–10 nominal monolayers, the gold substrate is fully covered by the sapphyrin molecules, thus yielding a true monolayer [51]. In the upper panel of Fig. 19, the RAS spectra for coverage between 12 and 20 nominal monolayers are reported: here it is shown that when additional sapphyrin layers grow onto the first complete layer, a new peak develops (initially at about 500 nm) whose amplitude increases with coverage until it becomes the dominating structure of the whole spectrum.

To identify the origin of spectral features detected by RAS, as at that time the optical anisotropy of a sapphyrin layer had not been studied yet, a rather crude approximation was used, modeling its optical behavior by Lorentz oscillators,

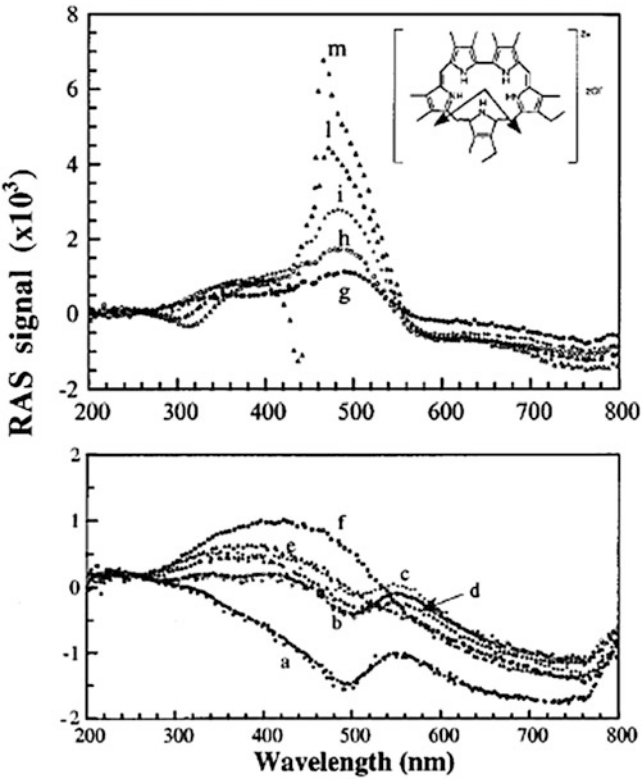

Fig. 19 *Bottom*: RAS spectra measured at LB layers of sapphyrin whose thicknesses nominally are in the range 0–10 monolayers: (*a*) polycrystalline gold (*filled dots*); (*b*) 2 ML (*empty dots*); (*c*) 4 ML (*crosses*); (*d*) 6 ML (*filled triangles*); (*e*) 8 ML (*empty triangles*); and (*f*) 10 ML (*filled squares*). *Top*: RAS spectra measured at LB layers of sapphyrin whose thicknesses nominally are in the range 12–20 monolayers: (*g*) 12 ML (*filled dots*); (*h*) 14 ML (*empty dots*); *i*) 16 ML (*crosses*); (*l*) 18 ML (*filled triangles*); and (*m*) 20 ML (*empty triangles*). The absolute sign of the RAS spectra is arbitrary. In the *inset*: structure of E_2M_8-sapphyrin. The two perpendicular optical dipoles in the plane of the molecule are indicated by *arrows* (From Di Natale et al. [32]. Reproduced with permission. Copyright 2000, AIP Publishing LLC.)

whose parameters were determined on the base of a semiempirical quantum chemistry approach, its structure being defined by using ab initio geometrical optimization [32]. The following results were obtained from calculations: (i) the optical anisotropy is not directly related to the sapphyrin ring itself, but it is mainly due to the peripheral substituents; (ii) the main anisotropy structure measured below 500 nm is associated to the in-plane optical anisotropy of the sapphyrin molecule. RAS results thus provide a clear evidence of the ordering of the sapphyrin molecules in the LB films studied. On the other hand, for coverages below one monolayer, the possibility of RAS to give significant information about

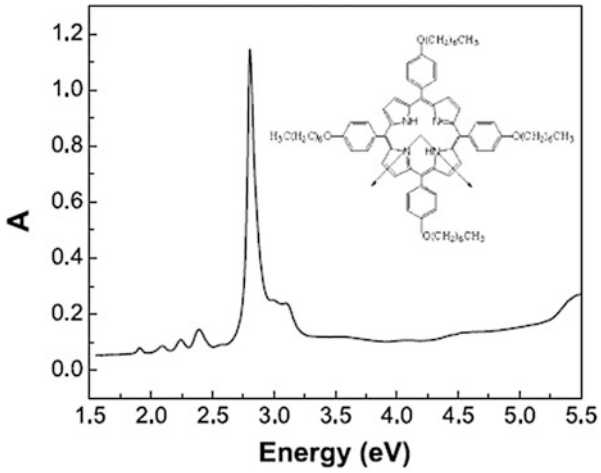

Fig. 20 UV-vis absorption spectrum measured for 20 nominal ML of H_2THOPP deposited onto quartz by Langmuir–Blodgett technique. Three overlapping bands are visible. Two of them (at 2.81 and 3.1 eV) are due to the splitting of the Soret band of the molecule at about 3 eV. A third weak band is present at 3 eV, being the relic Soret transition of the molecules not aggregated in the solid phase. In the *inset*: structure of 5,10,15,20-tetrakis-[4-(1-heptyloxy)phenyl] porphyrin (H_2THOPP) porphyrin. The dipoles of the molecule are indicated (From Goletti et al. [53])

the morphology and structure of the layer would have needed more accurate calculations to reach a precise attribution of the observed structures.

The same experimental procedure has been used later for LB layers of porphyrin, in particular a LB film, 20 monolayers thick, of 5,10,15,20-tetrakis-[4-(1-heptyloxy)phenyl]porphyrin (H_2THOPP) in a 1/4 M ratio with arachidic acid [52, 53]. The film was deposited onto rectangle-shaped quartz substrates and then silver coated at the surface pressure 25 mN/m. The molecular structure is represented in the inset of Fig. 20. The molecule possesses two dipoles mutually perpendicular in the molecular plane. In metalloporphyrins with D_{4h} symmetry, the related transitions are degenerate [54]. In free-base porphyrin (as H_2THOPP), due to their lower D_{2h} symmetry, these transitions are not exactly degenerate [54]. However, there is no difference observed experimentally between them [54, 55], so that in the discussion, the authors have assumed a D_{4h} symmetry for H_2THOPP.

As it was demonstrated in Goletti et al. [51], nominal coverages and effective coverages are not always coincident in LB layers. Then the authors used the expression "nominal monolayers" (although the validity of their conclusions is independent from that). UV-visible absorption spectrum of the layer deposited onto a quartz substrate is reported in Fig. 20. As elsewhere reported for similar porphyrins [54], two absorption bands are visible: one of lower intensity at 3.1 eV and one of higher intensity at 2.81 eV. Both of them are due to the splitting of the so-called Soret band at about 3 eV observed in the solution spectrum of H_2THOPP. Such a splitting arises from the coupling between neighboring molecules in the layer [56]. The transitions at lower photon energies (known as Q bands) do not suffer

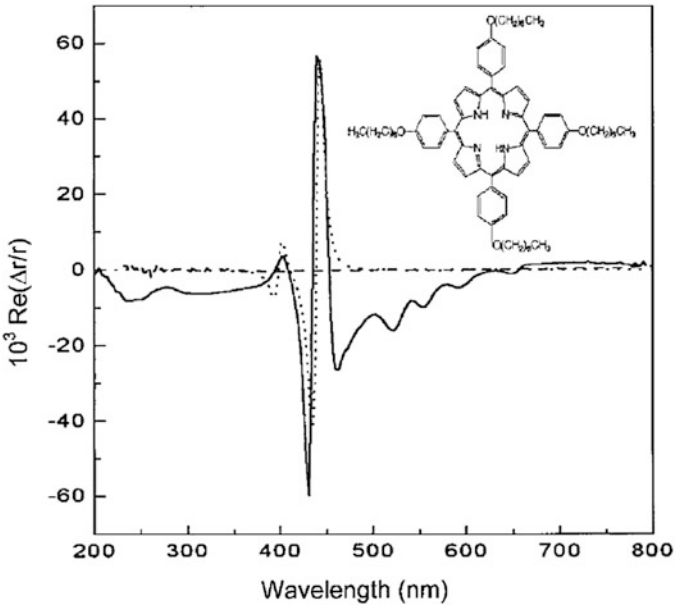

Fig. 21 Re($\Delta r/r$)spectrum measured at a 20-ML-thick Langmuir–Blodgett layer of H_2THOPP porphyrin deposited onto quartz. The absolute sign of the spectrum is arbitrary. The spectrum of an isotropic oxidized Si(001)sample has been reported for a comparison (*dashed line*). The *dotted line* represents a fit according to the derivative of the layer dielectric function (see text and cited ref). *Inset*: structure of H_2THOPP (From Goletti et al. [52])

similar splitting, and this feature has been attributed to the lower oscillator strengths of these transitions with respect to that of the Soret band [57]. It has also been shown that the 2.81 and 3.1 eV transitions have a predominant component in the plane of the molecule, along perpendicular directions [54].

In Fig. 21, the Re($\Delta r/r$) spectrum of 20 ML of H_2THOPP porphyrin deposited onto glass is reported. For a comparison, the RAS spectrum measured at an isotropic sample – an oxidized Si(001) surface – has been also drawn as zero line. It is evident that all the visible spectral features are characteristic of the organic overlayer: a dominant oscillation having extremes at 430 and 441 nm, plus other ancillary features at 401 nm (positive), 521 nm, 557 nm, 592 nm, and 650 nm (negative). The main oscillation (with a remarkable peak-to-peak amplitude of about 12%) lies in the energy region of the porphyrin Soret band, while the peaks at lower photon energies (above 500 nm) agree with the Q bands of the molecule [55]. Another film (20 ML, same porphyrin molecule) has been grown onto a metal (silver) layer to investigate the influence of the substrate in determining the overlayer optical properties. The corresponding RAS spectrum is drawn in Fig. 22. The overall line shape is very similar to the one measured for deposition onto glass (Fig. 21) and is dominated by a larger oscillation. For both samples, also the dependence of RAS spectra upon the azimuthal rotation by an angle ϕ around

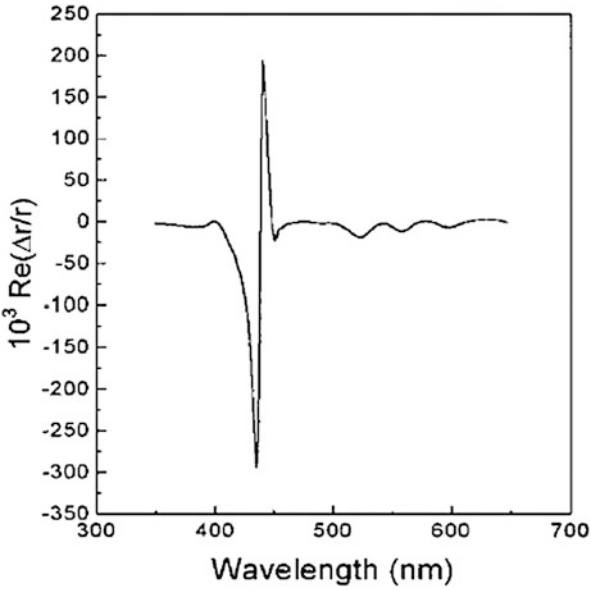

Fig. 22 Re($\Delta r/r$) spectrum measured at a 20-ML-thick Langmuir–Blodgett layer of H_2THOPP porphyrin deposited onto silver. The absolute sign of the spectrum is arbitrary (From Goletti et al. [52])

the axis perpendicular to the substrate has been measured. The maximum amplitude has been always recorded when directions α and β were aligned with the edges of the substrate. Spectra reported in Figs. 21 and 22 have been measured with this orientation of the sample. The relation connecting the signal amplitude to the angle ϕ displays the expected dependence upon sin (2ϕ) (Fig. 23).

It is clear from Eq. (4) that in general the RAS signal contains both the real and the imaginary anisotropies of the organic layer. When B is zero or negligible, the above expression can be simplified. This is the case for both materials utilized as substrates in Goletti et al. [52, 53]. The quartz is transparent above 300 nm. For silver, B is zero above 360 nm [58]. Consequently, in both cases, Re($\Delta r/r$) (and then $\Delta R/R_{\mathrm{RAS}}$) and $\Delta\varepsilon''_{\mathrm{porph}}$ are proportional and exhibit the same line shape. Since the value of coefficient A is higher for quartz than for silver in the Soret band region, the anisotropy $\Delta\varepsilon''_{\mathrm{porph}}$ of the porphyrin layer results higher in the latter case.

Also in this case, the substantial lack of reliable data (when Goletti et al. [52, 53] have been published) about the optical anisotropy of the porphyrin layer represented a significant limit to interpret the data. The authors assumed that the RAS spectrum could be simulated by using Lorentz oscillators to convey the optical properties of the molecule. The optical transition photon energies for the porphyrin layer were obtained from the absorption spectrum of the same samples. In particular, the experimental RAS spectrum has been reproduced with two Lorentz oscillators at 400 and 440 nm, fitting successfully the data by the energy derivative of the layer dielectric function, similarly to the case of vicinal Si(001) surfaces reported in literature [22, 23]. The interpretation of the RAS spectra of Figs. 21 and 22 as the derivative of the dielectric function of the organic layer would mean that increasing the thickness of the film, the optical properties of the outer layer

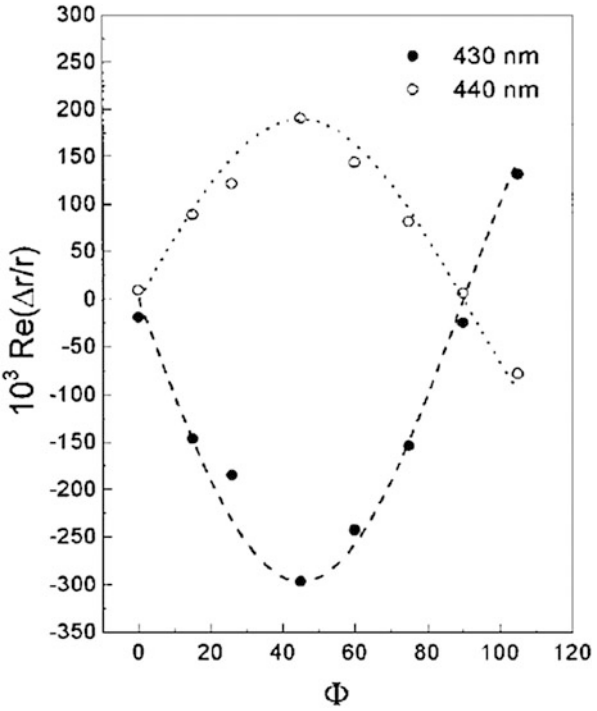

Fig. 23 Amplitude of the Re($\Delta r/r$) signal measured at 430 nm (*filled circles*) and 440 nm (*open circles*) for the sample whose RAS spectrum is reported in Fig. 22 versus the azimuthal angle ϕ (defined in the text). The fit of experimental data with the function $\sin(2\phi)$ is reported (*dashed* and *dotted lines*). In the configuration chosen, $\phi = 0$ means that the axes α and β form angles equal to, respectively, +45 and –45 with the longer symmetry axis of the rectangular sample, in its turn parallel to the direction along which the sample was dipped in the liquid (From Goletti et al. [52])

(similarly to the surface in inorganic crystals) become different from the inner layers (bulk), mimicking the surface-versus-bulk situation at a traditional crystalline solid. Strictly speaking, surface states are not expected to exist in molecular crystals, since no unsaturated bonds are present at the vacuum–crystal interface. Moreover, obvious intrinsic limits inherent to LB deposition make this growth technique incompatible with vacuum: all experiments have been performed in air. Nevertheless, the authors made the hypothesis that—although small—some effects of the particular environment experienced by molecules of the outer layer could be measured, thus paving the way to the application of these porphyrin systems for gas sensing (see sect 4.3).

In consideration of the symmetry of the single porphyrin molecule used in LB layers of Goletti et al. [52, 53], the detection of a nonzero RAS signal could be a surprising result. If we consider a symmetric molecule forming an angle θ with the substrate plane, an anisotropy factor $[1-\cos^2(\theta)]$ can be easily obtained by geometrical considerations. However, this would result in a RAS spectrum proportional to ε (dielectric function of the layer) and not to the derivative of ε. Consequently, an explanation of the line shape of Figs. 21 and 22 must be related to a different origin. However, it should be considered that porphyrin molecules in the LB film are interacting (as evidenced by UV-visible spectrum), and the resulting aggregation could account for the measured anisotropy. The authors made the hypothesis that the deep-lying layers are indeed inclined with respect to the

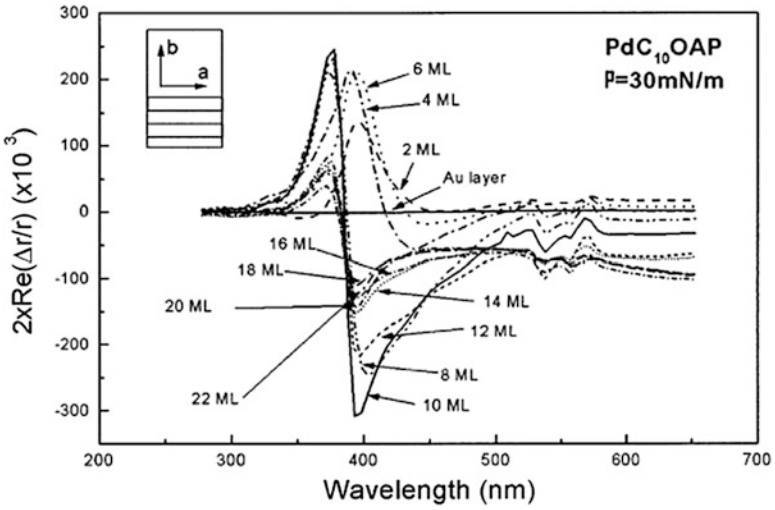

Fig. 24 2 Re($\Delta r/r$) spectra measured at Langmuir–Schaefer layers of $PdC_{10}OAP$ porphyrin deposited onto gold ($\Pi = 30$ mN/m). Total coverage ranges from 0 to 22 monolayers. The absolute sign of the quantity 2 Re($\Delta r/r$) $= 2(R_a - R_b)/(R_a + R_b)$ is arbitrary. In the *inset*: a and b directions of RAS axes (defined in the cited ref) with respect to the substrate. The layers (3 mm large) of different thicknesses deposited by the LS technique have also been reported (From Goletti et al. [59]. Reprinted with permission. Copyright 2002. American Chemical Society.)

substrate plane, while the topmost layers are nearly parallel to the substrate. This is the case for multiple layers of sapphyrins on gold substrates [32]. Then the symmetry-breaking mechanism could be due to the interaction of lower molecules, aligned along a specific direction, with the flat-lying molecules of the upper layers. Of course, one would expect that also the inclined molecules contribute to the anisotropy spectrum, but this contribution may be negligible for many reasons, for instance, smallness of the angle θ. The problem of the layer structure and its connection with the measured anisotropy is then definitively posed.

Also Langmuir–Schaefer (LS) layers have been investigated. In the LS method – often seen just as a variant of the Langmuir–Blodgett deposition – the films are transferred onto the substrate using the same LB experimental conditions, but pressing horizontally the compressed Langmuir film and then lifting the substrate upwards very slowly [34, 35]. As the staircase evolution of thickness in LB-deposited samples studied in Di Natale et al. [32] represented a key element in investigating the behavior of the related RAS spectra, the same procedure was followed when metalloporphyrin octaesters, having a true D_{4h} symmetry, were deposited onto a metal substrate using the LS technique, which also ensures a highly ordered deposition. The RAS line shape measurements were performed at every step of variable thickness. The main result reported in [59] is the abrupt change in the RAS line shape at 8–10-monolayer coverage: the line shape, which at lower coverage is essentially proportional to the Soret band absorption, becomes derivative-like (Fig. 24).

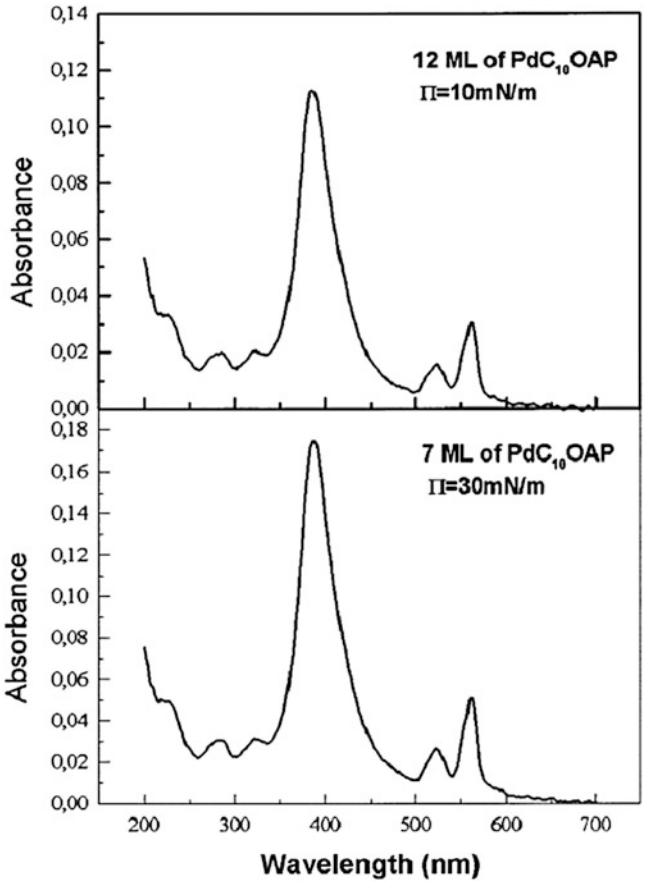

Fig. 25 UV-vis absorption spectrum measured for different layers of $PdC_{10}OAP$ deposited onto a quartz substrate by the Langmuir–Schaefer technique: (**a**) *upper panel*, 12 ML at $\Pi = 10$ mN/m; (**b**) *lower panel*, 7 ML at $\Pi = 30$ mN/m (From Goletti et al. [59]. Reprinted with permission. Copyright 2002. American Chemical Society.)

The typical absorption spectrum of the porphyrin layers is displayed in Fig. 25. In particular, these spectra are obtained for the $PdC_{10}OAP$ porphyrin deposited onto a quartz substrate at 10 mN/m (12 monolayers) and 30 mN/m (7 monolayers). The spectra feature the prominent Soret band at about 390 nm and the Q bands at longer wavelengths. Within the experimental accuracy, the spectra seem to be identical. However, a closer examination of the Soret band indicates small changes both in peak position and half width. In Fig. 24, $2\mathrm{Re}(\Delta r/r)$ spectra of $PdC_{10}OAP$ porphyrin layers deposited onto gold at the surface pressure $\Pi = 30$ mN/m have been reported, the thickness varying between 0 and 22 monolayers. For a comparison, the RAS spectrum measured at the uncovered, isotropic Au substrate has been reported as zero line. It is evident that all the visible spectral features are characteristic of the

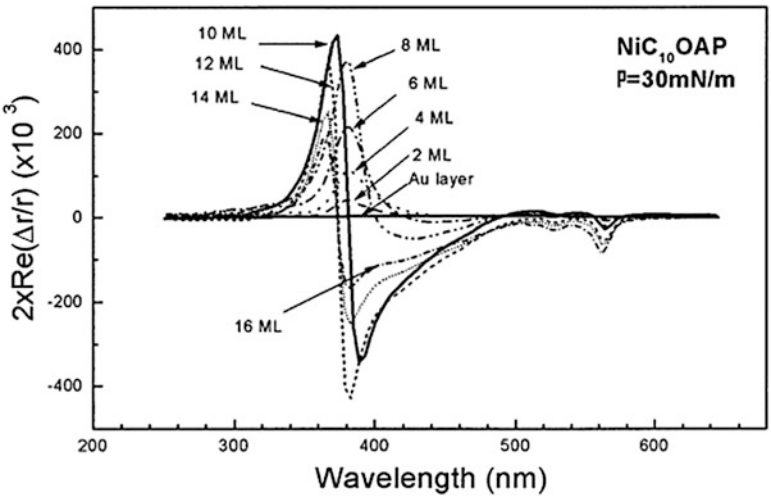

Fig. 26 2 Re($\Delta r/r$) spectra measured at Langmuir–Schaefer layers of $NiC_{10}OAP$ porphyrin deposited onto gold ($\Pi = 30$ mN/m). Total coverage ranges from 0 to 16 monolayers. The absolute sign of the quantity 2 Re($\Delta r/r$) $= 2(R_a - R_b)/(R_a + R_b)$ is arbitrary (From Goletti et al. [59]. Reprinted with permission. Copyright 2002. American Chemical Society.)

organic overlayer. The main structure always falls in the energy region of the Soret band (at about 390 nm), while the peaks at lower photon energies (522 and 561 nm) agree with the Q bands of the molecule.

Just after 2 monolayers, the anisotropy spectrum exhibits a well-defined peak at 395 nm, which is in fair agreement with the position of the absorption maximum (as reported in Fig. 25), but not totally. At 4 and 6 monolayers, apart from a negative broad minimum appearing above 420 nm, the spectra have a similar aspect. But at 8 monolayers, the change is evident: the positive maximum shifts to a lower wavelength (about 374 nm), and an almost symmetric minimum appears at 394 nm. On the whole, the spectrum assumes a "derivative" line shape. Up to 12 monolayers, no appreciable spectral changes occur. Above 14 monolayers, the amplitude diminishes at all photon energies, rapidly converging to a limit value which remains steady up to the maximum thickness of 22 monolayers.

When $PdC_{10}OAP$ layers are deposited on gold at the lower value of surface pressure $\Pi = 10$ mN/m, RAS spectra exhibit a completely different behavior: in the whole range of thickness (2–22 monolayers), the appearance is always peaklike, with a maximum at about 390 nm and amplitude increasing with coverage. No transition to the derivative-like line shape is observed. In Fig. 26, 2Re($\Delta r/r$) spectra of NiC10OAP layers deposited onto gold are reported. The dependence of the RAS signal upon thickness (here ranging from 0 to 16 monolayers (ML)) and the spectral characteristics are completely analogous to the case of $PdC_{10}OAP$. The main difference is the thickness value (10 ML) at which the spectral line shape varies,

passing from the "peaklike" to the "derivative-like" regime, probably depending upon the different molecules.

As in previous cases, it could be surprising that molecules expected to be isotropic produce anisotropy spectra (Figs. 24 and 26). However, it is known from spectroscopic results that porphyrin molecules in LB layers are likely adsorbed forming an angle θ with the normal to the substrate [32, 52, 60–62]. As a consequence, an anisotropy factor $[1-\sin^2(\theta)]$ is naturally introduced between the two directions sampled by the light electric field. In this case, the resulting $\mathrm{Re}(\Delta r/r)$ is proportional to the imaginary part of the dielectric function ε, explaining the behavior of the RAS spectra up to 6 (8) monolayers of $PdC_{10}OAP$ ($NiC_{10}OAP$) [60].

The interpretation of the derivative line shape appearing at 8–10 monolayers requires a different argument. By schematizing the samples within the three-layer model [37], in which the organic film is treated as an absorbing film of thickness d, much smaller than the light wavelength (an approximation that in our case may be criticized at higher coverage), it is possible to show that $\mathrm{Re}(\Delta r/r)$ is expressed in terms of the optical functions of the deposited organic layer and of the underlying semi-infinite substrate. The latter is assumed isotropic; actually, no appreciable anisotropy is detected by experiment (see the curves for the gold substrate in Figs. 24 and 26). The sudden line shape change observed would be due to some effect connected to the number of deposited layers producing a transition from an interface-dominated situation (substrate–monolayer and monolayer–air interfaces) to a bulk-dominated situation. A possible explanation of the transition could be a collective change in the average molecular tilt angle θ (defined as the angle between the molecular plane and the normal to the substrate) as the thickness is increased above 8–10 monolayers. More specifically, at low coverage, the molecules tend to be more inclined relative to the substrate, due to stronger interactions with it. As the thickness increases, the substrate influence decreases, and the molecules tend to straighten up. This however is a cooperative process so that there is a specific threshold thickness which separates one regime from the other. Electronic states are coupled to this morphology change since the average molecular separation changes (decreasing) as the average tilt angle decreases. This implies a stronger overlap of the electronic π orbitals. As a consequence, the weight of solid-state effects on the optical absorption line shape augments: in particular, the absorption maximum shifts to shorter wavelengths, and some broadening is induced. This is consistent with the observed change in the RAS line shape across the transition. At coverage values higher than 8 ML for $PdC_{10}OAP$ (10 ML for $NiC_{10}OAP$), optical spectra maintain a derivative appearance up to the thicker layer studied. The authors inferred that in this thickness range, the structure of the layer changes slightly with thickness, probably with the exception of some disorder resulting from growth, which reduces the total amplitude of the structure at 400 nm.

An experimental verification of the above model has been tried by careful study of the eventual changes in the optical absorption spectra as a function of the number of deposited layers and by precise determination of the thickness per monolayer using Atomic Force Microscopy (AFM). Within the accuracy of the AFM

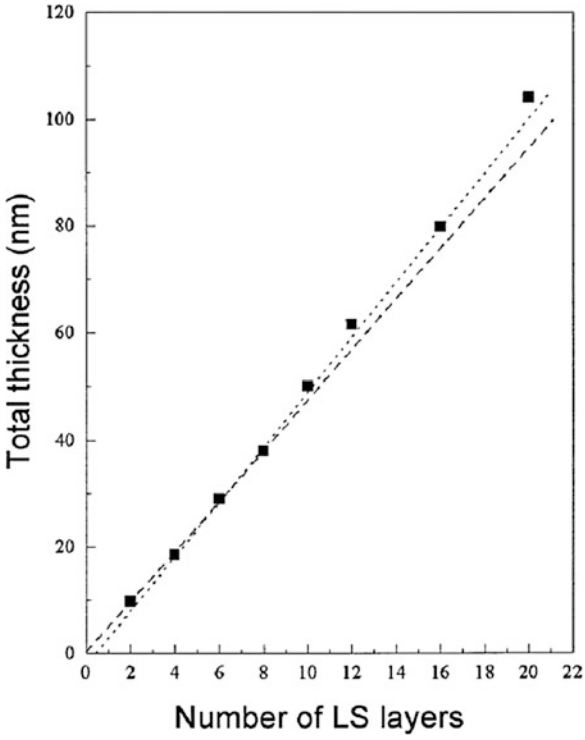

Fig. 27 Dependence of the film thickness (measured by AFM in air) on the number of deposited layers for $PdC_{10}OAP$ ($\Pi = 30$ mN/m). The *dashed* and *dotted lines* are obtained by fitting the data below and above 8 ML. The change of slope is compatible with a slight variation in the tilt angle of the molecule (From Goletti et al. [59]. Reprinted with permission. Copyright 2002. American Chemical Society.)

technique, it was determined that in the multilayers of $PdC_{10}OAP$ deposited at 30 mN/m, each deposited monolayer is 45–50 Å thick. In Fig. 27, AFM results indicate that either there is no change in the thickness per monolayer or, if there is any, it is barely above the error bars of measurement. Choosing a more conservative approach, the conclusion would be that such a quantity is a constant, that is, that no tilt angle change takes place in the neighborhood of the 8-layer coverage. However, to explain the observed band effects in the RAS spectra, only a minute change in the tilt angle (hence the average macrocycle distance) would be sufficient.

Actually, from Fig. 27, one can estimate that, just at 8 monolayers, there is a slight variation in the slope of the thickness dependence upon deposited layers, bringing a change in the coverage per monolayer of about 0.3–0.4 nm. This should mean about a 15% decrease in the average molecular distance in the tilted configuration. This change is certainly sufficient to considerably increase the molecular orbital overlap and hence explain the observed band effects.

On the contrary, in films of the same porphyrin deposited at lower pressure ($\pi = 10$ mN/m), each monolayer is just 14–15 Å thick. All these findings were confirmed by high-precision null-ellipsometry on the same deposited structures, assuming refractive index $n = 1.58$. The lower thickness measured for deposition with $\pi = 10$ mN/m is consistent with RAS data: as reported above, the spectra measured at such layers exhibit a peaklike line shape for all coverages.

The abovementioned results suggest that the porphyrins adopt different conformations as the surface pressure is increased. To understand if this is a consequence of structural changes already present in the Langmuir monolayer, null-ellipsometry measurements at the air–water interface were performed. A value for the monolayer thickness of about 13 Å up to a surface pressure of 10 mN/m was obtained, while above this pressure, the monolayer thickness increases progressively up to a value of 43–45 Å, which would nicely fit the size predicted for the macrocycle in an upright vertical position with the alkyl chains fully extended. A similar conformational change has already been observed in closely related porphyrin systems [61].

It is remarkable that such a change in the molecular packing happens at a rather large distance from the substrate–film interface. Such a structural change is not uncommon in molecular layers but usually is placed at a smaller distance from the substrate, typically 4–5 molecular layers [62–65]. To understand this unusual behavior, we must recall the mesogenic properties of molecules studied in [66]: it is reasonable that molecular order propagates over larger distances due to the strong tendency of liquid crystal materials to maintain their surface alignment in the bulk.

The first attempt to propose an explanation for the complex phenomenology represented by RAS results is reported in Mendoza and Vázquez-Nava [67]. The theoretical issue to solve is robust, and the authors propose a model in which the single porphyrin molecules are represented in their extreme skeleton. Each separate LB/LS layer (the intrinsic difference of the two methods is obviously meaningless in this approach, as the defects possibly introduced by the deposition are not considered) is schematized by an array of dipoles, whose orientation is characterized through two parameters: azimuthal angle ϕ and polar angle θ. To study the RAS effects due to the arrangement of the organic molecular layered system, the authors use a polarizable dipole model, based on the local electric field interaction, already successfully used to model the response of a true surface layer (silicon, in particular) in the second harmonic generation [68]. The LB layer is represented by L molecular layers, sitting onto an isotropic substrate (gold in the experiment of Goletti et al. [59]). In each layer, there are N identical, independent, nonoverlapping molecules drawn as polarizable entities ordered in a two-dimensional lattice. The 5 surface Bravais lattices have been tested, describing the order of the dipoles in a layer. In a plane, the dipoles have the same orientation, expressed in terms of the azimuthal angle and of the polar angle, with respect to the sample reference system (see Fig. 28). The planes are spaced by the distance d.

Three assumptions are then made: (i) In each plane, the dipoles have their own ϕ and θ; (ii) the interaction of the molecule with the incident light electric field is represented like an harmonic Lorentz oscillator, where the optical activity of the molecule is exemplified by point dipoles at the center of mass of the molecule; (iii) the local field, in the long-wavelength approximation, is given by the sum of two terms: the position-independent external field and the dipolar field produced by other dipoles. The total RAS signal is then expressed as the sum of the single-plane signals, each depending upon the particular ϕ and θ angle values.

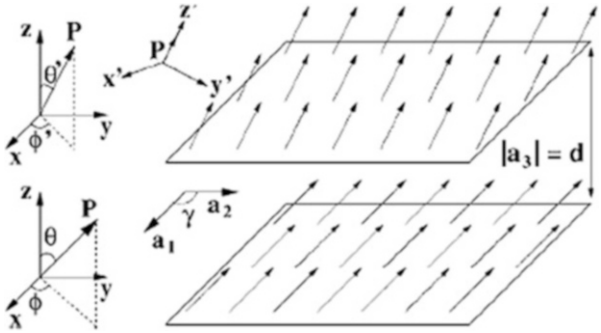

Fig. 28 Sketch of a system composed of molecular layers. The *arrows* represent the molecules (being polarizable entities) and the planes with *arrows* represent a layer of molecules, with equal θ and ϕ. The molecules on the *upper plane* show a change in the tilt and twist angle with respect to those of the *lower plane*. x (x′), y (y′), and z (z′) are the coordinates of the system (molecule). $\mathbf{a_1}$, $\mathbf{a_2}$, and $\mathbf{a_3}$ represent the primitive lattice vectors (From Mendoza and Vázquez-Nava [67]. Reprinted with permission. Copyright 2005 by the American Physical Society.)

The results show that for a system with more than one molecular layer, if the upper layers are allowed to change orientation with respect to the lower ones, the final spectrum simulates efficiently the particular oscillating line shape of RAS spectra (Fig. 29). In this way, it is then possible to correlate the experimental line shape to a well-defined change of structure due to the addition of a layer at a particular threshold value (in experiments 8–10 ML). In particular, tilting the dipoles of the upper layers towards the surface normal, a derivative-like line shape is obtained that goes from negative to positive values of the anisotropy as λ increases. If instead the tilt change is away from the surface normal, the oscillating spectrum goes from positive to negative, as λ increases. This means that the idea of correlating the RAS line shape to a particular defined structure in the layer, the outer layer different from the inner layers, is in principle correct. Nevertheless, the method is of questionable utility in real systems: (i) Too many parameters should be determined, some of them practically impossible to measure; (ii) from the point of view of calculations, the high number of free parameters reduces the possible impact of the model onto the effective and realistic comprehension of LB layers. In conclusion, although the model by Mendoza represents formally a confirmation and consequently an explanation of the experimental RAS results, its application is too intricate, unless the system is reduced to extremely reduced thickness, in practice not more than one or two layers on top of the (possibly isotropic) substrate. However, this also means that a different deposition method must be used to control more closely the structural details of such a thin layer, as well as its uniformity on the whole sample surface. Moreover, the possibility to vary the thickness continuously even at values lower than a true full layer could help the experimental investigation of the development of the line shape. LB and LS deposition methods, on the contrary, suffer limitations under both aspects: (i) A certain presence of defects is unavoidable, mainly for LS; (ii) the possibility to deposit less (and even

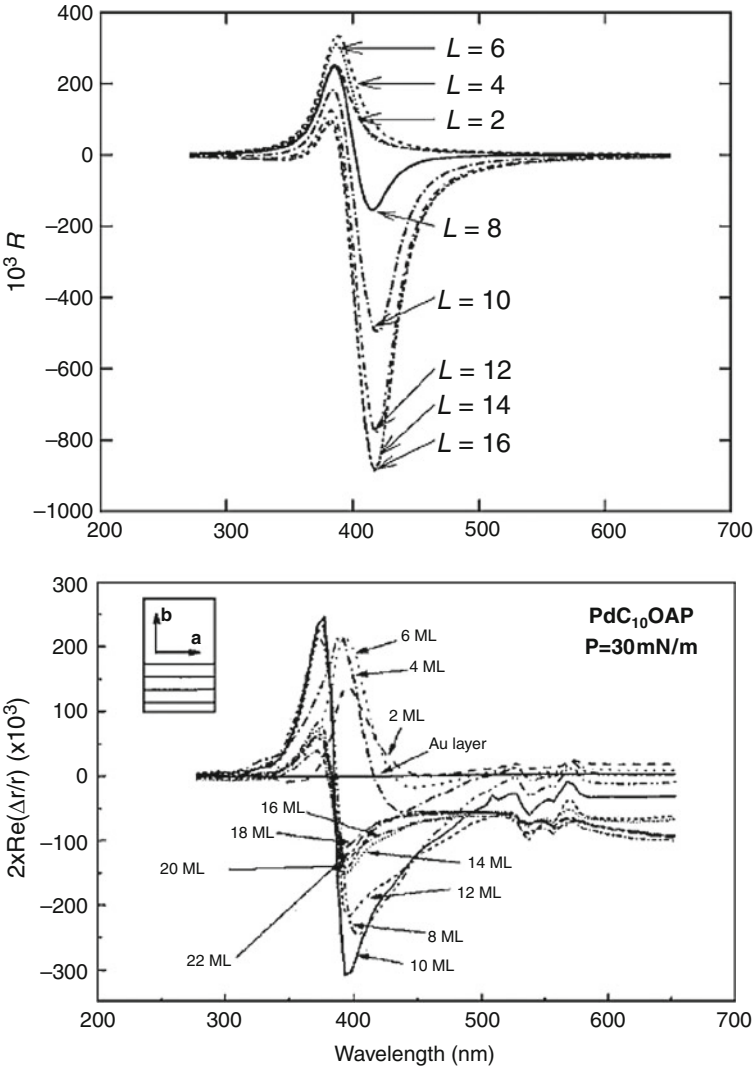

Fig. 29 *Upper panel*: R (see definition in [67]) versus photon wavelength for a rectangular 2D lattice and several values of L (L is the number of layers). $\phi = 42$, $\theta = 56°$, $\mathbf{a_1} = 9.4$ Å, $\mathbf{a_2} = 55/\text{a1}$ Å, $\mathbf{a_3} = 43$ Å, $\Delta\theta = -0.2$, and $\Delta\phi = 0.8$. In this case, the largest side of the rectangle is parallel to the *x*-axis. *Lower panel*: experimental results (taken from Goletti et al. [59], also reported in Fig. 24) (From Mendoza and Vázquez-Nava [67]. Reprinted with permission. Copyright 2005 by the American Physical Society.)

far less) than a single monolayer is intrinsically precluded. Evaporation in ultrahigh vacuum guarantees in principle the necessary control and accuracy needed in these new experiments and in addition offers the possibility to exploit spectroscopies normally available in UHV systems.

4.2 Ultrahigh-Vacuum-Deposited Layers

For the STM investigation of thin layers of porphyrins evaporated in UHV on highly oriented pyrolitic graphite (HOPG), simple free-base porphyrins without any peripheral substituents were chosen [69]. The strong motivation came from previous results [70] showing that the layer packing geometries could be strongly influenced by subtle differences in molecular structures and that moderately functionalized porphyrins tend to give unpredictable and intriguing arrangements. In particular, in [69], the authors focused on the 5,10,15,20-tetraphenyl-$_{21}$H,$_{23}$H-porphyrin (tetraphenylporphyrin, H_2TPP hereafter), sublimated under UHV conditions on HOPG and studied with STM and RAS as a function of the quantity of deposited molecules. The sublimation in vacuum was performed by heating a tungsten filament previously dipped in a H_2TPP solution at a concentration lower than 1%. The H_2TPP molecule deposition was estimated from the exposure time and partial pressure in the UHV chamber, calibrated during preliminary experiments. The data were acquired in situ, without breaking the vacuum.

The polarization axes configuration was defined measuring the dependence of RAS spectra upon the azimuthal rotation by an angle around an axis perpendicular to the substrate and looking for the maximum signal amplitude. As a result, the linearly polarized electric fields were aligned parallel to the edges of the rectangular graphite substrate. All the spectra have been recorded in the photon wavelength range 200–800 nm (1.5–5.5 eV). Particular attention has been used to measure the signal in the Soret band region (400–500 nm; 2.5–3.1 eV), where the main $\pi-\pi^*$ transition of the aromatic porphyrin cycle is [71, and references therein]. X-ray photoemission spectroscopy (XPS) and electron energy loss spectroscopy (EELS), being sensitive to the chemical and electronic structure of the molecules, showed that the vacuum-deposited H_2TPP molecules adsorb intact onto the graphite, although a not negligible interaction with the substrate is also detected [72].

In Fig. 30, RAS spectra acquired after successive H_2TPP depositions on the HOPG surface are shown (panel a) together with STM images associated to the most significant assembling configurations observed at the different coverage steps (panels b–e). The anisotropy signal of HOPG is structureless in the whole energy range: it has been subtracted from each spectrum acquired on the sample as a background. At less than 0.3 ML, STM showed isolated structures randomly distributed on the surface, while RAS was unable to register any anisotropy signal apart from the negligible signal of the graphite. At 0.3 ML, RAS started measuring a peak at around 434 nm, associated to the Soret band of the molecule although slightly red-shifted. This shift demonstrates that a molecular ordering exists with a preferential orientation and witnesses the existence of J-type aggregation: porphyrin molecules are organized as a tilted "deck of cards," where the tilt angle is meant with respect to the substrate plane [69]. At 0.5 ML, the RAS peak is still red-shifted, and an additional contribution – less intense but opposite in sign – is detected at about 444 nm. The overall line shape recalls the one observed in the case of porphyrin LB films [52, 53, 59]. We recall this finding has been interpreted as an

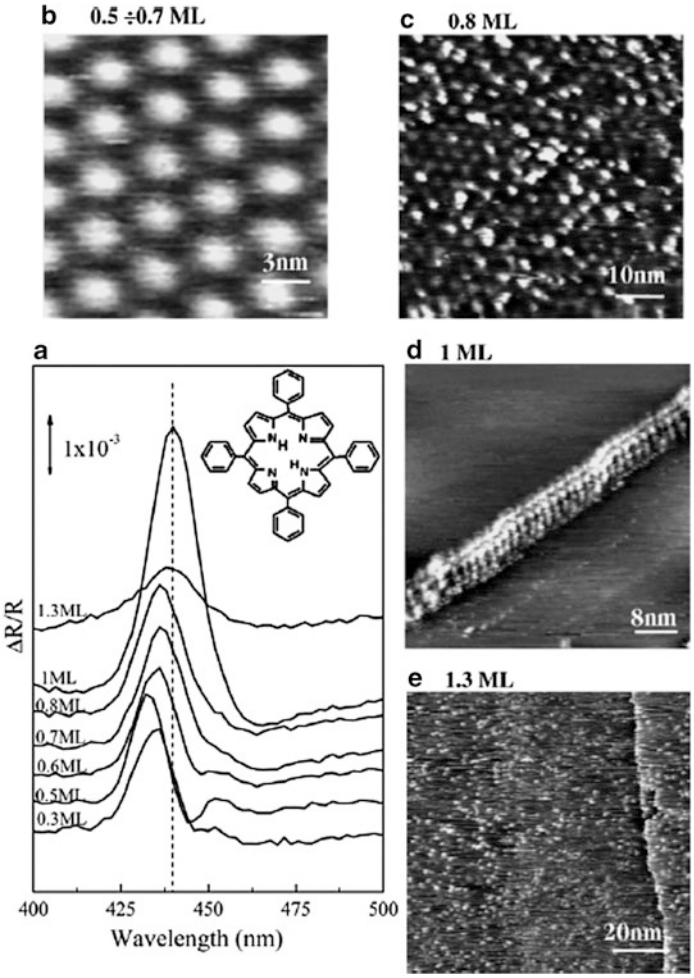

Fig. 30 RAS spectra as a function of the amount of deposited H_2TPP (*panel* **a**) and STM images (*panels* **b**–**e**) recorded at the corresponding values of the coverage. The *inset* in panel a reports the molecular structure (From Scarselli et al. [69])

indication of a change in the porphyrin alignment during the formation of additional top layers: in particular, the tilt angle modifies, as a consequence of the interaction of the molecules with the substrate, progressively screened by the underlying layers [59, 67].

STM images recorded at this coverage on different sample areas show that extended regions of the graphite substrate are covered by an ordered molecular adlayer, extending over hundreds of square nanometers. In panel b of Fig. 30, a detail of the ordered layer is highlighted, where bright structures, mostly circular in shape, are arranged in a quasi-hexagonal packing. Although it is reminiscent of the

underlying graphite substrate symmetry, there is about a factor of 10 between the two lattices. The mean diameter (1.8 nm) and height (0.35 nm) of these structures were estimated from the profile plots and compared to the mean distance of 1.77 nm separating hydrogen atoms in the para positions of opposite phenyl rings of the H_2TPP structure as obtained by theory. This agreement strongly suggests that each observed bright spot should correspond to a single H_2TPP molecule. As the periodicity of the molecules in the adlayer turns out to be 3.0 nm, the van der Waals surface of each molecule does not come into close contact with those of its nearest neighbors, with the minimum separation distance equal to about 1 nm. STM images obtained at slightly higher coverage (about 0.8 ML) show that an additional layer begins to form, with molecules laying preferably on top of the first ordered adlayer (panel c). Up to 1 ML, the maximum of the well-evident peak in RAS spectra is recorded almost at the same wavelength, while the intensity increment should be associated to the increasing extension of ordered adlayers of porphyrins (consistently with STM). The successive anisotropy signal decrease is a consequence of the layer disorder increasing with thickness.

The comparison of these results with expectations of the Mendoza model [67] is not very encouraging or conclusive. Although the low thickness of the layer has apparently reduced the complexity of the system and the number of variables whose values must be defined, the control of deposition during evaporation was not accurate enough to definitely end up to a really single monolayer and to avoid the contribution of a second layer (or even more). In particular, the slight changes of the wavelength position for the RAS peak observed with coverage in Fig. 30 could be connected to a varying contribution of additional layers onto the very first, as well as to rearrangements of the first layer. Also the conclusion that the ordered layer imaged at 0.5 ML is the layer directly adhering to the graphite could be questioned and assumed to be an ansatz rather than a clear-cut deduction from experimental evidences. In conclusion, a more stringent control of the thickness was still necessary, before simulating and then explaining convincingly the measured line shape.

If on this particular issue the results are not truly convincing, a scientific question arises from Scarselli et al. [69]. If the quasi-hexagonal ordered layer is really the first monolayer formed by molecules adsorbed flat onto graphite, from where does the optical anisotropy come from? The H_2TPP molecule is *per se* isotropic, at least in the time scale (from a few milliseconds to some seconds) at which the RAS data are acquired, and the symmetry itself of the lattice resulting after molecular packing is not able to explain any anisotropy. We should then invoke some electronic effect due to the structure of the layer, very likely due to the interaction between first neighboring porphyrins, able to remove in some way the degeneracy of the two active dipoles in the molecular plane.

The free-base porphyrin is intrinsically anisotropic at the single-molecule level: the two hydrogen atoms (see Fig. 31) are bonded to two opposite atoms of the four nitrogen atoms forming the inner ring of the molecule. The resulting configuration (where the dipoles along two perpendicular axes are evidently not equivalent) is called a tautomer, and a second equivalent state corresponds to hydrogen atoms bonded to the second couple of nitrogen atoms. The resulting polarization of this

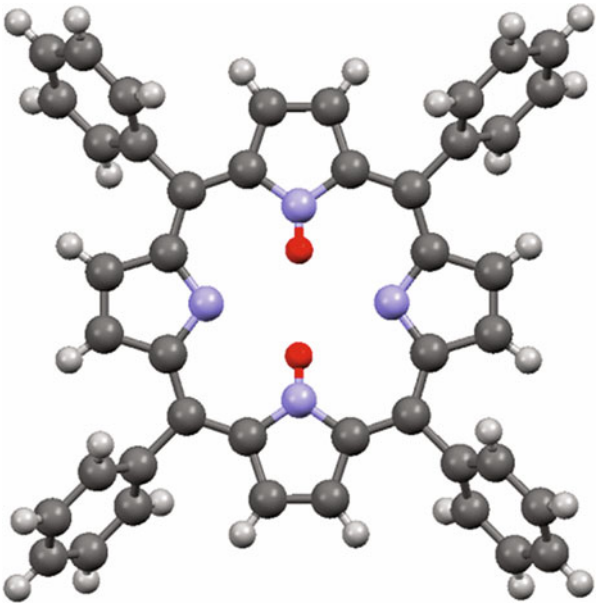

Fig. 31 Structure formula of the metal-free tetraphenylporphyrin (H_2TPP). The *red spheres* indicate the position of the two hydrogen atoms in the inner cavity of the molecule, in this case according to the structure of the tautomer frozen along the vertical direction. The molecule occupies a square surface with about a 12.2-Å-long side (From Bussetti et al. [73]). The two dipoles in the molecular plane are aligned as follows: one along the line passing through the two hydrogen atoms, the other perpendicular to this.

second tautomer is rotated by 90° with respect to the previous one. The transform from one configuration to the other (tautomerization) is extremely low costing in terms of energy at room temperature, as demonstrated in solution and in solid-state crystal structures: as a result, the time scale of tautomerization is extremely rapid, and then during acquisition of RAS signal, the overall anisotropy even at the single molecule must be expected to be zero. Nevertheless, as it is known that at lower temperature the tautomerization rate reduces strongly, in such condition, an anisotropy signal must be expected. When the H_2TPP layer is studied at room temperature, the tautomerization must be in some way prohibited or, more correctly, frozen because of the electronic arrangement of the layer. To give an answer to such a delicate issue, a pure two-dimensional layer is needed, and this condition was not fulfilled in the experiment of Scarselli et al. [69].

The decisive progress has been possible when a really careful deposition process has been achieved by exploiting the capability of organic molecular beam epitaxy to grow ultrathin and – within the possibility of the technique – homogeneous layers. Evaporation of H_2TPP onto HOPG has been performed in vacuum (base pressure during sublimation: 2×10^{-7} mbar) from a quartz crucible held at 550 K, while the HOPG was always at room temperature. The structural properties as well as the homogeneity of the resulting layer were investigated by AFM ex situ and by STM in situ [36].

Figure 32 (panel a) shows the surface morphology of a nominal 0.5 Å-thick film of H_2TPP, as imaged by atomic force microscopy (AFM). Large and flat graphite terraces appear, with a few steps separating them, approximately aligned along a direction that results orthogonal to the one along which HOPG was exfoliated

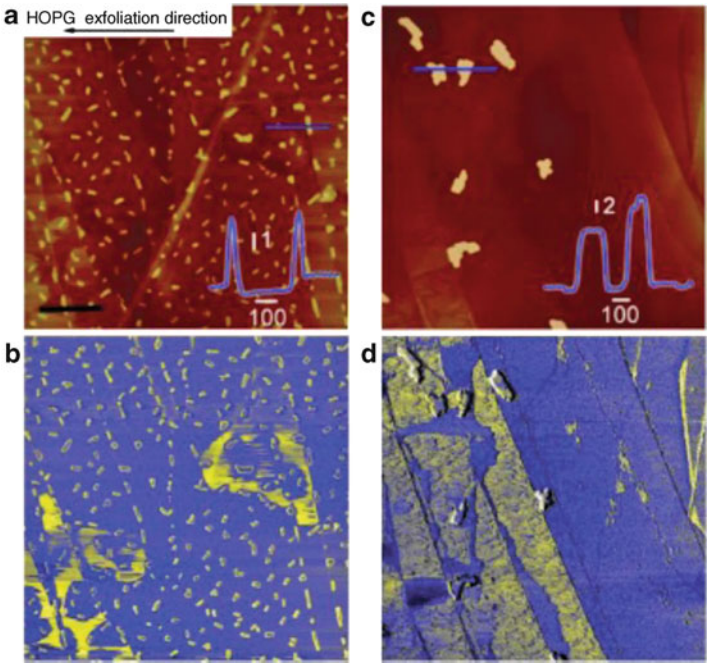

Fig. 32 AFM images of the surface morphology of H_2TPP films with different thickness. (**a**) 0.5 Å, immediately after sublimation in vacuum. The *black bar* on the *lower left* corner means 600 nm. The HOPG exfoliation direction is indicated; (**c**) the same film imaged in (**a**) after exposure to HCl vapors. In *panels* (**b**) and (**d**): phase contrast images of the regions in (**a**) and (**c**), respectively, showing the presence of two chemically different surfaces in the background. The height taken along the blue segments are reported on the *bottom right* of (**a**, **c**). Numbers next to the *scale bars*, close to the profile, are expressed in nanometers (From Bussetti et al. [36])

(in air) when the clean surface has been obtained. Several crystals (few nanometers in height) are also visible in the image, representing a 3D phase that coexists with the 2D phase covering the graphite plane. This is shown by the phase contrast image in Fig. 32, panel b, where the presence of two chemically dissimilar surfaces is represented by the different regions (with different colors) observed in the background. The authors have attributed the yellow regions to the bare HOPG surface and the blue ones to the H_2TPP thin layer (whose thickness below 1 nm is estimated from the cross-sectional profile in panel a).

The same sample has been then exposed to vapors of hydrochloric acid, thus obtaining the di-acid H_4TPP. From AFM, a strong change of the surface morphology results after this exposure (Fig. 32, panel c): while a very reduced number of 3D nanocrystals are still present, the 2D phase now covers almost totally the substrate (Fig. 32, panel d). Further exposure to HCl vapors has the effect of reducing more the density of 3D crystals, without apparently affecting the 2D wetting layer.

The coexistence of both the 2D and the 3D phase – clearly revealed in the images – explain the difficulty to extract a pure 2D layer to be investigated by RAS [69]. In fact, the presence of the 3D phase produces a well-known red-shifted term in the absorption of the aggregated molecules. Nevertheless, the authors were able to control the 2D and 3D presence by a chemical method, that is, the exposure to HCl vapors. A similar solvent vapor annealing has been reported also elsewhere as a method to heal the molecular assemblies at surfaces [74]. In this case it reveals a noteworthy efficiency in producing a true 2D phase.

The arrangement of the molecules in the resulting 2D phase is presented in Fig. 33, where a single domain of the H_2TPP layer is shown as imaged by STM. The molecules are organized in a square lattice, whose spacing is (1.48 ± 0.04) nm. Structure and size of the lattice are not compatible with the hexagonal symmetry of the substrate, being an effect of the molecule–molecule interactions, stronger than those existing between each porphyrin and the graphite surface, in agreement with recent theoretical calculations [75] and with experimental observation [76–78]. The orientation of square lattice axes appears to be nearly parallel to the exfoliation direction due to some influence of the graphite surface steps produced by exfoliation on the surface (see Fig. 32).

By measuring the tunneling current along two directions parallel to the symmetry axes of the lattice (drawn in Fig. 33), the spatial modulation of the signal displays corrugation maxima on the single molecules (in red in the image), with an evident asymmetry between α and β directions (see lower panels of Fig. 33), with a resulting oblate appearance. The same result has been reported elsewhere [76], demonstrating that each corrugation maximum is associated with the presence of a frozen H_2TPP tautomer. In consequence of that, all the molecules forming the domain in Fig. 33 appear to be oriented along the same direction (panel b of Fig. 33). The authors conclude that in the sample studied, the tautomerization (i.e., the coexistence of two energetically equivalent tautomeric forms on the surface, the one possibly transforming into the other) is suppressed at RT and that a stable and spatially organized array of tautomers is covering the whole graphite. The presence of one single domain of tautomers – aligned along the direction (labeled as β) parallel to the graphite surface steps – obviously produces the uniaxial anisotropy detected by RAS. Theoretical simulations also demonstrate that the 2D porphyrin layer is represented as an ordered ensemble of tautomers: each tautomer can be in one of two defined, distinct electronic states (T1 or T2) that are separated by an energy barrier whose value exceeds the thermal energy at RT. As such a system can be described within a two-dimensional Ising model [79], this finding naturally explains the spontaneous symmetry breaking below a certain (critical) temperature value T_0: below T_0, the system should display the long-range order detected by STM analysis and RAS (reported below).

In Fig. 34, RAS spectra for the H_2TPP (red and black lines) and H_4TPP (dash-dotted line) films on HOPG are presented. The anisotropy spectrum of clean graphite (dashed line) is reported as a zero reference spectrum (within the experimental accuracy), easily explained in terms of the HOPG symmetry.

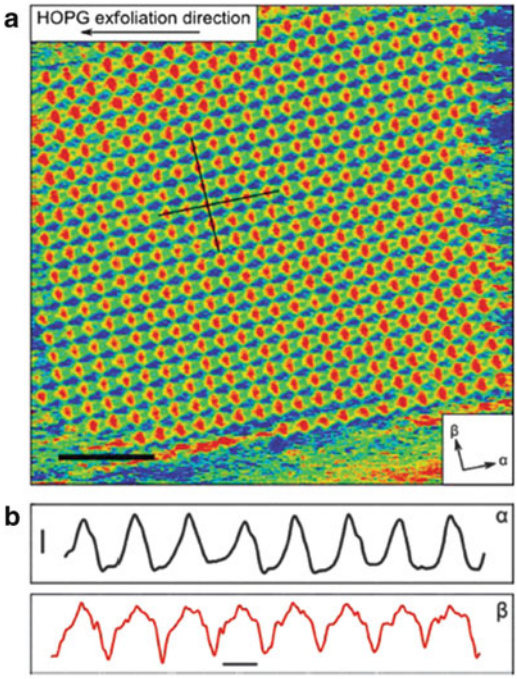

Fig. 33 (**a**) 36 nm × 36 nm STM image of a H_2TPP 2D domain on HOPG, showing the arrangement of molecules in a square unit cell ($V_{bias} = 0.4$ V, $I_{tunnel} = 50$ pA). The center of each porphyrin molecule in highlighted in *red*. The alignment of the inner H atoms of the molecules (frozen tautomers along the β direction) composing the domain is evident. The HOPG exfoliation direction is also indicated. The reported scale bar (*bottom left*) is 7 nm long. (**b**) STM signal profiles acquired along the α and β directions, respectively. The vertical and the horizontal *scale bars* are 50 pm and 1 nm, respectively. Data have been acquired at RT. In the inset: α and β directions of the RAS polarized electric fields, used to maximize the optical anisotropy signal of the sample (From Bussetti et al. [36])

The RAS spectrum is measured as $\Delta R/R = (R_\alpha - R_\beta)/R$ (R being the average value of the two polarized reflected intensities R_α and R_β) for linearly polarized electric fields aligned along the α and β directions reported in Fig. 33. The curve of the "as-deposited" H_2TPP layer, just after sublimation in the OMBE chamber, exhibits a sharp maximum at about 434 nm, consistent with the Soret band of the porphyrin. After exposure of the porphyrin layer to HCl vapors (protonation), the formation of di-acid H_4TPP molecules is induced as well as the extended and strong modification of morphology (Fig. 31, panel c). Also the RAS spectrum is radically changed (dash-dotted line) after sample protonation, with a well lower intensity and a broad appearance without any marked peak. This result agrees with the overall optical isotropy [80] of the H_4TPP film. After a successive heating step (flashing the sample at about 60°C), the pristine RAS line shape is practically recovered (full squares in Fig. 34), apart from a little but measurable red shift of the whole peak. The similarity of spectra for the "as-deposited" and the "annealed" layer is significant,

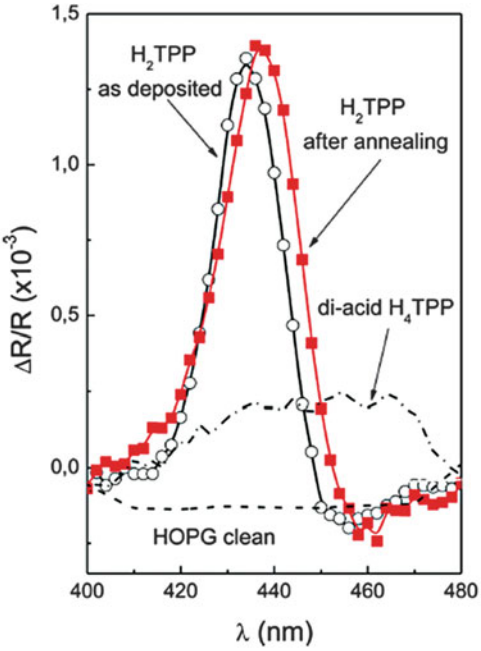

Fig. 34 Optical anisotropy of H_2TPP films on HOPG. The RAS spectrum measured immediately after H_2TPP deposition in vacuum is represented by the *black line* (*open circles*). The RAS spectrum acquired after the exposure of the porphyrin films to HCl vapors (di-acid H_4TPP) is drawn by the *dash-dotted line*. The *red line* (*full squares*) represents the spectrum measured on the sample after exposure to HCl vapors and subsequent heating at 60°C. The reference RAS signal of clean HOPG is the *dashed black line* (From Bussetti et al. [36])

as the surface morphology is well different in two conditions: in the former, 3D nanocrystals are spread on the surface, and in the latter, the 2D layer is totally predominant. We could conclude that the peaked RAS spectrum originated from the characteristic electronic structure of the true wetting layer alone.

Despite the strong effort in controlling the layer thickness pursued by authors in Bussetti et al. [36], an issue remains to be discussed: is the square lattice imaged by STM (Fig. 33) the true first porphyrin monolayer onto graphite? By STM, the answer could come from a careful and precise measurement of the step height with respect to the underlying graphite. But (at least on the basis of the published data in [36]) the bare hexagonal graphite has not been measured together with the organic layer (both lattices apparently are never present in the same published image). In addition, STM and AFM characterizations have been performed after the samples (prepared in UHV by OMBE) have been extracted from the growth vacuum chamber. In principle, one could doubt whether the sample has rearranged its structure with time during its permanence in atmosphere. To be conclusive, two further steps are then necessary: (1) to investigate the stability of the sample during the preparation in vacuum and after its extraction from the chamber, by using a technique able to monitor a significant property of the sample in both environments (e.g., RAS), and (2) to demonstrate if the thickness is definitely compatible with a single organic monolayer.

The application of RAS to extremely thin layers of H_2TPP in UHV has brought to convincing conclusions. But it was still necessary to disentangle the optical properties of the 2D layer from the 3D phase, the latter covering about 20% of the

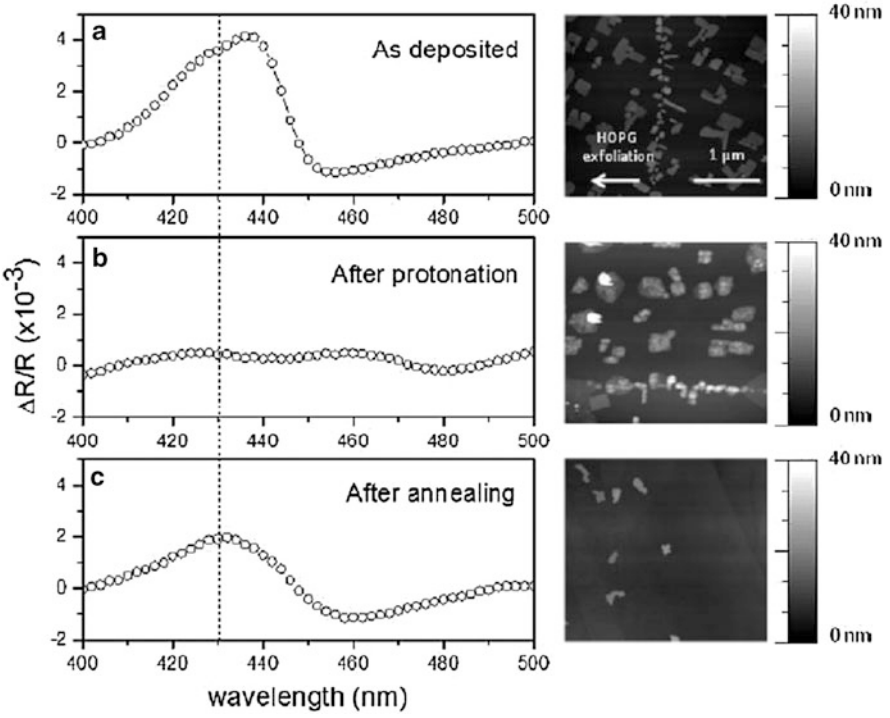

Fig. 35 (**a**) Experimental RAS spectra of a porphyrin thin film of 1 nm thickness, with the corresponding AFM image collected over a 3×3-μm^2-wide region. (**b**) Experimental RAS spectra of the same porphyrin thin film as in (**a**) after HCl exposure, with the corresponding AFM image collected over a 3×3-μm^2-wide region. (**c**) Experimental RAS spectra of the same porphyrin thin film as in (**b**) after annealing at 60°C for a few seconds, with the corresponding AFM image collected over a 3×3-μm^2-wide region (From Bussetti et al. [73]. Reprinted with permission. Copyright 2014. American Chemical Society.)

sample surface even at the lowest thickness investigated (0.05 ML, nominal thickness). This result has been finally achieved [73]: on one side by a careful chemical treatment of the sample to eliminate the 3D phase and to isolate a pure 2D layer and on the other side by analysis of the RAS spectra (in air and in vacuum) to obtain an unambiguous spectral fingerprint of such phases.

Figure 35 shows RAS spectra plus the corresponding AFM images measured (in air) at different H_2TPP films. In panel a, the nominal thickness of the porphyrin layer is 1 nm. The RAS signal maximum corresponds with the α polarized electric field aligned along the graphite exfoliation direction that breaks the substrate C_3 symmetry by forming steps and defects along a specific direction, thus inducing some preferential arrangement of the overlayer [36]. In the corresponding AFM image, the 2D and 3D porphyrin phases are both visible, with many crystallites covering about 20% of the sample surface: this means that in principle both phases

could contribute to the measured optical anisotropy. The RAS peak is clearly asymmetric with a maximum at about 440 nm.

After exposing the 1-nm-thick film to HCl to dissolve the 3D structures [36], then thermally treating the film at 60°C to recover tautomerism and optical anisotropy [36, 81, 82], the RAS response and AFM surface morphology of the film change. In panel b, after HCl exposure (i.e., after protonation switches off tautomerism), the RAS spectrum is almost zero, while AFM shows that 3D crystals have been nearly dissolved. In panel c, after a proper thermal treatment, the optical anisotropy is recovered (but the line shape is now more symmetric), and only few 3D structures are still visible. This demonstrates that by applying these two steps (HCl exposure then annealing) to an extremely thin porphyrin layer, one should be able to isolate the pure 2D layer and then the corresponding RAS anisotropy.

The results of the RAS and AFM characterization of a 0.05 ML sample are reported in Fig. 36. In panel a, the surface morphology only shows a 2D flat layer, substantiating the conclusion that the corresponding RAS spectrum can be considered characteristic for such a phase. In the RAS spectrum, centered on the Soret band of the molecule, a single symmetric peak at 432 nm, plus a small negative contribution at higher wavelength (reminiscent of a similar line shape in Fig. 30 [69]) is dominant. An interpretation and modeling of the layer optical anisotropy, as measured by RAS, is then possible within the three-layer model [37], in terms of the porphyrin layer dielectric function and of properly chosen Lorentz oscillators, respectively. In the limit of a small layer thickness (a condition that is certainly satisfied in this case), the $\Delta R/R_{\mathrm{RAS}}$ signal can be expressed in terms of the dielectric function of the anisotropic layer (the porphyrin 2D layer):

$$\Delta R/R_{\mathrm{RAS}} = (8\pi d/\lambda)(\mathrm{A}\,\Delta\varepsilon_2 - \mathrm{B}\,\Delta\varepsilon_1). \tag{7}$$

Here, $\Delta\varepsilon_2 = [\varepsilon_2]^{\alpha} - [\varepsilon_2]^{\beta}$ and $\Delta\varepsilon_1 = [\varepsilon_1]^{\alpha} - [\varepsilon_1]^{\beta}$ are the anisotropy of the imaginary and real parts of the layer along the α and β directions, respectively. In Eq. (7), d is the film thickness and λ is the wavelength of the impinging light ($d \ll \lambda$). A and B express the optical properties of the isotropic graphite substrate and are known from literature [13, 47]. The single porphyrin molecule has been then modeled in order to reproduce the experimental $\Delta\varepsilon_1$ and $\Delta\varepsilon_2$, by using two Lorentz oscillators to represent the two main optical transitions (at two different photon energies), which are preferentially excited by perpendicularly oriented linearly polarized light. The best fit result is reported in terms of $\Delta\varepsilon_1$ and $\Delta\varepsilon_2$ in Fig. 36, showing a very good agreement with the experimental data.

For a pure 2D porphyrin layer, this spectral analysis reaches two definitive results: (1) the RAS signal line shape is due to optical transitions placed along orthogonal directions and found at different wavelengths, and (2) on the basis of *ab initio* calculation, the two distinct optical transitions describing the optical properties of a 2D porphyrin layer are present in a single H_2TPP molecule, polarized along orthogonal directions (the one at higher wavelength polarized along the fixed H–H tautomer direction) [83].

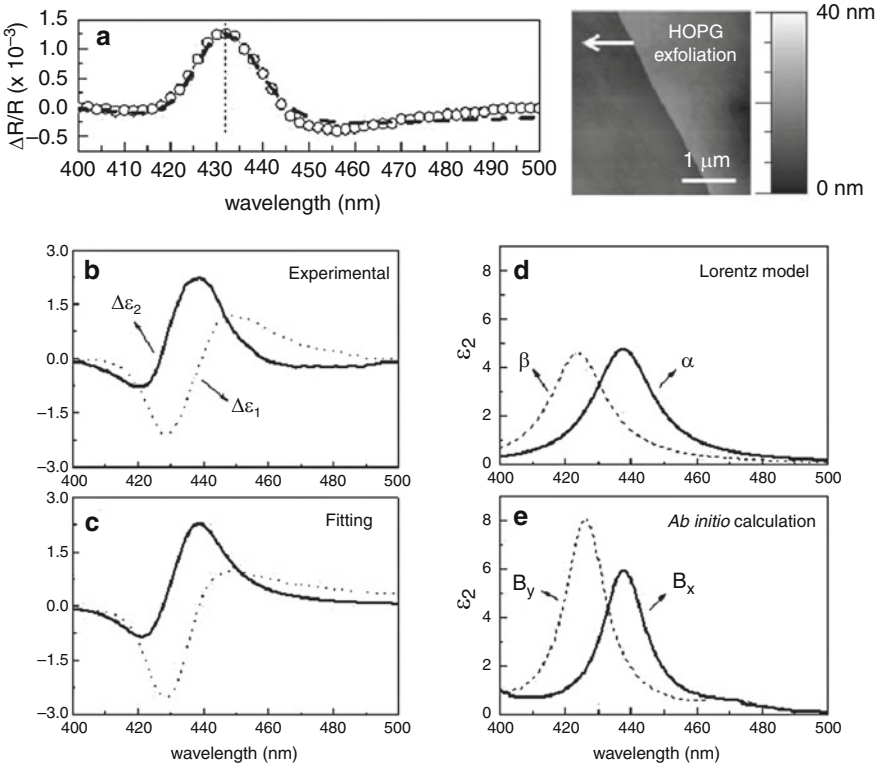

Fig. 36 (**a**) Experimental RAS spectra of a pure 2D porphyrin layer obtained from a thin film of 0.05 nm thickness, after HCl exposure and thermal treatment at 60°C for a few seconds, with the corresponding AFM image collected over a 3 × 3-μm^{2}wide region. (**b**) Experimental $\Delta\varepsilon_1$ and $\Delta\varepsilon_2$ dielectric function anisotropies of the porphyrin 2D layer, as extracted from the experimental RAS spectrum in *panel* **a**. (**c**) Best fit $\Delta\varepsilon_1$ and $\Delta\varepsilon_2$ dielectric function anisotropies of the porphyrin 2D layer, as extracted by fitting the experimental spectrum in *panel* **b** using two Lorentz oscillators. (**d**) ε_2 corresponding to the two best fit Lorentz oscillators used in *panel* **b**. (**e**) Calculated ε_2 (ab initio calculation) for a 2D square domain of porphyrin molecules, characterized by frozen tautomers all aligned along the same direction (From Bussetti et al. [73]. Reprinted with permission. Copyright 2014. American Chemical Society.)

Analysis of the RAS signal thus demonstrates that the frozen porphyrin tautomers are responsible for the optical anisotropy measured at RT [36] and that the optical properties of a given tautomer can be expressed in terms of two mutually perpendicular Lorentz oscillators, resonating at distinct wavelengths.

The same analysis has been completed for three samples with increasing thickness: 0.2, 1, and 5 nm. Experimental RAS spectra are shown in Fig. 37, together with the corresponding AFM images. The RAS spectra are different for films with different thickness, both in line shape and intensity, while from AFM, an evident coexistence of 2D and 3D morphology is appreciable. Consistently with the AFM characterization, the RAS spectra have been fitted by Voigt functions (a function

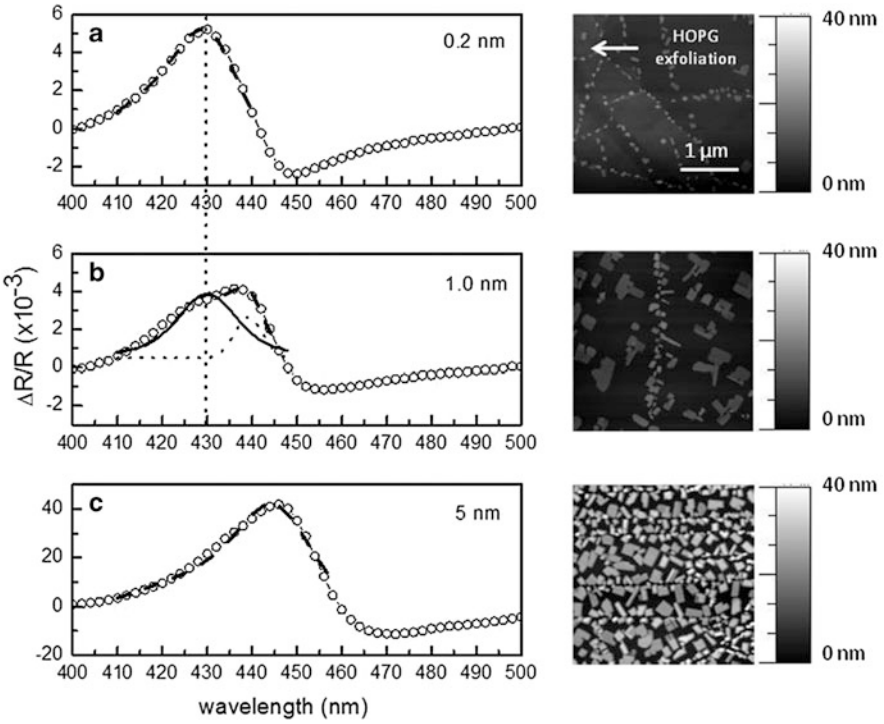

Fig. 37 Experimental RAS spectra of porphyrin thin films of (**a**) 0.2 nm, (**b**) 1 nm, and (**c**) 5 nm thickness, with the corresponding AFM images collected over 3×3-μm^2-wide regions. The best fit curve obtained for the RAS spectra are reported as *dashed lines*. The best fit curve of the RAS spectrum in *panel* **b** is a linear superposition of two Voigt curves: the one centered at 430 nm (*continuous line*) as a contribute of the 0.2-nm layer, which shows the RAS spectrum maximum centered at 430 nm, and the other one (*dotted line*), positioned at 439 nm, as a shifted contribute of the 5-nm layer, whose RAS spectrum maximum is at 444 nm (From Bussetti et al. [73]. Reprinted with permission. Copyright 2014. American Chemical Society.)

profile used in spectroscopy, which convolves a Lorentzian line shape with a Gaussian broadening) associated to the different phases (2D and 3D) shown by AFM. Both the 0.2-nm-thick film (which behaves as a slightly modified 2D phase, with a negligible 3D contribution) and the 5-nm-thick sample (where the 3D phase is definitely dominant) are fitted just by using a single Voigt curve, while the 1-nm-thick sample (intermediate between the other two cases) has been interpreted in terms of the contemporary presence of the 2D and the 3D phases, by using two Voigt curves that are linearly superimposed with different relative weight for different film thickness. The fits (dashed lines) are compared with the RAS spectra, validating an excellent agreement with the experimental data.

The demonstrated sensitivity of RAS spectra to the coexistence of the 2D and 3D phases, and more generally to the presence of an additional layer (or part of it) grown over the very first, offers the possibility to conclude that the "supposed"

single 2D layer imaged by STM in Fig. 33 is actually "the" first layer. For the close link established between the macroscopic optical anisotropy, detected by RAS, and the molecular aggregation characterizing the film structure, the RAS spectrum measured on the same layer (see Fig. 34) allows to conclude that this is very likely a single layer on top of graphite, as the peak position is not red-shifted with respect to the Soret band of the porphyrin molecule, and is in good agreement with the spectral position of the peak associated with the pure 2D phase (Fig. 36).

The different symmetry of the porphyrin layer lattice (square in [36], hexagonal in [69]) still remains a scientific issue to be investigated. In both cases, however, the lack of a built-in significant asymmetry of the lattice must be surpassed via some microscopic mechanism (as the Ising model plausibly invoked in [36]) to justify the observed optical anisotropy.

4.3 The Application of Thin Porphyrin Layers in Gas Sensing

Supramolecular aggregations of porphyrins (rods, rings, wires, nanofibers, and three-dimensional nanocrystals) are due to the action of weak forces that can be affected by the adsorption of molecules from either gas or liquid phase. This opens the way to the optical monitoring by RAS of the supramolecular properties of porphyrin films as an alternative and innovative approach to gas sensing.

Langmuir–Blodgett films (30 monolayers) of 5,10,15,20-tetrakis-[4-(1-heptyloxy)phenyl]-porphyrin (H_2THOPP) were deposited onto an oxidized Si(001) sample or on a quartz substrate [84]. The samples have been then inserted in a little plastic chamber with inlet and outlet gates for the gas flow. A homemade glass window (with Viton O-ring) allowed the optical access to the sample. The analyte concentration (ethanol plus nitrogen as gas carrier) was varied by two flux meters from 10^2 ppm up to 2×10^4 ppm (corresponding to saturated vapors). The samples have always been at room temperature. The authors have measured the variation produced in the UV-visible RAS spectrum of this layer during the exposure to ethanol, chosen for practical reasons (i.e., ease of use), although the interest for other gases (CO, CO_2, NO, NO_2) has a larger development in the sensors community. The RAS spectrum measured at the as-grown layer is assumed as baseline. The absolute sign of the spectrum is arbitrary, depending upon the phase of the lock-in. After the layer has been exposed to ethanol vapors, the base spectrum modifies, in particular in the Soret band region. The positive and negative extreme of the main oscillation (characteristic of the RAS spectrum in the Soret band region, not reported here [84]) behave differently during exposure: the positive peak increases its anisotropy by only some RAS units (Fig. 38), while the negative peak decreases its absolute value by some tens of RAS units (Fig. 39). The exposure time T of the sample to ethanol during a single cycle (ethanol concentration: 2×10^4 ppm) ranged between 120 and 180 s. By following the

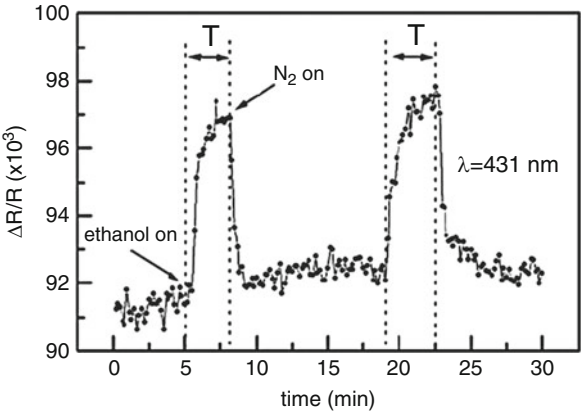

Fig. 38 Variation with time of the RAS signal at $\lambda = 431$nm during ethanol/nitrogen cycles, for a 30 ML thick H_2THOPP LB film deposited on an oxidized Si(001) substrate. The chosen photon energy corresponds with the maximum of the anisotropy oscillation measured in the Soret band region of the porphyrin film (from Bussetti et al. [84])

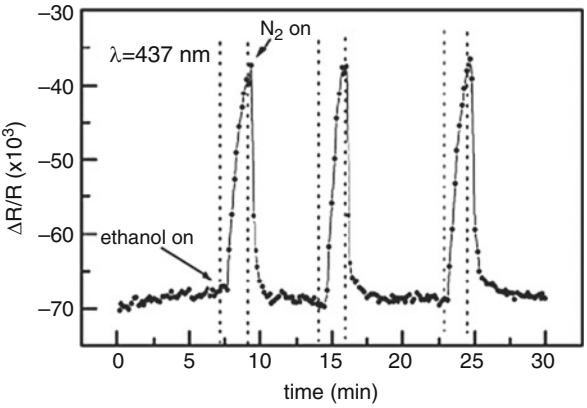

Fig. 39 Variation with time of the RAS signal at $\lambda = 437$ nm during ethanol/nitrogen cycles, for a 30 ML thick H_2THOPP LB film deposited on an oxidized Si(001) substrate. The chosen photon energy corresponds with the minimum of the anisotropy oscillation measured in the Soret band region of the porphyrin film. With respect to the data reported in Fig. 38, here the authors have used a slightly different time T for the exposure of the LB film to ethanol vapors (about 120 s, against about 180 s in Fig. 38) (from Bussetti et al. [84])

modification with time, it is evident that the signal variation did not reach its saturation, avoiding the long-lasting pollution of the sample observed otherwise, with possible damage of the layer. The full recovery of the original signal level, after exposure to a flow of high-purity N_2 gas, on the contrary happens after a few tens of seconds [85]. This result shows that in principle the optical anisotropy of the

layer, very likely modified (even slightly) by the interaction with the analyte, is sensitive to the exposure and could be used to transduce the gas-surface behavior for gas sensing purpose.

On the basis of these preliminary results, the investigation of analytes by RAS is then in principle possible, in terms of sensitivity, response time, and origin of the measured effect. In a further series of experiments, the investigation has been expanded to other volatile organic compounds (VOCs), choosing three typical molecules representative of distinct compound families: alcohols (ethanol), amines (trimethylamine), and alkanes (hexane) [86]. This choice allowed to investigate different interaction mechanisms: coordination to the metal ion in the center of the porphyrin (most important for amines), hydrogen bond (alcohols), and van der Waals forces (amines, alcohols, and alkanes). For liquid substances (ethanol, hexane), saturated vapors (obtained by N_2 bubbling) were diluted in pure nitrogen and injected into the measurement cell. Saturated vapor concentrations were calculated by Antoine's law. The optical anisotropy modification was measured for a thin LS layer of a Zn complex of 5,10,15,20-tetrakis(4-heptyloxypheny)porphyrin (Zn-HepOTTP). The molecular layer was deposited onto the surface of a quartz microbalance (QMB), a transducer whose capability to measure the adsorption of volatile compounds has been already demonstrated [87]. The RAS signal has thus been related to the adsorption process monitored by QMB.

In Fig. 40 (lower curves), the RAS spectra for a 30-ML-thick LS film are shown, before and after the sample exposure to increasing quantities of ethanol vapors: 3, 9, and 18%, corresponding to 2,314, 6,943, and 13,887 ppm, respectively. The synchronization of RAS and QMB signals (inset of Fig. 40) demonstrates the dependence of the RAS signal changes upon the amount of adsorbed gas molecules, as well as the reversibility of both signals. After cleaning in nitrogen flux, the LS layer has been then exposed (in similar conditions) to hexane and ammine vapors. In Fig. 41, ΔRAS spectra are reported, defined as the difference between RAS spectra measured after and before exposure: $\Delta RAS = RAS_{after} - RAS_{before}$. In this way, it has been possible to highlight even the tiniest variation due to the analyte.

From ΔRAS, some conclusions are drawn: (a) a higher sensitivity to the analyte is characteristic of a limited sets of wavelengths, dependent upon the porphyrin (here 407–410, 436, and 452 nm); (b) the RAS signal appears to be sensitive to the specific interaction between a porphyrin layer and analyte, definitely apparent at distinct wavelengths (ethanol and TMA produce anisotropy changes at the same spectral positions, differently from hexane); (c) when comparing different analytes, the strength of the interaction seems reflected in the total anisotropy amplitude. TMA affects the optical anisotropy more strongly than ethanol. Moreover, a linear dependence of the ΔRAS amplitude versus analyte concentration is suggested in all cases (inset of Fig. 41), although the number of data points is still limited.

The consequences of the above reported statements are significant for sensors. With respect to methods where the quantity of the analyte is measured with high precision but without any specificity to chemical details, here the modification of the layer optical spectrum gives a multifaceted information, providing additional details about the character of interaction. This means that the identification of

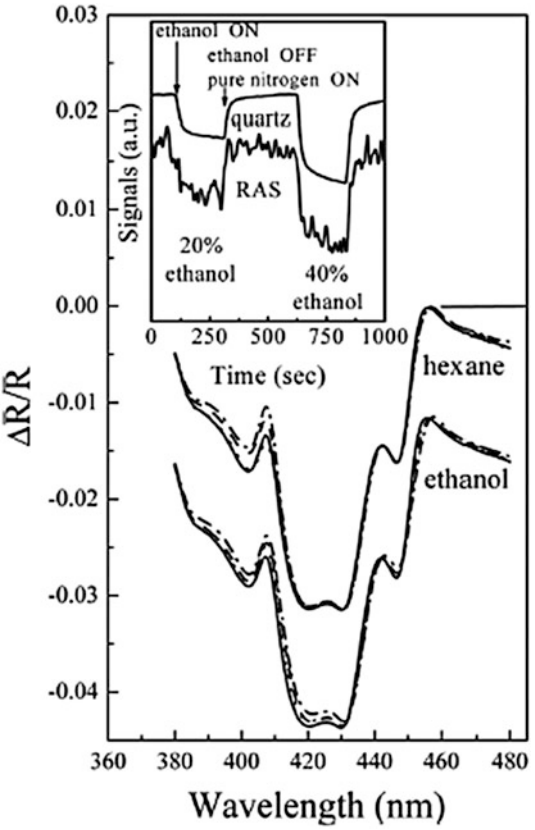

Fig. 40 *Lower curves*: $\Delta R/R_{RAS}$ spectra measured on a 30-ML-thick Zn-HepOTTP LS film: (i) before the exposure to ethanol vapors (*full line*) and (ii) after the exposure to ethanol vapors (3%, *dotted line*; 9%, *dashed line*; and 18%, *dash-dotted line*). *Upper curves*: $\Delta R/R_{RAS}$ spectra measured on a 30-ML-thick Zn-HepOTTP LS film: (i) before the exposure to hexane (*full line*) and (ii) after the exposure to hexane (3%, *dotted line*; 9%, *dashed line*; 18%, *dash-dotted line*). The reported zero line is referred to hexane: ethanol curves have been shifted by −0.01 with respect to hexane. The error bar is evaluated as ±0.0001. Each exposure stage was 210 s long. In the *inset*: (*a*) *curve below*: $\Delta R/R$ signal measured at 408 nm during the exposure to ethanol vapors of a 30-ML-thick Zn-HepOTTP LS film and (*b*) *curve above*: QMD signal measured simultaneously with RAS monitoring, during the exposure to ethanol vapors. In the time period reported in the figure, two exposure stages have been considered: 20% (15,430 ppm) and then 40% (30,860 ppm). When the ethanol flux is stopped, the sample is exposed to a pure nitrogen flux. The $\Delta R/R$ sign has been chosen to have a similar visual behavior of RAS and QMD signals. The signal-to-noise ratio is evidently lower than in extended spectra; this is due to the shorter integration time necessary to promptly follow the optical signal variation during the gas exposure (From Bussetti et al. [86]. Reproduced with permission. Copyright 2009, AIP Publishing LLC.)

vapors interacting with the sensing layer is in principle possible, via a proper multivariate analysis of RAS data. In addition, these data support that the eventual insertion of analyte molecules in the supramolecular porphyrin aggregate

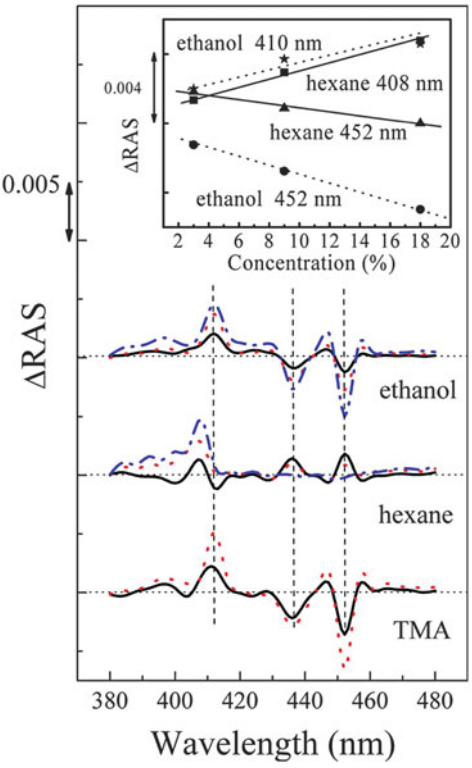

Fig. 41 ΔRAS, defined as the difference $\Delta R/R_{\text{after}} - \Delta R/R_{\text{before}}$ between RAS spectra measured before ($\Delta R/R_{\text{before}}$) and after ($\Delta R/R_{\text{after}}$) the exposure of a 30-ML-thick Zn-HepOTTP LS film to increasing quantities of volatile compounds. *Top*: ethanol 3% (*full line*), 9% (*dotted line*), 18% (*dashed line*). *Middle*: hexane 3% (*full line*), 9% (*dotted line*), 18% (*dashed line*). *Bottom*: trimethylamine 3% (corresponding to 90 ppm, *full line*), 9% (corresponding to 270 ppm, *dotted line*). Significant wavelengths (see text) have been evidenced by *vertical dashed lines*. *Inset*: ΔRAS signal amplitudes (from spectra) for ethanol and hexane at characteristic wavelengths versus nominal concentration of VOCs. The *lines* have been drawn to guide the eyes. The error bar in this case is evaluated as ±0.0002 (From Bussetti et al. [86]. Reproduced with permission. Copyright 2009, AIP Publishing LLC.)

modulates the optical anisotropy via the variation in the interaction between adjacent molecules. This information can be read out, leading to the possible chemical recognition of the single analytes.

LS systems offer in general a large surface-to-volume ratio, meaning a wide sensing area for adsorbing volatile molecules [85]. However, the higher structural order of LB layers is expected to provide a larger anisotropy signal, that is, a higher sensitivity to the adsorption process monitored by RAS. New experiments were then performed on an LB thin film of the same porphyrin used in [86], to exploit the more ordered arrangement of the molecules due to this deposition technique. In particular,

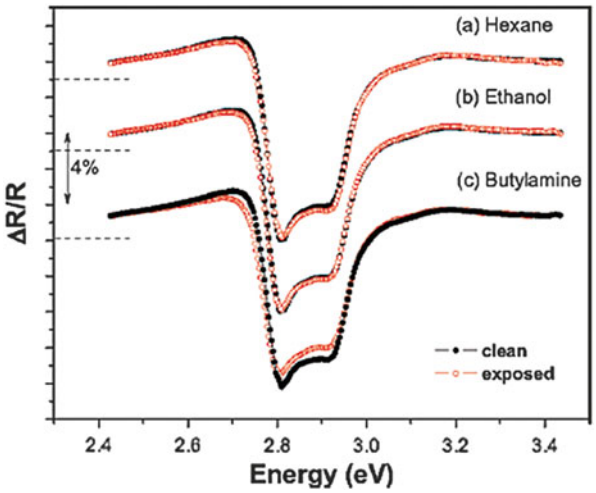

Fig. 42 $\Delta R/R_{\mathrm{RAS}}$ spectra measured on an 8-ML-thick Zn-HepOTTP Langmuir–Blodgett film: (*a*) before (*solid line*, *filled circles*) and after (*dashed line*, *empty circles*) the exposure to hexane vapors (18%); (*b*) before (*solid line*, *filled circles*) and after (*dashed line*, *empty circles*) the exposure to ethanol vapors (18%); (*c*) before (*solid line*, *filled circles*) and after (*dashed line*, *empty circles*) the exposure to butylamine (1%). Each exposure stage was 210 s long. The sign of $\Delta R/R$ has been chosen arbitrarily. Zero lines have been reported for each curve (From Bussetti et al. [88]. Reprinted with permission. Copyright 2011. American Chemical Society.)

in the new experiments, the optical anisotropy modification of an 8-monolayer LB thin film of a 5,10,15,20-tetrakis(4-heptyloxyphenyl) porphyrin (Zn-HepOTTP) was measured, in consequence of the exposure to three different VOCs [88].

It is interesting to mention that the optical anisotropy of the as-grown LB film was almost insensitive to analytes: despite the evident variation of the simultaneously monitored QMB signal (demonstrating the adsorption of VOC molecules on the film), RAS measured a nearly constant signal during exposure. It was necessary to perform a preliminary "activation" of the optical behavior of the layer: all the reported spectra have been recorded after a preliminary exposure of the as-grown film to saturated vapors of ethanol diluted with N_2 carrier gas (70%). After cleaning this activated sample in nitrogen flow, the optical anisotropy (previously inactive) of the LB film exhibited now a high sensitivity to volatile compounds introduced in the cell, comparable to the published LS film case [86]. On the contrary, the adsorption isotherms recorded by QMB before and after activation are identical, proving that further adsorption processes were unaffected by activation. The RAS spectrum for the activated LB film (before exposure to analytes) is reported in Fig. 42. It has a different line shape with respect to the corresponding spectrum of a thicker LS sample of the same porphyrin (see Fig. 40). This result is not surprising: the different film thickness (30 ML vs 8 ML) implies a likely different arrangement of the porphyrin molecules in the sample and, consequently, a different optical anisotropy.

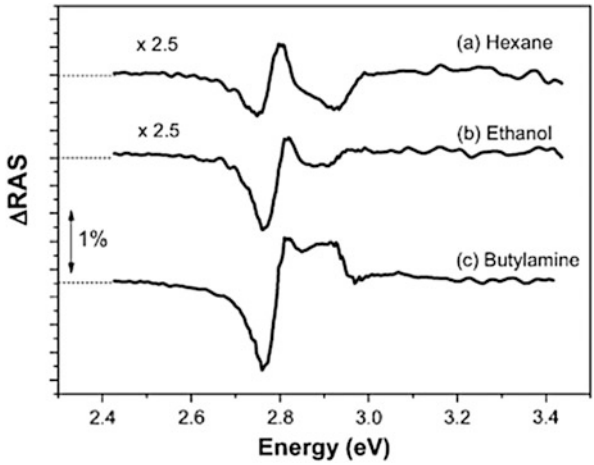

Fig. 43 ΔRAS, defined as the difference $\Delta R/R_{\text{after}} - \Delta R/R_{\text{before}}$ between RAS spectra (reported in Fig. 42) measured before ($\Delta R/R_{\text{before}}$) and after ($\Delta R/R_{\text{after}}$) the exposure of an 8-ML-thick Zn-HepOTTP Langmuir–Blodgett film to (*a*) hexane (18%), (*b*) ethanol (18%), and (*c*) butylamine (1%). ΔRAS values for hexane and ethanol have been multiplied by a factor of 2.5. Zero lines have been reported in all cases (From Bussetti et al. [88]. Reprinted with permission. Copyright 2011. American Chemical Society.)

Figure 42 displays the RAS spectra for the 8-ML-thick LB film before and after the activated sample has been exposed to, respectively, hexane (18%, corresponding to 27,180 ppm, curve a), ethanol (18%, corresponding to 10,656 ppm, curve b), and butylamine (1%, 1,475 ppm, curve c) vapors. The variation produced by adsorption is highlighted by the difference between RAS spectra measured after and before exposure: $\Delta\text{RAS} = \Delta R/R_{\text{after}} - \Delta R/R_{\text{before}}$. The effect of adsorption for the three cases is reported in Fig. 43. The line shape of hexane and ethanol displays a certain similarity: for the reported sign of $\Delta R/R$ (arbitrary choice), there is a sharp minimum at about 2.75 eV and then a maximum at about 2.82 eV, followed by a further broad minimum between 2.85 and 3.00 eV. The two structures at higher photon energies are nearly coincident with $\Delta R/R$ features previously related to, respectively, J-like (2.80 eV) and H-like (2.92 eV) aggregation.

The particular structural complexity of the LB layer, and a certain sample dependence of RAS line shape, hampers a more detailed description of the analyte-porphyrin interaction, but a general overview plus a methodology of investigation is then clearly proposed: a more in-depth study will become possible when a controlled, homogeneous, well-ordered organic system (possibly a single layer) will be studied, although a single monolayer is of low interest for sensing purpose, due to the corresponding low saturation limit. The porphyrin monolayer presented in [36, 73] offers an excellent opportunity to that aim.

The spectra reported in Fig. 43 demonstrate that the different interactions between analyte and porphyrin result in characteristic anisotropy modifications. The optical signature of the interaction is helpful when the film is exposed to

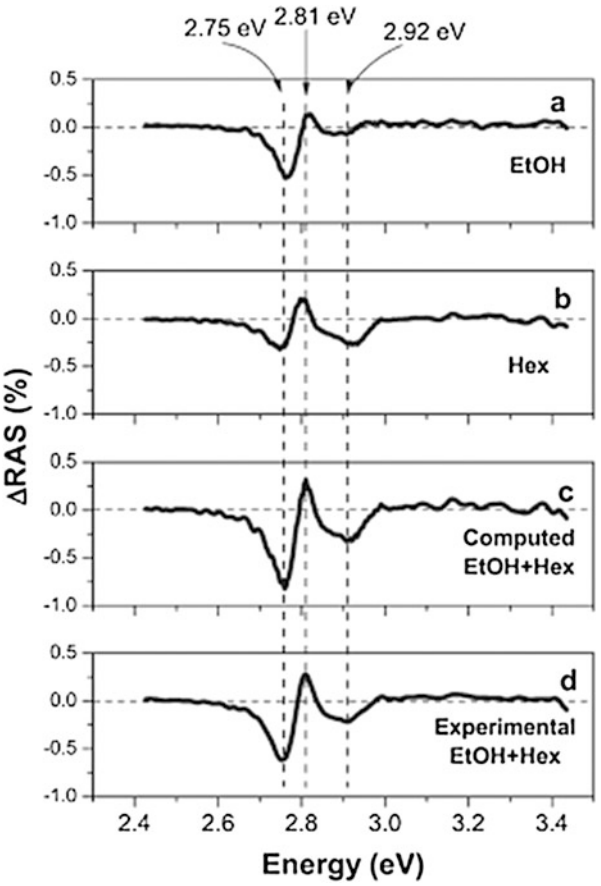

Fig. 44 ΔRAS spectra measured (*panel* **d**) and computed (*panel* **c**) for the exposure of the LB film to a mixture of analytes: A+B (A, ethanol, *panel* **a**; B, hexane, *panel* **b**). The dilution value for both ethanol and hexane was 18%. Zero lines have been reported in all cases (From Bussetti et al. [88]. Reprinted with permission. Copyright 2011. American Chemical Society.)

controlled mixtures of analytes. In particular, the LB film has been exposed to known mixtures of two analytes (hereafter indicated as A and B) in two distinct experiments: (1) analytes A and B were introduced simultaneously in the cell (mixture A+B, spectra reported in Fig. 44), and (2) at a certain time, the inlet of one of two analytes has been interrupted, then exposing the sample only to the residual analyte (spectra reported in Fig. 45). The signal measured during exposure to the mixture A+B (Fig. 44, panel d) is nearly coincident with the computed ΔRAS (Fig. 44, panel c) obtained by summing the single experimental ΔRAS measured separately when the film has been exposed only to A or B (at the same concentration value) (Fig. 44, panels a, b). Then, subtracting ΔRAS_A (for analyte A) from ΔRAS_{A+B} (for mixture A+B) one obtains exactly the signal measured for B only (ΔRAS_B) (Fig. 45). The same happens for the other analyte B, as we demonstrate for ethanol (Fig. 45, panel b) or for hexane (Fig. 45, panel d). The same commutative behavior is not apparent when butylamine enters the mixture. The coordination binding of butylamine to the porphyrin film can be confidently considered the reason of the different influence exhibited by this analyte. This strong interaction in

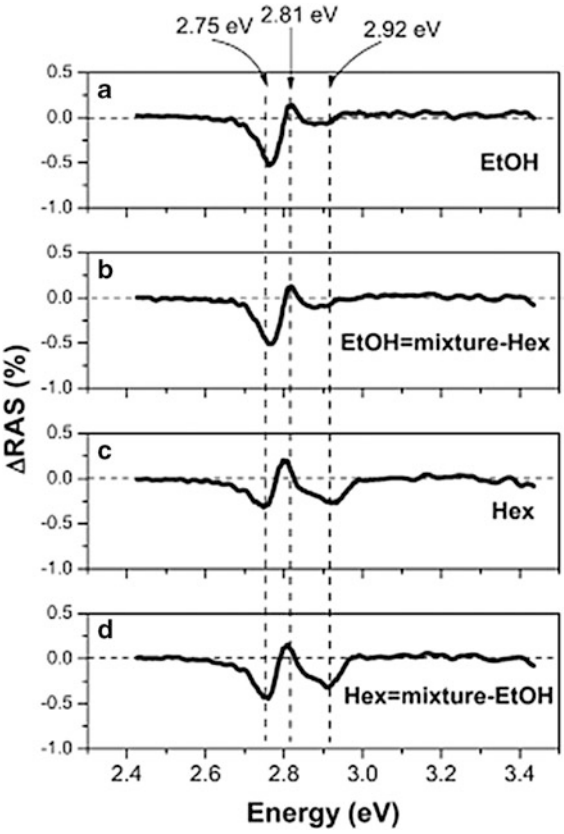

Fig. 45 ΔRAS spectra measured for the exposure of the LB film to a mixture of analytes A and B after the inlet of single analytes (A or B) has been separately interrupted (*panel* **b**, after hexane inlet interruption; *panel* **d**, after ethanol inlet interruption). The RAS spectra of analyte A (ethanol) and analyte B (hexane) are reported, respectively, in *panels* **a** and **c**. The dilution value for both ethanol and hexane was 18%. Zero lines have been reported in all cases (From Bussetti et al. [88]. Reprinted with permission. Copyright 2011. American Chemical Society.)

fact allows butylamine to displace both ethanol and hexane from the porphyrin binding sites, resulting in the nonlinear behavior of ΔRAS spectra variations when the film is exposed to mixtures containing butylamine.

The consequence is significant for sensing applications: measuring the signal of the film for known concentrations of single analytes, the optical anisotropy variations for VOCs could be listed in a sort of analyte library, to deconvolve into single components the complex RAS spectrum measured after the sensor has been exposed to an unknown mixture of those VOCs. More properly, this finding suggests the possibility to discriminate among volatile compounds according to the interaction mechanisms that binds the molecule to the porphyrin layer. In the case illustrated here, for each molecule, a dominant interaction mechanism can be found: dispersion interaction for hexane and coordination for ethanol. It is important to remark that in many other volatile compounds, more than one interaction mechanism can coexist: the study of the RAS signal in these situations will be the subject of successive investigations.

5 Conclusion

I have reviewed results obtained by monitoring the optical anisotropies of thin and ultrathin layers of porphyrins deposited via different methods onto solid substrates (Langmuir–Blodgett and Langmuir–Schaefer deposition, sublimation in vacuum). Spectra measured by RAS have been discussed and interpreted in terms of the morphological characteristics of the layer, occurring at different thickness and depending upon the deposition method as well as parameters like the substrate or its temperature. These results show the potential of RAS to characterize efficiently the deposition of organics, suggesting its use as an in situ and real-time spectroscopy to monitor the process, as already done in inorganic growth. This knowledge could have a significant application in optical gas sensors: despite the complexity of the interaction between the layer and gas molecules, analysis of the RAS signal could offer a way for single analyte recognition by an appropriate deconvolution of the experimental anisotropy readout.

Acknowledgments After the overview of about 15 years of investigations on the optical anisotropy of thin and ultrathin layers of porphyrins, since the very early tests on samples taken from the laboratory of R. Paolesse, I wish to acknowledge the collaboration with several colleagues and students, with whom I have shared ideas, discussions, experiments, enthusiasm, and – sometimes – delusion. A special thanks to M. Drago, G. Bussetti, A. Violante, R. Paolesse, C. Di Natale, P. Chiaradia, and A. Sassella. Finally, my sincere gratitude to G. Chiarotti, from whom I learned how to be an honest and (hopefully) decent experimentalist.

References

1. Kadish KM, Smith KM, Guilard R (eds) (2010) Handbook of porphyrin science, vol 12, Applications. World Scientific, Singapore
2. Harvey PD (2003) Recent advances in free and metalated multi-porphyrin assemblies and arrays; a photophysical behavior and energy transfer perspective. In: Kadish KM, Smith KM, Guilard R (eds) Handbook of porphyrins and phthalocyanines. Elsevier, Amsterdam, pp 63–249, Chapt. 113
3. Pemble ME, Turner AR, Shukla N, Bitzer T, Frederick BG, Kitching KJ, Richardson NV (1995) J Chem Soc Faraday Trans 91:3627
4. Chiaradia P, Del Sole R (1999) Differential-reflectance spectroscopy and reflectance-anisotropy spectroscopy on semiconductor surfaces. Surf Rev Lett 6:517–552
5. Forrest SR (1997) Chem Rev 97:1793
6. Forrest R, Burrows PE, Haskal EI, So FF (1994) Ultrahigh-vacuum quasiepitaxial growth of model van der Waals thin films. II. Experiment. Phys Rev B 49:11309
7. Azzam RMA, Bashara NM (1977) Ellipsometry and polarized light. North Holland, Amsterdam
8. Pickering C (1998) Thin Solid Films 313–314, 406–415
9. Kampen TU, Paraian AM, Rossow U, Park S, Salvan G, Wagner TH, Friedrich M, Zahn DT (2001) Phys Status Solidi A 188:1307
10. Tsankov D, Hinrichs K, Roseler A, Korte EH (2001) Phys Status Solidi A 188:1319

11. Pop DS, Kate SP, Rappich J, Hinrichs K (2014) Tunable optical constants of thermally grown thin porphyrin films on silicon for photovoltaic applications, Solar energy materials and solar cells 127: 169–173
12. LoSurdo M, Hingerl K (eds) (2013) Ellipsometry at the nanoscale. Springer, Berlin
13. Selci S, Ciccacci F, Chiarotti G, Chiaradia P, Cricenti A (1987) Surface differential reflectivity spectroscopy of semiconductor surfaces. J Vac Sci Technol A 5:327
14. Selci S, Cricenti A, Felici AC, Ferrari L, Goletti C, Chiarotti G (1991) Oxygen chemisorption on cleaved InP(110) surfaces studied with surface differential reflectivity. Phys Rev B 43:6757
15. Wooten F (1972) Optical properties of solids. Academic Press, New York
16. Proehl H, Dienel T, Nitsche R, Fritz T (2004) Formation of solid-state excitons in ultrathin crystalline films of PTCDA: from single molecules to molecular stacks. Phys Rev Lett 93:097403
17. Forker R, Dienel T, Fritz T, Müllen K (2006) Optical evidence for substrate-induced growth of ultrathin hexa-peri-hexabenzocoronene films on highly oriented pyrolytic graphite. Phys Rev B 74:165410
18. Weightman P, Martin DS, Cole RJ, Farrell T (2005) Reflection anisotropy spectroscopy. Rep Prog Phys 68:1251
19. Goletti C, Bussetti G, Chiaradia P, Sassella A, Borghesi A (2004) In situ optical investigation of oligothiophene layers grown by organic molecular beam epitaxy. J Phys Condens Matter 16: S4393–S4402
20. Bussetti G, Goletti C, Chiaradia P, Derry T (2007) Optical gap between dangling-bond states of a single-domain diamond C (111)-2× 1 by reflectance anisotropy spectroscopy. Europhys Lett 79:57002
21. Bussetti G, Goletti C, Violante A, Chiaradia P, Derry T (2009) The 2× 1-reconstructed cleavage surface of diamond: a challenging test for experiment and theory. Superlattices Microstruct 46:227–233
22. Mantese L, Bell KA, Rossow U, Aspnes DE (1997) J Vac Sci Technol B 15:1196
23. Bell KA, Mantese L, Rossow U, Aspnes DE (1997) J Vac Sci Technol B 15:1205
24. Sassella A, Borghesi A, Wagner TH, Hilfiker J (2001) J Appl Phys 90:3838
25. Goletti C, Bussetti G, Chiaradia P, Sassella A, Borghesi A (2003) Appl Phys Lett 83:4146–4148
26. Sassella A, Campione M, Moret M, Borghesi A, Goletti C, Bussetti G, Chiaradia P (2005) Phys Rev B 71:201311–1
27. Laicini M, Spearman P, Tavazzi S, Borghesi A (2005) Phys Rev B 71:045212
28. Aspnes DE, Harbison JP, Studna AA, Florez LT (1987) Phys Rev Lett 59:1687
29. Berkovits VI, Kiselev VA, Safarov VI (1989) Surf Sci 211–212:489
30. Salvati A, Chiaradia P (2000) Appl Opt 39:5820
31. Goletti C, Bussetti G, Chiaradia P, Sassella A, Borghesi A (2004) The application of reflectance anisotropy spectroscopy to organics deposition. Org Electron 5:73–81
32. Di Natale C, Goletti C, Paolesse R, Della SF, Drago M, Chiaradia P (2000) Optical anisotropy of Langmuir–Blodgett sapphyrin films. Appl Phys Lett 77(20):3164–3166
33. Kemp JC (1969) J Opt Soc Am 59:950, http://www.hindspem.com
34. Roberts G (ed) (1990) Langmuir-Blodgett films. Plenum, New York
35. Ulman A (1991) An introduction to ultrathin, organic films—From Langmuir–Blodgett to self-assembly. Academic, New York
36. Bussetti G, Campione M, Riva M, Picone A, Raimondo L, Ferraro L, Hogan C, Palummo M, Brambilla A, Finazzi M, Duò L, Sassella A, Ciccacci F (2014) Stable alignment of tautomers at room temperature in porphyrin 2D layers. Adv Funct Mat 24:957
37. McIntyre JDE, Aspnes DE (1971) Surf Sci 6:4370
38. Goletti C, Bussetti G, Arciprete F, Chiaradia P, Chiarotti G (2002) Infrared surface absorption in Si(111)2×1 observed with reflectance anisotropy spectroscopy. Phys Rev B 66:153307
39. Harrison P, Farrell T, Maunder A, Smith CI, Weightman P (2001) A rapid reflectance anisotropy spectrometer. Meas Sci Technol 12:2185–2191

40. Richter W (1993) Philos Trans R Soc Lond A 344:453
41. Mansley CP, Farrell T, Smith CI, Harrison P, Bowfield A, Weightman P (2009) A new UV reflection anisotropy spectrometer and its application to the Au(1 1 0)/electrolyte surface. J Phys D Appl Phys 42:115303 (5pp)
42. Johnson RL, Barth J, Cardona M, Fuchs D, Bradshaw AM (1989) Spectroscopic ellipsometry with synchrotron radiation. Rev Sci Instrum 60:2209
43. Wethkamp T, Wilmers K, Esser N, Richter W, Ambacher O, Angerer H, Jungk G, Johnson RL, Cardona M (1998) Thin Solid Films 313:745
44. Hogan C, Ferraro E, McAlinden N, McGilp JF (2013) Phys Rev Lett 111:087401
45. Fazi L, Hogan C, Persichetti L, Goletti C, Palummo M, Sgarlata A, Balzarotti A (2013) Intermixing and buried interfacial structure in strained Ge/Si(105) facets. Phys Rev B 88:195312
46. Riefer A, Rauls E, Schmidt WG, Eberhard J, Stoll I, Mattay J (2012) 2-Aminopyrimidine-silver(I) based organic semiconductors: Electronic structure and optical response. Phys Rev B 85:165202
47. Palik ED (1998) Handbook of optical constants of solids. Academic, USA
48. Esser N, Schmidt WG, Cobet C, Fleischer K, Shkrebtii AI, Richter W (2001) Atomic structure and optical anisotropy of III-V(001) surfaces. J Vac Sci Technol B 19:1756
49. Goletti C, Arciprete F, Almaviva S, Chiaradia P, Esser N, Richter W (2001) Analysis of InAs (001) surfaces by reflectance anisotropy spectroscopy. Phys Rev B 64:193301
50. Frederick BG, Power JR, Cole RJ, Perry CC, Chen Q, Haq S, Bertrams T, Richardson NV, Weightman P (1998) Adsorbate azimuthal orientation from reflectance anisotropy spectroscopy. Phys Rev Lett 80:4490–4493
51. Goletti C, Sgarlata A, Motta N, Chiaradia P, Paolesse R, Angelaccio A, Drago M, Di Natale C, D'Amico A, Cocco M, Troitsky V (1999) Kelvin probe and scanning tunneling microscope characterization of Langmuir–Blodgett sapphyrin films. Appl Phys Lett 75:1237–1239
52. Goletti C, Bussetti G, Chiaradia P, Paolesse R, Di Natale C, Mazzone E, D'Amico A (2001) A reflectance anisotropy spectroscopy investigation of porphyrin langmuir-blodgett films. Phys Status Solidi A 188:1339–1344
53. Goletti C, Paolesse R, Di Natale C, Bussetti G, Chiaradia P, Froiio A, Valli L, D'Amico A (2002) Optical anisotropy of porphyrin Langmuir–Blodgett films. Surf Sci 501:31–36
54. Schick GA, Schreiman IC, Wagner RW, Lindsey JS, Bocian DF (1989) J Am Chem Soc 111:1344
55. Huang X, Nakanishi K, Berova N (2000) Chirality 12:237
56. Hunter CA, Sanders JMK, Stone A (1989) Chem Phys 133:395
57. van Esch JH, Feiters MC, Peters AM, Nolte RJM (1994) J Phys Chem 98:5541
58. Johnson PB, Christy RW (1972) Phys Rev B 6:4370
59. Goletti C, Paolesse R, Dalcanale E, Berzina T, Di Natale C, Bussetti G, Chiaradia P, Froiio A, Cristofolini L, Costa M, D'Amico A (2002) Thickness dependence of the optical anisotropy for porphyrin octaester Langmuir-Schaefer films. Langmuir 18:6881–6886
60. Miller EK, Hingerl K, Brabec CJ, Heeger AJ, Sariciftici NS (2000) J Chem Phys 113:789
61. Facci P, Fontana MP, Dalcanale E, Costa M, Sacchelli T (2000) Langmuir 16:7726
62. Cristofolini L, Arisi S, Fontana MP (2000) Phys Rev Lett 85:4912
63. Della SF, Widany J, Frauenheim T (2000) Phys Status Solidi B 217:565
64. DeMaggio GB, Frieze WE, Gidley DW, Zhu M, Hristov HA, Yee AF (1997) Phys Rev Lett 78:1524
65. Fukao K, Miyamoto Y (2000) Phys Rev E 61:1743
66. Paganuzzi V, Guatteri P, Riccard P, Sacchelli T, Barbera J, Costa M, Dalcanale E (1999) Eur J Org Chem 1527
67. Mendoza BS, Vázquez-Nava RA (2005) Model for reflectance anisotropy spectra of molecular layered systems. Phys Rev B 72:035411
68. Arzate N, Mendoza BS, Vázquez-Nava RA (2004) J Phys Condens Matter 16:S4259

69. Scarselli M, Ercolani G, Castrucci P, Monti D, Bussetti G, Russo M, Goletti C, Chiaradia P, Paolesse R, De Crescenzi M (2007) A combined scanning tunneling microscopy and reflectance anisotropy spectroscopy investigation of tetraphenylporphyrin deposited on graphite. Surf Sci 601:2607–2610
70. Zou Z-Q, Wei L, Chen F, Liu Z, Thamyongkit P, Loewe RS, Lindsey JS, Mohideen U, Bocian DFJ (2005) Porphyrins Phthalocyanines 9:387
71. Khairutdinov RF, Serpone N (1999) J Phys Chem B 103:761
72. Scarselli M, Castrucci P, Monti D, De Crescenzi M (2007) Studies of the adsorption of tetraphenylporphyrin molecules on graphite. Surf Sci 601:5526–5532
73. Bussetti G, Campione M, Ferraro L, Raimondo L, Bonanni B, Goletti C, Palummo M, Hogan C, Duò L, Finazzi M, Sassella A (2014) Probing two-dimensional vs three-dimensional molecular aggregation in metal-free tetraphenylporphyrin thin films by optical anisotropy. J Phys Chem C 118:15649–15655
74. De Luca G, Treossi E, Liscio A, Mativetsky JM, Monsù SL, Palermo V, Samorì P (2010) Solvent vapour annealing of organic thin films: controlling the self-assembly of functional systems across multiple length scales. J Mater Chem 20:2493–2498
75. Bassiouk M, Álvarez-Zauco E, Basiuk VA (2011) J Nanosci Nanotechnol 11:5457
76. Sadegh Hassani S, Kim Y-G, Borguet E (2011) Langmuir 27:14828
77. Teugels LG, Avila-Bront LG, Sibener SJ (2011) J Phys Chem C 115:2826
78. Friesen BA, Wiggins B, McHale JL, Mazur U, Hipps KW (2010) J Am Chem Soc 132:8554
79. Onsager L (1944) Phys Rev 65:117
80. Gouterman M (1978) The Porphyrins, vol 3. Academic, New York
81. Bussetti G, Campione M, Raimondo L, Yivlialin R, Finazzi M, Ciccacci F, Sassella A, Duò L (2014) Unconventional post-deposition chemical treatment on ultra-thin H_2TPP film grown on graphite. Cryst Res Tech, doi: 10.1002/crat.201300406
82. De Luca G, Romeo A, Monsù Scolaro R, Ricciardi G, Rosa A (2007) Evidence of tetraphenylporphyrin monoacids. Inorg Chem 46:5979–5988
83. Palummo M et al (2009) Ab initio electronic and optical spectra of free-base porphyrins: the role of electronic correlation. J Chem Phys 131:084102(1)–084102(7)
84. Bussetti G, Corradini C, Goletti C, Chiaradia P, Russo M, Paolesse R, Di Natale C, D'Amico A, Valli L (2005) Phys Status Solidi B 242:2714
85. Richardson TH, Dooling CM, Worsfold O, Jones LT, Kato K, Shinbo K, Kaneko F, Tregonning R, Vysotsky MO, Hunter CA (2002) Colloids Surf A 198:843
86. Bussetti G, Cirilli S, Violante A, Chiaradia P, Goletti C, Tortora L, Paolesse R, Martinelli E, D'Amico A, Di Natale C, Giancane G, Valli L (2009) Optical anisotropy readout in solid-state porphyrins for the detection of volatile compounds. Appl Phys Lett 95:091906
87. Paolesse R, Di Natale C, Macagnano A, Sagone F, Boschi T, Scarsell M, Chiaradia P, Troitsky VI, Berzina TS, D'Amico A (1999) Langmuir 15:1268
88. Bussetti G, Violante A, Yivlialin R, Cirilli S, Bonanni B, Chiaradia P, Goletti C, Tortora L, Paolesse R, Martinelli E, D'Amico A, Di Natale C, Giancane G, Valli L (2011) Site-sensitive gas sensing and analyte discrimination in Langmuir− Blodgett porphyrin films. J Phys Chem C 115(16):8189–8194

Top Heterocycl Chem (2014) 34: 117–138
DOI: 10.1007/7081_2014_133

Published online: 3 August 2014

Langmuir–Blodgett Films of Porphyrins for Applications in Photovoltaics

Simona Bettini, Ludovico Valli, and Gabriele Giancane

Abstract The use of organic materials in the realization of devices for the conversion of solar energy is a hot topic in chemistry, physics, and material science since many years. While the attention is strongly paid toward the synthesis and engineering of new molecules with adequate chemical and physical properties, such materials have to be transferred onto solid substrates, in order to construct functioning devices with high reproducibility and optimizing the performances. Then, deposition technique plays a paramount role in the realization of a photovoltaic device. Moreover, photoactive thin films are often carried out by multilayer stacks with a high spatial organization, and this observation prompted out many researchers to use layer-by-layer, Langmuir–Blodgett (LB), or Langmuir–Schaefer (LS) methods as deposition techniques for the fabrication of such devices. One of the most used class of substances for depositing LB or LS thin films is represented by the porphyrin derivatives whose filmability features can be improved by means of chemical functionalization or by the co-spreading of filmmaker molecules such as octadecylamine or arachidic acid. Furthermore, porphyrins show a very high light harvesting, and they are well-known electron donors, as it happens in the photosynthesis process. In this chapter, several examples of LB and LS film of porphyrin derivatives both used for the realization of photovoltaic devices and for studying the charge transfer processes have been reported.

Keywords Fullerenes · Langmuir–Blodgett films · Langmuir–Schaefer films · Photovoltaics · Porphyrins

S. Bettini and L. Valli (✉)
Dipartimento di Scienze e Tecnologie Biologiche ed Ambientali, Università del Salento, 73100 Lecce, Italy
e-mail: ludovico.valli@unisalento.it

G. Giancane
Dipartimento di Beni Culturali, Università del Salento, 73100 Lecce, Italy

Contents

1 Principles of Solar Energy Conversion in Organic Active Layers

The processes that rule the mechanisms leading to the production of electrical energy from light in organic photovoltaic cells start from the absorption of a photon with appropriate energy, which promotes an electron transition toward an excited state (Fig. 1). This quasiparticle, made of a hole (h^+) and an electron (e^-) electrostatically bounded, is called exciton [1], and it diffuses into the material where it is generated. The couple h^+-e^- can recombine wasting the photon absorption, or if the diffusion length is long enough to allow the exciton to meet an internal field, represented, for example, by the interface between a donor element (D) and an acceptor one (A) [2], it can separate in two free charges that move toward the electrodes.

The following reactions can be used to summarize the above-described phenomena:

$$D + A \xrightarrow{h\nu} D^* + A \tag{1}$$

$$D^* + A \rightarrow D^{+^\circ} + A^{-^\circ} \tag{2}$$

The generation of electron–hole pairs takes place from π-HOMO to π*-LUMO band of the p-type [3] donor material. The electron transfer from the donor element to the LUMO of the acceptor generates the excited, but still neutral exciton with an e^--h^+ coupling energy smaller than the energy gap. Then, the exciton can diffuse up to meet the internal field generated at the donor-acceptor interface, and exciton separation occurs. The carriers are, then, transported toward the electrodes, and during the pathway, they can be trapped by defects of the organic matrices. In light of this, the transfer method used to obtain an adequate phase separation and an ordered film appears crucial to optimize the efficiency of an organic photovoltaic device [4].

Furthermore, the thickness of the organic layer should be thick enough to ensure a high photon absorption and should be thin enough to allow a high interface where excitons can dissociate.

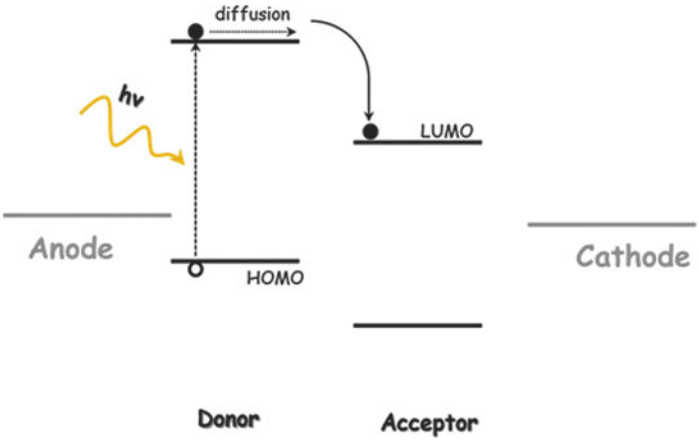

Fig. 1 Schematic representation of the charge transfer mechanism in an organic photovoltaic device

Finally, the separated charges are collected at the respective electrodes and injected in the electrical circuit.

The efficiency of the conversion of solar energy in electric energy depends, of course, on the energetic matching between the electron donor species and the acceptor one, but it is also strongly influenced by the charge transport efficiency that can worsen the device performance, especially for the fully organic solar cells. The presence of an unorganized matrix, where the electron donor species is interfaced with the electron acceptor element without a molecular control, may induce the formation of aggregates that strongly reduce the molecular interface. The separation of excitons can take place at the interface between the acceptor and donor elements, and then the formation of aggregates of same species reduces the possibility of charge separation with a consequent recombination of the excited state.

On the other hand, some of the most employed techniques for organic materials devices, such as drop casting or spin coating, induce the formation of highly disordered film, with low control of deposition parameters. Electron donor, electron acceptor species, and not-deposited regions are simultaneously present in the organic film. In such a scenario, charge recombination is highly probable for the presence in the same region of electron donor and acceptor materials; furthermore, not-uniform covering of the electrodes by the photo actives species can be think as the presence of potential walls impossible to be overcome with consequent loss of the separated charge state.

To avoid this situation, several deposition methods employ materials with self-assembling properties and also compounds with high spatial anisotropy, such as carbon nanotubes. Among the most efficient deposition techniques used to transfer organized photoactive organic layers, there are the molecular organic chemical vapor deposition, the molecular beam epitaxy, and the thermal evaporation. These

methods allow a precise molecular control during the transfer process, but they are extremely expensive and time-consuming. These reasons induced many researchers to direct their attention toward less expensive methods that ensure a good control of deposition parameters such as layer-by-layer (LbL), Langmuir–Blodgett [5] (LB), and Langmuir–Schaefer (LS) techniques [6].

2 Optimization of Photovoltaic Features of Langmuir–Blodgett Porphyrin Films

Photochemical and photophysical features of a photovoltaic material strongly depend on the molecular aggregation in the solid film. As largely reported in the literature, porphyrinoid Langmuir film formation is deeply influenced by the substituents on the macrocycle periphery [7, 8], and the molecular aggregation of the floating film can be managed by means of substances used as spacers and film promoters such as arachidic acid [9, 10] or octadecylamine [11].

A precisely defined packing of the chromophores is crucial to obtain an optimal exciton behavior; indeed, many approaches were used to investigate the optical and photochemical characteristics of the deposited thin porphyrinoid films [12], the role played by the defects residing in an LB film [13] or the influence of the spacer substances on the photovoltaic characteristics of the deposited porphyrinoid layers. For example, aggregation state drastically modifies the photovoltaic responses of hemin in solid LB film both of the pure macrocyclic species and in co-spread with *n*-octadecylamine [14]. H-aggregate generation in the thin film totally quenches the photovoltaic response of the deposited layer as a consequence of the interaction between the chromophores, affecting one of the most crucial features of a photovoltaic active layer, that is, the transport efficiency of photoinduced charge carriers. In order to prevent such a detrimental phenomenon, not only co-spread of spacing amphiphilic molecules and photoactive species was carried out but even polymers with amphiphilic properties were attached by covalent bonds to the porphyrin moiety [15]. Such an approach often allowed to deposit an LB film of almost monomeric domains, even if it does not necessarily involve an electronic isolation between adjacent domains. Indeed, weak interactions not detectable in the UV–vis spectra are strong enough to quench the steady-state fluorescence of the solid film, and the rare aggregates work as intermolecular and intramolecular energy and electron acceptors.

In place of or besides spacers and film promoter molecules able to influence the electronic features of the porphyrins and their derivative compounds, chemical species able to accept electrons from the exciton dissociation are used. The most employed electron acceptors are represented by the fullerene derivatives and carbon nanotubes, even though other relevant examples of electron acceptors are reported in the literature. In the next paragraphs, dyads, triads, and multilayered films of

porphyrinoids as electron donor will be reported in relation to the chemical species used as electron acceptor.

3 Fullerene Derivative-Based Solar Cells

One of the most used approaches in order to link an electron donor to an acceptor is the covalent bonding. Such a method allows to manage the distance between two species and offers also the chance to change the electric properties of the linker. On the other hand, the modifications induced in the chemical structure of the two linked elements to form the donor-bridge-acceptor species can be relevant for the physical and chemical features of the two compounds. Therefore, supramolecular approaches have been proposed to induce the formation of photoactive dyads (or triads). Electrostatic attraction has been used as the driving force to assemble a film of a four-charged anionic porphyrin ($TPPS_4$) and a fulleropyrrolidine derivative [16]. Negatively charged porphyrin was dissolved in the aqueous subphase, and a chloroform solution of the positively functionalized charged fulleropyrrolidine was spread at the air-water interface (in Fig. 2, the chemical structures of the two species are reported).

The electrostatic interaction between the water-soluble porphyrin and the floating film was monitored by means of the reflection spectroscopy, Langmuir curves, and Brewster Angle Microscopy (BAM). Reflection spectroscopy gives information about the chromophores at the interface: reflection variations of the bare subphase are correlated to the absorption spectrum of the spread molecules [17]. Therefore, the presence of the absorption band at 430 nm, imputable to the Soret band of the porphyrin derivative, clearly suggested that the water dissolved species reaches the interface by means of the electrostatic interaction (Fig. 3).

The electrostatic interaction is strong enough to ensure the transfer of the dyad onto ITO substrate by the Langmuir–Schaefer method.

In order to improve the interaction between the water dissolved molecules and the species spread on the subphase, a twofold charged functionalized fulleropyrrolidine was used (Fig. 4). Photoaction spectra of the LS films show a spectral profile very similar to the porphyrin LS film UV–vis absorption, confirming that the tetrapyrrole derivative was transferred on the ITO slide and suggesting the electron donor attitude of the derivatized porphyrin. Photoactivity of the LS film was highlighted by the current–voltage characterization that pointed out that the primary electron acceptor, the fullerene derivative, is placed onto the ITO, while the electron donor is in a remote position relative to the ITO electrode.

A C_{60} derivative with an imidazole ligand was used to form a supramolecular dyad with a water-soluble Zn porphyrin derivative (Fig. 5) [18]. The axial coordination between the metal ion of the porphyrin and the imidazole substituent of the fullerene derivative allowed the generation of a supramolecular dyad at the air-water interface that was transferred on an ITO substrate by the LB technique. Changing the transfer procedure, the authors managed, as they demonstrated by JV

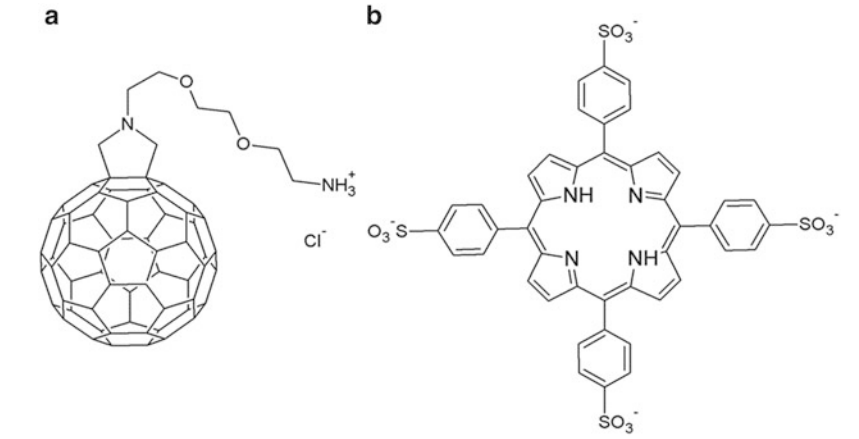

Fig. 2 Chemical structures of the porphyrin derivative (**a**) and functionalized fulleropyrrolidine (**b**) used to assemble an electrostatically bounded photoactive dyad used in [16]

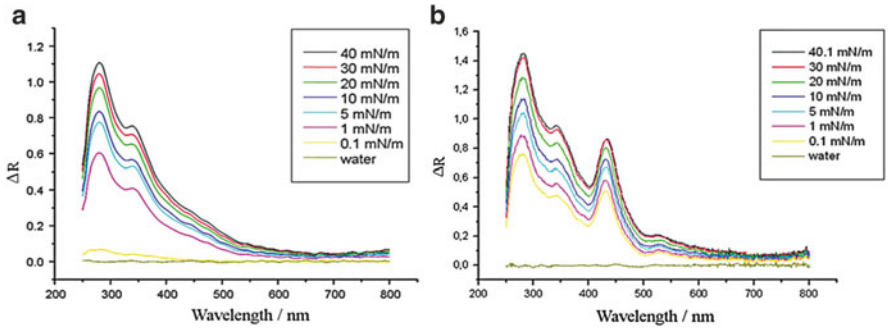

Fig. 3 Reflection spectra at increasing values of surface pressure of charged fulleropyrrolidine (**a**) and $TPPS_4$/charged fulleropyrrolidine at the air-water interface (**b**) (from [17])

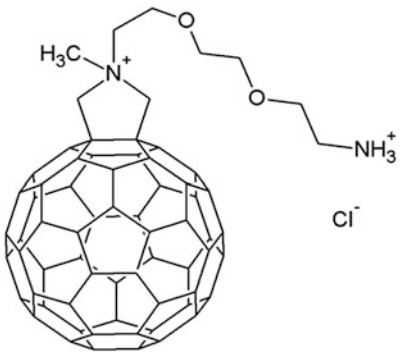

Fig. 4 Double cationic fulleropyrrolidine chemical structure

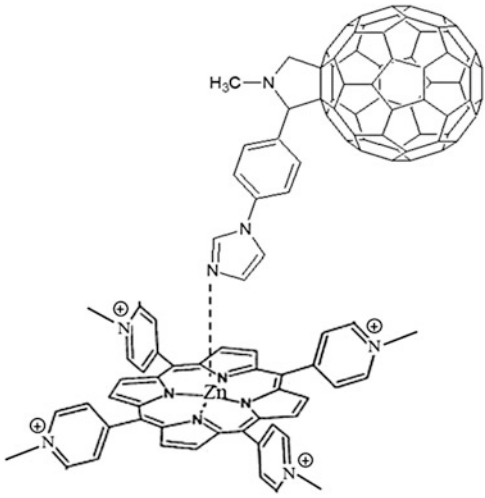

Fig. 5 The fulleropyrrolidine derivative used in [18] to chelate the Zn hydrosoluble porphyrin derivative

curves, the sequence of the donor and acceptor element placed on the substrate: when the deposition started withdrawing the ITO substrates up from the subphase, an ITO/electron donor/electron acceptor layered film was obtained, on the contrary when the semiconducting substrate was immersed through the subphase, the fullerene derivative was located in proximity of the ITO interface. The relative position of the two compounds with respect to the ITO interface strongly influenced the photoelectric behavior, revealing photocathodic response when the Zn porphyrin derivative was placed on the ITO surface and photoanodic features with better response when the fullerene derivative was in direct contact with the ITO electrode.

4 Covalently Bonded Dyads and Triads

Functionalization of species with electron donor and electron acceptor features is largely reported in the literature [19]. It is a very powerful method to manage, optimize, and implement some physical and chemical characteristics either of the single compound or of the whole system. For example, the distance between the electron donor and the electron acceptor elements plays a crucial role in the lifetime of the exciton and in the formation of the charge separated state [20–22]; furthermore, the electrical characteristics of the bridge between A and D can assist the charge transport, or it can simply work as a spacer [23].

A pyridine bridge was used to link a functionalized fulleropyrrolidine and a ruthenium porphyrin derivative [20]. A –C≡O ligand was attached to the porphyrin central metal atom, and an *n*-heptoxyl substituent was directly attached to the fulleropyrrolidine (Fig. 6) in order to improve the amphiphilic feature to the dyad.

Even if functionalized, such kind of compounds form large aggregates both in the floating layer and in solid LB films. For this reason, spacer molecules, such as

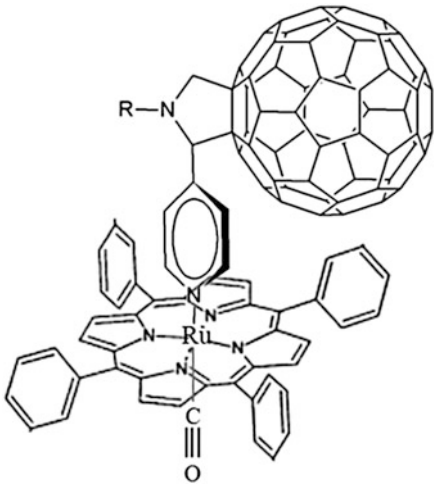

Fig. 6 Photoactive dyad obtained by covalent bonding of Ruthenium porphyrin derivative with amphiphilic features and a fulleropyrrolidine

octadecylamine (ODA) and arachidic acid (AA), are often co-spread together with the photoactive species. This approach prevents the rapid annihilation between the triplet porphyrin state and the fulleropyrrolidine that governs the fate of the excited state in the dyad ruthenium porphyrin derivative-bridge-fulleropyrrolidine. The isotherm curves of the AA/donor-acceptor co-spread floating film reported in Fig. 6 suggested that the dyad molecules were gradually squeezed out of the acid monolayer as a consequence of the barrier pressure. The LB deposition was repeated on different substrates, and a Y-type transfer was ever obtained; the thickness of the solid film confirmed a uniform dispersion of dyad molecules in the cadmium arachidate matrix. The dyad molecules were adequately separated from each other, and electron and energy transfer from the excited state of ruthenium functionalized porphyrin toward the acceptor element took place as pointed out by the transient absorption spectrophotometry.

In many cases, the strong π–π interactions between porphyrins and fullerenes induce the formation of a very rigid floating film that cannot be transferred by the LB method; hence, it is generally substituted by its horizontal variation, which is the Langmuir–Schaefer (LS) technique [6]. A covalent bonded C_{60}-Ni porphyrin dyad (Fig. 7) was transferred by means of the LS method, and the efficiency of the solar cell was compared with a layer-by-layer (LbL) C_{60}-Ni porphyrin photo-device [20]. More packed films and the preferential arrangement of the molecules of the dyad induced by the LS technique allowed to reach a double efficiency if compared to LbL device, highlighting the role of the deposition technique in the performance of a solar cell.

Tkachenco et al. used octadecylamine as well as a spacer and insulator layer [23]: they demonstrated that when a fulleropyrrolidine and a porphyrin bounded with a long linker were transferred by Y-type LB method, dyads of different layers were in close contact to each other, and intermolecular energy transfer between

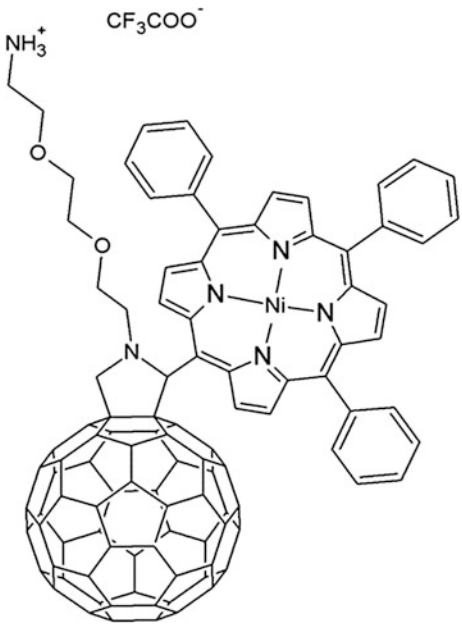

Fig. 7 Fullerene/nickel porphyrin dyad with a positive charge located on the fulleropyrrolidine for LB and LbL depositions

molecules in adjacent layers influenced the photoresponse. Intermediate ODA layers were deposited between donor–acceptor layers, and it was estimated that octadecylamine forced the molecules to a distance of 8 Å that is still too short for an optimized solar device.

The possibility to form "directionally" arranged photoactive films is a very appealing issue for solar organic device, and LB technique is ideal for assembling highly oriented layers. Particularly, as proposed in many studies [24–29], the functionalization of a covalent-bounded fullerene-porphyrin system allows to assemble molecular wires with a tight spatial alignment. Charvet and coworkers [24] used a substituent with a relatively flat unit with a hydrophilic terminal triethylene glycol chains, while C_{60} acted as a hydrophobic head (Fig. 8).

Highly efficient photoinduced electron transfer between the porphyrin moiety and the C_{60} was monitored by means of the fluorescence quenching. The photocurrent induced by a white lamp (30 mW/cm^2 illumination flux) was about 15 Å. The chemical functionalization in combination with the supramolecular packing induced by the LB technique leads to build a very promising photoconductive device.

With this aim, porphyrin–fullerene dyads covalently linked were functionalized with molecular chains with different properties. Changing the hydrophilic and hydrophobic features of the attached functionalizations (see Fig. 9a, c), it is possible to alternate the orientation of the molecules in opposite directions with respect to the air-water interface [25].

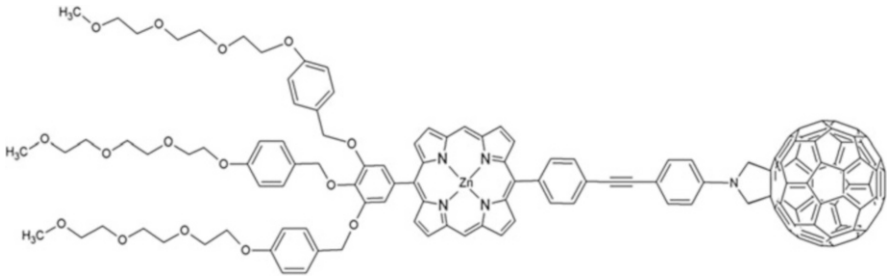

Fig. 8 Structure of zinc porphyrin–fullerene dyad used in [24]

For these molecules, octadecylamine was used as the film formation promoter, and it was demonstrated that LB deposition induces the generation of J aggregates, as measured by means of UV–vis spectroscopy. The relative position of the hydrophilic groups of the donor-acceptor molecules allowed to transfer the dyads without any variation in the orientation, and the charge recombination in the dyads in Fig. 9a, b occurred only in one definite direction, unlike what happened in the dyads in Fig. 9c, d where the recombination process took place in all directions.

Managing the direction of charge transfer and charge recombination, the efficiency of the photovoltaic device can be improved, since such an approach makes possible to reduce the charge-trapping and exciton recombination.

4.1 Role of the Interlayer in the Kinetics of Photoinduced Electron Transfer in LB Films

In addition to the preparation of porphyrin–fullerene monolayers, LB method was used to deposit one or more semiconducting organic interlayers. Lemmetyinen and coworkers reported many examples of such device architecture, with the aim to obtain long-living charge separated states. The well-known poly(3-hexylthiophene) (P_3HT) was used as interlayer in porphyrin–fullerene covalent dyads aligned according to the strategy reported in the previous paragraph. Lifetimes of porphyrin–fullerene LB film and porphyrin–fullerene/P_3HT LB layer were compared by means of transient absorption [26]. The observations carried out by flash photolysis measurements demonstrated an electron transfer from the polymer layer to the porphyrin–fullerene LB film and a final transient state with a positive charge on P_3HT and the negative one on the fullerene moiety of the covalently bounded dyad. The lifetime of the interlayer is about 150 μs, an order of magnitude longer than that of the porphyrin–fullerene monolayer.

The longer distance between the separated charges reduces the charge recombination process, and a longer living charge separated state was observed for the triad if compared with the dyad. The study of the action spectra of the triad showed a well-pronounced Soret band, although a very low absorption in correspondence of the P_3HT absorption was observed [27]. Such a phenomenon demonstrated that the

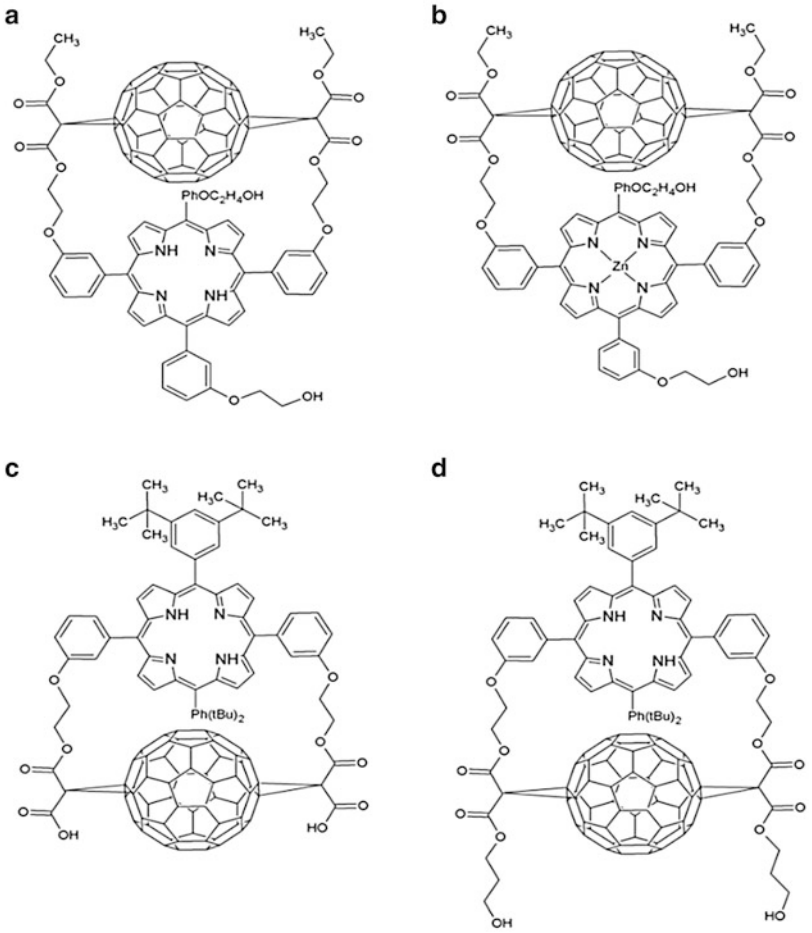

Fig. 9 Structures of porphyrin–fullerene dyads used to obtain a directional charge transfer in the LB photoactive films (**a**) 61,62-Diethyl [10,20-(3-(2-hydroxyethoxy)phenyl)porphyrin-5,15-diylbis (1- phenyl-3-oxy)-diethylene] 1,9:49,59-bismethano[60]fullerene-61,61,62,62-tetracarboxylate (**b**) 61,62-Diethyl [10,20-(3-(2-hydroxyethoxy)phenyl)-Zn(II)-porphyrin-5,15-diylbis(1- phenyl-3-oxy)-diethylene] 1,9:49,59-bismethano[60]fullerene-61,61,62,62-tetracarboxylate (**c**) 61,62-[10,20-bis(3,5-di-*tert*-butylphenyl)-porphyrin-5,15-diylbis(1-phenyl-3-oxy)diethylene]1,9:49,59-bismethano [60]fullerene-61,61,62,62-tetracarboxylate (**d**) di-3-hydroxypropoxy derivative of **c**

electron transfer in the bilayer structure occurred from the porphyrin to fullerene, and a secondary electron transfer from P_3HT to porphyrin cation took place. A model involving a ground state P_3HT-porphyrin derivative-fullerene derivative and two different energetic states P_3HT^+-Zn porphyrin derivative-fullerene was proposed by Vuorinen et al. [28]. Two charge separated states were referred to a polaron-like state, where the positive and negative charges were vertically aligned with the film plane, and a state formed when the charges moved from the donor or acceptor radical ion to neighboring site and polaron dissociated. Equations derived from such a model fitted very well the LB film ITO/ODA/Zn porphyrin derivative-

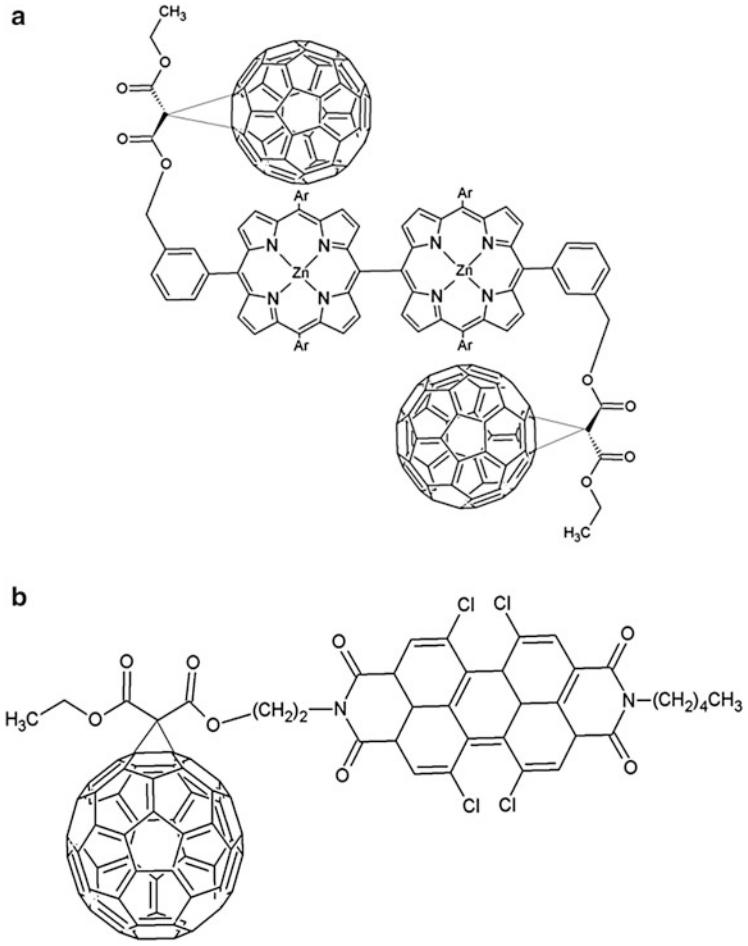

Fig. 10 Molecular structures of (**a**) $2C_{60}$-2Zn porphyrins and (**b**) perylene covalently linked with a C_{60} derivative

fullerene/P_3HT/ODA/aluminum, where ODA layers were used as insulator. According to the proposed model, the lateral charge diffusion in the donor cation and acceptor anion sublayers prolonged the charge recombination time of more than 9 orders of magnitude (from hundreds of picoseconds to hundreds of milliseconds), if compared with the compounds in solution.

Multicomponent organic molecular films with oriented porphyrin–fullerene dyad and polymers and molecules such as phthalocyanines and imides were used by Lemmetyinen and his research group in order to promote both energy and electron transfer toward the porphyrin moieties of the fullerene-porphyrin dyads or as final electron acceptor from C_{60} radical anion [30–32]. The presence of these intermediates causes an increase of the lifetime and of the efficiency of the charge

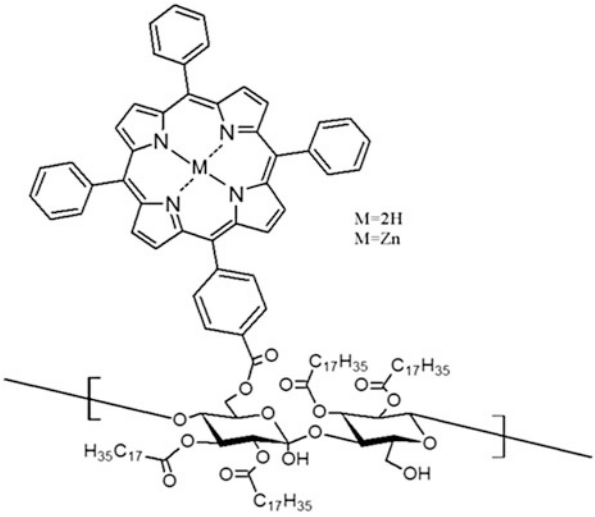

Fig. 11 Structure of cellulose derivatives functionalized with zinc and free-based porphyrin

and energy transfer. The role of perylene molecule in the photoinduced charge transfer process was highlighted comparing the photoresponse of a two electrode photoelectrochemical cells: the first one was realized transferring by LB method a $2C_{60}$-2Zn porphyrin (see Fig. 10a) and on the other device, a perylene covalently linked with a fullerene (see Fig. 10b).

In the case of the compound in Fig. 10b, a positive photocurrent was observed: electrons were transferred from the electrode to the excited organic system and then to the oxidized form of the redox mediator, that is, a solution of $Na_3Fe(CN)_6$ and $Na_4Fe(CN)_6$. When fullerene was coupled with the porphyrin (system in Fig. 10a), a negative current was recorded, and it was higher, as absolute value, than the current measured for the dyad in Fig. 10b, pointing out the better photoconversion features of the porphyrin dyad.

Furthermore, LB method allows to manage the position of the additional layer with respect to the donor-acceptor moiety of the photoactive molecules. As reported by Kotiaho et al. [33], the charge separation was strongly enhanced when gold nanoparticles capped with octanethiol were transferred by LS technique on an octadecylamine film, and then the covalently linked porphyrin–fullerene dyad (reported in Fig. 9c) was transferred with the porphyrin moiety faced toward the Au nanoparticles. On the contrary, the charge separation is depressed when the gold nanoparticles were placed adjacent to C_{60} moiety (Fig. 9a) [34].

Molecules assisting the charge transfer between the electron donor and the C_{60} moiety of the dyad were employed not only as added layer but they were even covalently linked to the photoactive molecules. For example, a cellulose derivative covalently attached to a free-based and Zn porphyrin (Fig. 11) was co-spread with C_{60} in different ratios [35].

The mixed monolayer was transferred by horizontal lifting method on ITO electrodes. The photocurrent measurements were performed on the LS films of

the free-base porphyrin derivative-cellulose:C_{60} and Zn porphyrin derivative-cellulose:C_{60} in a nitrogen-saturated 0.1 M Na_2SO_4 aqueous solution containing hydroquinone as a sacrifice electron donor. The action spectra of free-based porphyrin derivative-cellulose:C_{60}in a ratio 1:2 showed the best response, and the photoaction spectrum was very similar to the profile of the porphyrin moiety. As it is well known, it indicates that the porphyrin was the main molecule responsible for the photocurrent generation. Another interesting behavior pointed out by the authors was that photocurrent density increased until a thickness of 5 layers was reached: the direct electron transfer took place from the excited porphyrins toward the ITO electrode, and, probably as a consequence of electron and energy traps, this phenomenon was quenched for film with more than five layers.

5 Systems Without Fullerene Derivatives

Investigations by Desormeaux et al. [36] were prompted by previous studies on the photovoltaic properties of chlorophyll *a* [37, 38]. The knowledge of the effect of small variations in molecular structure on quantum efficiency of charge generation of the solar cell devices [39] has stimulated the use of chlorophyll *b* in order to appreciate its photovoltaic properties. Therefore, the photovoltaic peculiarities of sandwich cells of LB layers of chl*a*, chl*b*, and Zn porphyrin derivative, Zn(II) 12-carboethoxy-2,7,17-trihexyl-2,8,13,18-tetramethylporphyrin, have been explored (Fig. 12).

A layer of cadmium arachidate was deposited on the top aluminum electrode in order to hydrophobize the solid support. The dark short-circuit currents in all cases (cells containing chl*a*, chl*b*, and the porphyrin derivative) vary in the range 0.04–0.60 nA/cm^2, while the dark open-circuit current–voltage in the range 0.03–0.50 V. The same cells show short-circuit photocurrents that extend from 1.0 to 18.0 nA/cm^2 and open-circuit photovoltage up to 11 V. The internal resistance for all these cells range from 30 to more than 1,000 MΩ. The authors propose that the weak photovoltaic characteristics of such sandwich cells probably depend on the generation of an insulating layer of aluminum oxide and of the monolayer of the fatty acid, while the influence of the molecular structure of pigments is negligible. These conclusions were substantiated by several observations such as photocurrent vs. photovoltage graphs or the light intensity dependence of the photocurrents.

Gervaldo et al. synthesized metallated and unmetallated porphyrins, Zn(II)-, Cu(II)-, Pd(II)-, Ni(II)-, Co(II)-, and H_2-5-(4-carboxyphenyl)-10,15,20-tris (4-methylphenyl) porphyrin, in order to use them in photoelectrochemical devices as spectral sensitizers with the goal of broadening their response to the visible region (Fig. 13) [40].

Two approaches were followed: in the first one, the macrocycles were adsorbed on SnO_2 nanocrystalline large band gap semiconductor (ITO/SnO_2 electrodes have been functionalized with the porphyrins by immersion in their solution in a mixture of hexane and dichloromethane as the solvent), while in the second one, ITO electrodes were covered with LB films of the dyes. The LB layers were also

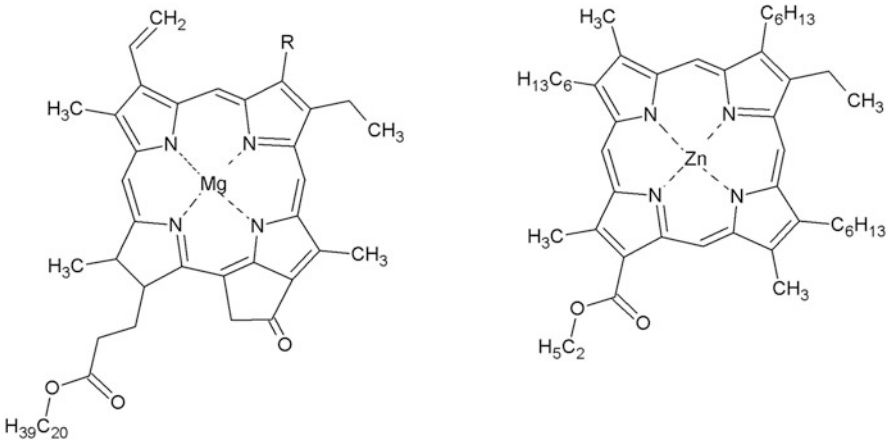

Fig. 12 Molecular structures of chl*a* (R=CH_3), chl*b*(R=CHO), and Zn(II)porphyrin derivative investigated by Desormeaux and coworkers (from [36])

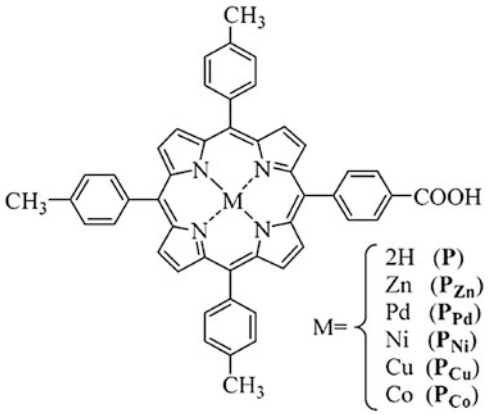

Fig. 13 Molecular structures of the sensitizing dyes employed by Gervaldo and coworkers (from [40])

investigated in the attempt to clarify the influence of molecular packing and intermolecular interactions on the cell performances. It was demonstrated that the central metal atom plays a crucial role as for the values of quantum yields of sensitized photocurrent generation are concerned. The derivative metallated with Pd(II) exhibited the highest quantum yields in both kinds of cells; in particular, the photocurrent quantum yields intensify when the porphyrin ground state oxidation potential becomes more anodic.

Ogi et al. considered that the architectures of LB films at the nanoscale level allow the investigations on interlayer electron transfer and energy transfer and to

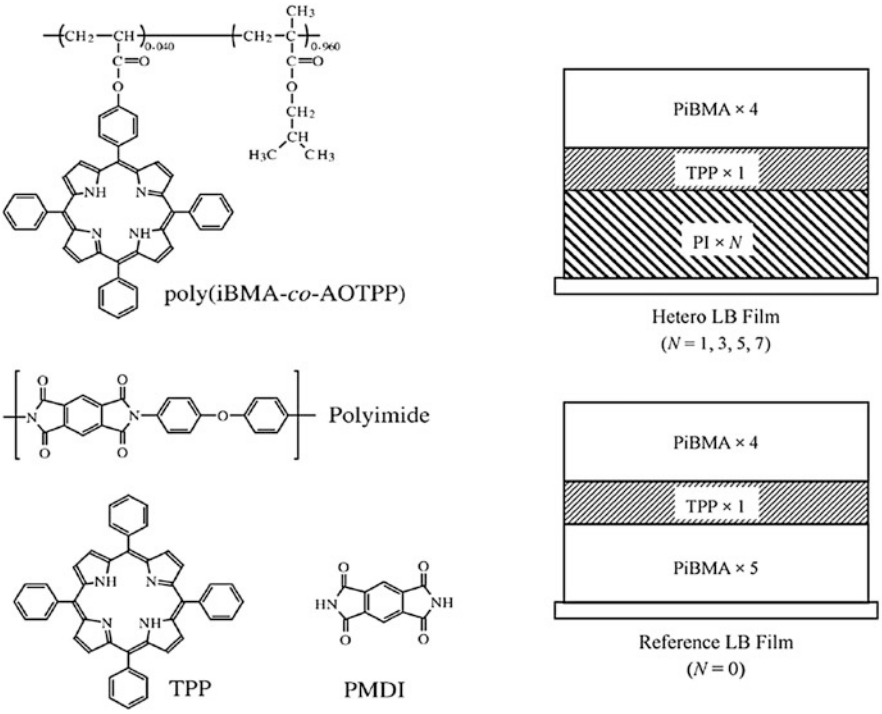

Fig. 14 The employed materials by Ogi and collaborators together with the structures of the fabricated hetero-LB films (from [41])

shed light on the peculiarities of each process [41]. A polyimide derivative was used as one of the materials constituting the LB films in consideration of enhanced chemical, mechanical, and thermal characteristics of polymeric substances. The typical thickness of a polyimide layer is about 0.40 nm. The ample availability of polyimide derivatives permits to modulate the electronic characteristics of the immobilized structures; in fact, the employed diimide moieties evidence substantial electron affinity and hence their resulting LB films electron-accepting characteristics. At the same time, porphyrins have been largely used as photo-absorbing and electron-donating substances. In the light of these considerations, Ogi and coworkers fabricated hetero-multilayers containing poly[isobutylmethacrylate-*co*-5-(4-acryloyloxyphenyl)-10,15,20-triphenyl-porphyrin], indicated as poly(iBMA-*co*-AOTPP), and polyimide. Therefore, in the immobilized films, the transfer process takes place from photoactivated porphyrins to the pyromellitic diimide moieties in polyimide derivatives. This phenomenon was studied through the quenching of the porphyrin fluorescence. The structure of the deposited hetero-LB films is reported in the next figure, where PI is the polyimide and TPP the tetraphenylporphyrin (Fig. 14).

The Perrin model [42] was applied to this case; the fluorescence intensity significantly diminishes as the number of polyimide layers increases. Then the

saturation observed from the fourth layer indicates that the separation between the tetraphenylporphyrin layer and the fourth polyimide layer is too extended to allow successful electron transfer processes.

In natural pigment assemblies, a quantum efficiency close to 100% has been observed: protein scaffolds are able to modulate the intermolecular separation that upgrades electron coupling and energy transfer. The idea of Sakakibara and coworkers [43, 44] was to covalently link porphyrins to cellulose in order to avoid two typical problems related to LB films, i.e., their stability and 2D organization; the improved arrangement is promoted by the rigidity of the cellulose backbone. Therefore, 2,3-di-*O*-stearoyl-6-*O*-[*p*-(10,15,20-triphenyl-5-porphyrinyl)-benzoyl]cellulose, already reported in Fig. 11, was ad hoc synthesized and immobilized as an LB film. In this way, in the light of the so-called role-sharing functionalization, the macrocycle derivatization is strategically and regioselectively inserted at the C-6 position, with the aim of remarkably deactivating self-quenching of the photoexcited porphyrins; at the same time, the stearoyl moieties at the C-2 and C-3 positions affect positively the processability, self-organization, and solubility. In fact, the average distance between two subsequent porphyrin cycles was estimated to be 1.03 nm, and the synthesized derivative carries out the purposed function of scaffold.

Analysis of the Langmuir curves of the derivative at the air-water interface indicates that the dye cycles are normally arranged with respect to the subphase surface, and the UV–vis absorption spectra of the LB films evidence a bathochromic shift suggesting a side-by-side π- (or J-) aggregation.

Photoelectrochemical measurements suggested the porphyrin ring as photoactive moieties with anodic currents arising from the electron transfer from the dye to the ITO electrode. The LB monolayer exhibited a quantum efficiency of 1.6% (0 V potential vs. SCE, $\lambda = 420$ nm, light intensity $= 2.0$ mW/cm^2) that is significantly improved in comparison with the values reported for other porphyrins in the literature [45]. Moreover, upon utilization of more positive potentials, the photocurrent quantum yields intensified up to 3.8–4.6% (0.2–0.3 V vs. SCE).

In a subsequent work, as already made by Gervaldo et al. for different substances [40], Sakakibara and Nakatsubo investigated the influence of the central metal in the dye cycles on the photocurrent performances of such cellulose-based materials [46]. Therefore, in addition to the free base, the derivatives metallated with copper (II), magnesium(II), palladium(II), and zinc(II) were synthesized and employed. The solvent used in the spreading solution was toluene, since at low concentrations, it minimizes the aggregation tendency observed when chloroform was employed. The most stable and densely packed floating layers on the aqueous subphase surface were obtained with the free base and the palladium porphyrin derivatives. The films were deposited onto the solid supports by the horizontal lifting method (Langmuir–Schaefer technique); the corresponding UV–vis spectra using quartz as the substrate showed bathochromic shifts and peak broadenings less intense than in the case of solutions in toluene. Investigations carried out using polarized light have evidenced very similar behavior for different derivatives, and this observation

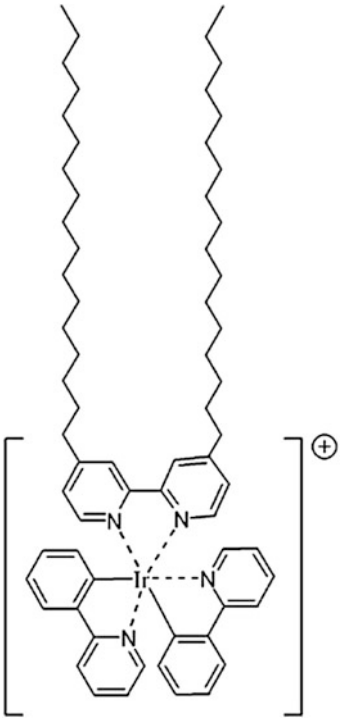

Fig. 15 Molecular structure of the Ir(III) metallo-surfactant used by Roldan-Carmona and coworkers (from [49])

suggests that the environment around the porphyrin rings is practically undistinguishable among derivatives.

As for the photoelectrochemical properties are concerned by studies on monolayers deposited on ITO, the derivative containing palladium evidenced the best properties. By excitation at the Soret band under no bias potential, the photocurrent quantum yields decrements in this order: Pd(II) derivative, 7.2%; free-base derivative, 1.4%; Zn(II), 0.92%; Cu(II), 0.68%; and Mg(II), 0.21%. The value in the case of Pd(II) arises up to 14% when a bias potential of +100 mV is used; this value is comparable with the one reported in other researches employing porphyrin derivatives [47, 48]. Finally, improved performances have been observed when the stearoyl groups at the C-2 and C-3 positions have been substituted by myristoyl (C_{14}) functionalizations.

Roldan-Carmona et al. studied films containing an amphiphilic monocationic Ir(III) metallo-surfactant, bis(2-phenylpyridine)(4,4′-diheptadecyl-2,2′-bipyridine)-iridium(III) chloride, and the commercial tetra-anionic $TPPS_4$ (Fig. 15) [49].

The two substances interact electrostatically and were co-spread in the molar ratio Ir complex:$TSPP_4 = 4{:}1$ in order to generate neutral floating layers. Such Langmuir films evidenced in the isotherm registered at the air-water interface a contraction of molecular area in comparison to that of pure Ir(III) complex. The UV–vis reflection spectra registered at the air-water interface have revealed the presence of both components of the dyad, without loss of the hydrosoluble

porphyrin molecules in the aqueous subphase. Analysis of the spectra suggests that at low surface pressure values, $TSPP_4$ molecules lie prone on the water surface, while upon compression, the bathochromic shift indicates the formation of dimers. The reorganization of the macrorings on the water surface during the barrier movement gives rise to an inclination of the dye macrocycles by about 40° with respect to the normal to the subphase surface. Finally, Brewster Angle Microscopy analysis of the mixed floating layers evidenced the formation of homogeneous monolayers with an improved organization in comparison with the pure Ir(III) complex.

The corresponding composite films were successfully deposited by the horizontal lifting Langmuir–Schaefer method; absorption spectroscopy performed in the UV–vis range suggests that the aggregation phenomena did not take place between layers.

Finally, also emission spectra of the dyad were investigated both in solution and onto solid supports. In solution, the emission spectrum of the Ir(III) complex/$TSPP_4$ mixture corresponds to the sum of the spectra of the two single components. But in the case of the LS films, the spectral pattern of the mixture evidences that the emission of the metal complex is suppressed, while the porphyrin emission increases. An elegant development of these investigations was to vary the spatial separation between the planes of the acceptor and the donor moieties; therefore, a composite film of dioctadecyldimethylammonium bromide (DOMA) and $TSPP_4$ was deposited upon a solid support earlier coated with the iridium(III) complex (with this approach, it is already known that the porphyrin molecules are exclusively in the monomeric form). The luminescence experiments showed that the emission of the metal complex is completely quenched, and hence the energy transfer to the macroring molecules is still efficient.

In a following experiment, the distance between the donor and the acceptor was augmented by a further intercalation of stearic acid monolayer creating the architecture Ir(III) complex/fatty acid/DOMA: $TSPP_4$. In this case, the emission of both the Ir(III) complex and the dye was efficient, thus manifesting that the energy transfer did not occur anymore.

References

1. Liang WY (1970) Excitons Phys Educ 5:226–228
2. Kanai K, Wu Z, Grossman JC (2010) Charge separation in nanoscale photovoltaic materials: recent insights from first-principles electronic structure theory. J Mater Chem 20:1053–1061
3. Morana M, Koppe M, Scharber MC, Waller D, Dennler G, Brabec CJ (2010) Design rules for efficient organic solar cells. In: Petrova-Koch V, Hezel R, Goetzberger A (eds) High-efficient low-cost photovoltaics: recent developments. Springer, Berlin
4. Sgobba V, Giancane G, Cannoletta D, Operamolla A, Hassan Omar O, Farinola GM, Guldi DM, Valli L (2014) Langmuir–Schaefer films for aligned carbon nanotubes functionalized with a conjugate polymer and photoelectrochemical response enhancement. ACS Appl Mater Interfaces 6:153–158

5. Hann RA (1990) In: Roberts G (ed) Molecular structure and monolayer properties in Langmuir–Blodgett films. Plenum, New York
6. Ulman A (1991) An introduction to ultrathin organic films from Langmuir–Blodgett to self-assembly. Academic, San Diego
7. Kroon JM, Sudholter EJR (1995) Self-organization of amphiphilic porphyrins at the air–water interface. Langmuir 11:214–220
8. Giancane G, Valli L (2012) State of art in porphyrin Langmuir–Blodgett films as chemical sensors. Adv Colloid Interfac 171–172:17–35
9. Arnold DP, Manno D, Micocci G, Serra A, Tepore A, Valli L (1997) Porphyrin dimers linked by a conjugated alkyne bridge: novel moieties for the growth of Langmuir–Blodgett films and their applications in gas sensors. Langmuir 13:5951–5956
10. Viseu MI, Goncalves da Silva AM, Antunes P, Costa SMB (2002) Organization of cationic porphyrins in mixed Langmuir–Blodgett films. An absorption and steady-state fluorescence study Langmuir 18:5772–5781
11. Gür B, Meral K (2012) Preparation and characterization of mixed monolayers and Langmuir–Blodgett films of merocyanine 540/octadecylamine mixture. Colloid Surface A 414:281–288
12. Costa SMB, Andrade SM, Togashi DM, Paulo PMR, Laia CAT, Viseu MI, Gonçalves da Silva AM (2009) Optical spectroscopy and photochemistry of porphyrins and phthalocyanines. J Porphyrins Phthalocyanines 13:509–517
13. Veselov A, Thür C, Churkharev V, Guina M, Lemmetyinen H, Tkachenko NV (2009) Photochemical properties of porphyrin films covering curved surfaces of optical fibers. Chem Phys Lett 471:290–294
14. Li L, Jin J, Yang W, Wang X, Zhang J, Li Y, Bai Y, Li T (2002) Studies on photovoltaic characteristics of hemin and its organized assembly by surface photovoltage spectroscopy. Colloid Surface A 198–200:717–721
15. Ogi T, Ito S (2006) Migration and transfer of excitation energy in homogeneously dispersed porphyrin monolayers prepared from amphiphilic copolymers. Thin Solid Films 500:289–295
16. Sgobba V, Giancane G, Conoci S, Casilli S, Ricciardi G, Guldi DM, Prato M, Valli L (2007) Growth and characterization of films containing fullerenes and water soluble porphyrins for solar energy conversion applications. J Am Chem Soc 129:3148–3156
17. Kuhn H, Mobius D (1993) Monolayer assemblies. In: Rossiter BW, Baetzold RC (eds) Physical methods of chemistry, investigations of surfaces and interfaces-part B. Wiley, New York
18. Marczak R, SgobbaV KW, Gadde S, D'Souza F, Guldi DM (2007) Langmuir−Blodgett films of a cationic zinc porphyrin − imidazole-functionalized fullerene dyad: formation and photoelectrochemical studies. Langmuir 23:1917–1923
19. Tasis D, Tagmatarchis N, Bianco A, Prato M (2006) Chemistry of carbon nanotubes. Chem Rev 106:1105–1136
20. Da Ros T, Prato M, Carano M, Ceroni P, Paolucci F, Roffia S, Valli L, Guldi DM (2000) Synthesis, electrochemistry, Langmuir–Blodgett deposition and photophysics of metal-coordinated fullerene–porphyrin dyads. J Organomet Chem 599:62–68
21. Guldi DM, Zilbermann I, Anderson GA, Kordatos K, Prato M, Tafuro R, Valli L (2004) Langmuir–Blodgett and layer-by-layer films of photoactive fullerene–porphyrin dyads. J Mater Chem 14:303–309
22. Tkachenko NV, Vehamanen V, Nikkanen J-P, Yamada H, Imahori H, Fukuzumi S, Lemmetyinen H (2002) Porphyrin–fullerene dyad with a long linker: formation of charge transfer conformer in Langmuir–Blodgett film. Chem Phys Lett 366:245–252
23. Guldi DM, Rahman GMA, Sgobba V, Ehli C (2006) Multifunctional molecular carbon materials—from fullerenes to carbon nanotubes. Chem Soc Rev 35:471–487
24. Charvet R, Ariga K, Hill JP, Ji Q, Khan AH, Acharya S (2011) Large scale assembly of ordered donor–acceptor heterojunction molecular wires using the Langmuir–Blodgett technique. Chem Commun 47:6825–6827

25. Vourinen T, Kaunisto K, Tkachenko NV, Efimov A, Lemmetyinen H (2005) Photoinduced electron transfer in Langmuir–Blodgett monolayers of porphyrin–fullerene dyads. Langmuir 21:5383–5390
26. Kaunisto K, Chukharev V, Tkachenko NV, Lemmetyinen H (2008) Long-lived charge separated state in molecular films containing porphyrin–fullerene dyad. Chem Phys Lett 460:241–244
27. Vourinen T, Kaunisto K, Tkachenko NV, Efimov A, Lemmetyinen H (2006) Photoinduced interlayer electron transfer in alternating porphyrin–fullerene dyad and regioregular poly (3-hexylthiophene) Langmuir–Blodgett films. J Photoch Photobio A 178:185–191
28. Kaunisto K, Vuorinen T, Vahasalo H, Chukharev V, Tkachenko NV, Efimov A, Tolkki A, Lehtivuori H, Lemmetyinen H (2008) Photoinduced electron transfer and photocurrent in multicomponent organic molecular films containing oriented porphyrin–fullerene dyad. J Phys Chem C 112:10256–10265
29. Kaunisto K, Chukharev V, Tkachenko NV, Efimov A, Lemmetyinen H (2009) Energy and electron transfer in multilayer films containing porphyrin–fullerene dyad. J Phys Chem C 113:3819–3825
30. Tolkki A, Kaunisto K, Efimov A, Kivistö H, Storbacka L, Savikoski R, Huttunen K, Lehtimäki S, Lemmetyinen H (2012) Directed electron transfer in Langmuir–Schäfer layers of porphyrin–fullerene and phthalocyanine–fullerene dyads in inverted organic solar cells. Phys Chem Chem Phys 14:3498–3504
31. Kaunisto K, Vahasalo H, Chukharev V, Tkachenko NV, Vivo P, Niemi M, Tolkki A, Efimov A, Lemmetyinen H (2009) Photoinduced charge transfer through films containing poly(hexylthiophene), phthalocyanine, and porphyrin–fullerene layers. Thin Solid Films 517:2988–2993
32. Vivo P, Alekseev AS, Kaunisto K, Pekkola O, Tolkki A, Churkharev V, Efimov A, Ihalainen P, Peltonen J, Lemmetyinen H (2010) Photoinduced electron transfer in thin films of porphyrin–fullerene dyad and perylenetetracarboxidiimide. Phys Chem Chem Phys 12:12525–12532
33. Katiaho A, Lahtinen R, Latvala H-K, Efimov A, Tkachenko NV, Lemmetyinen H (2009) Effect of gold nanoparticles on intramolecular exciplex emission in organized porphyrin–fullerene dyad films. Chem Phys Lett 471:269–275
34. Kotiaho A, Lahtinen RM, Tkachenko NV, Efimov A, Kira A, Imahori H, Lemmetyinen H (2007) Gold nanoparticle enhanced charge transfer in thin film assemblies of porphyrin–fullerene dyads. Langmuir 23:13117–13125
35. Sakakibara K, Nakatsubo F (2008) Effect of fullerene on photocurrent performance of 6-*O*-Porphyrin-2,3-di-*O*-stearoylcellulose Langmuir–Blodgett films. Macromol Chem Phys 209:1274–1281
36. Desormeaux A, Max JJ, Leblanc RM (1993) Photovoltaic and electrical properties of aluminum/Langmuir–Blodgett films/silver sandwich cells incorporating either chlorophyll *a*, chlorophyll *b*, or zinc porphyrin derivative. J Phys Chem 97:6670–6678
37. Tang CW, Albrecht AC (1975) Chlorophyll-*a* photovoltaic cells. Nature 254:507–509
38. Diarra A, Hotchandani S, Max JJ, Leblanc RM (1986) Photovoltaic properties of mixed monolayers of chlorophyll a and carotenoid canthaxanthin. J Chem Soc Faraday Trans 2 (82):2217–2231
39. Morel DL, Stogryn EL, Ghosh AK, Feng T, Purwin PE, Shaw RF, Fishman C, Bird GR, Piechowski AP (1984) Organic photovoltaic cells. Correlations between cell performance and molecular structure. J Phys Chem 88:923–933
40. Gervaldo M, Fungo F, Durantini EN, Silber JJ, Sereno L, Otero L (2005) Carboxyphenyl metalloporphyrins as photosensitizers of semiconductor film electrodes. A study of the effect of different central metals. J Phys Chem B 109:20953–20962
41. Ogi T, Benten H, Ito S (2007) Nano-structure of polyimide and poly(isobutyl methacrylate) monolayer films studied by interlayer electron transfer between porphyrin and pyromelliticdiimide moieties. Thin Solid Films 515:3107–3111

42. Perrin F (1924) Loi de dècroissance du pouvoir fluorescent en function de la concentration. Compt Rend 178:1978–1980
43. Sakakibara K, Ogawa Y, Nakatsubo F (2007) First cellulose Langmuir–Blodgett films towards photocurrent generation systems. Macromol Rapid Comm 28:1270–1275
44. Sakakibara K, Nakatsubo F (2008) Fabrication of anodic photocurrent generation systems by use of 6-*O*-dihydrophytylcellulose as a matrix or a scaffold of porphyrins. Cellulose 15:825–835
45. Choudury B, Weedon AC, Bolton JR (1998) Effects of molecular organization on photophysical behavior. 2. Photoelectrochemical and photocurrent quantum yield studies of the Langmuir–Blodgett monolayers of some surfactant porphyrins. Langmuir 14:6199–6206
46. Sakikabara K, Nakatsubo F (2010) Effect of central metals in the porphyrin ring on photocurrent performance of cellulose Langmuir–Blodgett films. Macromol Chem Phys 211:2425–2433
47. Imahori H, Kimura M, Hosomizu K, Sato T, Ahn T K, Kim S K, Nishimura Y, Yamazaki I, Araki Y, Ito O, Fukuzumi S (2004) Vectorial electron relay at ITO electrodes modified with self-assembled monolayers of ferrocene–porphyrin–fullerene triads and porphyrin–fullerene dyads for molecular photovoltaic devices. Chem Eur J 10:5111–5122
48. Morisue M, Haruta N, Kalita D, Kobuke Y (2006) Efficient charge injection from the S2 photoexcited state of special-pair mimic porphyrin assemblies anchored on a titanium-modified ITO anode. Chem Eur J 12:8123–8135
49. Roldán-Carmona C, González-Delgado AM, Guerreo-Martínez A, De Cola L, Giner-Casares JJ, Pérez-Morales M, Martín-Romero MT, Camacho L (2011) Molecular organization and effective energy transfer in iridium metallosurfactant–porphyrin assemblies embedded in Langmuir–Schaefer films. Phys Chem Chem Phys 13(2011):2834–2841

Top Heterocycl Chem (2014) 34: 139–174
DOI: 10.1007/7081_2013_113

Published online: 5 October 2013

Non-Covalent Interactions of Porphyrinoids with Duplex DNA

Alessandro D'Urso, Maria Elena Fragalà, and Roberto Purrello

Abstract Due to their unique physicochemical aspect porphyrinoid–DNA complexes have been widely studied for long time to develop a novel range of supramolecular constructs for application in medicinal chemistry. Owing to the intriguing properties of porphyrinoid macrocycles, they have been used for several applications in many scientific fields: biosensoristic, pharmaceutical, and technological. One of the more used biological templates to control porphyrinoid assembly is DNA. A completed overview on porphyrinoid–duplex DNA systems is here reported.

Keywords Induced CD · Nucleic acids · Porphyrinoids · Spectroscopy

Contents

Abbreviations

Br_8CoTMPyP4	Tetrakis-*N*-methylpyridyl-β-octabromo Co(II) porphyrin
CD	Circular dichroism
cis-H_2Pagg	5,10-Bis(4-*N*-methylpyridyl)-15,20-diphenyl porphyrin
cis-H_2TMPyPipP4	5,10-Di[4-[1-(4-phenylpiperazine-yl)-acetyloxocarbonyl]-phenyl]-15,20-di(4-*N*-methylpyridiniumyl)porphine

A. D'Urso, M.E. Fragalà, and R. Purrello (✉)
Department of Chemical Science, University of Catania, Catania, Italy
e-mail: rpurrello@unict.it

CT-DNA	Calf thymus DNA
Cu(2,3-tmtppa)4C	*N*,*N*′,*N*″,*N*″-tetramethyltetra-2,3-pyridinoporphyrazinato copper(II)
Cu(3,4-tmtppa)4C	*N*,*N*′,*N*″,*N*″-tetramethyltetra-3,4pyridinoporphyrazinato copper(II)
Cu(II)TMPyP4	5,10,15,20-Tetrakis(4-*N*-methylpyridyl)Cu(II)porphyrin
CuPz8+	2,3,7,8,12,13,17,18-Octakis(4-*N*-methylpyridyl) Cu(II) porphyra zine
DNA	Deoxyribonucleic acid
Fe(III)TMPyP4	5,10,15,20-Tetrakis(4-*N*-methylpyridyl)Fe(III)porphyrin
GeTMPyC	5,10,15-(4-*N*-methylpyridyl)Ge(IV)corrole
GQ	G-quadruplex
H_2BisDMImP4	5,15-Bis(1,3-dimethylimidazolium-2-yl)porphyrin
H_2DPDPFPP	5,15-(4-pyridyl)-10,20-(pentafluorophenyl)porphyrin
H_2TButPyP4	5,10,15,20-Tetrakis(4-*N*-n-butylpyridyl)porphyrin
H_2TDMImP4	Meso-tetrakis(1,3-dimethylimidazolium-2-yl)porphyrin
H_2TDMPzP4	Meso-tetrakis(1,2-dimethylpyrazolium-4-yl)porphyrin
H_2TEtOHPyP4	5,10,15,20-Tetrakis(4-*N*-(2-hydroxyethyl)pyridyl)porphyrin
H_2TMAP	5,10,15,20-Tetrakis(4-*N*,*N*′,*N*″-trimethylanilinium)porphyrin
H_2TMPyC	5,10,15-(4-*N*-methylpyridyl)corrole
H_2TMPyCMP4	5-(4-methoxycarbonylphenyl)-10,15,20-tris (4-*N*-methylpyridyl) porphyrin
H_2TMPyCP4	5-(4-Carboxyphenyl)-10,15,20-tris(4-*N*-methylpyridyl) porphyrin
H_2TMPyP2	5,10,15,20-Tetrakis(2-*N*-methylpyridyl)porphyrin
H_2TMPyP4	5,10,15,20-Tetrakis(4-*N*-methylpyridyl)porphyrin
H_2TMPyPFc	Tris(4-*N*-methylpyridiniumyl)mono (phenyl-OCH_2CH_2ferrocene) porphyrin
H_2TMPyPipP4	5-[4-[1-(4-phenylpiperazine-yl)-acetyloxocarbonyl] phenyl]-10,15,20-tris(4-*N*-methylpyridiniumyl)porphine
H_2TMPyPP4	5,10,15,20-Tetrakis(*N*-methyl-4-pyridin-4-yl-phenyl) porphyrin
H_2TPPS4	5,10,15,20-Tetrakis[4-sulfonatophenyl]porphyrin
H_2TPrPyP4	5,10,15,20-Tetrakis(4-*N*-propylpyridyl)porphyrin
H_2TPrPyPP4	5,10,15,20-Tetrakis{[4-(1-pyridyl)propoxy]phenyl} porphyrin
H_2TSPc	*N*,*N*′,*N*″,*N*‴-tetrasulfonated phthalocyanines
H_2T9F4TAP	Meso-tetrakis [2,3,5,6-tetrafluoro-4-(2-trimethylammoniumethyl amine)phenyl]porphyrin
H_2T9OPP4	Meso-tetrakis[4-[(3-trimethylaminopropyl)oxy]phenyl] porphine
H_2T9PyP4	Meso-tetrakis[4-*N*-(3-trimethylaminopropyl)pyridyl] porphine
ICD	Induced circular dichroism
LD	Linear dichroism

m-H_2TCP^{4-}	5,10,15,20-Tetrakis[3-(nido-carboranyl)phenyl]porphyrin
MnDMPyFPC	5,15-(4-*N*-methylpyridyl)-10-(pentafluorophenyl)Mn(III) corrole
$MnTDEt_{Est}PyP4$	5,10,15,20-Tetrakis(4-*N*-diethylesterepyridyl)Mn(III) porphyrin
MnTMPyC	5,10,15-(4-*N*-methylpyridyl)corroleMn(III)
MPIX	Mesoporphyrin IX
NiTPPS4	5,10,15,20-Tetrakis[4-sulfonatophenyl] Ni(II) porphyrin
NMM	*N*-methylmesoporphyrin IX
NMR	Nuclear magnetic resonance
p-H_2TCP^{4-}	5,10,15,20-Tetrakis[4-(nido-carboranyl)phenyl]porphyrin
PDT	Photodynamic therapy
poly(dA–dT)	Poly(deoxyadenylic-deoxythymidylic)acid
poly(dG–dC)	Poly(deoxyguanylic-deoxycytidylic) acid
RLS	Resonance light scattering
RNA	Ribonucleic acid
T_m	Melting temperature
trans-H_2Pagg	5,15-Bis(4-*N*-methylpyridyl)-10,20-diphenyl porphyrin
VCD	Vibrational circular dichroism
Zn(II)TMPyP4	5,10,15,20-Tetrakis(4-*N*-methylpyridyl)Zn(II)porphyrin
ZnPz8+	2,3,7,8,12,13,17,18-Octakis(4-*N*-methylpyridyl) Cu(II) porphyra zine
ZnTPPS4	5,10,15,20-Tetrakis[4-sulfonatophenyl] Zn(II) porphyrin

1 Introduction

As a result of Watson–Crick hydrogen bonds, π–π stacking, and electrostatic repulsion between the negatively charged phosphates, DNA mostly forms double-helical structure vive. Depending on the sequence and the environment, the duplex can exist in various conformations, from the most commonly found right-handed B form to the compact A form and the unusual left-handed Z form (Fig. 1).

However, DNA does not exist exclusively as duplex but can also form various secondary structures. Watson–Crick hydrogen bonds form the abovementioned anti-parallel duplex, but alternative base pairing (Hoogsteen, reverse Hoogsteen, etc.) allows the formation of triplex and quadruplex structures. These structures might be responsible for the regulation of some genes [1]. RNA can adopt single- and double-helical structures, as well as several conformations depending on sequences and biological roles [2]. Identification of the different structures and specific sequences of nucleic acids, by functional probes, might allow to know the mechanism and treat some diseases.

Interactions of natural products with genetic material (DNA and RNA) have been at the center of large number of studies for several years. Over regulatory protein gene expression, as DNA and RNA polymerases or releasing factors that

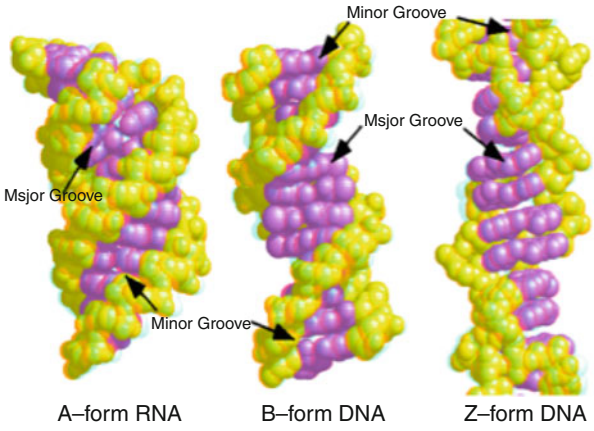

Fig. 1 Different duplex conformation of DNA

bound and distinguish specific base sequences in single or double helices of nucleic acids, a lot of natural molecules are able to recognize selectively sites on DNA and RNA, and some of these can interfere with processes controlling the flow of genetic information (replication, transcription, and transduction). The most significant characteristic of all these molecules is the presence of (hetero-)aromatic chromophores having the ability to intercalate with DNA basis by π–π interactions, inhibiting the transcription process. Synthetic derivatives of natural compound have been used as antibiotic (actinomycin D [3, 4] and rifamycin [4]) or as antitumor (daunomycin); however, other molecules such as proflavine, ethidium ion, and porphyrinoids have been studied owing to the high efficiency in PDT [5–8].

Porphyrinoids are ideal compounds to be incorporated into DNA due to peculiar characteristics: (1) high molar absorptivity coefficient of the main absorption band (called Soret band) owing to the large aromatic structure, (2) the possibility to tune the electronic properties of the molecules by implementing small variation in the macrocycle ring or introducing metal ions in the core, (3) absorption spectrum in the 360–750 nm range, far from spectroscopic interference of nucleic acid absorption, and (4) ability to act as photosensitizers in the presence of oxygen. This latter characteristic promoted the interest of scientific community to study the binding of porphyrinoids with DNA in order to use them in PDT. It has been demonstrated that a photosensitizer needs to be bound to DNA in order to produce photodynamic damage [9], and the efficiency of this process depends on the type of interaction of the photosensitizer [10, 11]. Thus, the understanding of mechanism involved in the binding of porphyrinoids with DNA can help to find a porphyrinoid with specific base degradation activity. For these reasons several synthetic derivatives of porphyrinoids have been proposed to improve the non-covalent interactions with DNA.

There are several spectroscopic techniques for the investigation and characterization of porphyrinoid–DNA systems such as UV–Vis, fluorescence, RLS, CD, and NMR. As concerns the utility of the various techniques, it is, noteworthy, singularly used to give fast, intuitive but not always detailed information about the type of interaction. Only analyzing by more than one of those methods is possible to

thoroughly characterize the title interactions by exploiting the different and specific information coming from each technique. Circular dichroism measurements are, in general, more specific because interactions of these non-chiral macrocycles with nucleic acid (which are conformationally chiral) induce a dichroic band (ICD) in the absorption region of the achiral ligands (porphyrinoids), whose shape and intensity are diagnostic of the type of interaction.

In addition to medical applications, porphyrinoid–DNA systems can be prompted in technologic field as molecular device. DNA is a perfect scaffold for the creation of functional π systems as it has a number of favorable characteristic such as (1) spontaneous self-assembly of oligonucleotides with complementary sequences, (2) well-known and characteristic structures, and (3) several methods to study binding of molecules on DNA. In fact, according with fundamentals of supramolecular chemistry, based on dynamic and reversible behavior, it is possible to design stable systems by using right combination of modulable non-covalent interactions (electrostatic, hydrophobic, Van der Waals, hydrogen bonds, etc.).

2 Cationic Porphyrins with Duplex DNA

No doubt, H_2TMPyP4 (Fig. 2) is the first and the most used porphyrinoid compound to study the interaction with oligonucleotides. This success is owed to the particular characteristics of H_2TMPyP4: (1) four peripheral positive charges that lead to electrostatic recognition with anionic phosphate groups of nucleotides, (2) the weak tendency to self-aggregate below millimolar concentration [12], and (3) extensive π system. Since 1979, when Gupta and coworker published the first paper on non-covalent interactions of porphyrin and DNA [13], H_2TMPyP4 has been investigated in detail as probe for several DNA secondary and ternary structures and as DNA-target in PDT. Then a large amount of derivatives have been synthetized to improve selectivity, detection, and efficiency in PDT.

As underlined by Gupta, the interaction between CT-DNA and H_2TMPyP4 depends by several factors (concentration of probe and DNA, conformation of DNA, ionic strength, and temperature). Scatchard analysis, viscometry, thermal denaturation, and CD experiments have been carried out to investigate the binding of porphyrins to DNA. The sum of these data strongly suggests that H_2TMPyP4 binds to CT-DNA in two and possibly three ways. The first is an electrostatic-type binding between the cationic charges of the porphyrin and the anionic phosphates of DNA backbone. The second is an intercalation of the porphyrin between DNA base pairs. The third mode requires partially or fully denatured DNA and involves a porphyrin-base interaction. The electrostatic interaction was demonstrated by showing the dependence of the spectroscopic features observed with ionic strength variation; in fact, the bimodal nature of the hyperchromicity in the absorbance–temperature transition measurements (Fig. 3) was attributed to the two modes by which the porphyrin is bound to DNA.

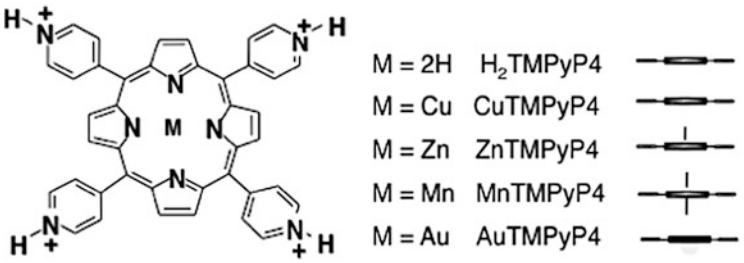

Fig. 2 Molecular structure and schematic side view of tetracationic porphyrin

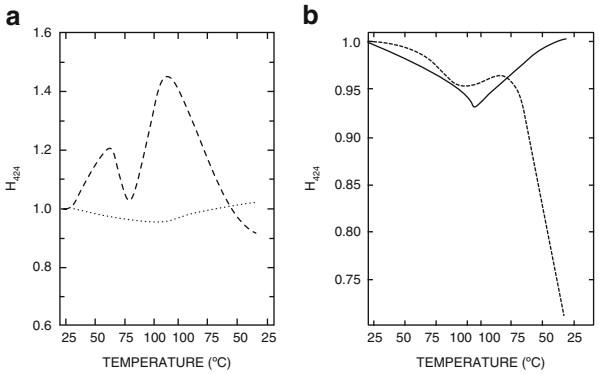

Fig. 3 Hyperchromicity vs temperature at 424 nm for H_2TMPyP4–DNA complex ($r = 0.061$) in BPES buffer. (**a**) Without NaCl (*black continues line*), *dotted line* is H_2TMPyP4 alone; (**b**) With 1 M NaCl (*dotted line*), *continues line* is H_2TMPyP4 alone. Modified from [13]

The low-temperature transition represents a weak electrostatic binding and the high-temperature transition represents intercalative binding. This interpretation is supported by the results, where the low-temperature transition has been blocked by a high concentration of counterions, which inhibits the electrostatic interaction, and by the increased predominance of the low-temperature transition found at very low ionic strength. The evidences that allow to classify H_2TMPyP4 as intercalating agent are (1) an increase in T_m and viscosity, correlated, respectively, with an enhanced stability of the porphyrin–DNA complex and with an increase in the chain length of DNA, both resulting from the insertion of the ligand between bases; (2) intense hypochromic effect (H > 20%) and large red shift ($\Delta\lambda > 15$ nm) of the Soret band upon binding to DNA even at high ionic strength, where electrostatic interaction is blocked or at least minimized; and (3) an induced circular dichroism (ICD) signal that appears in the porphyrin absorption region. Moreover, they suggested that intercalation of H_2TMPyP4 may reflect the existence of DNA "breathing" [14–16]; in fact, H_2TMPyP4 is too bulky to intercalate without rupturing hydrogen bonds between DNA base pairs and distorting the double helix.

The third binding mode is suggested by absorbance value attained by the porphyrin–DNA complexes upon cooling to room temperature after the melting experiments. In all cases analyzed (different molar ratio of porphyrin/DNA and ionic strength), the Soret absorption values tend to be lower than the initial values obtained upon mixing the two components, DNA and porphyrin. This indicates an increase in binding of H_2TMPyP4 to denatured DNA (Fig. 3).

The presence of the sterically bulky *N*-methylpyridyl groups might be expected to hinder the classical modes of intercalation as shown by molecules such as proflavine or ethidium; however, another evidence of this binding mode has been demonstrated by Fiel and Munson [17]. They showed by electrophoresis experiment that closed circular supercoiled DNA from ColE1 in the presence of H_2TMPyP4 migrates to relaxed circular DNA form. This latter experiment demonstrated the ability of H_2TMPyP4 to unwind closed circular supercoiled DNA, a feature diagnostic for intercalation of this compound into DNA [18–20]. They carried out the same experiment in the presence of FeTMPyP4 which is not expected to intercalate for steric reason due to the fact that tetrapyrrole rings are puckered to accommodate the Fe(III) bound to a chlorine in the axial position; in fact, in accordance with this, FeTMPyP4 doesn't unwind closed circular supercoiled DNA.

These pioneering studies stemmed interests in characterizing the porphyrinoid–DNA interactions, in so far as several factors affect the binding modes. It is clear that the type of interaction depends on both the structural properties of the porphyrinoid derivatives and DNA sequences and conformation, however, as well the experimental conditions, i.e., molar ratio of porphyrin/DNA and ionic strength influence the binding mode.

Concerning the dependence on ionic strength of the porphyrinoid–DNA complexes, Pasternack developed a simple theory for the influence of ionic strength on binding of H_2TMPyP4 to DNA [21]. For the former system the results are typical of other intercalators, i.e., a plot of log K vs log $[Na^+]$ is linear albeit with a slope which suggests that the "effective charge" of the porphyrin is closer to two than the formal charge of + 4. Indeed, when a model of the intercalated porphyrin is constructed, not all of the *N*-methylpyridyl groups form contacts with phosphate moieties. Moreover, he demonstrated, by UV and CD experiments on H_2TMPyP4/CT-DNA complex at different concentrations of $[Na^+]$, that porphyrin-base specificity changes with ionic strength; in particular, porphyrin moves from G–C-rich regions to AT-rich regions as the ionic strength increases. Finally, he concluded, unifying notion in his studies and in the previous ones [22, 23], that not only the avidity but also the nature of polyelectrolyte small molecule interactions may well be very sensitive to the bulk ionic strength.

The connection among porphyrin binding mode, base pair composition, and spectroscopic signatures arose out of systematic studies with several porphyrinoid derivatives and a variety of DNAs, i.e., synthetic polymers as poly(dG–dC) and poly(dA–dT) or natural mixed sequences of CG and AT.

As mentioned above, extensive evidence demonstrates that H_2TMPyP4 does indeed bind intercalatively to double-stranded DNA, unwinding of closed circular DNA [13, 17, 24–27]. This former and other methods have been employed to

characterize the binding of the metal derivative complexes of the "TMPyP4 porphyrin" family. It has been found that metal porphyrins which exist as (or can easily be converted to) four-coordinate species such as Cu(II)TMPyP4, Au(III) TMPyP4, Ni(II)TMPyP4, and PdTMPyP4 (Fig. 2) are capable of intercalating, as is the planar metal-free, free-base form. On the other hand, metal derivatives containing one (Zn(II)TMPyP4 and Fe(III)TMPyP4) or two (Mn(III)TMPyP4, Fe(III)TMPyP4, Ni(II)TMPyP4, Co(III)TMPyP4, and V(II)(=O)TMPyP4) axial ligands (Fig. 2) are blocked from intercalation and instead form external complexes in which the metalloporphyrin locates in a DNA groove [24, 28–30]. These findings for metalloporphyrins and synthetic DNAs established a very convenient UV and CD spectroscopic signature for these interactions; a large red shift ($\geq$5 nm) and substantial hypochromicity ($\geq$30%) of the absorption maximum and a negative induced CD band in the Soret region are diagnostic of intercalation, whereas a small red shift ($\leq$8 nm) and little hypochromicity ($\leq$10%) or even hyperchromicity of the absorption maximum and a positive ICD feature indicate external, groove binding [24].

Other studies have shown that H_2TMPyP4 exhibits sequence-selective DNA interactions [24, 25, 31, 32]. The binding to A–T regions has been considered to be nonintercalative, whereas that to G–C sequences has been defined as intercalative. These generalizations about porphyrin–DNA interactions provided a basis for interpreting a variety of experimental results including the observation (based upon supercoiled DNA unwinding studies) that, unlike H_2TMPyP4, FeTMPyP4 does not intercalate into DNA [17]. The key factor in preventing intercalation of this latter derivative according to the model, already reported, is the presence of axial ligands at the iron center. For H_2TMPyP4 interaction with natural DNAs, two induced CD bands are observed under certain solution conditions, a negative band at about 440 nm and a positive one at shorter wavelength about 430 nm (Fig. 4). Bisignate CD spectra of this type can arise from chromophore aggregation, but such proves not to be the case here. The profile of the CD spectrum is roughly independent of drug load and represents two distinct binding modes (intercalation and external, electrostatic binding) with the distribution of the porphyrin between these modes dependent on ionic strength [17, 21]. At a fixed concentration of porphyrin and DNA, H_2TMPyP4 tends to intercalate at low salt concentration (providing a negative induced CD feature near the Soret maximum at 446 nm), but as salt is added, external binding becomes relatively more favorable with the appearance of a positive induced CD feature [21].

Among the factors that must be considered to distinguish intercalation and external binding is the position of the *N*-methyl group in the pyridyl substituent, which may hinder the rotation of the *N*-methylpyridyl groups to a position more nearly coplanar to the porphyrin core. The rotational barrier to coplanarity has been measured for the indium, titanium, and ruthenium tetraphenylporphyrins as $\Delta G^* \sim$ 15 kcal/mol if the ortho position of the meso-substituent ring system is occupied by hydrogen and coplanarity of the meso-substituents is required [33, 34]. For solutions of ortho substituted of H_2TMPyP4 (H_2TMPyP2, Fig. 5) with poly (dG–dC), poly(dA–dT), and DNA, there is virtually no change in the Soret maximum, indicating minimal interaction with the bases of these duplexes. A substantial

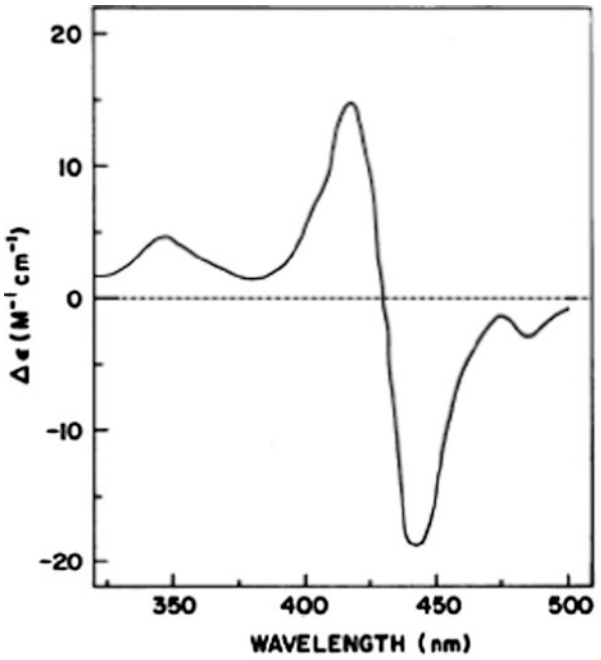

Fig. 4 CD spectrum of H_2TMPyP4 (2.8 μM) in the presence of CT-DNA ($r = 0.184$) in BPES buffer. Modified from [13]

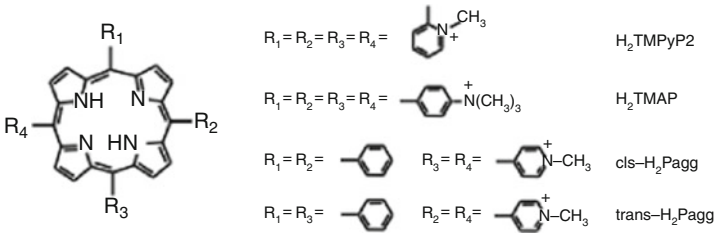

Fig. 5 Molecular structure of H_2TMPyP4 derivatives

positive CD band is induced in the visible region with poly(dA–dT), but no band is observed with poly(dG–dC). Thus, the inability of the meso-substituents to rotate toward a coplanar position prevents intercalation and severely limits the interaction of the porphyrin moiety with the bases of the nucleic acid. Another important consideration arises from these results: although the complex formed with poly (dA–dT) with the axially liganded metalloporphyrins or H_2TMPyP2 may not be due to intercalation, they must involve more than purely electrostatic forces with the phosphate backbone. If only coulombic forces were involved, then similar complexes would be expected with poly(dG–dC). These latter porphyrins may

form complexes with poly(dA–dT) in which they are only partially intercalated or in which they are bound in a groove of the helix. It is known that poly(dA–dT) is far more flexible than poly(dG–dC) [17, 35–37].

The number of cations is also an important factor that governs the porphyrin binding mode to the DNA [38–43]. Neither *trans*- nor *cis*-H_2Pagg (Fig. 5), which contains two positive charges, intercalates between the base pairs of the native DNA and poly(dG–dC) even at the lowest ratio [43]. Upon binding to poly(dA–dT), both *trans*- and *cis*-H_2Pagg are stacked with characteristic bisignate CD spectra in the Soret absorption region at low ratios (0.02–0.08). However, *trans*-H_2Pagg exhibited a groove-binding mode at the lowest ratio (*R* 0.02) [43]. The binding mode to DNA and poly(dG–dC) was similarly stacked along the polynucleotide stem [44].

Over the most used and indicative methods of study including UV–Vis absorption and electronic CD spectroscopy [45–55], reports of studies employing other techniques helped to confirm and extend the models for porphyrin binding presented above. Banville et al., using a combination of NMR and viscometric titration techniques [27], confirmed that NiTMPyP4 and H_2TMPyP4 intercalate while axially liganded ZnTMPyP4 does not. The NMR spectroscopy was used by Leontis to demonstrate intercalation of H_2TMPyP4 at the central 5′-CG-3′ step of the mixed sequence of DNA[51], while footprinting experiments [30, 56, 57] have demonstrated the existence of prominent binding at both CpG and TpA sites, although this latter technique is unable to ascribe these to particular binding modes. Kelly et al. [26] demonstrated that fluorescence and topoisomerase studies of DNA complexes are useful for distinguishing intercalators (like H_2TMPyP4) from non-intercalators (like ZnTMPyP4). Geacintov et al. [58], using linear flow dichroism techniques, also concluded that five-coordinate ZnTMPyP4 is an outside binder, with the plane of the porphine core making an angle of 62–67° with respect to the twofold DNA helical axis, whereas H_2TMPyP4 is perpendicular to this axis as expected for an intercalator. They confirmed that the binding mode for the metal-free derivative changes with salt concentration in the manner previously proposed [21]. Kim and coworker by CD and LD provided a simple explanation of the preference of H_2TMPyP4 for intercalation in G–C sequence, studying the binding mode of H_2TMPyP4 to poly(dI–dC). They observed that removing the amino group of guanine base, which is located in the minor groove and provides steric hindrance for an incoming drug, the spectroscopic feature for the H_2TMPyP4 poly(dI–dC) systems is very similar to that of the H_2TMPyP4 poly(dA–dT) complex. These evidences indicate that amino group not only provides steric hindrance for minor groove binder but also takes an important role in stabilizing the intercalated porphyrins [59].

Further evidence for H_2TMPyP4 being distributed between intercalated and outside bound forms comes from fluorescence lifetime studies [60, 61], while ESR, luminescence, and ENDOR measurements are consistent with CuTMPyP4 intercalation [62–65], and resonance Raman (RR) results [66–71] support the proposal relating porphyrin structure and base pair composition to binding mode [17, 72]. VCD spectroscopy used by Urbanova demonstrated the priority of intercalation to the external minor groove binding. The intercalation is accompanied by

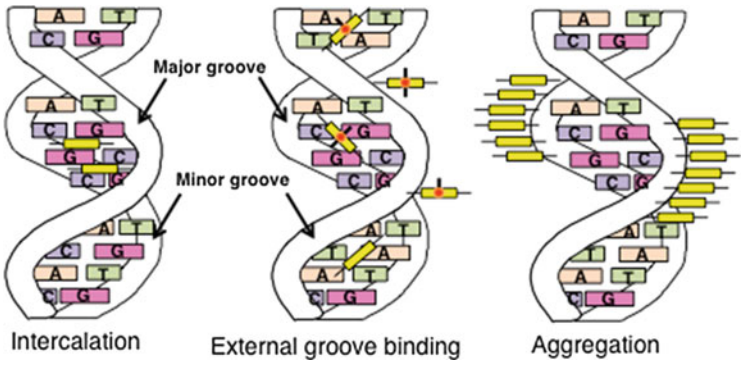

Fig. 6 Schematic summary of several porphyrin–DNA-binding modes

DNA distortions, in the region of G–C base pairs. The G–C intercalating sites are saturated at ratio 4:1–5:1; consequently, H_2TMPyP4 interacts with DNA by minor groove binding and external binding at phosphate backbone at high concentration of H_2TMPyP4 [73–75]. While a recently published X-ray structure raises the possibility that CuTMPyP4 binds to DNA via "hemi-intercalation" involving a "flipped-out" cytosine base [76], luminescence studies imply that this bonding model may not be applicable in solution [77]. Molecular modeling study achieved by Neidle has showed that only the CpG site can have full ligand intercalation, since the thymine methyl group sterically hinders such geometry at TpA sites [57].

In summary, certain generalizations concerning the relationship of DNA composition to porphyrin binding mode seem secure. Intercalation is favored in regions of DNA rich in G–C base pairs [17] with the CpG site being particularly attractive for this binding type [64, 78]. External binding by monomeric, ground-state porphyrins occurs primarily in the minor groove and especially in regions rich in A–T base pairs (although some major groove binding has been detected for Co(III) TMPyP4, V(II)(=O)TMPyP4 [79], ZnTMPyP4 [80], and MnTMPyP4 [81, 82] at a high drug load or if no A–T base pairs are present) (Fig. 6). One experiment that allows to distinguish between minor and major groove binder is by using poly (dI–dC); in this polynucleotide, in fact, the major groove is similar to that of the G–C pair, while its minor groove resembles the A–T base pairs (assuming the same secondary structure for all polynucleotides). Therefore, if porphyrinoids bind at the minor groove, the spectral properties of the poly(dA–dT) and poly(dI–dC) complexes are expected to be similar. On the other hand, the spectral properties of the porphyrin–poly(dG–dC) and poly(dI–dC) complexes will be similar if H_2TMPyP4 binds at the major groove. This method was used by Kim to characterize the binding of V(II)(=O)TMPyP4 with DNA. As a result, V(II)(=O)TMPyP4 binds to the minor groove of all DNA at lower ratios while stacks at the outside of DNA at higher ratios [83]. Yamamoto demonstrated by NMR, CD, and UV study that H_2TMPyP4 binds in the major groove of d(GCTTAAGC) because the size of the groove in duplex DNA depends upon the sequence. In fact, the major groove of

the TTAA region becomes narrower than in A–T alternate sequence and hence is expected to provide a more suitable pocket for H_2TMPyP4 binding than the minor groove [84]. The external, groove binding is "end on" for the most part and causes some disruption of the A–T hydrogen bonding pattern. If the steric features of the porphyrin are such as to prevent close contact with the minor groove of DNA, the A–T specificity is relaxed [30] and the binding becomes almost entirely based on electrostatic interactions ("territorial" binding).

Issues regarding the aggregation state of DNA-bound porphyrins have interested investigators almost from the very beginning. A very early report indicated that, when added to DNA under high drug load conditions, H_2TMAP aggregates on the DNA surface [85]. The induced circular dichroism signal under these conditions is bisignate and conservative. Although the magnitude of the features is not much different from those for monomeric porphyrins, it was thought that this complex involved an extended array of porphyrins. However, other evidence (circular dichroism and RLS) suggests that these aggregates probably are more modest in size. Similar results were obtained for NiTMPyP4 with poly(dA–dT) [24], but once again, it is likely that aggregation is limited, in contrast to the extended assemblies described below. In studies of DNA-bound *trans*-H_2Pagg, induced circular dichroism signals of an unusual shape and size are observed [39, 42, 86]. The signals are bisignate, markedly nonsymmetric, and from one to two orders of magnitude larger than for bound H_2TMPyP4 or H_2TMAP; values of $\Delta\varepsilon \sim 10^3\ M^{-1}\ cm^{-1}$ are observed. The shape and especially the size of the CD signals could be best accounted for in terms of an extended, electronically coupled, organized array of porphyrin molecules [87]. The shape of CD signal of aggregated porphyrin (H_2TMPyP4) on polynucleotides was used by Kim to recognize the alternating and non-alternating arrangement of DNA bases. In particular as the population of the porphyrin increases (i.e., high porphyrin/DNA ratio), stacking interaction between porphyrins becomes dominant and this interaction is strong enough to move the porphyrins bound to the groove or intercalated, changing the binding mode; in fact, a bisignate CD signal appears. The sign of excitonic CD depends on the order of the DNA bases; the CD spectra of H_2TMPyP complexed with non-alternating homopolymer poly(dA) · poly(dT) or poly(dG) · poly(dC) are characterized by a positive band at short wavelengths followed by a negative band at long wavelengths. In contrast, those complexed with alternating polynucleotide poly(dA–dT) or poly(dG–dC) were opposite to those of non-alternating homopolymers (Fig. 7). Hence, they concluded the signs of excitonic CD depend on the arrangement of the DNA bases, not on the nature of them [88].

In addition to the metal-free derivative, *trans*-CuPagg was also found to produce large induced CD signals. However, under similar conditions, the concentration of salt required to induce *trans*-CuPagg aggregation is higher than that required for the self-assembly of the naked *trans*-H_2Pagg [40]. This is in contrast to *trans*-AuPagg which gives induced CD patterns similar to those for CuTMPyP4 or other monomeric four-coordinate metalloporphyrin intercalators on binding to DNA [40]. Furthermore, the extent of aggregation of *trans*-H_2Pagg and *trans*-CuPagg depends

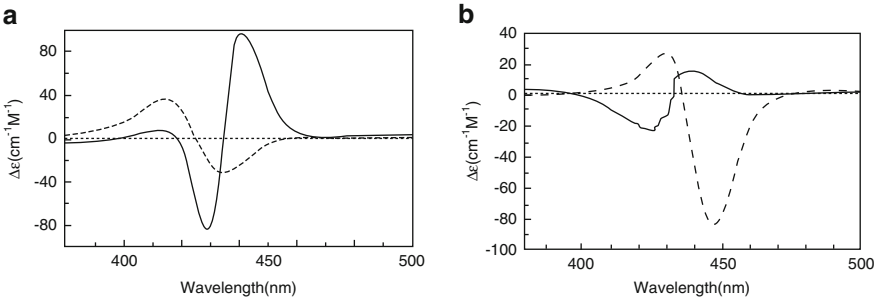

Fig. 7 CD spectra of H_2TMPyP4 5 μM (**a**) in the presence of poly(dA–dT) (*continuous line*) or poly(dA) · poly(dT) (*dashed line*) and (**b**) in the presence of poly(dG–dC) (*continuous line*) or poly (dG) · poly(dC) (*dashed line*). In all experiments, porphyrin/DNA ratio is 0.4. Modified from [88]

on template composition; it is promoted by a template consisting entirely of G–C base pairs as compared to one having fewer (CT-DNA) or no G–C units (poly (dA–dT)) [42]. As part of studies on DNA-bound porphyrin assemblies, the utility of a nonconventional light-scattering method (in which the radiation employed is within absorption Soret maximum) was demonstrated [40, 89]. For extended, electronically interacting chromophore arrays, a remarkable enhancement of light scattering is observed within these absorption envelopes. These so-called enhanced RLS signals are useful not only for identifying such assemblies but for characterizing them as well [89, 90].

In fact, this technique was used by Pasternack and coworker to control the extent of porphyrin aggregation on a nucleic acid scaffold. When more affine intercalator binder, Au(III)TMPyP4, is added to a preformed intercalated *trans*-H_2Pagg/DNA complex, a slight decrease in the magnitude of the ICD bands of the latter porphyrins can be detected, concomitant with the appearance of a new negative component around 410 nm due to intercalated AuTMPyP4. This observation suggests that the gold(III) derivative, bearing five positive charges, competes effectively with *trans*-H_2Pagg (which is a dicationic species) for binding sites in the double helix, partially displacing the latter species. Upon addition of NaCl, aggregation is fostered, and large bisignated ICD signals are detected in the Soret region. At a fixed concentration of *trans*-H_2Pagg, the intensity of the ICD signal and the corresponding RLS intensity, hence the extent of aggregate, depend linearly on the concentration of the added Au(III)TMPyP4 [91].

An important aspect studied by Kim is the ability of the porphyrins to quench the fluorescence of intercalated ethidium. Energy and charge transfer along DNA has been a subject of intense study since the stacked π-orbitals of DNA base pairs were found to be an effective medium for electron and hole transfer [92–98]. The biological importance of charge transport has been highlighted by the discovery of distance oxidative damage to DNA in the cell nucleus [99, 100]. Strong overlap between emission spectrum of ethidium and the absorption spectrum of porphyrins when they simultaneously bind to DNA was found suggesting the mechanism

behind energy transfer is, at least in part, the Förster-type resonance energy transfer (FRET). The minimum distance in base pairs between ethidium and porphyrin required to permit the excited ethidium to emit a photon was the longest for CoTMPyP4 being 17.6 bp and was the shortest for CuTMPyP4 and NiTMPyP4 at 8.0 bp. The variation in the distance was almost proportional to the extent of the spectral overlap, the common area under emission spectrum of ethidium and absorption spectrum of porphyrin, supporting the FRET mechanism, whereas the effect of the orientation factor which was considered by relative binding geometry was limited [101, 102].

3 Substituted Cationic Porphyrins

In the previous paragraph, we analyzed the interaction of free base and metallo derivatives of H_2TMPyP4 and very similar cationic derivatives with DNA. One of the approaches developed, after the characterization of the binding mode of model porphyrin, H_2TMPyP4, with DNA is that to use porphyrins with chemical modification in the peripheral position or in the core ring in order to enhance the DNA-binding affinity and DNA-photocleavage efficacy. In this paragraph we explore the role of the length of peripheral substituent, the distance between neighboring positive charges of porphyrinoids, the number of positive charge, and the composition of the chemical modification.

3.1 Porphyrin Derivatives with Chemical Modifications in the Peripheral Positions

The first studies concerning the influence of the length of peripheral substituent were conducted with *N*-alkyl substituted porphyrins. From these studies arose that alkyl substituents don't modulate the binding interactions. Dabrowiak [103] showed that the DNA cleavage properties of MnTDEt_{Est}PyP4 ethyl ester substituted (Fig. 8) are the same of those obtained with model compound, MnTMpyP4 [104], suggesting an end-on bound via the minor groove binding in a melted or partially melted region of DNA. Marzilli et al. [105] by RR, NMR, UV, viscosity, and equilibrium dialysis measures with H_2TPrPyP4, H_2TEtOHPyP4, and Ni(II) derivatives (Fig. 8) obtain very similar results compared to those with H_2TMPyP4 species. It is suggested that both H_2TPrPyP4 and H_2TEtOHPyP4 bind to G–C regions of DNA in the same intercalative manner as H_2TMpyP4 with the *N*-alkyl substituent extended into the solvent. For A–T regions of DNA, the binding of H_2TPrPyP4 and H_2TEtOHPyP4 is nonintercalative, as found previously for H_2TMPyP4. The NiTPrPy4 and NiTEtOHPyP4 cations bind to these polymers (poly(dG–dC), poly(dA–dT), and CT-DNA) in a similar manner to the apo-porphyrins. The similar Raman spectral

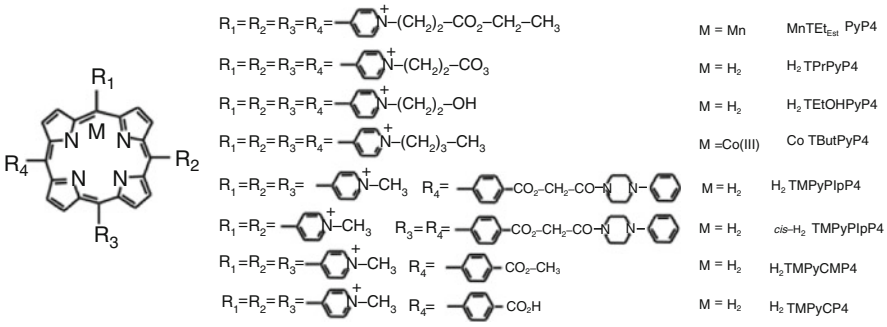

Fig. 8 Structure of several porphyrin derivatives

changes for the two Ni porphyrins upon addition of [poly(dA–dT)] suggest that partial intercalation is not occurring because models indicate that it would be difficult to accommodate the bulkier *N*-alkyl substituents.

Kim and coworker [106] based on their CD, LD, and contact energy transfer measurements on H_2TMPyP4, H_2TButPyP4, CoTMPyP4, and CoTButPyP4 concluded that the length of the side chain does not affect the binding geometry of porphyrin. In fact, non-metallo-porphyrins are confirmed to be intercalated to poly(dG–dC), while they bind to the minor groove of the poly(dA–dT). They demonstrated that the binding geometries of metalloporphyrins are different when complexed with poly(dA–dT) and poly(dG–dC) although both can be considered as groove binding; in particular, the metalloporphyrin–poly(dG–dC) complexes exhibited 30–40° angle between the molecular plane of the porphyrin and the polynucleotide helix axis, while the angle between the transition moment of the drug and the helix axis of poly(dA–dT) is 45–50° as observed for most minor groove-binding drugs. For these reasons, they proposed that porphyrins may be located in the major groove of poly(dG–dC). Finally, they showed that the excited energy can be transferred from the nucleobases even to the porphyrin which is known to bind to the "outside" of the polynucleotide. In contrast to the strong energy transfer from nucleobases to the bound porphyrin observed for the non-metallo-porphyrin–poly (dA–dT) complex, the excited energy of the nucleobases was not transferred to porphyrins when Co(III) was present. Two factors, distance and relative orientation, may affect the efficiency of the energy transfer. Since the orientations of the porphyrin in the presence and absence of the central metal were similar when bound to poly(dA–dT), the difference in the fluorescence energy transfer may be attributed to the distance between the porphyrin and nucleobases. The central octahedral metal complex may inhibit the deep insertion of porphyrin from the groove. Similar to the poly(dA–dT) case, the metalloporphyrin–poly(dG–dC) complexes exhibit a null energy transfer, indicating that the metalloporphyrin molecule is quite distant from the nucleobases. It is not surprising that a strong energy transfer occurs for the intercalated porphyrin because, by definition, porphyrin is in contact with the nucleobases.

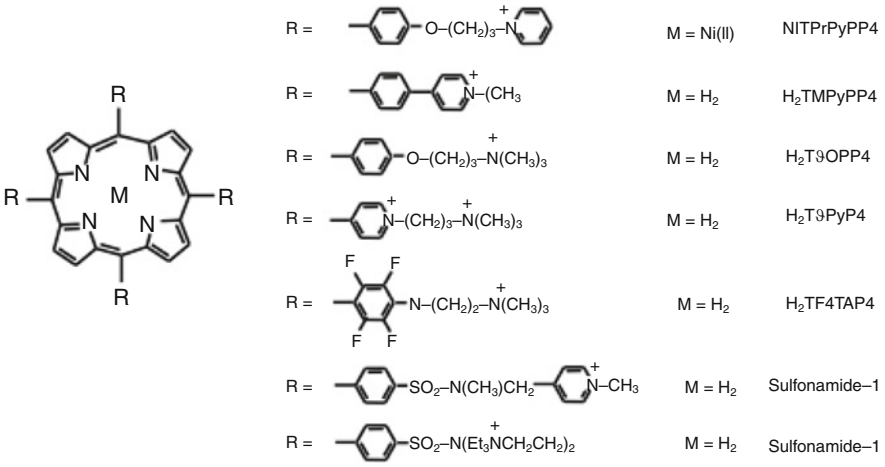

Fig. 9 Structure of porphyrins meso-derivatives

Also introducing bioactive moieties, as piperazine [107, 108], onto the periphery of the porphyrin, the DNA-binding mode is not affected. Li and coworker studied the binding properties of cationic porphyrin–phenylpiperazine hybrids (H_2TMPyPipP4, *cis*-H_2TMPyPipP4, Fig. 8) to CT-DNA by using absorption, fluorescence, and CD spectra. They observed that with a moderate ionic strength, the binding of porphyrin with one or two (at *cis* position) phenylpiperazines, introduced onto the periphery of cationic porphyrin intercalation of porphyrin into CT-DNA, occurred. They analyzed, as well, the effect of one carboxymethyl group and one carboxyl group (H_2TMPyCMP4 and H_2TMPyCP4, Fig. 8) inserted in one of the four *meso*-positions of the H_2TMPyP4 showing that the interaction with DNA was complex and involves both intercalation and outside binding [109].

Increasing the distance of peripheral charge in the meso-position from the core of the porphyrin, it is possible to avoid intercalation processes over outside binding by self-stacking. This has been obtained by Zhou and Kim using different modified porphyrins, H_2TPrPyPP4 (Ni(II) derivative as well) and H_2TMPyPP4, respectively (Fig. 9) [110, 111]. By several spectroscopic techniques, they observed that these porphyrins can bind to DNA by outside binds by self-stacking both at low and high porphyrin/DNA ratio. A qualitative explanation for the observed self-stacking is that the porphyrins with alkyl-connected N-position of pyridine can strongly interact with the anionic phosphates of DNA and lead to hydrophobic complex.

A very interesting study was published by Marzilli and coworker using tentacle porphyrin H_2T9OPP4, which is an electron-rich porphyrin, consistent with the greater electron-donor phenoxy aromatic substituents (Fig. 9). By CD, UV, and fluorescence spectroscopy they have found extensive self-stacking of H_2T9OPP4 along the DNA, under all condition studied. They suggest that the long flexible arms probably favor the outside self-stacking binding. However, they observed at least two different types of self-stacking, highly stacked and intermediate stacked,

that they associated to binding of free-base and protonated form of $H_2T9OPP4$, respectively [112, 113]. Due to the relatively high pK_a of $H_2T9OPP4$ (pK_a 4.6), it is possible for the porphyrin to be bound to CT-DNA as the protonated species at physiological pH [114]. The protonated porphyrin exhibits DNA-binding characteristics that are different from those of the free base, of the red shift in fluorescence, and of the Soret absorption band [114]. This hypothesis is also confirmed by CD data; in fact, conservative-type ICD spectrum, observed in the presence of CT-DNA, changes to a simple positive CD band upon protonation of $H_2T9OPP4$ indicating that the binding mode underwent a transition from outside binding with high intense self-stacking to simple outside binding.

By comparing these results with those obtained using another tentacle porphyrin ($H_2T9PyP4$ Fig. 9) similar in size to $H_2T9OPP4$, but bearing eight positive charges, showing negative ICD signal with poly(dG–dC) indicating intercalation binding [115], and another electron-deficient tentacle porphyrin, having bulky substituent, showing external binding, ($H_2T9F4TAP$, Fig. 9) [116], they concluded that the results presented provided clear evidence that porphyrin intercalation does require both planar traversing groups and an electron-deficient porphyrin core. The studies with tentacle porphyrins thus indicated that, while the influence of porphyrin electron richness on the binding mode of relatively thin porphyrins was not important, pyridinium groups appear to be necessary for intercalation. To solve this doubt they designed a new porphyrin, expanding the size of the pyridinium-containing porphyrins by placing a linking group between the porphyrin core and the pyridinium groups. These groups are linked to the 4-position of the phenylene group of the porphyrin by secondary ($-SO_2NHR$) or tertiary ($-SO_2NR2$) sulfonamide groups (Fig. 9) [117]. The authors designed these porphyrins to determine whether the new porphyrins containing N-MPy groups (sulfonamide-1) would be intercalators and whether the new porphyrins lacking N-MPy groups (sulfonamide-2) would allow to gain some insight into factors that might influence outside binding interactions. The DNA-induced changes in the porphyrin Soret region (a positive induced CD feature and, at high DNA concentration, increases in the Soret band and fluorescence intensities) indicate that the new porphyrins interact with DNA in an outside, non-self-stacking binding mode. This finding allows the authors to conclude that direct attachment of the *N*-alkylpyridinium groups to the porphyrin ring in such a way that the *N*-alkylpyridinium group can become nearly coplanar with the porphyrin ring is necessary for intercalation to occur [118].

The extensive exploration of cationic porphyrins has been mainly limited to porphyrins with six-membered rings as meso-substituents. Inoue and coworker report on the porphyrins meso-substituted by diazole rings such as imidazoles ($H_2TDMImP4$) and pyrazoles ($H_2TDMPzP4$) (Fig. 10) which have recently become of interest [119–122]. These two compounds interact with CT-DNA in different binding modes from that $H_2TMPyP4$, in particular $H_2TDMImP4$ outside binds to the minor groove of CT-DNA while $H_2TDMPzP4$ intercalates into CT-DNA [54]. Then they analyzed the interaction of the metallo derivatives (M = Mn(III), Ni(II), Cu(II), or Zn(II)) of $H_2TDMPZP4$ with CT-DNA, poly(dA–dT), and poly(dG–dC). NiTDMPzP4 and CuTDMPzP4 intercalate into the 5′GC3′ sequence of CT-DNA;

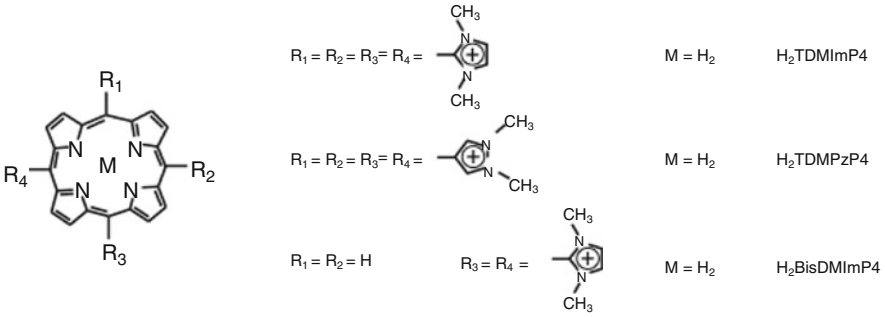

Fig. 10 Molecular structures of porphyrin substituent

and H_2TDMPzP4, NiTDMPzP4, and CuTDMPzP4 are intercalated into poly (dG–dC) and are outside bound to the major groove of poly(dA–dT). MnTDMPzP4 is bound edge on at the 5′TA3′ step of the minor groove of CT-DNA, while ZnTDMPzP4 is bound face on at the 5′TA3′ step of the major groove of CT-DNA and is outside bound to the minor groove of poly(dA–dT), but, surprisingly, is intercalated into poly(dG–dC) [55, 123, 124]. In order to investigate the effect of number of five-membered ring substituents, still Inoue studied the binding of H_2BisDMImP4, bearing two diazole rings (Fig. 10), and some metallo derivatives such as Cu(II) and Zn(II) [125]. The copper(II) complex, CuBisDMImP4, intercalates into the base pairs of DNA such as CT-DNA, poly(dA–dT), and poly(dG–dC) to stabilize the DNA duplex due to its high affinity for them. In contrast, the zinc(II) complex, ZnBisDMImP4, binds edge on to CT-DNA, poly(dA–dT), and poly (dG–dC) as an outside binder.

Over the studies achieved with substituted porphyrins aiming to understanding the characteristics involved in DNA binding, there are several groups that synthetized different porphyrin derivatives for other purposes. Dixon and coworker [126] designed a molecule with donor and acceptor covalently attached each other, to provide a new approach to probe the role of the DNA in controlling ET processes. The ferrocenyl porphyrin used, H_2TMPyPFc (Fig. 11), exhibits intercalation binding at low ionic strength and outside binding at increased ionic strength. When H_2TMPyPFc is intercalated into DNA, the average rate of photoinduced intramolecular electron transfer is not appreciably reduced, suggesting that electronic coupling between the D–A pair is strong even under conditions where close contact is restricted. Garcia et al. [127] in order to improve the PDT efficiency in cancer cells suggest to increase the selectivity of photosensitizing porphyrin. The strategy adopted is to use polyamine-conjugated porphyrins and investigate the DNA photocleavage. All compounds analyzed are efficient singlet oxygen generators and show a high photostability. UV–Vis spectral changes indicate that *cis*-dipolyamine protoporphyrin IX derivatives, **1** and **2** (Fig. 11), strongly bind to DNA, a result underscored by the DNA-photocleavage efficiency of these compounds. These results also suggest

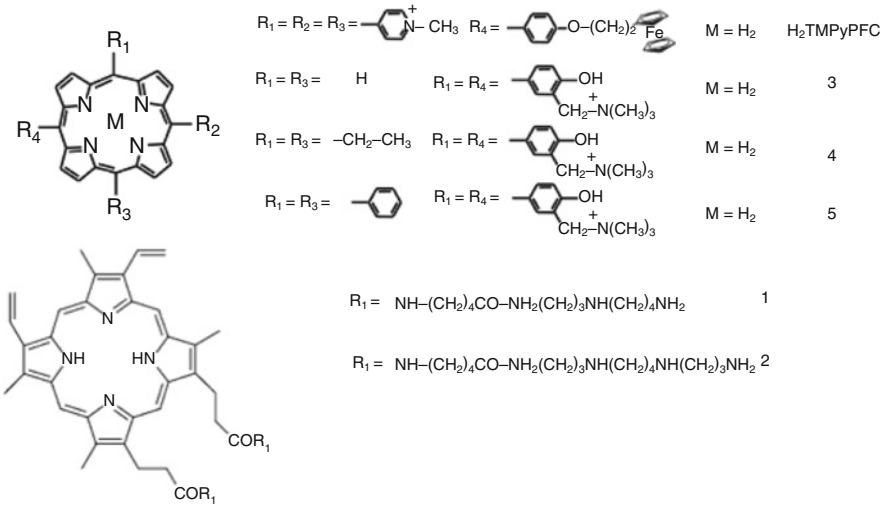

Fig. 11 Molecular structures of porphyrinic derivatives

that the number, together with the positions of the polyamines on the macrocycle, plays important roles in determining their binding to DNA and therefore their photocleavage abilities.

Porphyrins designed by Zhou and coworker with phenol quaternary ammonium in the meso-positions, **3**, **4**, **5** (Fig. 11), exhibit DNA photocleavage and induce apoptosis in HeLa cells as well [128, 129]; however, no studies on the binding modes were carried out for this compound. Following the same idea, i.e., to design a high selective photosensitizer with anticancer activity, Swavey achieved several studies with polypyridyl ruthenium(II)-substituted porphyrins. In order to create multimetallic supramolecular complexes as potential antitumor agent, he started to incorporate pentafluorophenyl groups into the periphery of the porphyrins (H_2DPDPFPP, Fig. 12), leading to enhanced excited state lifetimes [130]. Then in order to add water solubility to the porphyrin complexes, ruthenium polypyridyl moieties have been coordinated to peripheral groups of the porphyrin core **6** (Fig. 12). The ruthenium groups, in addition to adding a cationic charge, are stable in many oxidation states under physiological conditions. With these porphyrins gel electrophoresis studies with linearized pUC18 indicate an interaction between the metallated porphyrin and DNA which is confirmed by UV–Vis titrations with CT-DNA giving a binding constant of ca. 10^5 M^{-1}. When buffered, pH 7, solutions of circular plasmid DNA containing the ruthenium porphyrin are irradiated with a 50 W tungsten lamp, and cleavage of the DNA is observed [131, 132]. The insertion of Cu(II) metal in the core of the porphyrin (**7**, Fig. 12) gives unexpected effect on the stabilizing of the HOMO orbitals of the Ru(II) peripheral unit [133]. An extension of these works involves the addition of a square planar platinum(II) complex to the porphyrin through coordination to a meso-pyridyl nitrogen. The choice of platinum originates from the well-known anticancer drug *cis*-platin (*cis*-dichlorodiamineplatinum(II)) which has been

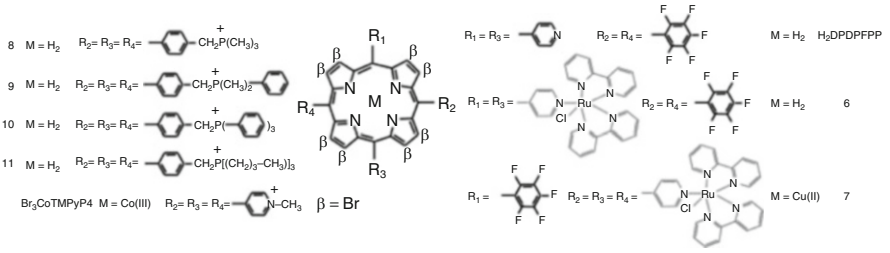

Fig. 12 Structures of porphyrin derivatives

used for over 30 years for the treatment of a variety of cancers [134]. The new complex binds to plasmid DNA more efficiently than the well-known anticancer drug *cis*-platin, as determined by gel electrophoresis. The rate of binding is increased by irradiating the samples with visible light. One explanation is that irradiation of the Cu/Ru/Pt complex increases the rate of hydrolysis of the platinum moiety which subsequently binds to the DNA [135].

Kubat and colleagues [136, 137] studied the effect of phosphonium substituent on the aggregation process on DNA. They point out the importance of the supramolecular assemblies of porphyrins onto DNA, because the enforced helical structures of photoactive and redox active molecules such as porphyrins can be utilized for construction of molecular-based devices. By applying absorption, fluorescence, and light-scattering spectra, they have shown that all phosphonium porphyrins described in their study (**8**, **9**, **10**, **11**, Fig. 12) were found to bind to the phosphate backbone of a nucleic acid with a significant preference for A–T base pair sequences. These porphyrins show a great tendency to aggregate in the solution. It was demonstrated that the stacking interaction between porphyrin units (cofacial aggregates) and the hydrophobic interactions between alkyl/aryl residues of the phosphonium moieties and the porphyrin macrocycles stabilize the aggregated forms. Such stabilization of the aggregates is stronger than coulombic attraction between the positively charged phosphonium moieties and the phosphate backbone of nucleic acids. The direct result of this behavior is that the porphyrin derivatives are deposited on the DNA surface in the same form as they were in solution.

Again, with the aim to create a molecule highly efficient in the DNA scission, Yellappa and coworker [138] designed a metallopyridyl porphyrin, with 8 Br substituent in the β-pyrrole position in order to make more electrophilic the core of the porphyrin (Br_8CoTMPyP4, Fig. 12). Induced CD bands were noticed in the Soret region of the complexes due to the interaction of these complexes with different polynucleotides, and an analysis of the CD spectra supported a mainly external mode of binding. The electrochemical studies coupled with the gel electrophoresis results clearly suggest that the cleavage occurs at the A–T base pairs and not at the G–C base pairs. In line with the aim of this former study, Pandey [139] analyzed the influence of the substituents in the non-meso-positions of the

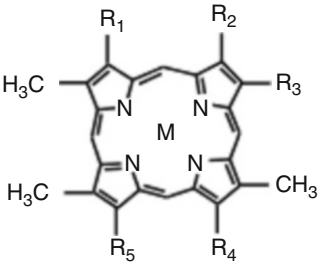

12	$R_1 = R_3 =$ –CH=CH–CH_2–$\overset{+}{N}(CH_3)_3$	$R_2 = -CH_3$	$R_4 = R_5 = (CH_2)_2CO_2CH_3$	M = Zn(II)
13	$R_1 = R_4 =$ –CH=CH–CH_2–$\overset{+}{N}(CH_3)_3$	$R_3 = -CH_3$	$R_2 = R_5 = (CH_2)_2CO_2CH_3$	M = Zn(II)
14	$R_1 = R_3 =$ –CH=CH–CH_2–$\overset{+}{N}(CH_3)_3$	$R_2 = -CH_3$	$R_4 = R_5 = (CH_2)_2CO_2CH_3$	$M = H_2$
15	$R_1 = R_3 =$ –CH=CH–CH_2–$\overset{+}{N}(CH_3)_3$	$R_2 = -CH_3$	$R_4 = R_5 = (CH_2)_2CO_2CH_3$	M = Ni(II)
16	$R_1 = R_4 =$ –CH=CH–CH_2–$\overset{+}{N}(CH_3)_3$	$R_3 = -CH_3$	$R_2 = R_5 = (CH_2)_2CO_2CH_3$	$M = H_2$
17	$R_1 = R_4 =$ –CH_2–$\overset{+}{N}(CH_3)_3$	$R_2 = -CH_3$	$R_4 = R_5 = (CH_2)_2CO_2CH_3$	M = Zn(II)
18	$R_1 = R_3 =$ –CH_2–$\overset{+}{N}(CH_3)_3$	$R_2 = -CH_3$	$R_4 = R_5 = (CH_2)_2CO_2CH_3$	$M = H_2$

Fig. 13 Structure of non-meso-substituted porphyrins

porphyrin core, on the ability to bind and cleave DNA in the presence of light. They analyze several non-meso-derivatives (Fig. 13) by absorption, circular dichroism, unwinding assays, and the DNA photocleavage showing that non-meso-substituted cationic porphyrins bind, as well as photocleave, DNA efficiently. The results point toward intercalation of the Zn(II) porphyrins **12** and **13**. The nature of the binding obtained for zinc porphyrins **12** and **13** is surprising, due to the presence of the nonplanar substituents as well as the presence of metal zinc; both of these characteristics are thought to block intercalation [24, 140, 141]. Furthermore, the negative ellipticity obtained in the visible CD spectrums with calf thymus DNA and poly(dG–dC) for porphyrins **14**, **15**, and **16** indicates an intercalative mode of binding; however, this binding mode is not supported by unwinding assay.

Again, the positive peak in the CD spectra obtained with poly(dG–dC) and negative peak in the presence of poly(dA–dT) for porphyrin **17** completely differ from the ellipticity obtained under similar conditions for meso-substituted cationic porphyrins. The DNA-photocleavage characteristics of this series of cationic porphyrins were found to depend on the structural characteristics of the porphyrins such as (1) increase in the length of the side chain that is seen to increase the efficiency of cleavage (**18** vs **14**), (2) the position of the side chain on the porphyrin ring (**14** having substituent in 3 and 8 positions is more efficient of **16** supporting substituent in 3 and 13 positions), and (3) the presence of the chelating metal in **17**, **12**, and **13** as compared to the non-metallo-porphyrins **18**, **14**, and **16**, respectively.

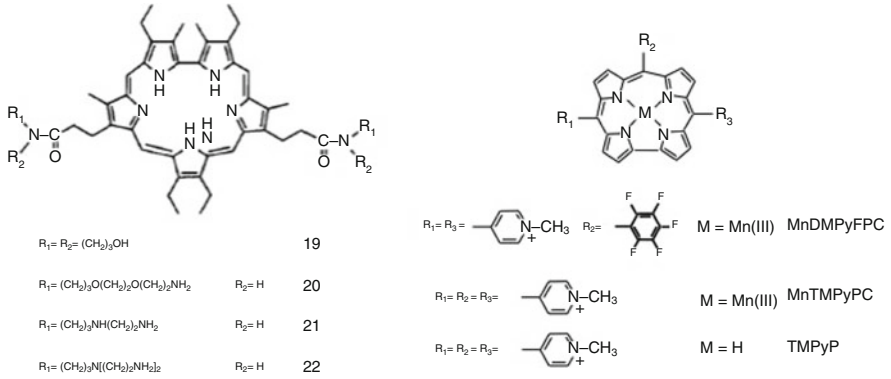

Fig. 14 Polyamine-conjugated sapphyrins and molecular structure of corroles

3.2 Porphyrinoid Derivatives with Different Composition of the Core Ring

Modifications in the macrocycle ring of the porphyrinoids cause variation in the photophysical proprieties of the macrocycle, i.e., red shift of the Soret band. This effect increases the photocleavage capabilities of chromophores, when irradiated at red-shifted wavelengths (>600 nm) [142, 143]. This region is preferable, as it is here that the bodily tissues are most transparent [144]. In the context of this program Sessler reported that sapphyrin **19** (a pentapyrrolic "expanded" porphyrin) is capable of photocleaving DNA when irradiated at wavelengths above 620 nm [142–145]. In an attempt to increase the efficiency as photosensitizer of the sapphyrins, Sessler synthetized three sapphyrin derivatives, with polyamine conjugates **20**, **21**, and **22** (Fig. 14) comparing results with non-conjugate sapphyrin compound [146, 147]. Having the inner cavity larger and more basic than normal porphyrins [148], sapphyrin derivatives are protonated and positively charged at neutral pH. This characteristic allows to chelate the anionic phosphate backbone of DNA in a precise, rigid fashion [149]. They found that amino-functionalized sapphyrin derivatives **20**, **21**, and **22** showed significantly more effective cleavage than compound **19**.

On the contrary corroles have a smaller ring than porphyrin, however they show a better efficacy in inhibiting tumor progression and metastasis in animal models than analogous porphyrins. Gross synthetized manganese(III) corrole with two pyridinium groups, MnDMPyFPP (Fig. 14), to study the interactions with DNA and then compared these with analogue porphyrin. By CD experiments, he observed that although the spectrum of MnDMPyFPC is composed of both negative and positive components, that of the analogous porphyrin derivative displays only a positive CD band that is also of much lower ellipticity. He suggests that the corrole is capable of both intercalate and outside binding with DNA, whereas the analogous porphyrin is only capable of outside binding [150]. Moreover, cationic manganese corrole has been proved catalytic activity for the oxidative cleavage DNA [150,

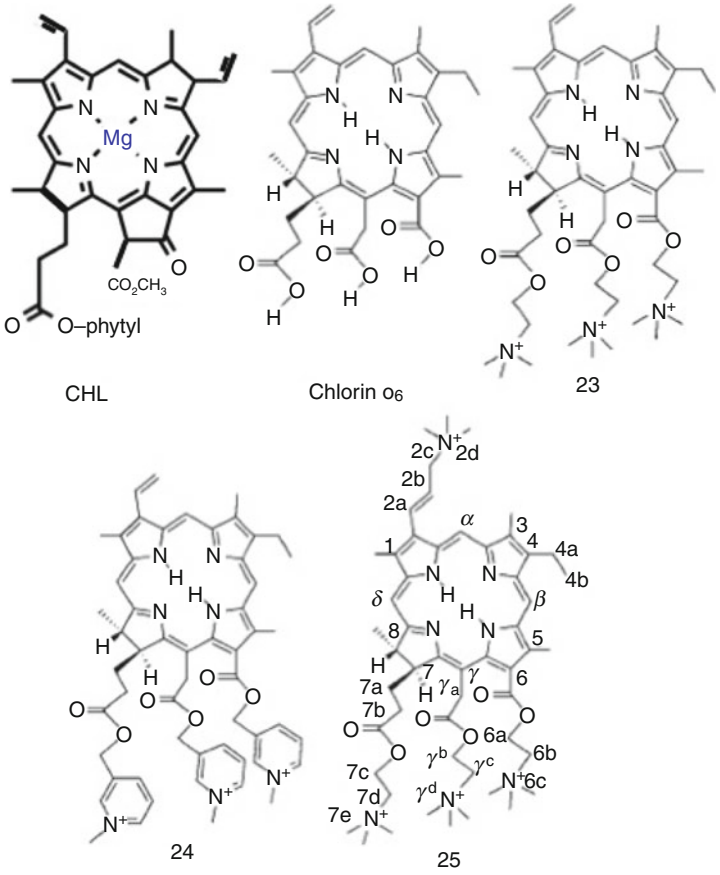

Fig. 15 Chlorophyll and derivatives

151]. Lu presented the DNA cleavage mediated by water-soluble manganese (III) corrole MnTMPyC, which binds strongly to CT-DNA manifesting an outside groove binding tuned by absorption spectra, viscosity measurements, and induced CD spectra [152]. Purrello et al. characterized the binding of H_2TMPyC and Ge (II) derivatives with CT-DNA by using UV and CD techniques, demonstrating the ability of the free-base corrole to intercalate into the basis of DNA causing conformational distortion of the duplex. Also the binding of GeTMPyC with CT-DNA involves duplex distortion; however, this molecule is an external groove binder [153].

Another porphyrinoid macrocycle used as DNA photocleaver is chlorophyll (CHL) (Fig. 15). Structural analysis of DNA–CHL complexes is carried out by Neault and Tajmir-Riahi, with Fourier transformed infrared difference spectroscopy. Spectroscopic results showed that CHL is an external DNA binder with no affinity for DNA intercalation. At low pigment concentration ($r = 1/160$, 1/80, and 1/40), there are two major binding sites for CHL on DNA duplex: (1) Mg-PO_2 and

(2) Mg-N7 (guanine). The pigment distributions are 60% with the backbone PO_2 group and 20% with the G–C base pairs. The chlorophyll interaction is associated with a major reduction of B-DNA structure in favor of A-DNA. At high chlorophyll content ($r = 1/10$), helix opening occurs, with major spectral alterations of the G–C and A–T bases. At high chlorophyll concentration (1/5), pigment aggregation is observed, which does not favor CHL–DNA complexation.

Unfortunately, the poor solubility or self-aggregation of the chlorophyll derivatives in the buffer solution not only hinders their intercalation into the base pairs of the double-helical DNA but also deactivates the photoexcited dye molecules [154, 155]. To avoid this problem Inoue designed and synthesized three cationic water-soluble chlorin e6 (Fig. 15) derivatives, **23**, **24**, and **25** (Fig. 15). The DNA unwinding assay, melting temperature experiments of double-stranded DNA, and the induced CD and visible absorption spectra have revealed that **23** and **25** are intercalated into the base pairs of the double-helical DNA, while **24** is bound to outside the minor groove of the double-helical DNA. The cationic water-soluble chlorin e6 derivatives effectively cleave the double-helical DNA under photoirradiation and the DNA-photocleavage activity increases in the order **25** > **23** > **24** [156].

Due to the intense red shift observed in absorption spectrum, phthalocyanines and analogues such as porphyrazine are among the porphyrinoids more studied as photosensitizer. Interaction of Cu(2,3-tmtppa)4**C** and Cu(3,4-tmtppa)4**C** (Fig. 16) with calf thymus DNA was studied by UV–visible and CD spectroscopies and viscometric method. The existence of extensive hypochromicity, large red shift, and negative CD in the visible part of Cu(3,4-tmtppa)4C spectra suggested an intercalation binding mode. Analysis of the moderate hypochromicity, red shift, and bisignate CD in the Q-band absorption region of Cu(2,3-tmtppa)4C spectra possibly led us to the coexistence of intercalation and outside binding modes [157, 158].

Then Hoffman synthetized a new class of cationic tetraazaporphyrins, the octa-methyl-pyridyl porphyrazines, including CuPz8+ and ZnPz8+ (Fig. 16) [159]. These octacationic macrocycles are directly functionalized at the **β**-pyrrole carbons with pyridyl groups to provide a higher charge per macrocycle, to decrease aggregation, and to avoid problems of isomer purification. The spectrum of Cupz8+ red shifts as DNA is added, which is interpreted as indicative of π stacking of the charged macrocycle as it binds electrostatically to the outside of the DNA duplex. The spectrum of Znpz8+ does not shift, indicative of simple electrostatic surface binding [160].

4 Anionic Porphyrins with Duplex DNA

The formation of porphyrin–DNA complexes, which is believed to be an important step leading to antitumor activity, as shown above, is known to be facilitated by the electrostatic attractions between the periphery of cationic porphyrins and the anionic phosphate backbone. On the other hand, the interaction of anionic

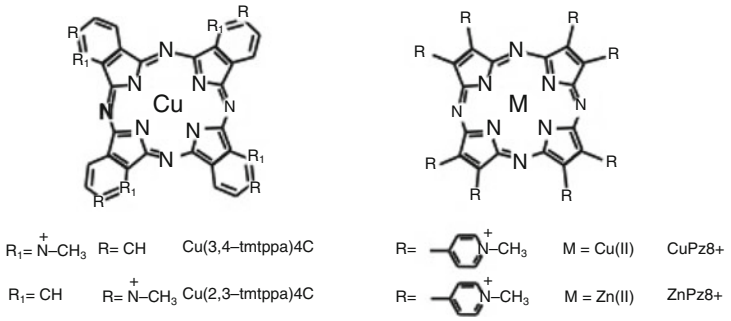

Fig. 16 Molecular structures of Phthalocyanine and porphyrazine derivatives

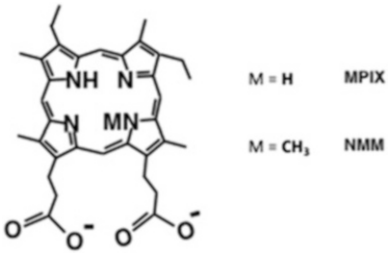

Fig. 17 Molecular structure of NMM and MPIX porphyrinoids

molecules with DNA has not been as well studied [161]. These studies show that the counterintuitive binding of anionic porphyrins to a twofold array of negative charges is driven by molecular recognition processes that can be deeply affected by the spatial distribution of the anionic substituents.

Li et al. [162] study the binding affinities of different DNA aptamers to NMM (Fig. 17) by footprinting experiments. The paper aims to isolate DNA aptamers for anionic porphyrins to study their ability to selective recognition of homologous porphyrins with minimal structural differences, i.e., MPIX (Fig. 17), and whether such discriminating aptamers would show chetalase-like activity. Ferrochelatase enzymes catalyze the insertion of Fe^{2+} ions into protoporphyrin IX, a key step in the biosynthetic pathway to heme [163]. The bent porphyrin NMM has been found to be a potent inhibitor of this enzyme, possibly because it resembles the transition state for the insertion of metal ions into its natural substrate, protoporphyrin IX [164]. This property was taken advantage of by Cochran and Schultz [165] to generate catalytic antibodies [166] that mimicked ferrochelatase.

Three approaches were attempted; one was methylation protection using dimethyl sulfate, which reveals the involvement of specific guanine N7 nitrogens in hydrogen bonding or in metal binding. The other two techniques were partial digestion by DNase I and DNA strand cleavage by bound hemin or meso-hemin moieties in the presence of superoxide (KO_2). Small- (PS) and full-sized (P) families

of aptamer clones have been used to scrutinize their ability to bind NMM. As a result among both P and PS families, the aptamers able to bind NMM contain guanine-rich regions. The selected aptamers used to study the binding affinities were able to bind NMM with sub-micromolar affinity, but the discrimination capability between NMM and MPIX, despite the lower affinity toward the latter, is not very high in the used experimental conditions. The binding sites of NMM involve the guanine N7 nitrogens in hydrogen bonding or metal binding. Iron (III) porphyrins, in the presence of strong oxidizing agents, are able to promote strand DNA cleavage, thus suggesting the capability of hemin (or meso-hemin) bound to aptamers to define binding domains as in situ footprints.

To summarize, for the small aptamers (PS2) DMS and hemin/KO_2, footprinting data indicated that the guanine-rich domains are responsible for binding porphyrins. The DNase I digestion data suggested that, for PS2, the conformation changes and the enzyme accessibility can extend well beyond the domains defined by the other two footprinting techniques.

Mutually consistent data referred to aptamers and short nucleotide oligomer indicate that NMM didn't bind to a preexisting higher-order structure formed by G-rich motif, but, more likely, induce distinctive folding patterns for the binding motif, thus influencing the overall folded structure of a number of aptamers.

UV absorption spectroscopy and CD spectroscopy investigated the mode of binding of NMM to folded aptamers. The UV data show a strong hypochromic effect (~10%), in the NMM (1 μM) Soret region, in the presence of an excess (5 μM) of PS2. No significant shift (~1 nm) is observed. As to the CD data, the short oligonucleotide did not give any CD signal in the absence of NMM while a more structured signal is observed in the presence of NMM, thus pointing to an overall nonhelical content of this small DNA molecule. PS2 gives the expected B-DNA CD spectrum that remains almost unvaried in the presence of NMM. No porphyrin CD-induced signal is observed in the porphyrin Soret region.

In the present study, the guanine quartets (G-quartets) might be responsible for NMM binding. The formation of G–G Hoogsteen hydrogen bonds can be responsible for the methylation protection observed for some of the studied aptamers even in the absence of NMM.

The interaction of NMM with folded DNA structures that possibly contain one or more G-quartets cannot be promoted by a classic intercalation mechanism as suggested by UV and CD measurements. In fact, the interaction of DNA-binding drugs with G-quartets through classical intercalation mechanism between adjacent G-quartets is accompanied by significant red shift and about 20% hypochromicity of the visible (ethidium) adsorption band.

Lauceri et al. [167] investigated the interactions of carboranylated porphyrin with DNA (Fig. 18). Water-soluble anionic nido-carboranyl-containing porphyrins have been proposed as boron delivery drugs in boron neutron capture therapy (BNCT) of tumors [168–171].

They highlight the importance of porphyrin inner core protonation. In fact, p-H_2TCP^{4-} has a high p*K*a (7.4), thus resulting to be fully protonated at pH 7. Spectral UV evidence (small red shift ~2 nm) and hypochromicity (~10%),

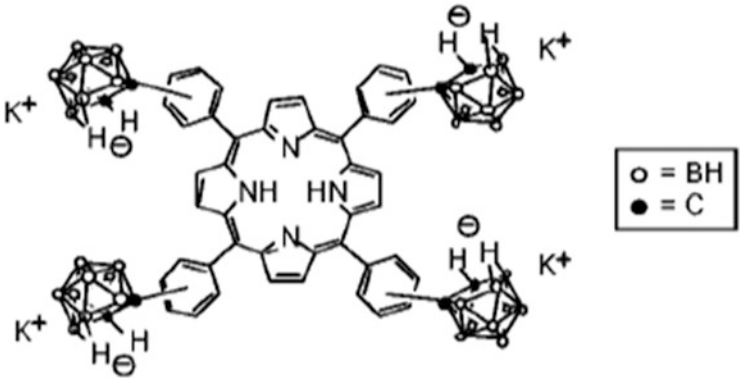

Fig. 18 Molecular structure of carboranylated porphyrins

small conservative ICD in the Soret region, and RLS measurements confirm the interaction of p-H_4TCP^{2-} with DNA. Working at pH 9.5, when only about 1% of porphyrin is protonated, these spectroscopic evidences are no more detectable, confirming the relevance of the protonation state to encourage the binding with DNA. However, similar studies on m-H_2TCP^{4-} having a lower p*K*a (~5) indicated that this porphyrin, completely deprotonated at pH 7, is able to interact with DNA. Spectroscopic features such as UV hypochromicity (ca. 20%) of the Soret band at 412 nm (monomeric form), increasing in the intensity of the band at 424 nm, which is assigned to the self-aggregated form, and enhancing of RLS intensity, suggested self-aggregation of m-H_2TCP^{4-} onto the DNA matrix. The small initial CD signal, due to chiral aggregates of m-H_2TCP^{4-}, changes upon addition of DNA, suggesting the preferential binding of one or more chiral aggregates of m-H_2TCP^{4-}, able to fit DNA template through enantioselective binding.

Phthalocyanines, as discussed above, represent another class of macromolecules able to interact with DNA [172]. In particular, positively charged phthalocyanines possess promising photosensitizing properties for the photodynamic therapy of cancer [173]. Anionic copper tetrasulfonated phthalocyanines (H_2TSPc Fig. 19) are able to interact with calf thymus DNA (CT-DNA). The binding process, enthalpically driven, is mainly due to an axial ligation of copper (II) with carbonyl group of thymine and/or the ring nitrogen of the base pair group. Thus, an outside groove-binding mode is suggested. The binding constant ranges from 9.8×10^5 to 0.4×10^5 M^{-1}. The fluorescence of Cu(tspc) was efficiently quenched upon addition of CT-DNA, with a K_{SV} of 5.9×10^3 M^{-1}.

Very recently, Balaz et al. [174] presented a characterization of free-base tetrasulfonato anionic porphyrin (H_2TPPS, Fig. 19) and two metalloderivatives (NiTPPS, ZnTPPS) in the presence of poly(dG–dC) sequence. Based on UV–Vis absorption (very small hypochromic effect and no shift) and CD (no induced CD signal in the Soret absorption region) data, they have concluded that the electrostatic repulsion between negative charges of porphyrin sulfonate groups and B-DNA phosphate backbone effectively prevented interactions of anionic porphyrins.

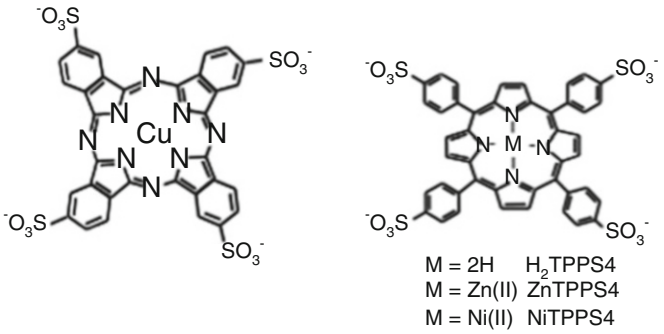

Fig. 19 Molecular structures of anionic phthalocyanines and porphyrins

References

1. Neidle S, Balasubramanian S (2006) Quadruplex nucleic acids. The Royal Society of Chemistry, London
2. Belmont P, Constant J-F, Demeunynck M (2001) Nucleic acid conformation diversity: from structure to function and regulation. Chem Soc Rev 30:70–81
3. Seanger W (1988) Principles of nucleic acid structure. Springer, New York
4. Stryer L (1989) Biochimica. Zanichelli, Bologna
5. Dougherty TJ, Gomer CJ, Henderson BW, Jori G, Kessel D, Korbelik M, Moan J, Peng Q (1998) Photodynamic therapy. J Natl Cancer Inst 90:889–905
6. Pandey RK, Zheng G (2000) Porphyrins as photosensitizer in photodynamic therapy. In: Guilard R, Kadish KM, Smith KM (eds) The porphyrin handbook. Academic, Boston
7. Dougherty TJ, Grindey GB, Fiel RJ, Weishaupt KR, Boyle DG (1975) Photoradiation therapy II. Cure of animal tumors with hematoporphyrin and light. J Natl Cancer Inst 55:115–121
8. Fiel RJ, Mark EH, Datta Gupta N (1975) Res Commun Chem Pathol Pharmacol 10:65–76
9. Boye E, Moan J (1980) The photodynamic effect of hematoporphyrin on DNA. J Photochem Photobiol 31:223–228
10. Fiel RJ, Datta-Gupta N, Mark EH, Howard JC (1981) Induction of DNA damage by porphyrin photosensitizers. Cancer Res 41:3543–3545
11. Croke DT, Perrouault L, Sari MA, Battioni JP, Mansuy D, Helene C, Le Doan T (1993) Structure-activity relationships for DNA photocleavage by cationic porphyrins. J Photochem Photobiol B 18:41–50
12. Levine HI, Fiel RJ, Billmeyer FW Jr (1976) Very low-angle light scattering. A characterization method for high-molecular-weight DNA. Biopolymers 15:1267–1281
13. Fiel RJ, Howard JC, Mark EH, Datta Gupta N (1979) Interaction of DNA with a porphyrin ligand: evidence for intercalation. Nucleic Acids Res 6:3093–3118
14. Sobell HM, Reddy BS, Bhandary KK, Jain SC, Sakore TD, Seshadri TP (1977) Cold springs. Harbor Sym 42:87–102
15. Li HJ, Crothers DM (1969) Relaxation studies of proflavine~DNA complex—kinetics of an intercalation reaction. J Mol Biol 39:461–477
16. McGhee JD, von Hippel PH (1975) Formaldehyde as a probe of DNA structure. I. Reaction with exocyclic amino groups of DNA bases. Biochemistry 14:1281–1296
17. Fiel RJ, Munson BR (1980) Binding of meso-tetra (4-*N*-methylpyridyl) porphine to DNA. Nucleic Acids Res 12:2835–2842
18. Waring M (1970) Variation of the supercoils in closed circular DNA by binding of antibiotics and drugs: evidence for molecular models involving intercalation. J Mol Biol 54:247–279

19. Clewell DB, Helinski DR (1969) Supercoiled circular DNA–protein complex in *Escherichia coli*: purification and induced conversion to an open circular DNA form. Proc Natl Acad Sci U S A 62:1159–1166
20. DeLeys RJ, Jackson DA (1976) Dye titrations of covalently closed supercoiled DNA analyzed by agarose gel electrophoresis. Biochem Biophys Res Commun 69:446–454
21. Pasternack RF, Garrity P, Ehrlich B, Davis CB, Gibbsl EJ, Orloff G, Giartosio A, Turano C (1986) The influence of ionic strength on the binding of a water soluble porphyrin to nucleic acids. Nucleic Acids Res 14:5919–5931
22. Norden B, Tjerneld F (1982) Structure of methylene blue–DNA complexes studied by linear and circular dichroism spectroscopy. Biopolymers 21:1713–1734
23. Giartosio A, Ferraro A, Lavaggi MV, Allegra P, Turano C (1984) The interaction of bisbenzimide with DNA. Physiol Chem Phys Med NMR 16(6):481–490
24. Pasternack RF, Gibbs EJ, Villafranca JJ (1983) Interactions of porphyrins with nucleic acids. Biochemistry 22:2406–2414
25. Pasternack RF, Gibbs EJ, Villafranca JJ (1983) Interactions of porphyrins with nucleic acids. Biochemistry 22:5409–5417
26. Kelly JM, Murphy MJ, McConnell DJ, Ohlligin C (1985) A comparative study of the interaction of 5,10,15,20-tetrakis (*N*-methylpyridinium-4-yl)porphyrin and its zinc complex with DNA using fluorescence spectroscopy and topoisomerisation. Nucleic Acids Res 13:167–184
27. Banville DL, Marzilli LG, Wilson WD (1983) ^{31}P NMR and viscometric studies of the interaction of meso-tetra(4-*N*-methyl-pyridyl)porphine and its Ni(II) and Zn(II) derivatives with DNA. Biochem Biophys Res Commun 113:148–154
28. Lin M, Lee M, Yue KT, Marzilli LG (1993) DNA-porphyrin adducts. Five-coordination of DNA-bound VOTMpyP(4) in an aqueous environment: new perspectives on the V = O stretching frequency and DNA intercalation. Inorg Chem 32:3217–3226
29. Dougherty G (1988) Intercalation of tetracationic metalloporphyrins and related compounds into DNA. J Inorg Biochem 34:95–103
30. Bromley SD, Ward BW, Dabrowiak JC (1986) Cationic porphyrins as probes of DNA structure. Nucleic Acids Res 14:9133–9148
31. Carvlin MJ, Mark E, Fiel R, Howard JC (1983) Intercalative and nonintercalative binding of large cationic porphyrin ligands to polynucleotides. Nucleic Acids Res 11:6141–6154
32. Banville DL, Marzilli LG, Strickland JA, Wilson WD (1986) Comparison of the effects of cationic porphyrins on DNA properties: influence of GC content of native and synthetic polymers. Biopolymers 25:1837–1858
33. Eaton SS, Eaton GR (1975) Rotation of phenyl rings in metal complexes of substituted tetraphenylporphyrins. J Am Chem Soc 97:3660–3667
34. Eaton SS, Fiswild DM, Eaton GR (1978) Effect of para substituent on rates of phenyl ring rotation in gallium complexes of para-substituted tetraphenylporphyrins. Inorg Chem 17:1542–1545
35. Early TA, Kearns DR, Hillen W, Wells RD (1981) A 300- and 600-MHz proton nuclear magnetic resonance investigation of a 12 base pair deoxyribonucleic acid restriction fragment: relaxation behavior of the low-field resonances in water. Biochemistry 20:3756–3764
36. Strickland AJ, Marzilli LG, Wilson WD (1990) Binding of meso-tetrakis (*N*-methylpyridiniumyl) porphyrin isomers to DNA: quantitative comparison of the influence of charge distribution and copper (II) derivatization. Biopolymers 29:1307–1323
37. Park T, Shin JS, Han SW, Son J-K, Kim SK (2004) Stacking of meso-tetrakis(3-*N*-methylpyridiniumyl)porphyrin on poly[d(a-T)2]: importance of the distance between Porphyrin's positive charges. J Phys Chem B 108:17106–17111
38. Ismail M, Rodger PM, Rodger A (2000) Drug self-assembly on DNA: sequence effects with *trans*-bis(4-*N*-methylpyridiniumyl) diphenyl porphyrin and Hoechst 33258. J Biomol Struct Dyn 11:335–348

39. Pasternack RF, Giannetto A, Pagano P, Gibbs EJ (1991) Self-assembly of porphyrin on nucleic acids and polypeptides. J Am Chem Soc 113:7799–7800
40. Pasternack RF, Bustamante C, Collings PJ, Giannetto A, Gibbs EJ (1993) Porphyrin assemblies on DNA as studied by a resonance light-scattering technique. J Am Chem Soc 115:5393–5399
41. Sari MA, Battioni JP, Dupre D, Mansuy D, Le Pecq JB (1988) Cationic porphyrin-DNA interactions: importance of the number and position of the charges. Biochem Pharmacol 37:1861–1862
42. Gibbs EJ, Tinoco I Jr, Maestre MF, Ellinas PA, Pasternack RF (1988) Self-assembly of porphyrins on nucleic acid templates. Biochem Biophys Res Commun 157:350–358
43. Jin B, Ahn JE, Ko JH, Wang W, Han SW, Kim SK (2008) Effect of the position and number of positive charges on the intercalation and stacking of porphyrin to poly[d(G-C)2], poly[d(A-T)2], and native DNA. J Phys Chem B 112:15875–15882
44. Jung JA, Lee SH, Jin B, Sohn Y, Kim SK (2010) Effect of number and position of positive charges on the stacking of porphyrins alone poly[d(a-$T)_2$] at high binding densities. J Phys Chem B 114:7641–7648
45. Pasternack RF, Antebi A, Ehrlich B, Sidney D, Gibbs EJ, Bassner SL, Depoy LM (1984) Interactions of porphyrins with nucleotides and nucleic acids. J Mol Catal 23:235–242
46. Uno T, Bando M, Tanigawa M, Shimabayashi S (1997) Interactions of water-soluble porphyrin with DNA and RNA triplexes. J Inorg Biochem 67:116
47. Hong S, Huh S (2003) Spectroscopic studies on binding interactions of cationic porphyrin derivatives with double helical d(CGCGAATTCGCG)2. Bull Korean Chem Soc 24:137–140
48. Chen X, Liu M (2003) Induced chirality of binary aggregates of oppositely charged water-soluble porphyrins on DNA matrix. J Inorg Biochem 94:106–113
49. Pasternack RF, Ewen S, Rao A, Meyer AS, Freedman MA, Collings PJ, Frey SL, Ranen MC, de Paola JC (2001) Interaction of copper(II) porphyrins with DNA. Inorg Chim Acta 317:59–71
50. Gibbs EJ, Maurer MC, Zhang JH, Reiff WM, Hill DT, Malicka-Blaszkiewicz M, McKinnie RE, Liu HQ, Pasternack RF (1988) Interactions of porphyrins with purified DNA and more highly organized structures. J Inorg Biochem 32:39–65
51. Guliaev AB, Leontis NB (1999) Cationic 5,10,15,20-tetrakis(*N*-methylpyridinium-4-yl)porphyrin fully intercalates at 5′-CG-3′ steps of duplex DNA in solution. Biochemistry 38:15425–15437
52. Lugo-Ponce P, McMillin DR (2000) DNA-binding studies of Cu(T4), a bulky cationic porphyrin. Coord Chem Rev 208:169–191
53. Tabata M, Sarker AK, Nyarko E (2003) Enhanced conformational changes in DNA in the presence of mercury (II), cadmium (II) and lead (II) porphyrins. J Inorg Biochem 94:50–58
54. Tjahjono DH, Akutsu T, Yoshioka N, Inoue H (1999) Cationic porphyrins bearing diazolium rings: synthesis and their interaction with calf thymus DNA. Biochim Biophys Acta 1472:333–343
55. Tjahjono DH, Mima S, Akutsu T, Yoshioka N, Inoue H (2001) Interaction of metallopyrazoliumylporphyrins with calf thymus DNA. J Inorg Biochem 85:219
56. Ward B, Skorobogaty A, Dabrowiak JC (1986) DNA binding specificity of a series of cationic metalloporphyrin complexes. Biochemistry 25:7827–7833
57. Ford K, Fox KR, Neidle S, Waring MJ (1987) DNA sequence preferences for an intercalating porphyrin compound revealed by footprinting. Nucleic Acids Res 15:2221–2234
58. Geacintov NE, Ibanez V, Rougee M, Bensasson RV (1987) Orientation and linear dichroism characteristics of porphyrin-DNA complexes. Biochemistry 26:3087–3092
59. Lee Y-A, Lee S, Cho T-S, Kim C, Han SW, Kim SK (2002) Binding Mode of meso-tetrakis (*N*-methylpyridinium-4-yl)porphyrin to poly[d(I-C)2]: effect of amino group at the minor groove of poly[d(G-C)2] on the porphyrin-DNA interaction. J Phys Chem B 106:11351–11355

60. Shen Y, Myslinski P, Treszczanowicz T, Liu U, Koningstein JA (1992) Picosecond laser-induced fluorescence polarization studies of mitoxantrone and tetrakisporphine/DNA complexes. J Phys Chem 96:7782–7787
61. Lui Y, Koningstein JA, Yevdokimov Y (1991) Relative cross section and time-resolved fluorescence of porphyrin–DNA complexes. Can J Chem 69:1791–1795
62. Dougherty G, Pillbrow JR, Skorobogaty A, Smith TD (1985) Electron spin resonance spectroscopic and spectrophotometric investigation of the binding of tetracationic porphyrins and porphyrazines with calf thymus DNA. Unequivocal evidence for intercalation. J Chem Soc Faraday Trans 81:1739–1759
63. Greiner SP, Kreilick RW, Marzilli LG (1992) Model for the porphyrin-DNA binding site: ENDOR investigations of Cu-porphyrins binding to DNA. J Biomol Struct Dyn 9:837–851
64. Hudson BP, Sou J, Berger DJ, McMillin DR (1992) Luminescence studies of the intercalation of Cu(Tmpyp4) into DNA. J Am Chem Soc 114:8997–9002
65. Dougherty G, Pasternack RF (1992) Base pair selectivity in the binding of copper (II) tetrakis (4-*n*-methylpyridyl)porphine to polynucleotides under closely packed conditions. Biophys Chem 44:11–19
66. Bujte K, Nakamoto K (1990) Interaction of water-soluble Cu(II), Ni(II), and Co(III) porphyrins with polynucleotides. J Inorg Biochem 39:75–92
67. Bujte K, Schneider JH, Kim JJ, Wang Y, Ikuta S, Nakamoto K (1989) Interactions of water-soluble porphyrins with hexadeoxyribonucleotides: resonance raman, UV–visible and 1H NMR studies. J Inorg Biochem 37:119–134
68. Nonaka Y, Lu DS, Dwivedi A, Strommen DP, Nakamoto K (1990) Ir and Raman spectroscopic studies on coulombic interaction between water-soluble porphyrins and nucleic acids. Biopolymers 29:999–1004
69. Schneider JH, Odo J, Nakamoto K (1988) Interaction of water-soluble metalloporphyrins with nucleic acids studied by resonance Raman spectroscopy. Nucleic Acids Res 16:10323–10338
70. Yue KT, Lui M, Gray TA, Marzilli LG (1991) Nickel(II) porphyrin binding to anionic biopolymers investigated by resonance Raman and optical Spectroscopy. Inorg Chem 30:3214–3222
71. Prochazka M, Turpin P-Y, Stepanek J, Bok J (1999) Metallation kinetics of a free base porphyrin in surface-enhanced resonance Raman scattering active Ag colloid system as a probe of porphyrin–nucleic acids interaction. J Mol Struct 482–483:221–224
72. Pasternack RF, Gibbs EJ (1996) Metal ions in biological systems. In: Sigel A, Sigel H (eds) Probing of nucleic acids by metal complexes of small molecules, vol 33. Marcel Decker, New York, pp 367–397
73. Novy J, Urbanova M, Volka K (2005) Vibrational and electronic circular dichroism and absorption spectral study of the DNA–5,10,15,20-tetrakis(1-methylpyridinium-4-yl)porphyrin interaction. J Mol Struct 748:17–25
74. Novy J, Urbanova M, Volka K (2007) Electronic and vibrational circular dichroism spectroscopic study of non-covalent interactions of meso-5,10,15,20-tetrakis(1-methylpyridinium-4-yl)porphyrin with (dG–dC)10 and (dA–dT)10. Vib Spectr 43:71–77
75. Novy J, Urbanova M (2007) Vibrational and electronic circular dichroism study of the interactions of cationic porphyrins with (dG–dC)10 and (dA–dT)10. Biopolymers 4:349–358
76. Lipscomb LA, Zhou FX, Presnell SR, Woo RJ, Peek ME, Plaskon RR, Williams LD (1996) Structure of DNA-porphyrin complex. Biochemistry 35:2818–2823
77. McMillin DR, McNett KM (1998) Photoprocesses of copper complexes that bind to DNA. Chem Rev 98:1201–1220
78. Strickland JA, Banville DL, Wilson WD, Marzilli LG (1987) Metalloporphyrin effects on properties of DNA polymers. Inorg Chem 26:3398–3406
79. Cho DW, Jeong DH, Ko JH, Kim SK, Yoon MJ (2005) Raman spectroscopic studies on interactions of water soluble cationic oxovanadyl (IV) meso-tetrakis(1-methylpyridium-4-yl) porphyrin with nucleic acids. J Photochem Photobiol 174:207–213

80. Liu Y, Koningstein A (1993) Structure studies of H2TMpyP4 and ZnTMpyP4 bound to DNA using laser-induced dichroism in solution. J Phys Chem 97:6155–6160
81. Kuroda R, Tanaka H (1994) DNA–porphyrin interactions probed by induced CD spectroscopy. J Chem Soc Chem Commun 1575–1576
82. Nitta Y, Kuroda R (2006) Quantitative analysis of DNA–porphyrin interactions. Biopolymers 81:376–391
83. Park TG, Ko JH, Ryoo AY, Kim J-M, Cho DW, Kim SK (2006) Binding modes of V(=O) meso-tetrakis(*N*-methylpyridinium-4-yl) porphyrin to various synthetic DNAs studied by polarized spectroscopy. Biochim Biophys Acta 1760:388–394
84. Ohyama T, Mita H, Yamamoto Y (2005) Binding of 5,10,15,20-tetrakis(*N*-methylpyridinium-4-yl)-21H,23Hporphyrin to an AT-rich region of a duplex DNA. Biophys Chem 113:53–59
85. Carvlin MJ, Datta-Gupta N, Fiel RJ (1982) Circular dichroism spectroscopy of a cationic porphyrin bound to DNA. Biochem Biophys Res Commun 108:66–73
86. Pasternack RF, Gibbs EJ (1993) Porphyrin assembly formation on helical biopolymers. J Inorg Organomet Polym 3:77–88
87. Pasternack RF, Goldsmith JI, Szep S, Gibbs EJ (1998) A spectroscopic and thermodynamic study of porphyrin/DNA supramolecular assemblies. Biophys J 75:1024–1031
88. Lee S, Jeon SH, Kim B-J, Han SW, Jang HG, Kim SK (2001) Classification of CD and absorption spectra in the Soret band of H_2TMPyP bound to various synthetic polynucleotides. Biophys Chem 92:35–45
89. Pasternack RF, Collings PJ (1995) Resonance light scattering: a new technique for studying chromophore aggregation. Science 269:935–939
90. Collings PJ, Gibbs EJ, Starr TE, Vafek O, Yee C, Pomerance LA, Pasternack RF (1999) Resonance light scattering and its application in determining the size, shape, and aggregation number for supramolecular assemblies of chromophores. J Phys Chem B 103:8474–8481
91. Monsù Scolaro L, Romeo A, Pasternack RF (2004) Tuning porphyrin/DNA supramolecular assemblies by competitive binding. J Am Chem Soc 126:7178–7179
92. Schuster GB (2000) Long-range charge transfer in DNA: transient structural distortions control the distance dependence. Acc Chem Res 33:253–260
93. Giese B (2002) Long-distance electron transfer through DNA. Annu Rev Biochem 71:51–70
94. Giese B (2002) Electron transfer in DNA. Curr Opin Chem Biol 6:612–618
95. Wagenknecht H-A (2003) Reductive electron transfer and transport of excess electrons in DNA. Angew Chem Int Ed 42:2454–2460
96. Lewis FD (2005) DNA molecular photonics. Photochem Photobiol 81:65–72
97. Wagenknecht H-A (2006) Electron transfer processes in DNA: mechanisms, biological relevance and applications in DNA analytics. Nat Prod Rep 23:973–1006
98. Boon EM, Barton JK (2002) Charge transport in DNA. Curr Opin Struct Biol 12:320–329
99. Núñez ME, Holmquist GP, Barton JK (2001) Evidence for DNA charge transport in the nucleus. Biochemistry 40:12465–12471
100. Núñez ME, Noyes KT, Barton JK (2002) Oxidative charge transport through DNA in nucleosome core particles. Chem Biol 9:403–415
101. Jin B, Min KS, Han SW, Kim SK (2009) DNA-binding geometry dependent energy transfer from4′,6-diamidino-2-phenylindole to cationic porphyrins. Biophys Chem 144:38–45
102. Kim YR, Gong L, Park J, Jang YJ, Ji K, Kim SK (2012) Binding geometry of m-meso-tetrakis (*n*-methylpyridinium-4-yl)porphyrin to DNA and their efficiency as an acceptor in DNA mediated energy transfer. J Phys Chem B 116:2330–2337
103. Raner G, Ward B, Dabrowiak JC (1988) Interaction of cationic manganese porphyrins with DNA. A binding model. J Coord Chem 19:17–23
104. Ward B, Skorobogaty A, Dabrowiak JC (1986) DNA cleavage specificity of a group of cationic metalloporphyrins. Biochemistry 25:6875–7883
105. Gray TA, Yue KT, Marzilli LG (1991) Effect of *N*-alkyl substituents on the DNA binding properties of meso-tetrakis (4-*N*-alkylpyridinium-4-yl) porphyrins and their nickel derivatives. J Inorg Biochem 41:205–219

106. Yun BH, Jeon SH, Cho T-S, Yi SY, Sehlstedt U, Kim SK, Hwa YB, Sun H (1998) Binding mode of porphyrins to poly[d(A-T)2] and poly[d(G-C)2]. Biophys Chem 70:1–10
107. Clark GR, Squire CJ, Gray EJ, Leupin W, Neidle S (1996) Designer DNA binding drugs: the crystal structure of a meta-hydroxy analog of Hoechst 33258 bound to d(CGCGAATTCGCG)2. Nucleic Acids Res 24:4882–4889
108. Satz AL, White CM, Beerman TA, Bruice TC (2001) Double-stranded DNA binding characteristics and subcellular distribution of a minor groove binding diphenyl ether bisbenzimidazole. Biochemistry 40:6465–6474
109. Jia T, Jiang Z-X, Wang K, Li Z-Y (2006) Binding and photocleavage of cationic porphyrin–phenylpiperazine hybrids to DNA. Biophys Chem 119:295–302
110. Kang J, Wu H, Lu X, Wang Y, Zhou L (2005) Study on the interaction of new water-soluble porphyrin with DNA. Spectrochimica Acta A 61:2041–2047
111. Lee M-J, Jin B, Lee HM, Jung MJ, Kim SK, Kim J-M (2008) Direct stacking of non-metallic planar porphyrin to DNA. Bull Korean Chem Soc 29:1533–1538
112. Mukundan NE, Petho G, Dixon DW, Kim MS, Marzilli LG (1994) Interactions of an electron-rich tetracationic tentacle porphyrin with calf thymus DNA. Inorg Chem 33:4676–4687
113. Mukundan NE, Petho G, Dixon DW, Kim MS, Marzilli LG (1995) DNA-tentacle porphyrin interactions: AT over GC selectivity exhibited by an outside binding self-stacking porphyrin. Inorg Chem 34:3677–3687
114. Petho G, Elliott N B, Kim M S, Lin M, Dixon D W, Marzilli L G J (1993) Evidence for formation of DNA-bound protonated porphyrin adducts even at pH 7. Chem Soc Chem Commun 1547–1548
115. Marzilli LG, Petho G, Lin M, Kim MS, Dixon DW (1992) Tentacle porphyrins: DNA interactions. J Am Chem Soc 114:7575–7577
116. McClure JE, Baudouin L, Mansuy D, Marzilli LG (1997) Interactions of DNA with a new electron-deficient tentacle porphyrin: meso-tetrakis[2,3,5,6-tetrafluoro-4-(2-trimethylammoniumethyl-amine)phenyl]porphyrin. Biopolymers 42:203–217
117. Manono J, Marzilli PA, Fronczek FR, Marzilli LG (2009) New porphyrins bearing pyridyl peripheral groups linked by secondary or tertiary sulfonamide groups: synthesis and structural characterization. Inorg Chem 48:5626–5635
118. Manono J, Marzilli PA, Marzilli LG (2009) New porphyrins bearing positively charged peripheral groups linked by a sulfonamide group to meso-tetraphenylporphyrin: interactions with calf thymus DNA. Inorg Chem 48:5636–5647
119. Kobuke Y, Miyagi H (1994) Supramolecular organization of imidazolyl-porphyrin to a slipped cofacial dimer. J Am Chem Soc 116:4111–4112
120. Milgrom LR, Dempsey PJF, Yahioglu G (1996) 5,10,15,20-Tetrakis(N-protected imidazol-2-yl)porphyrins. Tetrahedron 52:9877–9890
121. Bruix M, Elguero J, Meutermans W (1992) Synthesis and atropisomerism of meso-tetrapyrazolylporphyrins. J Chem Res (S) 370–371
122. Werner A, Sanchez-Migallon A, Fruchier A, Elguero J, Fernandez-Castano C, Foces-Foces C (1995) Porphyrins with four azole substituents in meso-positions: X-ray crystal structure of meso-tetrakis(1-benzylpyrazol-4-yl)porphyrin at 200 K. Tetrahedron 51:4779–4800
123. Tjahjono DH, Kartasasmita RE, Nawawi SM, Yoshioka TAN, Hidenari Inoue A (2006) Binding of tetrakis(pyrazoliumyl)porphyrin and its copper(II) and zinc(II) complexes to poly (dG–dC)2 and poly(dA–dT)2. J Biol Inorg Chem 11:527–538
124. Tjahjono DH, Suhendar PB, Yoshioka N, Inoue H (2010) Binding of nickel(II) tetrakis (dimethylpyrazolium-4-yl) porphyrin to poly(dG–dC)2 and poly(dA–dT)2. J Porph Phthal 14:305–313
125. Yamamoto T, Tjahjono DH, Yoshioka N, Inoue H (2003) Interaction of dicationic bis (imidazoliumyl) porphyrinatometals with DNA. Bull Chem Soc Jpn 76:1947–1955

126. Thornton NB, Wojtowicz H, Netzel T, Dixon DW (1998) Intramolecular quenching of porphyrin fluorescence by a covalently linked ferrocene in DNA scaffolding. J Phys Chem B 102:2101–2110
127. Garcia G, Sarrazy V, Sol V, Le Morvan C, Granet R, Alves S, Krausz P (2009) DNA photocleavage by porphyrin–polyamine conjugates. Bioorg Med Chem 17:767–776
128. He H, Tian T, Wang P, Wu L, Xu J, Zhou X, Zhang X, Cao X, Wu X (2004) Porphyrin–DNA cross-linking agent hybrids: chemical synthesis and biological studies. Bioorg Med Chem Lett 14:3013–3016
129. He H, Zhou Y, Liang F, Li D, Wu J, Yang L, Zhou X, Zhang X, Cao X (2006) Combination of porphyrins and DNA-alkylation agents: synthesis and tumor cell apoptosis induction. Bioorg Med Chem 14:1068–1077
130. Yang SI, Seth J, Strachan J-P, Gentemann S, Kim D, Holten D, Lindsey JS (1999) Tuning the building blocks for porphyrin-based photonic devices. J Porph Phthaloc 3:117–147
131. Narra M, Elliott P, Swavey S (2006) Synthesis, characterization and DNA interactions of 5,15-(4-pyridyl)-10,20-(pentafluorophenyl) porphyrin coordinated to two[Ru(bipy)2Cl] + groups. Inorg Chim Acta 359:2256–2262
132. Davia K, King D, Hong Y, Swavey S (2008) A porphyrin–ruthenium photosensitizer as a potential photodynamic therapy agent. Inorg Chem Commun 11:584–586
133. Craver E, McCrate A, Nielsen M, Swavey S (2010) Tris-ruthenium(II)/copper(II) multimetallic porphyrin: synthesis, characterization, DNA binding and supercoiled DNA photocleavage studies. Inorg Chim Acta 363:453–456
134. Lippard SJ (1995) Progress in inorganic chemistry: bioinorganic chemistry, vol 48. Wiley, Sydney
135. Xu Z, Swavey S (2011) Photoinduced DNA binding of a multi-metallic (Cu(II)/Ru(II)/Pt(II)) porphyrin complex. Inorg Chem Commun 14:882–883
136. Langa K, Anzenbacher P Jr, Kapusta P, Kral V, Kubat P, Wagnerova DM (2000) Long-range assemblies on poly(dG–dC)2 and poly(dA–dT)2: phosphonium cationic porphyrins and the importance of the charge. J Photochem Photobiol B 57:51–59
137. Kubat P, Lang K, Kral V, Anzenbacher P Jr (2002) Preprogramming of porphyrin-nucleic acid assemblies via variation of the alkyl/aryl substituents of phosphonium tetratolylporphyrins. J Phys Chem B 106:6784–6792
138. Yellappa S, Seetharamappa J, Rogers LM, Chitta R, Singhal RP, D'Souza F (2006) Binding, electrochemical activation, and cleavage of DNA by cobalt(II) tetrakis-*N*-methylpyridyl porphyrin and its β-pyrrole brominated derivative. Bioconjug Chem 17:1418–1425
139. Mettath S, Munson BR, Pandey RK (1999) DNA interaction and photocleavage properties of porphyrins containing cationic substituents at the peripheral position. Bioconjug Chem 10:94–102
140. Sari MA, Battioni JP, Dupre D, Mansuy D, Lepecq JB (1996) Mode of interaction and apparent binding constants of meso-tetraaryl porphyrins bearing between one and four positive charges with DNA. Biochem Biophys Res Commun 141:643–649
141. Sari MA, Battioni JP, Dupre D, Mansuy D, Lepecq JB (1990) Interaction of cationic porphyrins with DNA: importance of the number and position of the charges and minimum structural requirements for intercalation. Biochemistry 29:4205–4215
142. Sessler JL, Sansom PI, Kral V, O'Connor D, Iverson BL (1996) Sapphyrin−oligonucleotide conjugates. Novel sequence-specific DNA photomodifying agents with increased binding affinity. J Am Chem Soc 118:12322–12330
143. Magda D, Wright M, Miller RA, Sessler JL, Sansom PI (1995) Sequence-specific photocleavage of DNA by an expanded porphyrin with irradiation above 700 nm. J Am Chem Soc 117:3629–3630
144. Wan S, Parrish JA, Anderson RR, Madden M (1981) Transmittance of nonionizing radiation in human tissues. Photochem Photobiol 34:679–681
145. Kral V, Furuta H, Shreder K, Lynch V, Sessler JL (1996) Protonated sapphyrins. Highly effective phosphate receptors. J Am Chem 118:1595–1607

146. Sessler JL, Andrievsky A, Sansom PI, Kral V, Iverson BL (1997) Enhanced DNA photocleavage and binding properties of sapphyrin–polyamine conjugates. Bioorg Med Chem Lett 7:1433–1436
147. Iverson BL, Shreder K, Kral V, Smith DA, Smith J, Sessler JL (1994) Interactions between expanded porphyrins and nucleic acids. Pure Appl Chem 66:845–850
148. Sessler JL, Burrell AK (1991) Expanded porphyrins. Top Curr Chem 161:177–273
149. Iverson BL, Shreder K, Kral V, Sansom P, Lynch V, Sessler JL (1996) Interaction of sapphyrin with phosphorylated species of biological interest. J Am Chem Soc 118:1608–1616
150. Gershman Z, Goldberg I, Gross Z (2007) DNA binding and catalytic properties of positively charged corroles. Angew Chem Int Ed 46:4320–4324
151. Liu HY, Liu LY, Zhang L, Ying X, Wang X-L, Jiang H-F, Chang C-W (2007) Oxidative DNA cleavage catalyzed by Mn(III) corroles. Chem J Chin Univ 28:1628–1630
152. Lu J, Liu HY, Shi L, Wang XL, Ying X, Zhang L, Ji LN, Zang LQ, Chang CK (2011) DNA cleavage mediated by water-soluble manganese corrole. Chin Chem Lett 22:101–104
153. D'Urso A, Nardis S, Pomarico G, Fragalà ME, Paolesse R, Purrello R (2013) Interaction of tricationic corroles with single/double helix of homopolymeric nucleic acids and DNA. J Am Chem Soc 135:8632–8638
154. Zenkevich E, Saguna E, Knyukshto V, Shulga A, Mironov A, Efremova O, Bonnett R, Songca SP, Kassem M (1996) Photophysical and photochemical properties of potential porphyrin and chlorin photosensitizers for PDT. J Photochem Photobiol B 33:171–180
155. Ricchelli F (1995) Photophysical properties of porphyrins in biological-membranes. J Photochem Photobiol B 29:109–118
156. Taima H, Okubo A, Yoshioka N, Inoue H (2006) DNA-binding properties and photocleavage activity of cationic water-soluble chlorophyll derivatives. Chem Eur J 12:6331–6340
157. Gantchev TG, Ali H, van Lier JE (1993) Interactions of chloroaluminium-tetramethyl-tetrapyridino-porphyrazine with DNA. Eur J Biochem 217:371–376
158. Asadi M, Safaei E, Ranjbar B, Hasani L (2005) A study on the binding of two water-soluble tetrapyridinoporphyrazinato copper(II) complexes to DNA. J Mol Struct 754:116–123
159. Anderson ME, Barrett AGM, Hoffman BM (1999) Super-charged porphyrazines: synthesis and physical properties of octacationic tetraazaporphyrins. Inorg Chem 38:6143–6151
160. Anderson ME, Barrett AGM, Hoffman BM (2000) Binding of octa-plus porphyrazines to DNA. J Inorg Biochem 80:257–260
161. Chatterjee SR, Srivastava TS, Kamat JP, Devasagayam TPA (1998) Photocleavage of plasmid pBR322 DNA by some anionic porphyrins. J Porphr P 2:337–343
162. Li Y, Geyer R, Sen D (1996) Recognition of anionic porphyrins by DNA aptamers. Biochemistry 35:6911–6922
163. Lavallee DK (1988) Porphyrin metalation reactions in biochemistry. Mol Struct Energ 9:279–314
164. Dailey HA, Fleming JE (1983) Bovine ferrochelatase. Kinetic analysis of inhibition by *N*-methylprotoporphyrin, manganese, and heme. J Biol Chem 258:11453–11459
165. Cochran AG, Schultz PG (1990) Antibody-catalyzed porphyrin metallation. Science 249:781–783
166. Schultz PG, Lerner RA (1995) From molecular diversity to catalysis: lessons from the immune system. Science 269:1835–1842
167. Lauceri R, Purrello R, Shetty SJ, Vicente MGH (2001) Interactions of anionic carboranylated porphyrins with DNA. J Am Chem Soc 123:5835–5836
168. Vicente MGH, Shetty SJ, Wickramasinghe A, Smith KM (2000) Syntheses of carbon–carbon linked carboranylated porphyrins for boron neutron capture therapy of cancer. Tetrahedron Lett 41:7623–7627
169. Haushalter RC, Rudolph RW (1978) Meso-tetracarboranyl porphyrins. J Am Chem Soc 100:4628–4629
170. Kahl SB, Joel DD, Nawrocky MM, Micca PL, Tran KP, Finkel GC, Slatkin DN (1990) Uptake of a nido-carboranylporphyrin by human glioma xenografts in athymic nude mice and

by syngeneic ovarian carcinomas in immunocompetent mice. Proc Natl Acad Sci U S A 87:7265–7269
171. Miura M, Gabel D, Oenbrink G, Fairchild RG (1990) Preparation of carboranyl porphyrins for boron neutron capture therapy. Tetrahedron Lett 31:2247–2250
172. Dezhampanah H, Darvishzad T, Aghazadeh M (2011) Thermodynamic and spectroscopic study on the binding of interaction anionic phthalocyanine with calf thymus DNA. Spectroscopy 26:357–365
173. Wohrle D, Iskandar N, Graschev G, Sinn H, Friedrich EA, Maier-Borst W, Stern J, Schlag P (1990) Synthesis of positively charged phthalocyanines and their activity in the photodynamic therapy of cancer cells. Photochem Photobiol 51:351–356
174. Choi JK, D'Urso A, Balaz M (2013) Chiroptical properties of anionic and cationic porphyrins and metalloporphyrins in complex with left-handed Z-DNA and right-handed BDNA. J Inorg Biochem 127:1–6

Index